FORSCHUNGSZENTRUM JÜLICH GmbH

Institut für Festkörperforschung

Hydrogen and Hydrogen-Helium Mixtures under High Pressure

A Density Functional and Molecular Dynamics Study

Oliver Pfaffenzeller

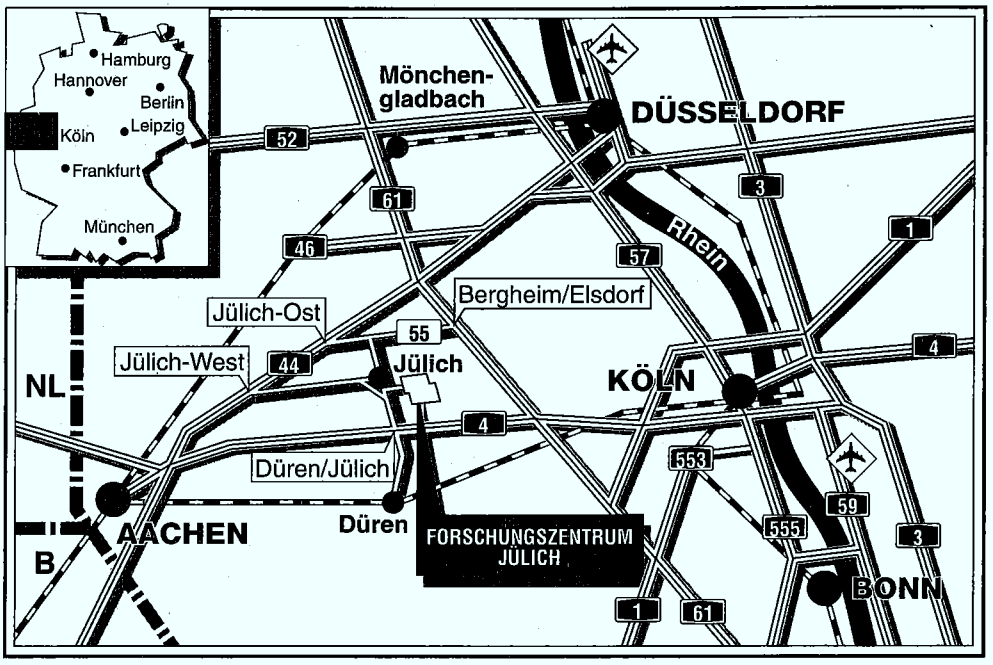

Berichte des Forschungszentrums Jülich ; 3281
ISSN 0944-2952
Institut für Festkörperforschung Jül-3281
D82 (Diss. RWTH Aachen)

Zu beziehen durch: Forschungszentrum Jülich GmbH · Zentralbibliothek
D-52425 Jülich · Bundesrepublik Deutschland
Telefon: 02461/61-6102 · Telefax: 02461/61-6103 · Telex: 833556-70 kfa d

Hydrogen and Hydrogen-Helium Mixtures under High Pressure

A Density Functional and Molecular Dynamics Study

Oliver Pfaffenzeller

Contents

Preface

What kind of element is hydrogen? Its deceptively simple composition of electrons and protons contrasts with a miscellany of displayed phenomena and a protean versatility. Its special role among the elements continues to fascinate a large community of physicists. On one hand hydrogen is only one electron short of having a closed shell and ranks with fluorine, chlorine and the halogens as group VII elements. Similar to those elements it forms tightly bound molecules under normal conditions, the bond being mediated by the sharing of electrons (covalency). On the other hand one can regard hydrogen as a group I element. Like the alkali metals it has one (outer) electron at its disposal for chemical interactions. However it is a "reluctant alkali" [9] and the analogy only holds at high pressures. In the Mbar pressure range the H molecules give up their identity and the pressure transforms molecular, insulating hydrogen into an atomic metal. Since the required pressures are at the limit of or beyond current experimental capabilities ($\sim$ 2.5 Mbar), much of our knowledge about the high pressure phases of hydrogen relies on theoretical investigations. It has been pointed out that the complex behavior of hydrogen in the molecular-atomic transition region defies treatment with simple, empirical models. Instead, accurate simulations require the full quantum mechanical determination of the interaction, e.g. in the framework of density functional theory [12]. Here we apply a combination of molecular dynamics and density functional theory (Car-Parrinello method) to study the high pressure behavior of hydrogen. This method allows us to investigate hydrogen in a wide pressure range ($\sim$ 1 – 100 Mbar). We examine the gradual dissociation of the hydrogen molecules, the change in the ground state structure, and the onset of metallization. At the highest pressure we enter the domain of plasma physics.

In the universe the high pressure phases of hydrogen are realized e.g. in the giant planets, Jupiter and Saturn, which consist mainly of hydrogen and a smaller amount of helium. Presently Jupiter is in the focus of attention through "the Galileo Mission" [89], i.e. the investigation of the planetary atmosphere by the Galileo spacecraft. For the interpretation of the collected data, knowledge of the physics of the interior in these planets is indispensable. For example, the large magnetosphere of Jupiter is due to the metallization of hydrogen in the inner envelope of Jupiter. Its high pressure properties, e.g. the conductivities of metallic

hydrogen, are needed as input to models of the external magnetic field.
Another experimental observation that requires a theoretical explanation is the large excess energy radiation of the giant planets. For example, Jupiter radiates almost twice the amount of energy it receives from the sun. To explain the excess energy output, R. Smoluchowski [173] invoked phase separation of hydrogen and helium in the interior of Jupiter. Helium droplets nucleate from the heavier phase and sink to the center of the planet releasing gravitational energy. Phase separation is desirable as an explanation for the excess energy radiation of Saturn but not Jupiter. In view of its astrophysical importance, the study of hydrogen at high pressures is one of the key problems in modern physics and astrophysics [61]. For a quantitative understanding of the physics in the interiors of the giant planets it is crucial to go beyond the study of the pure phase. We investigate an astrophysical H-He mixture at Mbar pressures. The inert helium atoms are a major perturbation to the hydrogen system, leading to significantly different structural and electronic properties. We also compute the demixing temperatures for high pressure H-He mixtures and discuss the implications for the interiors of the giant planets.
In the following we introduce the reader to a small part of the "Hydrogen World" [149] and the disturbance of this world by helium "intruders", and we hope to capture some of the fascinating complexity of two "simple" systems.

Chapter 1

Review of Hydrogen and Hydrogen-Helium Mixtures

1.1 Hydrogen

1.1.1 Introduction

Hydrogen (H), with only one electron and one proton, is the simplest atomic species that exists and comprises 90 % of the universe. In spite of its (apparent) simplicity, H displays a miscellany of interesting physical phenomena that have been studied extensively. Under normal conditions ($P = 1.013$ bar, room temperature), H forms a tenuous light gas consisting of diatomic H_2 molecules. At $T = 14$ K and $P = 1.013$ bar H crystallizes in molecular form in an hexagonal close packed (hcp) solid with nearly ideal packing ($c/a = (8/3)^{1/2}$) and the molecules rotating freely around their positions. In the H_2 molecule the proton spins add up to either $I = 0$ (para-H_2) or $I = 1$ (ortho-H_2). Since the total wave function has to be antisymmetric, the antisymmetric spin singlet state of para-H_2 requires a symmetric spatial wave function and the symmetric spin triplet states of ortho-H_2 an antisymmetric spatial wave function. The rotor eigenfunctions $Y_J^m(r)$ with even total angular momentum are even under inversion $\vec{r} \longrightarrow -\vec{r}$ and odd total angular momentum implies odd symmetry with respect to inversion. It follows that the possible rotational states for para-H_2 are $J = 0,2,4,...$ and for ortho-H $J = 1,3,5,...$ At low enough temperatures only the energetically lowest rotational states are occupied. Para-H_2 is rotationally symmetric ($J = 0$), and no preferred orientation of the molecules exists in either the free molecule or the solid. In solid ortho-H_2 with $J = 1$ the electric quadrupole-quadrupole (EQQ) interactions drive a phase transition at $T = 4$ K to an ordered structure. The favored structure consists of molecules on the positions of a face centered cubic (fcc) lattice with the four molecules in the conventional unit cell aligned along the different body-diagonals ([111], [11$\bar{1}$], [1$\bar{1}$1], and [$\bar{1}$11] in the crystallographic notation; see figure 1.1). This structure minimizes the most important

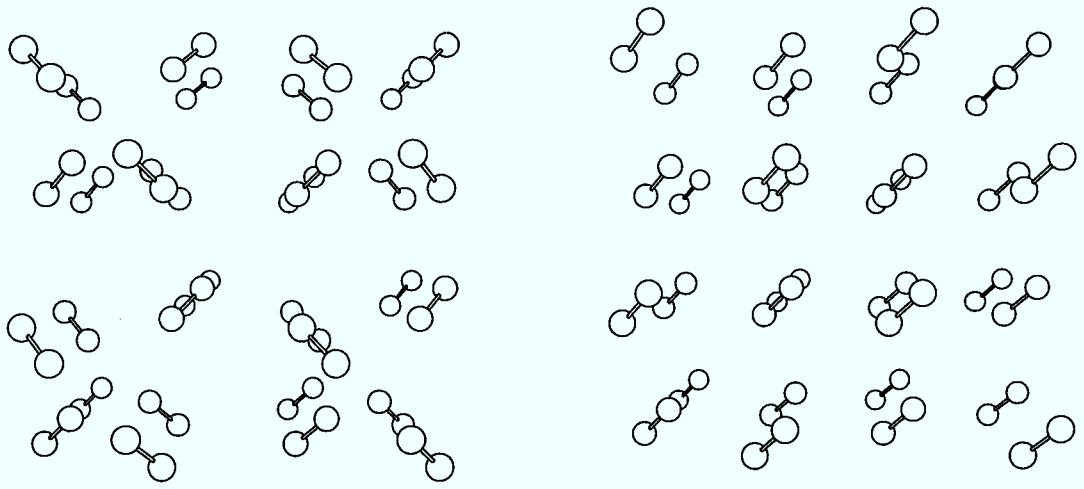

Figure 1.1: The Pa3 structure (*left*). The centers of the molecules form a fcc lattice. The four crystallographically different molecules are aligned along the different body-diagonals [111], [11$\bar{1}$], [1$\bar{1}$1], and [$\bar{1}$11]. On the *right* side a fcc lattice with the all molecules aligned along the [111] axis is shown.

contribution to the anisotropic interactions (the EQQ) and plays an important role in the search for the ground state structure at higher pressures. Henceforth we will refer to this structure by its crystallographic name, Pa3. At $T = 0$ K ortho-H_2 is metastable and slowly transforms to para-H_2. Distinguishing both species is crucial at low pressures where the composition of the sample exerts a strong influence on the low temperature properties. In the high pressure range the molecular wave functions overlap, J ceases to be a good quantum number, and the distinction between ortho- and para-H_2 is no longer meaningful. Below Para-H_2 is implied when the prefix para/ortho is omitted.
Hydrogen has two isotopes, Deuterium (D) and Tritium (T). Radioactive T is inconvenient to investigate, but D has been treated for the same pressure range as H. The comparison of the experimental high-P results of H and D is very important, because it allows to learn about the mass-dependence of physical properties. The molecular solid at low pressures is now well characterized [171, 193]. The molecules in the hcp solid have the same bond length as free molecules (1.40 a.u.). The intermolecular distance is much larger (7.18 a.u.). In many respects the H solid resembles rare-gas solids. For example, the charge distribution of the H_2 molecules is nearly spherical, the individual molecules interact via induced dipole-dipole interaction, and the solid is an insulator with a band gap of 16 eV. Pressurized H has attracted attention for a long time. As early as 1926 Fowler [52] found that H will form a dense plasma for extreme pressures and temperatures. In a seminal paper 1935 Wigner and Huntington [196] predicted H to metallize at a pressure of 25 GPa, far beyond the experimental capabilities at

that time. For the regime of the insulator-metal transition a variety of exotic properties have been proposed. In 1968 Ashcroft [6] suggested metallic H to be a high-T_c superconductor. Barbee et al. [15, 13] used density functional theory (DFT, see section 2.1.2) and the frozen-phonon method to calculate the superconductivity transition temperature for different structures of atomic H at high pressures. They predicted the transition to occur between 120 and 230 K at $r_s = 1.3$ ($P = 4$ Mbar). (Density is often measured in terms of the electronic spacing parameter r_s, defined by $4\pi/3(r_s r_b)^3 \equiv 1/n$, where n is the average density of electrons and r_b is Bohr's radius ($0.529177 \cdot 10^{-8}$ cm)).
The mechanism of the insulator-metal transition has drawn a lot of attention. Excitonic behavior could delay the metallization. Insulating molecular H has electronic excitons with intermediate binding in the forbidden gap between the valence and conduction band [87]. As discussed in [88, 63], at the semiconductor-semimetall transition electrons and holes can combine to form a non-conducting phase. The ordinary Bloch wave ground state of the crystal could become unstable against the spontaneous formation of excitons if the exciton binding energy exceeded the energy gap. This instability is expected to occur in any crystal that can be made to change continuously at low temperature from a semimetal to an indirect gap semiconductor by varying the lattice constant under pressure. As will be discussed later, H was proposed to exhibit an indirect band gap closure under pressure [154, 55]. Another possible mechanism deferring metallization is Anderson-type localization arising from rotational disorder of the molecules rather than static disorder [7].
In 1972 Brovman et al. [27] suggested that H might exist in a metallic state at atmospheric pressure. It would have an energy much higher than the molecular state and a nearly one order of magnitude higher density and therefore would be metastable. The same authors also proposed H to have a liquid ground state in the metallic phase driven by quantum fluctuations [28]. Oliva and Ashcroft [140] showed that a liquid metallic phase would constitute a two-component Fermi liquid with a specific heat and thermal expansion coefficient much greater than in the corresponding solid due to the presence of proton quasiparticle excitations in the liquid [140].

1.1.2 Experimental Techniques

The metallization of H has been subject of popular presentations. The newspaper "The Economist" published an article about this problem [187] and Physics World devoted an entire issue "in celebration of H" [149]. Metallizing H is not as simple as The Economist suggests (see figure 1.2) and it is appropriate to say a few words about how to "really" do it. There are two experimental ways to pressurize a material, dynamical high pressure (shock compression) and static high pressure. Shock waves are generated either by high explosives or gas guns [201]. For the investigation of H a method to attain static high pressures, the

Figure 1.2: The metallization of H as seen from the newspaper "The Economist". The actual procedure is not quite as simple as the newspaper suggests. The figure was taken from [187].

diamond-anvil cell, is of great importance. Although it is described in many monographs [168, 170, 201, 169, 115, 116] it is worthwhile to give a brief outline to describe the opportunities and restrictions of this experimental approach to H under high pressure. A schematic drawing of a diamond-anvil cell is given in figure 1.3. The sample is confined between the tips of the anvils. Because of the enormous stress on the anvils they are made of flawless diamonds. Since pressure is force divided by area the pressure will be the stronger the smaller the anvil tips are. For high pressures the tips are very small (20 ... 600 μm in diameter) leading to a severe limitation of the method, the small sample volume. There is a tradeoff between sample volume and maximum pressure. For example, at 50 GPa, the volume can be as large as a nanoliter; in the multimegabar range it is subpicoliter. Therefore the minimum sample volume (and correspondingly the wave length of the probing radiation) for a given type of measurement limits the attainable pressure.

Dynamical high pressure has played an important role in the investigation of H, too. The highest pressures in shock compression experiments on H were generated by a group from Livermore [133, 76, 195]. Their apparatus, a gas gun, is

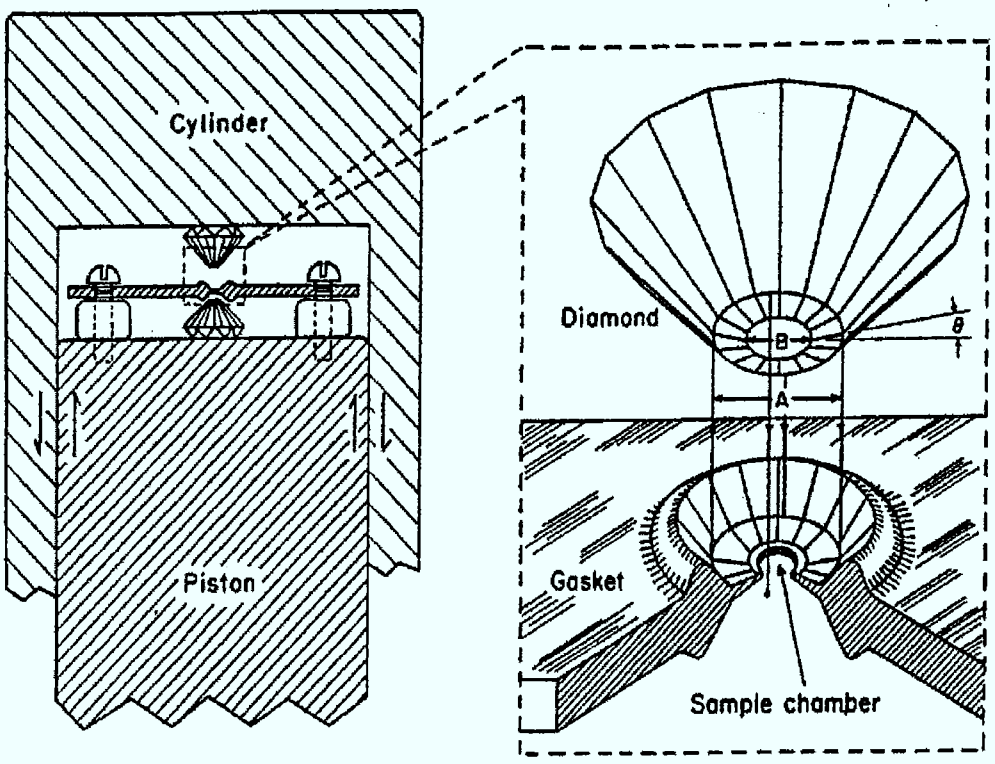

Figure 1.3: Schematic drawing of a diamond-anvil cell. The size of the device is extremely small. The tip B is 20 to 600 μm in diameter. The entire apparatus is a tabletop (or even laptop) device. The figure was taken from [116].

sketched in figure 1.4. Strong shocks are generated in liquid H and D samples by impact of projectiles driven by a two-stage light-gas gun. When the shock reaches the 2nd window of higher shock impedance than the fluid samples, the shock is reflected and the sample is reshocked to a new state of higher pressure and temperature. The shock reverberates between baseplate and window, eventually reaching a quasi-constant state. The shock temperatures are measured optically using a multi-channel fiber-optic-coupled optical pyrometer. The shock pressure can be determined from the measured impactor velocity and the known Hugoniot equations of state of the impactor. With this method a maximum pressure of 180 GPa was reached [195].
In the next section the most important experimental results at high pressures and low temperatures will be outlined. The higher temperature investigations via shock compression will be addressed in section 1.1.5, which treats the finite temperature properties of high pressure H.

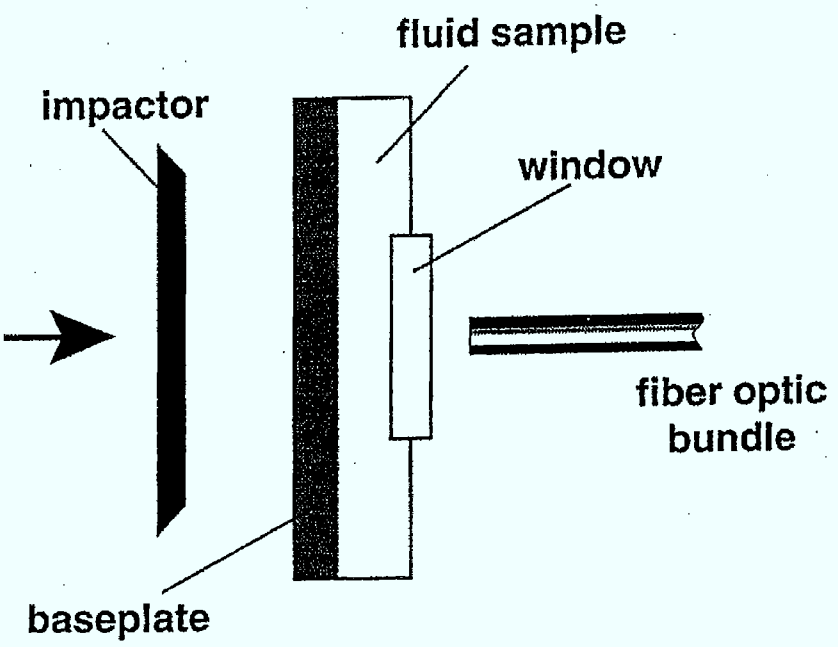

Figure 1.4: Schematic drawing of the apparatus used by [76, 195]. The impactor generates a strong shock wave on impact with the baseplate. The shock traverses the baseplate and then the liquid H and is reflected when it reaches the 2nd window. The sample is reshocked from the reflected shock. The first and the second shock are observed as sharp rises in the luminosity. Luminosities are measured versus time with a multi-channel photomultiplier array coupled with fiber optics to the sample holder.

1.1.3 Experimental Results

Among the experimental probing techniques applied to H and D at moderate pressures ($P \leq 50$ GPa) are [116]

- x-ray diffraction for structure analysis
- neutron scattering for structure analysis
- Brillouin spectroscopy for probing the elasticity of H.

These techniques fail at higher pressures, because of the small sample volume. At higher pressures spectroscopy is applied for probing the excitations of the dense solid, especially the vibrational excitations such as intramolecular stretches (vibrons), rotations (rotons), and lattice vibrations (phonons). For the investigation of the low temperature phase diagram at $P \geq 50$ GPa

- Raman spectroscopy and
- infrared (IR) vibrational spectroscopy

are of special importance. Raman spectroscopy can be applied to study the intramolecular bonds. Infrared dipole absorption is forbidden in the free hydrogen molecule but becomes allowed as a result of intermolecular interactions in the dense solid and provides a means to probe the interactions between the individual molecules. The diamond anvil cell measurements identified three different phases in the high pressure regime ($P \geq 100$ GPa)

1. Phase I
   Although H is a bad scatterer of x-rays (the scattering intensity is proportional to Z^2), experiments have been performed on H up to 42 GPa exploiting synchrotron radiation and improved detection systems. Mao, Hemley, and coworkers [118, 71, 78] found an orientationally disordered hcp lattice with the c/a ratio decreasing from its ideal value of $c/a = 1.63$ to 1.61 at $P = 42$ GPa indicating increased anisotropy of the crystal. For the detection of the other phases Raman and IR spectra were decisive (see figure 1.5).

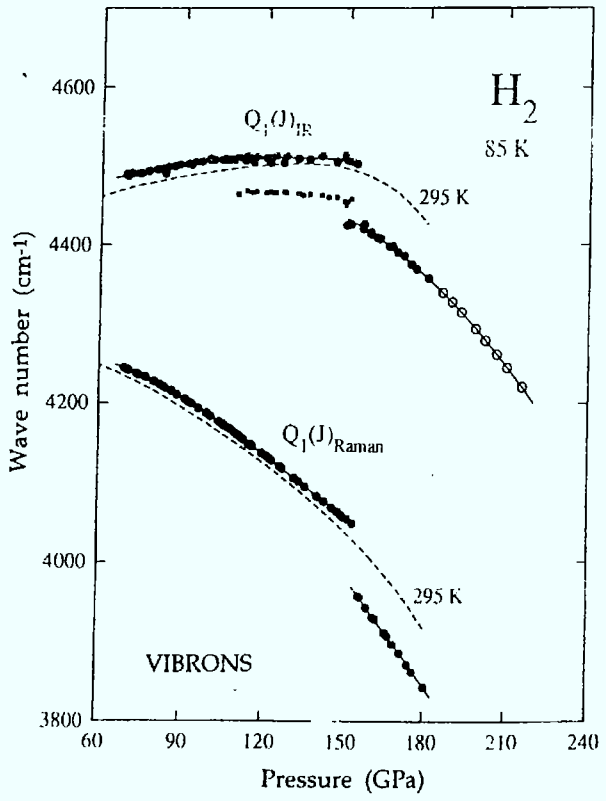

Figure 1.5: Pressure dependences of the Raman and infrared vibron frequencies $[Q_1(J)_{\text{Raman}}]$ and $[Q_1(J)_{\text{IR}}]$ at 85 K showing the I-II phase transition at 110 GPa and the II-III phase transition at 150 GPa. The 295-K data (Phase I) are given by the dashed curves. The figure was taken from [116].

2. Phase II: The broken symmetry phase (BSP)
   Lorenzana, Silvera and Goettel [110] detected a discontinuity of 15 cm^{-1} in the frequency of the Raman vibron at 110 GPa and T = 8 K (which is not seen in figure 1.5 because of the higher temperature) and a new peak in the IR vibron 45 cm^{-1} below the principal vibron. The splitting of the vibron may indicate that the orientationally ordered structure has a lower symmetry than hcp (therefore the name "broken symmetry phase"). If so, one of the much studied structures, an hcp lattice with the molecules aligned along the c-axes (mhcp-c, see figure 1.8) is ruled out as a candidate, because it has the same point symmetry as the molecular lattice with random orientation.

3. Phase III: H-A phase
   Phase III was detected in 1988 when Hemley and Mao [69] discovered a discontinuity of about 100 cm^{-1} in the Raman vibron of an ortho/para H_2 mixture at 150 GPa and 77 K. Hanfland et al. [65] found in 1993 that the IR vibron exhibits a discontinuity coinciding with that in the Raman spectrum. Recent measurements showed the existence of a triple point at about $T = 125$ K and $P = 155$ GPa [70] (see figure 1.6). Lorenzana, Goettel

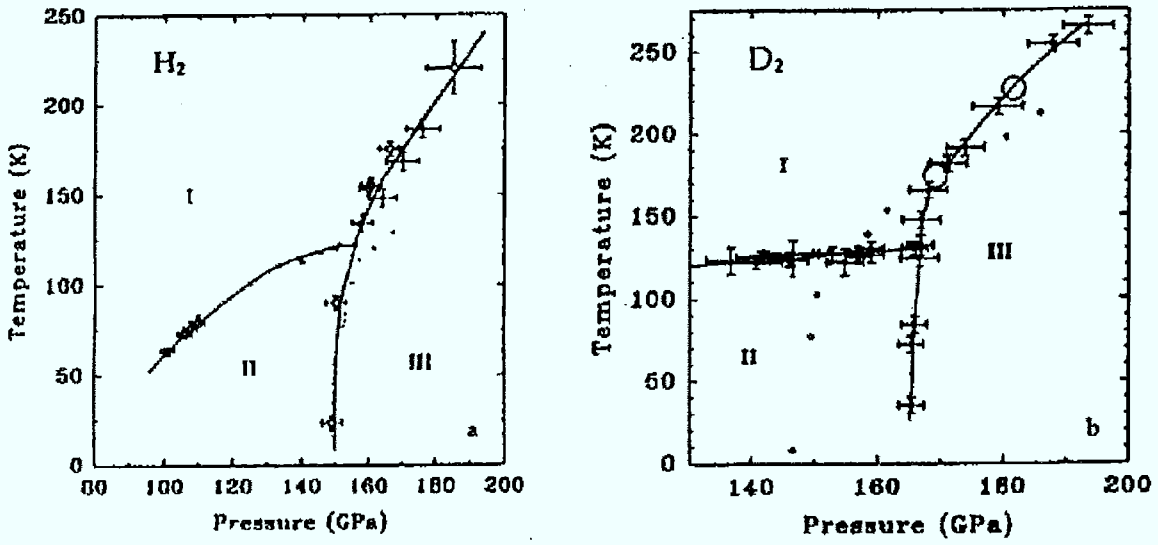

Figure 1.6: Phase I-II-III triple points of H_2 and D_2 constructed from experimental data. The figure was taken from [70].

and Silvera [110] investigated the temperature and ortho/para composition dependence of the phase line and called phase III "H-A phase". It has been proposed that phase III is the long sought after "metallic" phase

of hydrogen [116], and that the indirect band gap closes in a molecular structure. Further experimental studies of the optical reflectivity have *not* confirmed this proposition [42]. The complex structure of the vibronic peaks seems to suggest a low-symmetry structure of this phase with at least 8 molecules (16 atoms) per unit cell.

4. Beyond phase III:
   Mao and Hemley [119] performed optical studies on H up to more than 250 GPa. The Raman vibron does not disappear up to this pressure. Thus 250 GPa constitutes a lower limit for the transition to an atomic state for which excitations of molecules do no longer exist. Although a sudden increase in optical opacity around 250 GPa would suggest that the sample becomes metallic, no conclusive experimental evidence for metallization exists in this pressure range [115].

The experimental situation for H and D is summarized in figure 1.7. Note that

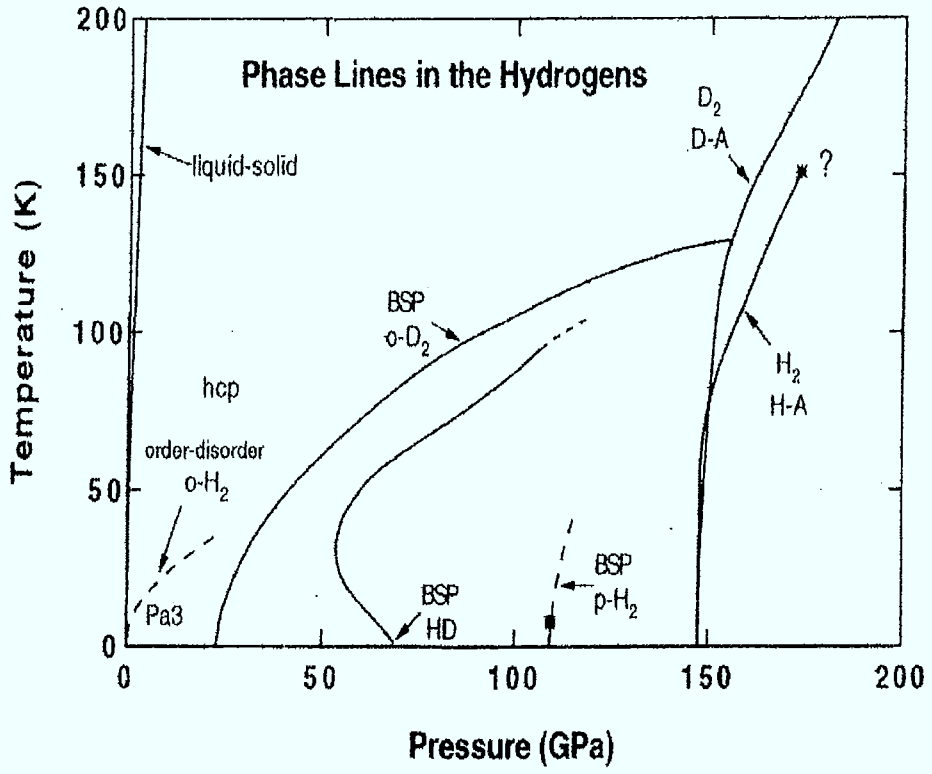

Figure 1.7: A phase diagram for H and D. Dotted lines indicate expected behavior. The critical point of the H-A line of H is probably a triple point (see figure 1.6). The figure is taken from [42].

no definitive structure information can be derived from the scarce experimental data in phases II and III.

1.1.4 Theoretical Results in the Mbar Range for Low Temperatures

The first prediction of the metallization pressure by Wigner and Huntington was 25 GPa, much too low as we know today. Since then numerous calculations treated H in the molecular-atomic transition regime. The main uncertainty stems from the fact that the true ground state structure is unknown. Its knowledge is indispensable for the prediction of the physical properties. Most calculations rely on guesses. As will be seen (chapter 6), the Car-Parrinello scheme, a dynamical method, provides a systematic improvement over static computations for searching and testing possible candidates for the ground state structure.
In 1975 Ramarker, Kumar, and Harris [154] used the Hartree-Fock method to search for metallization. They performed calculations on a simple cubic (sc) molecular structure and a body centered cubic (bcc) atomic structure. More important than their value for the transition pressure, 210 GPa, was their observation that metallization occurs by band gap closure in the molecular phase. Their work suggested the idea that the transition to an atomic structure and the metallization of H are two different transitions, the metallization occurring at lower pressure in the molecular phase by indirect band gap closure (The same mechanism was found in molecular iodine, which is gradually metallized between 4 and 17 GPa. The dissociation of the iodine molecules does not take place until the substantially higher pressure of $\sim$ 70 GPa [122]). This idea was corroborated by Friedli and Ashcroft [55] and Wood and Ashcroft [197] who used a more realistic structure for the molecular phase, Pa3. On the decrease of the intermolecular distances anisotropic interactions come into play, the EQQ being the most important one. The structure that minimizes the EQQ is Pa3, the ground state structure of ortho-H. Thus Pa3 is a better guess than sc (but still not the correct one).
In 1981 Chakravarty et al. [198] used DFT to compute a metallization pressure of 200 GPa. They also pointed out (as earlier Strauss and Ashcroft [183]) that the energy differences between different structures in the Mbar regime are much smaller than the energy in the zero point motion of the protons.
Min, Jansen, and Freeman [125] used a full-potential linearized augmented plane wave (LAPW) method (i.e.,a mixed basis set for the expansion of the wave functions with the electronic many-body problem being treated in the framework of DFT) to study the high pressure phases of H [125]. Performing computations on a Pa3 structure in the molecular phase and a sc lattice in the atomic phase they found a metallization pressure of 170 $\pm$ 20 GPa and a pressure of 400 $\pm$ 100 GPa for the transition to the atomic state. When in 1988 Mao and Hemley

detected the transition to the H-A phase at 150 GPa these results gave rise to the assumption that finally the metallic, molecular phase had been found. Yet up to now there is no clear experimental evidence for metallization [42]. The pressure dependence of the band gap in the molecular H solid cannot be studied directly in a diamond anvil cell due to the strong UV absorption of diamond. However, the pressure dependence of the electronic absorption edge in hydrogen can be determined indirectly by measuring the dispersion of the refractive index in the visible (see e.g. [48]). From the experimental data one can extrapolate that direct band gap closure requires pressures above 300 GPa [116]. The study of the Drude absorption curve was not conclusive with regard to indirect band gap closure (see e.g. [42]) and further investigations must be awaited.
The experimental successes inspired some sophisticated theoretical investigations. Ceperley and Alder [31], Natoli, Martin, and Ceperley [129, 130] and Natoli [128] used quantum Monte Carlo (MC) methods incorporating the zero point motion of protons. Ceperley and Alder studied isotropic fcc (i.e., random orientation of the molecules on fcc lattice sites), Pa3, hcp with the molecules aligned along the [111] direction and γ-nitrogen lattices in the molecular phase and cubic lattices in the atomic phase and found an ordering transition at 100 GPa and a transformation from molecular Pa3 to a fcc or bcc atomic phase at a pressure of 300 ± 40 GPa. They also reported the effect of the zero point motion to be significant ($\sim$ 0.3 eV/atom, much larger than the energy differences between different ground state structures). Natoli et al. studied mhcp-c and mhcp-o (see figures 1.8 and 1.9)

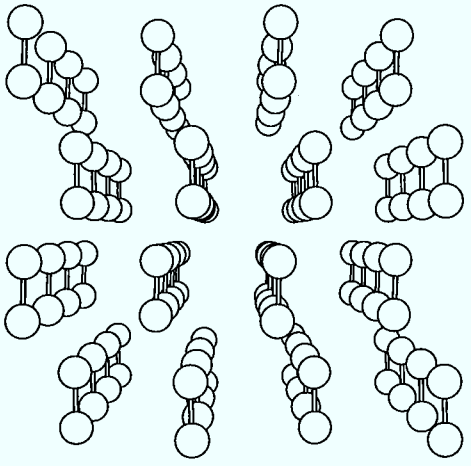

Figure 1.8: The mhcp-c structure. The molecules are on hcp lattice sites with the molecules aligned along the c-axis.

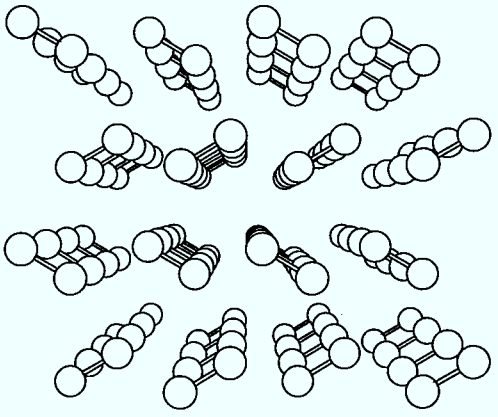

Figure 1.9: The mhcp-o structure. The molecules are on hcp lattice sites and form 60^o angles with the c-axis and 60^o angles with the molecules of the next layers.

in the molecular [130] and a variety of structures (see figure 1.10) in the atomic phase [129]. They predicted the molecular-atomic transition to be from a molecu-

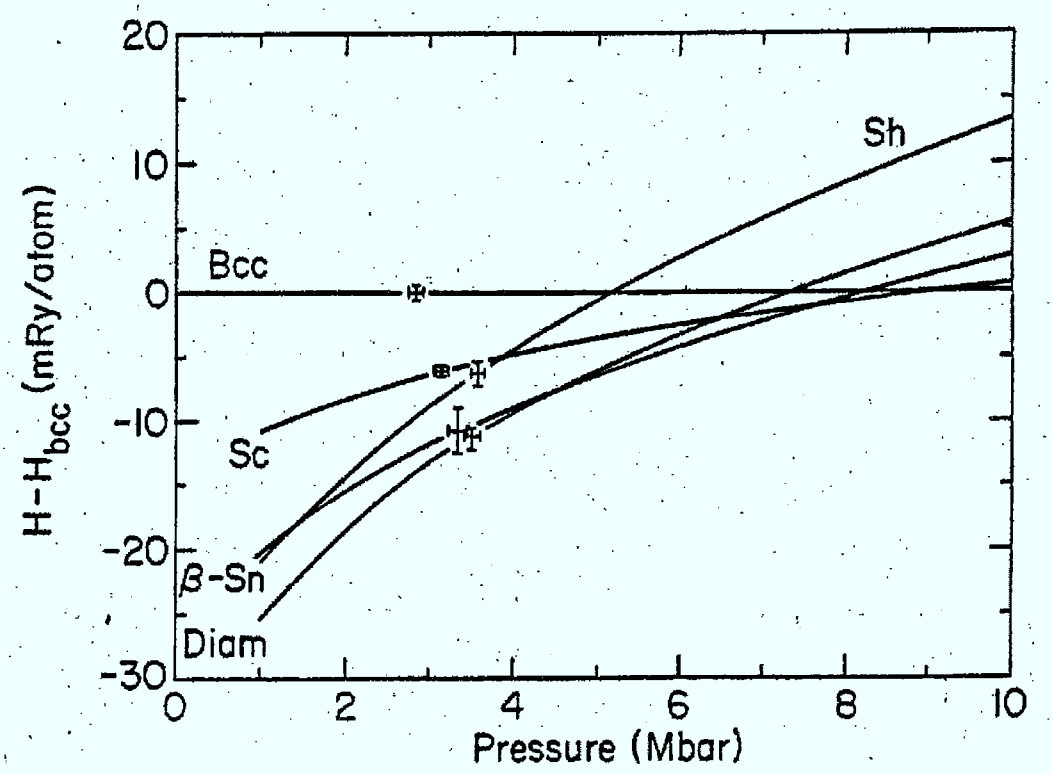

Figure 1.10: Qantum MC results for the enthalpy differences of different atomic structures. The reference structure is bcc, which in the high pressure limit bcc will be the favored structure due to the lowest Madelung energy. The figure was taken from [128].

lar mhcp-o lattice to an atomic diamond structure at a pressure of 230 $\pm$ 25 GPa. The relevant energy differences are small. Ar $r_s = 1.45$ the mhcp-o structure was preferred by 0.07 eV/atom over the diamond structure, whereas at $r_s = 1.31$ the diamond structure is more stable by 0.16 eV/atom. Natoli [128] also showed the importance of the inclusion of the zero point motion, which has to be treated beyond the harmonic approximation ("frozen phonon") because of anharmonic effects. For example his diffusion Monte Carlo calculations without zero point contribution for the simple hexagonal (sh) structure at r_s =1.31 resulted in a total energy of -1.0325 Ry/atom, whereas diamond had a higher energy, -1.0235 Ry/atom. The inclusion of the zero point energy changed the energetical order of the structures. The total energy of the sh structure became -0.988 Ry/atom versus an energy of -0.993 Ry/atom for the diamond structure. Natoli pointed

out that although LDA is good in providing the correct trend for the ordering of structures, it may fail in giving the correct details where two structures lie energetically very close together. However, statistical and systematical errors in his quantum Monte Carlo calculations are comparable in size to the energy differences sought.
Path-integral Monte Carlo calculations were used to study the molecular ordering of H_2 in the pressure range of 50-200 GPa [114, 96]. These studies reported ordering transitions, but could not clearly identify them with the experimentally observed phase transitions.
Extensive studies of H under high pressure were performed with density functional theory (also see chapter 6). Barbee et al. [16] studied several structures with DFT/LDA and included the zero point motion via an estimation of the harmonic part of the zero point motion energy (quasiharmonic approximation). They proposed a phase transition to a low coordinate phase built up of layers and filaments at 380 ± 50 GPa and to a close packed structure (bcc) at 860 ± 100 GPa (see figure 1.11). An extended study [14] confirmed this trend. Garcia

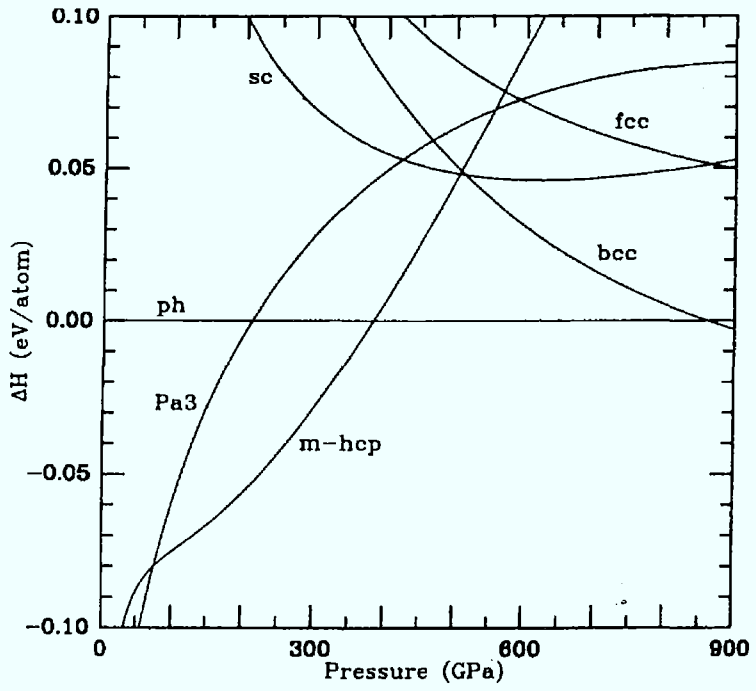

Figure 1.11: The enthalpy differences of different atomic and molecular structures computed via DFT/LDA and the quasiharmonic approximation for the zero point motion energy [16]. The reference configuration is the simple-hexagonal phase (ph).

et al. [59] computed the metallization pressure for H_2 molecules on a hcp lattice. They found the pressure to be extremely sensitive to the orientation of the molecules in the solid. The metallization pressure changed more than 100 GPa for different orientations. The orientation of the molecules on a hcp lattice was optimized by Kaxiras, Broughton, and Hemley [95] and Kaxiras and Broughton [94] in the pressure range of the transition to the H-A phase ($\sim$ 150 GPa). They found mhcp-o to be the best candidate for the ground state structure. Nagara and Nakamura [127] extended the search to structures with 4 molecules per unit cell and showed a structure called $Pca2_1$ to be favored over mhcp-o. They predicted molecular dissociation to occur at 600 GPa. The most recent calculations on the metallization pressure of H were performed by Chacham and Louie [34] and Suhr, Barbee, and Mailhiot [184]. Chacham and Louie applied a first-principle quasiparticle method to avoid the errors stemming from the commonly applied local density approximation (LDA, see section 2.1.2). The LDA provides a good description of ground-state properties of solids, but fails in quantitatively describing the excitation spectra, giving band gaps that are typically too small by a factor of two. For a quantitative study of metallization by band overlap, the inclusion of many-electron effects in calculating the quasiparticle band gap is necessary. Chacham and Louie computed quasiparticle energies in the framework of Hedin's GW approximation, in which the electronic self-energy is approximated by a convolution of the one-electron Green's function and the dynamically screened Coulomb interaction. They treated H_2 molecules on a hcp lattice with random orientation and aligned along the c-axis (mhcp-c), and found metallization pressures of 300 and 151 GPa, respectively. Although the metallization pressure of the mhcp-c structure is suggestively close to the H-A line (149 GPa), the experimental result certainly corresponds to a different transition, because other structures, such as mhcp-o and $Pca2_1$, are more stable. The big discrepancy in the transition pressure for the two different orientations confirms the high sensitivity of the metallization pressure to the molecular orientation found by Garcia et al. [59]. Suhr, Barbee, and Mailhiot [184] studied different molecular orientations on a $Pca2_1$ lattice. They proposed the observed H-A transition to be an insulator-metal transition plus orientational transition. Using a frozen phonon approximation they demonstrated that the zero point energy can be substantially lower (up to 50 meV/dimer) in metallic structures than in insulating ones. Thus in calculating the metallization pressure the inclusion of the proton zero point motion is crucial. It is also important to point out the high energy resolution needed. For comparing the total energies of different structures the inclusion of many $\vec{k}$-points (or alternatively many atoms in the unit cell) is mandatory. For example, Suhr, Barbee and Mailhiot used 768 $\vec{k}$-points in their computations. Simulated annealing studies of the ground state structures [75, 191] showed that the ground state structure probably is more complicated than those structures considered.

The following tentative scenario of the pressure dependence of the ground state structure summarizes the most important results:

- For low pressures, $P \leq 42$ GPa, experiments prove the ground state structure to be hcp, the molecules are disordered and the solid is insulating. For higher pressures reliable structure experiments are not feasible and the determination of the ground state structure relies on theoretical investigations in combination with indirect experimental methods.

- Between 42 and $\sim$ 300 GPa a molecular or nearly molecular ground state structure is favored. Experimentally two transitions have been observed, at 110 GPa (BSP) and 150 GPa (H-A). Quantum MC calculations ([114, 96]) suggest an ordering transition in this pressure regime. Thus the BSP transition could be an ordering transition from a randomly oriented hcp lattice to possibly mhcp-o, $Pac2_1$, or mhcp-c. If the ground state structure is mhcp-c then it does not prevail up to 150 GPa, i.e., another transition occurs between 110 and 150 GPa, because other structures such as mhcp-o and $Pac2_1$ are more stable around 150 GPa (see section 6 and [128, 130]). At higher pressures more complex unit cells are favored (see [127, 75, 191] and section 6). Therefore the H-A transition could be a transition to a more complex structure, possibly the string-like structure discussed in chapter 6. In this pressure regime geometrically very different structures lie energetically close together. For this reason it is likely that other transitions occur between 150 and 300 GPa.

- At $\sim$ 300 GPa the molecules dissociate and a low coordinate atomic structure is favored, possibly a diamond, filamentary simple-hexagonal or rhombohedral structure (see figure 1.10, figure 1.11 and [14]).

- Between $\sim$ 300 and $\sim$ 1000 GPa other transitions to probably higher coordinate structures may occur. Possible candidates for structures are the β-Sn and the simple cubic structure.

- At $\sim$ 1000 GPa bcc finally becomes the most stable structure [16, 14, 128]. bcc is the expected end point, because at high pressures the Madelung energy dominates and the bcc lattice has the largest Madelung constant. Thus in the high pressure limit H crystallizes in an atomic, close packed lattice, bcc, which has one atom per primitive unit cell and is metallic.

- At much higher pressures, $P \geq 10^{10}$ GPa, the quantum fluctuations cause the ground state to be liquid.

Thus in the low ($P \leq 42$ GPa) and very high ($P \geq 1000$ GPa) pressure range the ground state structures are well established but in the intermediate pressure range from 42 - 1000 GPa only tentative phase diagrams can be constructed

and structural trends given. The exact metallization pressure is a matter of uncertainty, too. The lower bound, 150 GPa, is set by experiment. However, whether the H-A transition is an insulator-metal transition remains unclear. Also, whether the metallization occurs by indirect band gap closure in the molecular phase is an open question. In all likelihood the atomic phase is metallic, although there is no trivial evidence.(Some of the proposed structures in the atomic phase (e.g., diamond) have an even number of electrons in the primitive unit cell and may be insulators.) 150 and 300 GPa.
A clarification of the situation is difficult, because

- in the 50-1000 GPa regime several structures lie energetically close together, requiring an electronic structure method with
- high energy resolution, i.e., the inclusion of a large number of $\vec{k}$-points.
- The energetically favored structures are possibly more complex than those one can describe with two or four molecules per unit cell. The shape of the unit cell may be complicated and should be included in the optimization. The introduction of the cell parameters in the dynamics is a standard technique in classical molecular dynamics ("Parrinello-Rahman method"). This technique was introduced into first principles MD only recently [51].
- The zero point motion of protons plays a decisive role. Anharmonic effects are not negligible. Frozen phonon calculations can be wrong by up to 100 % [128].

To solve all these problems together is far beyond current feasibility. The only practical approach is to study the crucial physical contributions piece by piece and to try to put the individual pieces together. On the way to a complete picture the treatment of high pressure H with the Car-Parrinello method plays an important role. It allows us to study trends by dynamical optimization of structures, to perform simulated annealing runs to find new structures, and to test the stability of structures by heating the system. In addition the Car-Parrinello extends the scope of electronic structure methods to the exploration of finite temperature properties.

1.1.5 H at Elevated Temperatures

The investigation of the finite temperature properties of hydrogen is crucial for an understanding of the physics of the giant planets (see section 1.2) and the phenomena associated with nuclear fusion. On the experimental side shock-compression experiments [133, 76, 195] are important, because they can probe hydrogen at higher T (93-180 GPa and T = 2200-4400 K in the latter publication). The experiments in diamond anvil cells presently are limited to about

1500 K [201]. Another advantage of these experiments is the larger sample volume. Conductivity measurements can be performed. The implications of these experiments for hydrogen will be discussed in chapter 10. It will be seen that in many respects high pressure hydrogen resembles an alkali metal (see also [72]). Another important result of this work is the observation that the effective interactions between atoms in the monatomic state are much less repulsive than in the molecular one. In consequence, the dissociation energy is a function of pressure. It decreases monotonically with increasing density from 4.8 eV at ambient pressure to zero at the molecular-atomic transition pressure where the molecular-atomic transition takes place. A naive extrapolation of an equation of state from the low density range will give a curve too stiff in the high-P regime, because it does not account for the energy that goes into the gradual dissociation of the molecules.

For finite temperatures many less first principles calculations were performed than for the study of the ground state structure. Hohl et al. [75] investigated H for r_s = 1.78-1.31 (35-350 GPa) and for temperatures up to 3000 K. They observed the weakening of the intramolecular bonds with increasing pressure and the decrease of the dissociation energy for molecular H. Furthermore they demonstrated the inaccuracy of simple models for dense H, such as the treatment of high pressure H as a mixture of H_2 molecules and H atoms. The dissociation of the molecules is a continuous process and in the transition regime even more complex entities form, consisting of two or more H atoms aligned in filaments. The definition of bonds between H atoms and the identification of molecules is far from being clear, because at finite temperature dissociation occurs continuously across a wide pressure range.

Theilhaber treated H in the molecular and in the metallic regime [188, 189]. For r_s = 1.0 he found the one component plasma (OCP) model (see section 7) to overestimate the melting temperature by at least a factor of two. Kohanoff and Hansen [100] investigated H in the metallic regime (r_s = 0.5 and 1.0) and compared their results with OCP and a perturbative method that treats the coupling between electrons and ions within linear screening theory. Kwon et al. [105], Kwon, Kress, and Collins [106], and Collins et al. [41, 40] investigated H over a wide density (0.1-3 g/cm^2) and temperature (1-5 eV) range using ab initio molecular dynamics and tight binding methods. They showed that in the limit of high T and/or high P the OCP model provides a good description; but for a wide P- and T-range the electron-ion interaction has to be incorporated in the treatment. An interesting extension of the Car-Parrinello method was introduced by Alavi et al. [2, 3]. These authors applied finite temperature density functional theory to H in the pressure range where metallization occurs. (They replaced the functional for the total energy of the electronic system by a functional for the Helmholtz free energy. The new functional incorporates the effects of thermal electronic excitations.)

The accuracy of theoretical descriptions strongly rely on the method used. At

lower pressures ($P \leq 2.5$ GPa) pair-potentials can be applied to model the intermolecular interaction (see [171]). In the GPa range the attractive many-body forces become important, and the equation of state computed with pair potentials tends to be too stiff [71]. Hemley et al. [71] introduced an additional ad-hoc short-range term to account for the many-body forces and fitted their experimental data to the modified two-body potential. In this way they obtained a theoretical equation of state that agrees well with the experimental data (see chapter 5). Besides from being unsystematic this procedure suffers from the disadvantage that it will fail at higher pressures, because an additional two-body term does not provide a mathematically correct description of many-body interactions (see the discussion in chapter 5). Also, such a simple description treats the molecules as rigid entities and will be inapplicable in the pressure regime where the molecules dissociate. Holmes, Ross, and Nellis [76] and Saumon and Chabrier [160] constructed models where a fraction of the molecules is dissociated, i.e., two species coexist, H and H_2. Although these models provide a better equation of state for high pressure than treatments restricted to molecules, the picture of a mixture of H and H_2 is far too simple. As mentioned before and discussed in section 7.1, the definition of molecules in the pressure range of dissociation is somewhat arbitrary and more complex entities arise. Even a model with H-H, H-H_2 and H_2-H_2 two-body interactions will fail in describing many physical processes, such as the forming and breaking of bonds.

Thus for an adequate description of the properties of H at Mbar pressures the explicit inclusion of the electronic structure is mandatory. As Kwon, Kress, and Collins [106] demonstrated, the tight-binding approach provides a useful tool. Another approximation is provided by the Thomas-Fermi model. Zérah, Clérouin, and Pollock [204, 37] used a combination of the Thomas-Fermi method and molecular dynamics to simulate H plasmas [204, 37] and to compute the equation of state at high pressures ($r_s = 1.0$ and 2.0) [144]. The most complete and precise treatment of the interactions (and the electronic structure) so far is provided by ab initio molecular dynamics (section 2.2).

For a wide pressure range in the metallic regime none of the contributions to the interactions is small enough to be treated as a small perturbation (the ion-ion interaction, the electron-ion interaction and the electron-electron interaction). Only at very high pressures and/or temperatures the electron-ion interaction may be treated perturbationally, and finally, for even higher pressures/temperatures, electrons and ions can be simulated as two separate systems via the jellium model and OCP, respectively.

1.2 Hydrogen-Helium Mixtures - An Excursion to Astrophysics

The collision of comet Shoemaker-Levy 9 with Jupiter in 1993 (e.g. see [108]) aroused much interest in the largest planet of our solar system. The present space probe "Galileo" had quite a few predecessors (Voyager I, Voyager II, Pioneer 10, Pioneer 11 and some others) probing the outer envelope of Jupiter. Much is known about Jupiter. In 1980 Stevenson even stated [179]: "In many respects, the interior of Jupiter is better understood than the interior of any other planet, including the earth".
The good understanding is a consequence of the simplicity of the composition. A comparison of the mass-radius relationship for zero temperature spheres of various composition [179] shows that the radii of Jupiter ($\approx$ 71500 km) and Saturn ($\approx$ 60300 km) are close to the maximum radius ($\approx$ 80000 km for a pure H sphere) for a gravity stabilized zero-temperature body. Since the thermal heat content of a planet is much less than the gravitational energy the zero-temperature data provide a reasonable approximation and specify the composition of the giant plants as predominantly hydrogen.
Information about the state of matter deep within these planets can be obtained from observational data, such as

1. Chemical composition of the atmosphere
2. Heat radiation
3. Magnetic fields
4. Response of the planet to rotational perturbations (gravitational multipole moments)
5. Free oscillation frequencies of the planet

These observational data provide constraints for planetary models. Jupiter and Saturn are believed to consist of a central rock core surrounded by an envelope of fluid H, He, and a small contribution of heavier elements. Usually, the envelope is modelled by a fluid H-He mixture where a He contribution of 7-10 atomic per cent is assumed [179, 80, 33]. The temperature profile in these planets is believed to be adiabatic, the adiabats ranging from about 1 bar and 100 K at the outer atmosphere to 45 Mbar and 20000 K for Jupiter and 10 Mbar and 10000 K for Saturn at the core (see figure 1.12). The main uncertainties stem from

- the equation of state of H. Usually the equation of state for the planetary interior is constructed from equations of state for H and He. He is well tractable in the relevant pressure range (see section 1.3) but H is difficult

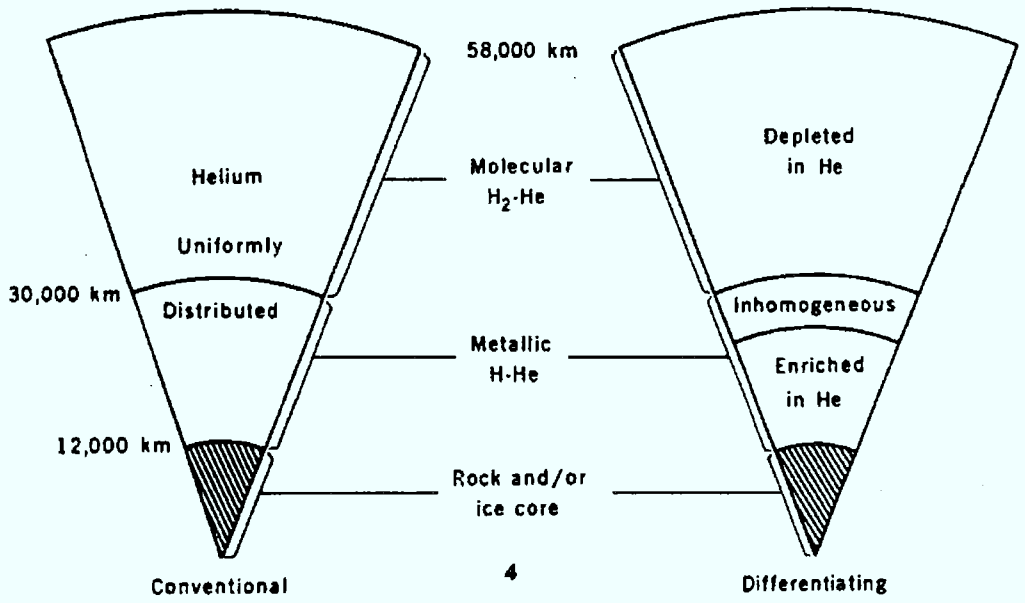

Figure 1.12: Section of Saturn without and with phase separation. The interior of Jupiter probably looks like the left drawing (not differentiating) with about a 12000 km larger radius and a larger fraction of the envelope being in the metallic phase. The figure was taken from [179].

to treat in the range of the plasma phase transition (PPT, as the astrophysicists call the transition of H from an insulating to a conducting state). This transition may be first order for temperatures relevant for Jupiter and Saturn [161, 33].

- composition of the planets. The true fraction of He is unknown and still subject to some speculations. Duffy et al. [47] even claimed that the He fraction has to be much larger than hitherto assumed (15 instead of 7-10 atomic per cent for models with a homogeneous envelope) for the models to be compatible with measured sound velocities of H under high pressures. The effect of the contribution of heavier elements is not well investigated.

- inhomogeneities in the distribution of the elements. The suggestion that phase separation between H and He might occur in the envelope of the giant plants is of major importance [173, 159].

The last item presents the motivation for part of this work. In the following it is discussed in more detail. Both planets exhibit a large excess heat radiation, i.e., they radiate much more energy than they absorb from the sun. The measured heat radiation can be used to estimate the age of the planets. Following the

account of [177] we present a simple way to perform this estimation:
We assume that the planetary envelopes are homogeneous and adiabatic, and the energy source of the excess heat radiation is assumed to be the radiation of internal heat stored during the formation of the planets, i.e., radiative cooling. Then the excess luminosity L is equal to the rate of change of internal thermal energy:

$$L = 4\pi R^2 \sigma (T_e^4 - T_0^4) = -\frac{d}{dt}\left(\frac{4}{3}\pi R^3 \bar{C}_v T_i\right), \tag{1.1}$$

where R is the radius, σ is the Stefan-Boltzmann constant, T_e is the actual effective temperature, T_0 is the effective temperature in the absence of an internal heat source, $\bar{C}_v$ is the average specific heat per unit volume, and T_i is some average internal temperature. The interior is assumed to be adiabatic, and T_i and T_e can be related by

$$T_i = T_e \left(\frac{P_i}{P_e}\right)^n, \tag{1.2}$$

where P_i is a characteristic internal temperature, P_e is the effective pressure (i.e., the pressure at optical depth unity in the atmosphere) and $n \approx 0.25$ is the average adiabatic index. It can be argued ([177]) that P_i and P_e change much more slowly then T_i and T_e and can be regarded as constant during most of the evolution. Thus T_i is approximately proportional to T_e. Furthermore, it can be shown that T_i changes much more rapidly than R or $\bar{C}_v$. Then 1.1 is to a good approximation an ordinary differential equation that can be solved by separation of the variables

$$t_f - t_i = \frac{\frac{4}{3}\pi R^3 \bar{C}_v T_{i,f}}{4\pi R^2 \sigma \left(T_{e,f}^4 - T_0^4\right)} \frac{T_{e,f}^4 - T_0^4}{T_{e,f}} \int_{T_{e,i}}^{T_{e,f}} \frac{dT_e}{T_0^4 - T_e^4}, \tag{1.3}$$

where the indices i and f refer to the initial and final state. Let t_i be the time when cooling sets in and t_f our present time. Then the age of the planet can be obtained by

$$\begin{aligned} t_0 &= \alpha \cdot \frac{\text{present heat content}}{\text{present excess luminosity}} \\ \alpha &\equiv (1 - q^4) \int_1^{x_m} \frac{dx}{x^4 - q^4}, \end{aligned} \tag{1.4}$$

where $q = T_0/T_{e,f}$, $x = T_e/T_{e,f}$ and $x_m = T_{e,i}/T_{e,f}$. This crude model gives

$t_0 \approx (4 \pm 1) \cdot 10^9$ years for Jupiter and

$t_0 \approx (2 \pm 1) \cdot 10^9$ years for Saturn.

Refined calculations do not differ substantially from the above crude analysis. Both planets are expected to have the age of our solar system, 4.5 billion years. Within error bars the models assuming a homogeneous H-He mixture give this

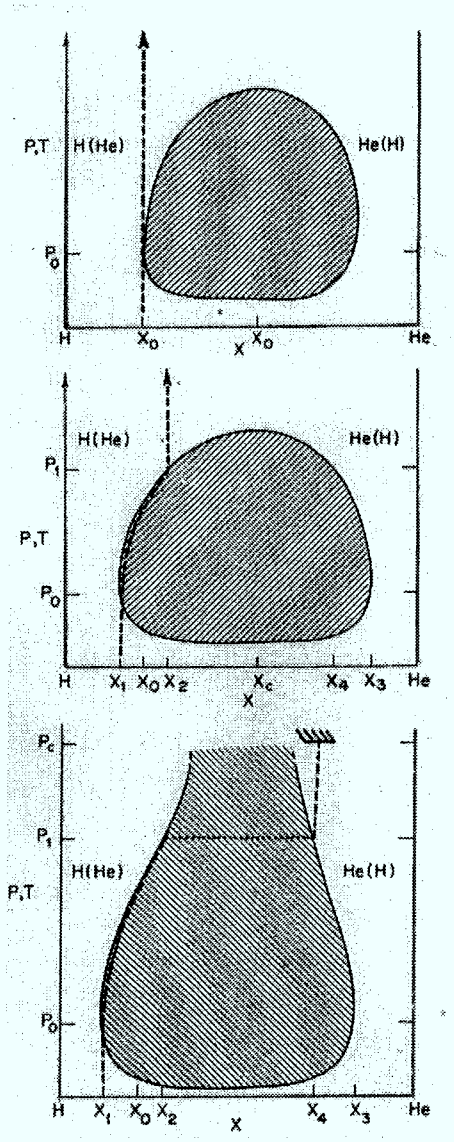

Figure 1.13: The inhomogeneous evolution of a H-He planet at three different stages of the evolution. The dashed line is the helium number fraction as a function of the pressure within the planet. The region of immiscibility is shaded. The center of the planet (or the surface of a small rocky core) is $P = P_c$. In (a)(*top*), the planet is homogeneous, but phase separation is about to begin at $P = P_0$. In (b)(*middle*), the planet has cooled down more, and the region of immiscibility has expanded somewhat. An inhomogeneous layer forms, but the He-enriched central region is still predominantly H. In (c)(*bottom*), the planet is cooler still, and now the inner region is predominantly He. The figure was taken from [177].

age for Jupiter, but the result for Saturn is too small by a factor of two.
A possible solution to this dilemma is the inclusion of phase separation in the model for Saturn leading to an inhomogeneous He distribution [179, 80, 33]. As discussed below, if there was phase separation then it would occur in the regime of atomic, metallic H, probably near the molecular-metallic transition. Figure 1.13 shows different stages in the evolution of a planetary model that includes immiscibility. In the early phase of the evolution of the giant planets it is likely that the temperatures were too high for phase separation. The envelope was homogeneous, and the He contribution corresponded to the primordial solar abundance $x_0 \approx 0.1$. In the course of the evolution the planet cooled and at some time phase separation set in (see figure 1.13 (*top*)). For later stages of the

evolution three regions with different compositions exist:

1. A homogeneous, fully convective region where the pressure is too small for phase separation to occur, i.e., $P \leq P_0$, where P_0 is the pressure when immiscibility sets in. In this region the He is depleted with respect to the primordial abundance, $x_1 < x_0$.

2. The inhomogeneous region of demixing with $P_0 \leq P \leq P_1$, where P_1 is the upper pressure bound for demixing. This region consists of a supercooled H-He mixture out of which helium-rich droplets nucleate, which can grow up to about 1 cm in diameter [177]. These droplets wander to the center of the planet, drawn by gravitation. In this inhomogeneous region the He contribution changes from $x_1 < x_0$ to $x_2 > x_0$.

3. Near the core a third region ($P > P_1$) prevails that is homogeneous and convective. The He abundance is enhanced with respect to the primordial one, i.e., $x = x_2 > x_0$.

For the nucleation of the helium-droplets two different stages in the evolution can be distinguished (see figure 1.13). At the earlier stage the droplets wander along the right-hand-boundary of the immiscibility region. When they reach the third homogeneous region for pressures $P > P_1$ they continue to follow the phase boundary until they either reach the critical point $x = x_c$ or the center of the planet. The first scenario (the more likely one) is shown in the middle part of figure 1.13. The droplets evaporate when they have reached the critical point x_c. Later in the evolution, the He contribution of the third region exceeds the critical value $x_2 > x_c$. Then the innermost region has the same He abundance as the He-rich droplets when they enter the region. A composition discontinuity occurs at $P = P_1$, the boundary of region 3 (see figure 1.13 (*bottom*)). A predominantly helium core forms.
It can be shown that the energy release from differentiation can be approximated by

$$Q_{Grav} \approx \left(\frac{dM}{dt}\right)_{\mathrm{He}} gH, \tag{1.5}$$

where $(dM/dt)_{\mathrm{He}}$ is the rate at which a helium mass is moved down a distance H in a gravity field g [177]. Furthermore, it can be shown that the released gravitational energy predominantly contributes to the energy radiation of the planet and is to a smaller fraction bound up in thermal energy by heating the inner envelope. Models that include a gravitational energy contribution available for additional radiations, or equivalently a higher excess luminosity, require a 4 or 5 times slower cooling rate for the present era than models assuming a homogeneous mixing [177]. The possible first-order character of the molecular-metallic transition and a possible energy contribution from the natural radioactivity of

carbonaceous chondrites are additional complications not considered so far. However, both can be shown to be lower order effects in the amount of energy radiated [80, 33]. More refined models that include phase separation in the envelope of Saturn (and partly the possible first order character of the molecular-metallic transition) account for the missing factor of two, giving roughly the expected age of 4.5 billion years [179, 80, 33]. Thus phase separation seems to be a good candidate to explain the enhanced energy flow of Saturn. It is also corroborated by measurements of the He contribution in the atmosphere of Saturn, which is depleted of He in comparison with Jupiter, Saturn and the primordial sun (see figure 1.14). However, if demixing in H-He mixtures under astrophysical condi-

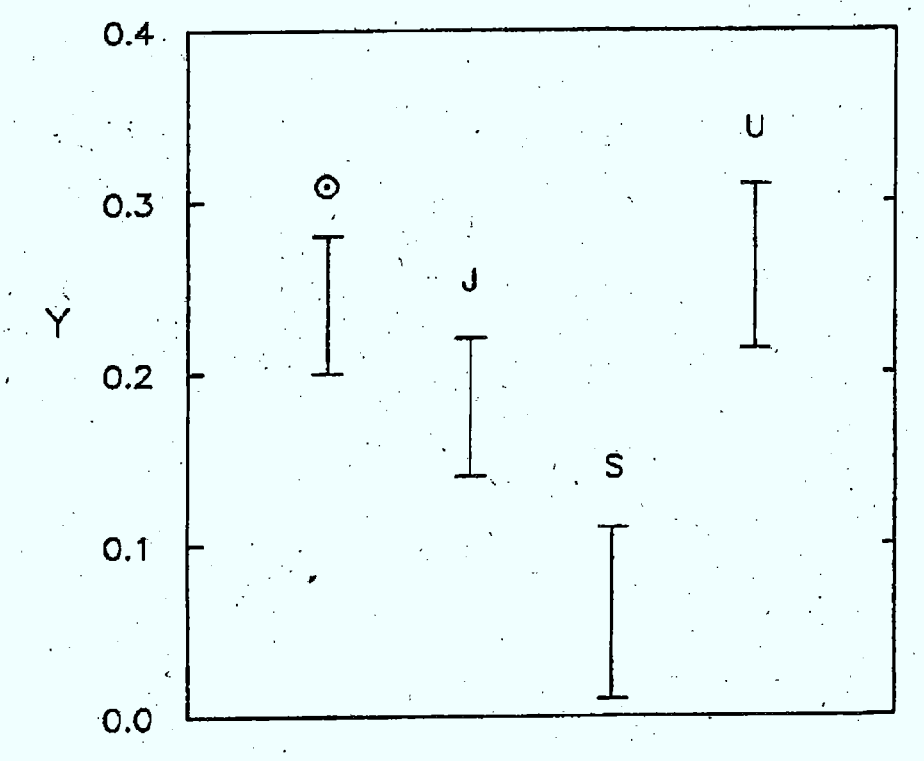

Figure 1.14: The abundance of helium relative to hydrogen in the atmospheres of Jupiter, Saturn, Uranus, and the primordial sun. The overall ratio helium to free hydrogen in the Jovian planets is assumed to be the same as that in the primordial sun. Therefore deviations from the primordial ratio in the atmosphere indicate internal differentiation of helium from hydrogen. The figure is taken from [80].

tions is the correct explanation for the too large excess energy radiation from Saturn is still an unsolved question. Stevenson and Salpeter [178, 177] assumed the critical temperature for phase separation close to the PPT to be about 10000

K. This result lies in the range of the adiabats describing Jupiter and Saturn. Stevenson and Salpeter provided a crude approximation for these adiabats. They proposed the Jovian adiabat to be $T \approx 10.000\ \rho^{\frac{1}{2}}$ K, where ρ is the density in g/cm^3, and the Saturnian adiabat to have the same form but 10-20 % colder. In their paper they propose the PPT to take place at about 3 Mbar, where the densities are roughly 0.9 g/cm^3 for the molecular phase and 1.1 g/cm^3 for the atomic, metallic phase. Assuming the Saturnian adiabat to be 15 % colder, the temperatures for Jupiter and Saturn in the metallic phase at 3 Mbar are about 10500 K for Jupiter and 9000 K for Saturn. The critical temperature (10000 K) just falls between these two numbers and suggests phase separation for Saturn, but no demixing in Jupiter. This result is consistent with the fact that the models assuming homogeneous H-He mixtures give the correct age for Jupiter, while phase separation is needed for Saturn to explain the excess heat radiation, and is consistent with the experimental results mentioned above. However, Stevenson and Salpeter's findings show the delicacy of the problem rather than solve it. An error of 1000 K in the adiabats or the critical temperature can change the situation altogether (no demixing or demixing in both planets). Here we will concentrate on the materials science aspects of the question of demixing rather than on the astrophysical aspects. That means, the problem of fitting the correct adiabats to the observational constraints will not be addressed. We just want to mention that the uncertainties in the physical composition of the envelope or the assumption that the envelope is really fully convective (a radiative zone would lead to substantially lower temperatures [32]) lead to errors larger than needed to overturn Stevenson and Salpeter's results.

We will address only one input of the astrophysical models, the computation of the critical temperature for demixing in an astrophysical H-He mixture. To complete the picture of the giant planets given in Stevenson and Salpeter's paper it is important to mention their conclusions for the molecular phase. They pointed out that the critical temperature in the molecular phase is at least a factor of two lower than in the metallic one, certainly too low to play any role in the physics of the giant plants. This result is corroborated by experimental investigations of the critical temperature via the diamond anvil cell [167, 165, 166] up to 75 kbar, which lies substantially below the adiabats describing the giant planets. The experimental results have been extrapolated to the Mbar regime [192] demonstrating that the critical temperature for 1 Mbar is about 2500 K, far below the temperature of astrophysical relevance. The possible scenario proposed by Stevenson and Salpeter is summed up in figure 1.15, where the solubility of He in H as a function of pressure and the adiabats of Jupiter and Saturn are shown.

Stevenson and Salpeter pointed out that their (and many of the subsequent) calculations suffer from the inadequate description of the electronic structure, namely by the perturbative treatment of the electronic response to the ionic arrangement. Helium is pressure ionized at a much higher pressure than H ($P \sim$ 11 TPa, see section 1.3) ,and, as analyzed quantitatively by Klepeis et al. [99]

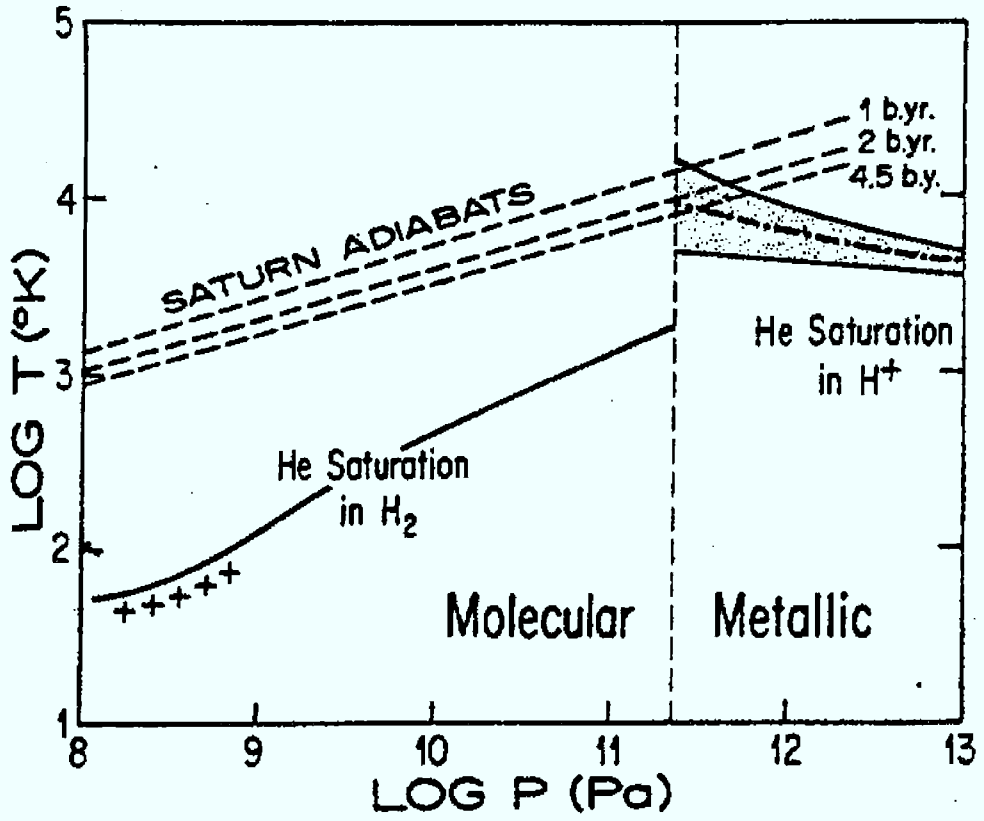

Figure 1.15: Helium saturation for a cosmic mixture and several Saturn adiabats for different evolutionary ages. In the metallic regime three different theoretical curves are shown. The crosses are experiments. The figure was taken from [179].

the He admixing leads to low-lying, tightly-bound energy levels that prohibit a nearly-free electron approach. Nevertheless, most of the quantitative treatments of astrophysical H-He mixtures so far deal with fully pressure-ionized systems, i.e., H^+-He^{++}, and use perturbative methods to include the electron-ion interaction.

The years after the proposition of phase separation spawned quite a few theoretical investigations of astrophysical H-He mixtures. With the exception of Klepeis et al. [99] (who included only ideal finite temperature terms for the free energy) all computations of critical temperatures for demixing proceeded in three steps:

1. A model for the Helmholtz free energy is constructed.

2. The difference of the Gibbs free energy between the mixture and the pure phases is obtained from the Helmholtz free energy results,

$$\Delta G(P,T,x) = G(P,T,x) - xG(P,T,1) - (1-x)G(P,T,0). \qquad (1.6)$$

3. The regions in the (P, T, x)-space where $\partial^2 G/\partial x^2(P, T, x) < 0$ are unstable towards phase separation. For an astrophysical composition, $x \approx 0.1$, a double tangent construction leads to the phase separation curve (see section 9.1).

The first quantitative investigation was launched by Stevenson [175]. Since his results served as a reference calculation for the following ones it is worth discussing his proceeding in more detail. He considered a fully pressure-ionized H-He mixture and computed perturbative corrections. His model free energy had the form $F = F_{eg} + F_{hs} + E_M + E_{BS} + \Delta F_{int} + F_Q$. The first terms, F_{eg} and $F_{hs} + E_M$, are the free energies of the unperturbed systems, i.e., of free electrons and ions. He approximated the free energy of a homogeneous electron gas, F_{eg}, by the well-known term of the zero-temperature contribution plus a finite-temperature correction. The finite-temperature correction is small for astrophysical temperatures and was left out in most of the subsequent calculations. The ions were regarded as hard spheres and included in the model free energy via the term for an equivalent neutral hard sphere liquid, F_{hs} ,and the Madelung energy, E_M, which accounts for the long-range Coulomb repulsion of the ions. The electron-ion interaction was treated perturbatively through E_{BS} and ΔF_{int}. The "band-structure energy" E_{BS} describes the polarization of the electrons by the ions, i.e., the inhomogeneity of the electronic system, within the framework of linear response, and ΔF_{int} is a correction to the ionic contribution due to the fact that screened particles interact rather than protons and α-particles. Finally, F_Q is the lowest order high-temperature quantum correction, which is typically small and left out in most of the consecutive calculations. Stevenson constructed from his free energy the Gibbs free energy and obtained phase separation for temperatures smaller than 8000 K and pressures typical of the metallic regime (4-40 Mbar for Jupiter).

Hansen, Torrie, and Vieillefosse's calculations [147] substantially differ from Stevenson's approach only in so far as they computed the Helmholtz free energy of the classical H^+-He^{++} two component-plasma within the hypernetted-chain framework. Comparing their results with Stevenson's they concluded that "the overall agreement between his and our results is satisfactory considering the very different approach". Their critical temperatures are somewhat lower.

Extensive studies on H-He mixtures were performed with the Monte Carlo (MC) method. Hubbard [79] and de Witt and Hubbard [81] used MC methods to study dense H-He mixtures and applied a model free energy to compute thermodynamical quantities. Electron screening effects were also described by linear response theory treating the He atoms as α-particles with a cloud of screening electrons. Hubbard and de Witt [82] addressed the demixing problem in 1985. They used an effective screened potential between the ions where the screening of the ions was included via the dielectric function obtained by linear response theory. Their MC simulations provided the statistical averages of several physical

observables. Then they approximated the Helmholtz free energy by three terms, $F = F_0 + E_{eg} + F_I$, where F_0 is the free energy of an ideal gas of H and He nuclei, E_{eg} is the ground state energy of a homogeneous electron gas, and F_I is the term due to the interaction of the charges in the system. The first two terms are well-known from theoretical considerations. For the interaction term they assumed a functional expression derived from the OCP model and theoretical considerations. The expression for the free energy served them to derive analytical expressions for physical observables, such as the internal energy, pressure, and heat capacity, which directly are amenable to the MC method. Hubbard and de Witt fitted the analytical expression to their simulation results, and that way determined the free parameters in their free energy model. Within this free energy model they computed a critical temperature of 7500 K at 8 Mbar.
The molecular H-He mixture was treated via MC, too. Marley and Hubbard [120] used effective intermolecular potentials derived from shock compression and other experiments in Monte Carlo simulations of mixtures of molecular H and He. They derived a model free energy and compared their results with those of Hubbard and de Witt for the metallic regime. Equating the chemical potentials of the molecular H-He and the metallic H-He mixture they predicted the transition to a metallic mixture to occur at $P = 5$ Mbar for the temperatures prevailing in the interiors of the giant planets. This pressure is probably too high, as will be discussed later (section 7). Limitations of Marley and Hubbard's approach stem from the application of He-He and H_2-H_2 potentials that were fitted to experimental data for pressures of a few hundred kbar in the Mbar regime and a H_2-He potential that has not been tested for the high pressure range. For H this description fails to account for the softening of the potentials close to the dissociation of the molecules due to many-body effects (see chapter 5).
A very similar approach to Hubbard and de Witt's calculations [82] was applied by Pollock and Alder [151]. It is surprising that they obtained considerably higher critical temperatures ($\approx$ 12000 K at 10 Mbar for an astrophysical mixture), because technically the two computations only differ in the fit formula assumed for the free energy and the screening function. Pollock and Alder pointed out that their results should not be applied to the demixing problem in the giant planets, because a screened H^+-He^{++} mixture is not an adequate model in this pressure regime. Instead they claimed a H^+-He^+ mixture to be a better model for astrophysical pressures. Since the pressure ionization of He only occurs at a pressure one order of magnitude higher it is more realistic to assume He to be partly ionized. The screened H^+-He^+ mixture gave substantially lower phase separation temperatures. At a pressure of 10 Mbar and a temperature of $T \approx$ 5500 K they found no indications for demixing.
Thus perturbation theory is inadequate for the description of the strong screening of the He atoms at astrophysical pressures. A more complete, however crude treatment of the electron distribution around the He atoms is provided by the Thomas-Fermi-Dirac theory. Mac Farlane and Hubbard [50] applied the Thomas-

Fermi-Dirac method and perturbation theory to compute the Gibbs free energies of mixing for bcc and fcc lattices of H and He to examine the effect stemming from the strong screening of the He atoms. They predicted that the correct treatment of the electronic structure will lead to lower critical temperatures than computed with perturbative methods. Their results were confirmed by Mac Farlane [49], who used the Thomas-Fermi-Dirac method to compute the critical temperature for demixing for astrophysical H-He mixtures in the metallic phase at pressures of 10, 100, and 1000 Mbar obtaining temperatures of $\approx$ 0 K, 500 K, and 1500 K, respectively. He concluded that phase separation does not occur in the interiors of the giant planets. The results of Pollock and Alder, Mac Farlane and Hubbard, and Mac Farlane suggest that a more elaborate treatment of the electron distribution around the He atoms would lead to lower critical temperatures than those obtained for a screened H^+-He^{++} mixture ($\approx$ 7000 - 12000 K).
However, this notion was contradicted by the results of Klepeis et al. [99], who applied the DFT/LDA framework, the best description of the electronic structure in computing phase separation for H-He mixtures so far, to metallic H-He mixtures in the Mbar range. They computed a critical temperature of 15000 $\pm$ 2000 K and found the critical temperature to be nearly independent of pressure in the range of 5 – 20 Mbar. They concluded that phase separation is an ongoing process in both giant planets and suggested a revision of the Jupiter models according to their result. However, in their approach they performed zero temperature computations including the $T\Delta S$ term only via the ideal part. As will be discussed in section 9.1, more crucial is the neglect of relaxation effects: They substituted He atoms for H pairs and computed the enthalpy differences but did not account for the stronger repulsion of the He atoms.
Thus the situation remains unclear. Demixing temperatures from 0 K to 15000 K have been proposed. Every scenario is possible from demixing in both planets to no phase separation at all in astrophysical H-He mixtures. In addition there are the error bars on the adiabats describing the giant planets. But before comparing with the internal temperatures of the giant planets the situation concerning the critical temperatures of H-He mixtures in the Mbar range has to be clarified. More refined approaches are needed to diminish the uncertainty in the temperature (presently 15000 K !) as much as possible. An attempt to improve the situation is made in section 9.1. Another promising approach is provided by the method of Alavi, Parrinello, and Frenkel [3], which is presently applied to H-He mixtures in the high pressure range [1].

1.3 Helium

The emphasis of our studies of He lies on the effect of He alloying on pure H rather than on pure He itself, which serves us only as a reference point. Therefore, the survey of the He phase diagram will be kept brief. Helium has been studied

extensively [43, 201] and exhibits a variety of interesting physical properties. It is the only element that is not solid at T = 0 K and ambient pressure due to the large effect of the zero-point motion. Landau's theory is used to study both isotopes He_4 and He_3 at low temperatures and pressures. In the following only He_4 will be addressed, because it is the isotope prevalent in nature and investigated in our simulations. He_4 crystallizes at 2.5 K in an hcp solid. The crystal structure has been studied up to a pressure of 58 GPa [117, 112] and found to remain hcp for T = 0 K. At zero temperature theory predicts a sequence hcp $\longrightarrow$ fcc $\longrightarrow$ hcp $\longrightarrow$ bcc [201]. Like hydrogen helium can be treated within the OCP model at very high pressure ($P \geq 100$ TPa) and crystallizes in a bcc lattice. In the pressure range where we study He and H-He mixtures (1-25 GPa) He is likely to crystallize in an hcp solid (possibly fcc). Contrary to H He is still a good insulator in this pressure regime (see the density of states of He in section 5). Young, McMahan, and Ross [202] computed the metallization pressure using the linear-muffin-tin-orbitals (LMTO) electron-band-theory method and found He to become metallic only at 112 Mbar. It has been pointed out that many-body effects play a crucial role at elevated pressures [111, 112] and demonstrated that pair potentials give a too stiff equation of motion in the range of about 20 GPa, because they fail to include the softening by many-body forces [107] (also see the discussion in section 5). A tentative phase diagram is provided by [111] (figure 1.16). The properties of the highly compressed pure phase will be discussed in chapter 8.

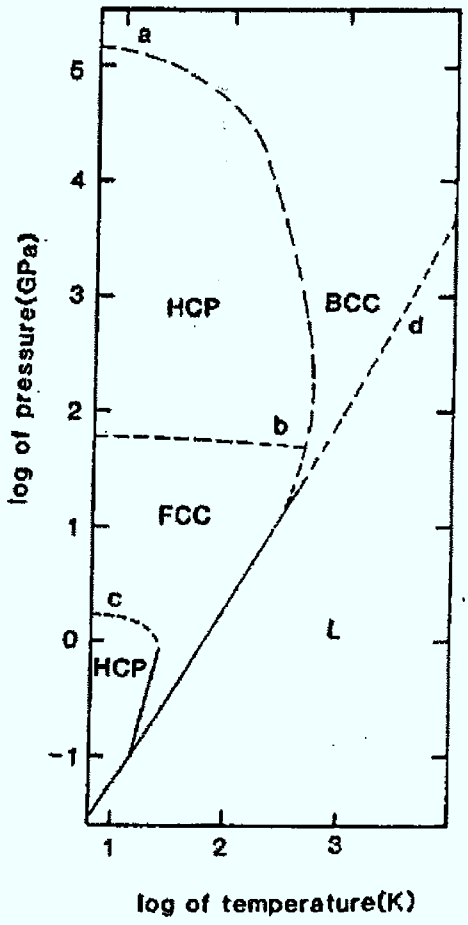

Figure 1.16: Hypothetical phase diagram of ^{4}He; the pressures and temperatures are plotted on logarithmic scales. The full lines indicate experimental results for the low-density fcc-hcp phase transition and of the melting curve. The phase diagram is completed by theoretically determined phase lines (dashed). The figure is taken from [111].

Chapter 2

The Car-Parrinello Method

2.1 The Car-Parrinello Method and Density Functional Theory

When Car and Parrinello published their seminal paper [29] ten years ago they started a new branch of computer simulations extending the range of conventional electronic structure calculations and the scope of molecular dynamics as well. Since then their scheme has been applied to many problems, for example the determination of the physical properties of disordered systems, processes relevant to semiconductor technology, the diffusion of H in Si, the study of surface reconstruction, atomic clusters, ion conductivity, fullerenes and plasma physics. The method and their applications have been described in several review articles [30, 155, 57, 139, 143, 58] and are addressed here only to the extent that is relevant to our work.

The key to the understanding of the Car-Parrinello (CP) scheme is that it merges two different fields, density functional theory (DFT) and molecular dynamics (MD). Dependent on the field of interest two different points of view of the method are assumed:

The central application of DFT is the total energy calculation of complex systems. The comparison of the total energy for different geometries provides the energetically favored configurations that dominate their physical properties. To achieve the optimization of the geometries of complex systems in space the Car-Parrinello scheme can be successfully applied in combination with simulated annealing. However, the scope of the method extends to the investigation of the finite temperature properties of condensed matter, too. It can be used as a method to perform MD with an ab initio, i.e., parameter-free, potential.

Below both approaches are presented. First (section 2.1.1) conventional DFT is extended to a simulated annealing method for electronic and ionic degrees of freedom. A special case is the optimization of the electronic degrees of freedom only, which is an example for modern iterative techniques to minimize the energy

functional. These techniques were developed in the wake of the Car-Parrinello method. Some of them are described in section 2.1.4.
In the second part of this chapter (section 2.2) we will start with conventional MD and introduce the DFT expression for the total energy as potential into the MD Lagrangian.

2.1.1 Introduction

Since its development in 1964 [74] DFT has become one of the most important computational techniques in condensed matter physics. When in 1985 Car and Parrinello proposed their method, DFT had already a wide range of applications in structural studies of molecules, solids, surfaces and interfaces, point defects, phonons, calculation of forces and stresses, dielectrical theory, and linear response theory (for reviews see [174, 85, 93, 150], an introduction is provided by [60]). There is an extensive literature covering the theoretical aspects of DFT, too (see for example [93, 46, 62]). Therefore, this chapter will be restricted to the ingredients necessary for the CP scheme. The first section describes the fundamentals of DFT. Crucial for an efficient implementation of the CP scheme is an adequate treatment of both, the electron-electron interaction and the electron-ion interaction. Whereas the tractability of the electron-electron interaction relies on a physical concept, DFT, the treatment of the electron-ion interaction is a mere technical problem. A solution to this problem is described in the second section (2.1.3), pseudopotentials. In the third section (2.1.4) the minimization of the electronic degrees of freedom will be addressed, and finally in the fourth section (2.1.5) the ionic degrees of freedom will be included. In the following we use atomic units (a.u.), i.e., $\hbar = m = e = 1$.

2.1.2 Density Functional Theory

DFT goes back to a theorem of Hohenberg and Kohn [74]. Here it is presented in a more elegant and general version of Levy [109].
For simplicity the electronic ground state is assumed to be non-degenerate (extension for degenerate ground-state [101]). We consider N electrons in an external potential $V_{\text{ext}}(\vec{r})$, i.e., the many-particle Hamiltonian is

$$\mathcal{H} = \sum_{i=1}^{N} \frac{\vec{p}_i^2}{2} + \frac{1}{2} \sum_{i,j=1}^{N} V_{\text{ee}}(\vec{r}_i, \vec{r}_j) + \sum_{i=1}^{N} V_{\text{ext}}(\vec{r}_i) \equiv T + V_{\text{ee}} + \sum_{i=1}^{N} V_{\text{ext}}(\vec{r}_i). \quad (2.1)$$

T is the kinetic energy operator and V_{ee} represents the electron-electron interaction. Levy introduced the functional

$$F[n] \equiv \min_{\psi \to n} \langle \psi | T + V_{\text{ee}} | \psi \rangle . \quad (2.2)$$

The minimum is taken over all antisymmetric wave functions $\psi(\vec{r}_1, ..., \vec{r}_N)$ that give the one-particle density $n(\vec{r})$

$$n(\vec{r}) = \int d\vec{r}_2 ... d\vec{r}_N \psi^*(\vec{r}, \vec{r}_2, ..., \vec{r}_N)\psi(\vec{r}, \vec{r}_2, ..., \vec{r}_N). \tag{2.3}$$

It is easy to show that for all densities n

$$E[n] = \int d\vec{r} V_{\text{ext}}(\vec{r})n(\vec{r}) + F[n] \geq E_{\text{GS}}, \tag{2.4}$$

where E_{GS} is the ground state energy. The equality holds if and only if $n = n_{GS}$, i.e., for the ground state density. The proof is elementary and makes use of the Ritz variational principle [123].
Kohn and Sham [102] cast the problem into a form that allows the practical calculation of ground state properties like $E[n]$

$$E[n] = T_o[n] + \int d\vec{r} V_{\text{ext}}(\vec{r})n(\vec{r}) + \frac{1}{2}\int d\vec{r} d\vec{r}' \frac{n(\vec{r})n(\vec{r}')}{|\vec{r} - \vec{r}'|} + E_{\text{xc}}[n]. \tag{2.5}$$

T_o denotes the kinetic energy of the non-interacting system, i.e., $V_{\text{ee}} = 0$, and E_{xc}, the exchange- and correlation-contribution, comprises all other contributions in addition to the first three terms.
Variation for the density with the constraint of constant particle number N (μ is the corresponding Lagrangian multipliers)

$$\frac{\delta}{\delta n}\left(E[n] - \mu\left(\int n(\vec{r})d\vec{r} - N\right)\right) = 0 \tag{2.6}$$

gives

$$\frac{\delta E[n]}{\delta n(\vec{r})} = \frac{\delta T_o}{\delta n(\vec{r})} + V_s(\vec{r}) = \mu, \tag{2.7}$$

where V_s represents an effective one-particle potential

$$\begin{aligned} V_s(\vec{r}) &= V_{\text{ext}}(\vec{r}) + \int d\vec{r}' \frac{n(\vec{r}')}{|\vec{r} - \vec{r}'|} + \frac{\delta E_{\text{xc}[n]}}{\delta n(\vec{r})} \\ &\equiv V_{\text{ext}}(\vec{r}) + V_{\text{Ht}}(\vec{r}) + V_{\text{xc}}(\vec{r}). \end{aligned} \tag{2.8}$$

In this form the problem is equivalent to a system of non-interacting particles in an external potential V_s, leading to a system of Schrödinger-like differential equations, the Kohn-Sham equations

$$\left(-\frac{1}{2}\nabla^2 + V_s(\vec{r})\right)\psi_i(\vec{r}) = H\psi_i(\vec{r}) = \epsilon_i\psi_i(\vec{r}), \quad i = 1, ..., N. \tag{2.9}$$

The problem is well suited for practical calculations, because the individual equations are only coupled via V_s. The Kohn-Sham orbitals, $\psi_i(\vec{r})$, are auxiliary quantities, which readily provide the one-particle density

$$n(\vec{r}) = \sum_{i=1}^{N} |\psi_i(\vec{r})|^2. \tag{2.10}$$

In principle this scheme leads to the ground state density and via the density to the ground state energy. In practice $E_{\rm xc}$ has to be approximated, because a practical expression for the exact quantity is unknown. Then the Kohn-Sham equations can be solved self-consistently, i.e., by the iteration scheme

start with a guess for the $\psi_{i,\rm in}$

1. construct the density n from (2.10)
2. set up the potential V_s using ψ_i and n
3. solve the Kohn-Sham equations (2.9) for $\psi_{i,\rm out}$
4. use $\psi_{i,\rm out}$ as input for step 1.

stop when $\psi_{i,\rm out} = \psi_{i,\rm in}$

The success of DFT is partly due to the existence of a simple and very practical approximation for $E_{\rm xc}$, the local density approximation (LDA), which has the form of $E_{\rm xc}$ for the homogeneous electron gas

$$E_{\rm xc}^{\rm LDA}[n(\vec{r})] \equiv \int n(\vec{r}) \epsilon_{\rm xc}(n(\vec{r})) d\vec{r}. \tag{2.11}$$

In this way the problem of solving for the functional $E_{\rm xc}^{LDA}[n(\vec{r})]$ reduces to the evaluation of the function $\epsilon_{\rm xc}(n(\vec{r}))$ which has been calculated and parametrized several times. In our calculations we used the parameterization by S. H. Vosko, L. Wilk, and M. Nusair [194].

Many ground state properties calculated with DFT/LDA have accuracies typically in the range of $10^{-3}...10^{-1}$, for example cohesive energies and ground state geometries. Whereas the absolute value of the total energy is overestimated by up to 1 eV/atom energy differences can be computed with chemical accuracy of 0.1 eV/atoms. The reason is that the contributions where LDA does worst, namely the total energy of the individual constituent atoms, cancel. An example for ground state geometries are the lattice constants of regular solids. Thus, for example, the agreement between the calculated and experimental equilibrium lattice constants is within 1% for covalent (Group IV) semiconductors, and within 2% for partially ionic (III-V) semiconductors. The agreement of theoretical and experimental lattice constants worsens for increasing ionicity [174]. For many

systems improvements in the accuracies by a factor of typically $3-5$ have been achieved by using gradient corrections, i.e., including the gradient of the density in the functional form of E_{xc}

$$E_{\mathrm{xc}} = \int d\vec{r} f(n(\vec{r}), |\nabla n(\vec{r})|). \tag{2.12}$$

The form of the function f is obtained by formal gradient expansion or a combination of physical principles and phenomenological fitting (see for example the contributions of Geldart and Perdew in [62]).

2.1.3 Pseudopotentials

For most calculations of physical properties via DFT, the electronic wave functions are expanded in a set of basis functions. The most elementary choice for the basis functions are plane waves, which render the evaluation of all occurring matrix elements comparatively easy. (For a local pseudopotential they can even be computed analytically.) However, the expansion of the real wave functions in plane waves does not converge fast. The core wave functions are localized and the orthogonality of the valence wave functions leads to rapid oscillations in the core region, which preclude the representation by a manageable number of plane waves.
The pseudopotential approach overcomes these difficulties. It relies on the observation that the chemical and physical properties of matter are largely determined by the behavior of the valence electrons whereas the core states remain inert. Moreover outside the core region the variation of the potential is small and the valence wave functions are often free-electron like. In pseudopotential theory the potential felt by the valence electrons in the core region is modified. The modification is made in such a way as to eliminate the rapid oscillations in the core region, while preserving as exactly as possible the valence band structure, i.e., reproducing the energy eigenvalue spectrum. Thus an expansion in plane waves becomes feasible. The modified potential ("pseudopotential") is used instead of the real potential V_{ext} to describe the interaction between electrons and ions.
The first pseudopotentials were constructed by J. C. Phillips and L. Kleinmann [148] who derived from the OPW method an effective potential (pseudopotential) acting on the valence orbitals only. In the beginning pseudopotentials were mostly fitted to experimental data and used for the perturbative calculation of screening effects and total energies. Nowadays the potentials reproduce the valence eigenvalue spectrum of atomic ab initio calculations and are employed for the direct, numerical solution of Schrödinger's equation.
Besides their accuracy, transferability is the main criterion for the quality of pseudopotentials. The potentials are constructed to reproduce the eigenvalue spectrum of a reference configuration. They are called transferable if the same

ionic pseudopotential can be used for different atomic arrangements. In modern pseudopotential applications high transferability was obtained by introducing norm-conserving pseudopotentials [64, 10]. Besides norm conservation most modern pseudopotentials obey three other general conditions. The restrictions are

1. The pseudo wave function generated from the pseudopotential contains no nodes.

2. The radial pseudo wave function is equal to the true-potential wave function beyond a chosen cutoff r_c, i.e., $\psi_l^{PP}(r) = \psi_l(r)$ for $r \geq r_c$.

3. The charge enclosed within r_c must be equal for the two wave functions (norm conservation)

$$\int_0^{r_c} |\psi^{PP}(r)|^2 r^2 dr = \int_0^{r_c} |\psi(r)|^2 r^2 dr.$$

4. The valence eigenvalue spectra are equal, i.e., $\epsilon_l^{PP} = \epsilon_l$.

The cutoff radius r_c defines the core region ($r \leq r_c$). Its choice requires to compromise between transferability and computational efforts. Reducing the value of r_c improves the transferability but at the same time increases the number of plane waves needed for convergence. Criterion (1.) sets a lower limit on the size of r_c, because r_c must lie outside the outer node of the full-potential wave function. It is necessary to obtain a smooth pseudopotential that allows the expansion in plane waves. The norm conservation (criterion 3.) ensures via Gauss' theorem that the real and pseudo wave function, $\psi_l(r)$ and $\psi_l^{PP}(r)$, yield the same integrated charge inside a sphere of radius R (R $\geq r_c$). This criterion is important to obtain a good transferability. Assuming a spherical screening approximation (which will be specified below) one can prove the following identity for the radial part of the pseudo wave function $\psi^{PP}(r)$ [10]

$$-\frac{1}{2}\left[\frac{d}{d\epsilon}\frac{d}{dr}\ln R_l(r,\epsilon)\right]\Bigg|_{r=r_c,\epsilon=\epsilon_l} = \frac{1}{r_c^2 R_l^2(r_c,\epsilon_l)}\int_0^{r_c} R_l^2(r) r^2 dr. \qquad (2.13)$$

Because of criteria (2.) and (3.) the right hand side of (2.13) is equal for ψ_l^{PP} and ψ_l if $R_l(r) \geq r_c$. Apart from normalization $d/dr \ln R_l$ uniquely specifies the solution of a linear second order differential equation as the radial Schrödinger equation. The atomic valence eigenvalues ϵ_l will be shifted when the atom takes part in chemical bonding. Equation (2.13) ensures that the change in real and pseudo wave functions have the same energy variation to first order at $r = r_c$.
Presently, most pseudopotentials are generated from atomic all electron calculations. Within the framework of DFT/LDA (see section 2.1.2) we start by

constructing the radial pseudo wave function R_{nl}^{PP} and inverting the radial Kohn-Sham equation

$$\left[-\frac{1}{2}\frac{d^2}{d^2r}+\frac{l(l+1)}{2r^2}+V[n,r]\right]rR_{nl}^{PP}(r)=\epsilon_{nl}rR_{nl}^{PP}(r), \tag{2.14}$$

where

$$V[n,r]=-\frac{2}{r}+V_H[n,r]+V_{\rm xc}^{LDA}(n(r)). \tag{2.15}$$

We obtain the screened pseudopotential

$$V_{scr,l}^{PP}(r)=\epsilon_l-\frac{l(l+1)}{2r^2}+\frac{1}{2rR_l^{PP}(r)}\frac{d^2}{dr^2}\left[rR_l^{PP}(r)\right]. \tag{2.16}$$

From equation 2.16 it is clear that the pseudo wave functions have to be nodeless (criterion 1.) in order to avoid singularities outside the origin. Furthermore, the pseudopotential will depend on the angular momentum l. To obtain the ionic pseudopotential, $V_{scr,l}^{PP}$ has to be unscreened

$$V_{ion,l}^{PP}=V_{scr,l}^{PP}-V_H^{PP}-V_{\rm xc}^{PP}. \tag{2.17}$$

Because of the l-dependence each angular momentum component of the wave function will see a different potential and an ionic pseudopotential operator has to be introduced

$$\hat{V}_{ion,l}^{PP}(r)=V_{ion,local}^{PP}(r)+\sum_l V_{nonlocal,l}(r)\hat{P}_l, \tag{2.18}$$

where $\hat{P}_l$ projects out the l-th angular momentum component and

$$V_{nonlocal,l}(r)=V_{ion,l}^{PP}(r)-V_{ion,local}^{PP}(r). \tag{2.19}$$

Criteria (1.-4.) and the procedure described above are far from specifying the pseudopotential uniquely. In our simulations we generated pseudopotentials using a scheme by Troullier and Martins [190] who exploited this freedom of choice to optimize the smoothness of their pseudopotentials. Their scheme is sketched below:
In order to avoid a singularity at $r=0$ that could not be well described by plane waves, the pseudo wave functions are constrained to have the following asymptotic behavior

$$R_l\longrightarrow r^l \quad \text{for} \quad r\longrightarrow 0 \qquad \text{(see equation 2.16)}.$$

A possible form of the pseudo wave function that satisfies the condition is

$$R_l^{PP}(r)=\begin{cases} R_l(r) & \text{if} \quad r\geq r_c \\ r^l exp\left[p(r)\right] & \text{if} \quad r\leq r_c \end{cases}, \tag{2.20}$$

where $p(r)$ is some suitably chosen polynomial. Troullier and Martins used

$$p(r) = c_o + c_2 r^2 + c_4 r^4 + c_6 r^6 + c_8 r^8 + c_{10} r^{10} + c_{12} r^{12}. \tag{2.21}$$

For V^{PP} to be continuous, $R_l^{PP}(r)$ and its first two derivatives have to be continuous at $r = r_c$ (see equation 2.16). The norm conservation provides another constraint. Three parameters of freedom are left and three constraints may be introduced to optimize the smoothness of the potential. Troullier and Martins chose the continuity of the third and fourth derivative at $r = r_c$ and they required zero curvature of the screened pseudopotential at the origin, i.e., $V''_{scr,l}(0) = 0$. Once we have constructed the pseudo wave functions we proceed as described above by inverting the Schrödinger equation and unscreening the resulting pseudopotential. An example for a pseudopotential with s- and p-angular momentum

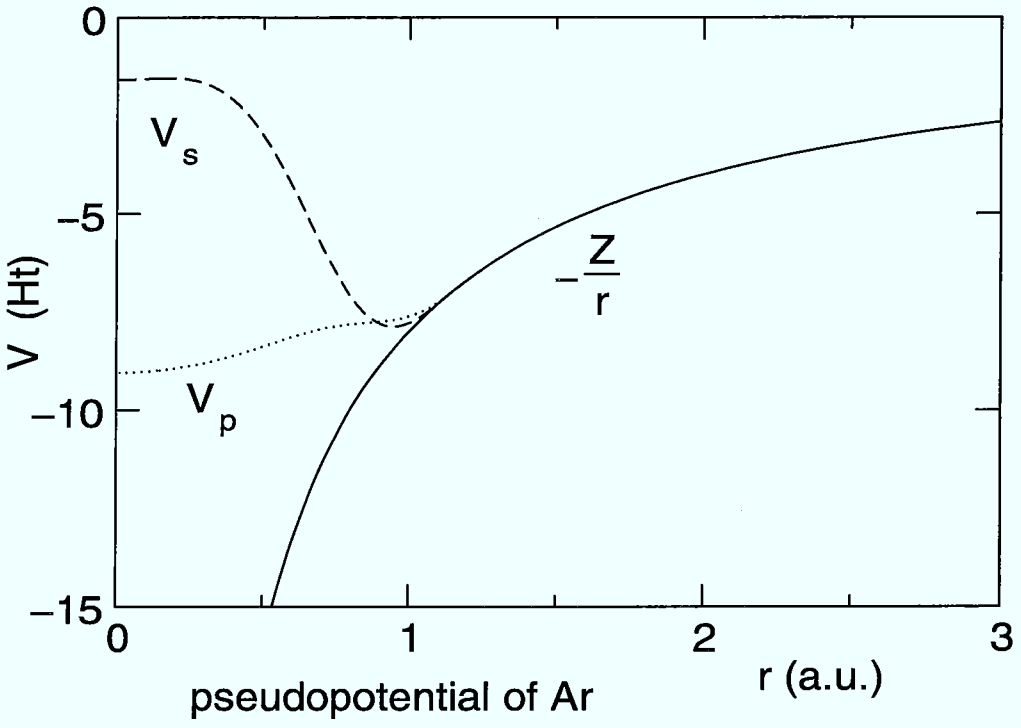

Figure 2.1: Illustration: Troullier-Martins pseudopotential of Ar with local s-component (V_s) and non-local p-component (V_p). r_c was 1.2 a.u.

component is shown in figure 2.1.

2.1.4 Modern Iterative Methods for Energy Minimization

The conventional way to solve the Kohn-Sham equations is to diagonalize the Hamiltonian matrix self-consistently. Since the cost of a standard diagonalization grows as $O(M^3)$, where M is the number of functions in the basis set expansion, this procedure becomes very expensive for large systems (and especially for a plane wave basis). More modern techniques exploit the fact that only the N occupied Kohn-Sham orbitals are required to obtain the ground state energy within DFT. The partial diagonalization of only the N lowest orbitals reduces the cost to $O(N^2M)$ [143].
One can map the matrix eigenvalue equations onto a multidimensional minimization problem. Instead of solving the Kohn-Sham equations we insert the Kohn-Sham orbitals via (in the following we sum over all occupied orbitals, and it is assumed that each orbital is occupied by two electrons)

$$n(\vec{r}) = 2\sum_{i=1}^{N} |\psi_i(\vec{r})|^2 \tag{2.22}$$

and

$$T_o = \sum_i \int \psi_i^*(\vec{r}) \left(-\frac{1}{2}\nabla^2\right) \psi_i(\vec{r}) d\vec{r} \tag{2.23}$$

into the expression for the total energy

$$\begin{aligned} E[\{\psi_i\}] &= 2\mu \sum_i \int \psi_i^*(\vec{r}) \left(-\frac{1}{2}\nabla^2\right) \psi_i(\vec{r}) d\vec{r} + \int d\vec{r} V_{\text{ext}}(\vec{r}) n(\vec{r}) \\ &+ \frac{1}{2} \int \frac{n(\vec{r}) n(\vec{r}')}{|\vec{r} - \vec{r}'|} d\vec{r} d\vec{r}' + E_{\text{xc}}[n(\vec{r})]. \end{aligned} \tag{2.24}$$

One way to solve this problem is to perform simulated annealing for electrons only, as described in the following section. A more efficient way than using Newton's dynamics is to employ first order equations of motion as realized in the steepest descent algorithm:
A fictitious dynamics is introduced in the space of wave functions and the gradient with respect to the Kohn-Sham orbitals is computed

$$\dot{\psi}_i(\vec{r}, t) = -\frac{1}{2} \frac{\delta E_{tot}}{\delta \psi_i^*(\vec{r}, t)}. \tag{2.25}$$

The dot denotes the time derivative and the functional derivative is computed by

$$\frac{\delta E_{tot}}{\delta \psi_i^*}(\vec{r}, t) = 2H\psi_i(\vec{r}, t). \tag{2.26}$$

It is necessary to add the constraints

$$\int \psi_i^*(\vec{r}, t) \psi_j(\vec{r}, t) d\vec{r} = \delta_{ij} \tag{2.27}$$

to ensure orthogonality during the minimization. The "time"-dependence is fictitious, since in the steepest descent procedure only the end product matters and the time is just a parameter used to label different configurations in the space of the $\{\psi_i\}$. Equation 2.25 defines a trajectory in the $\{\psi_i\}$-space that leads to the minimum value of $E_{tot}[\{\psi_i\}]$. At the minimum the gradient becomes zero, $\dot{\psi}_i(\vec{r},t) = 0$, and (2.26) becomes (where Λ is the matrix of the Lagrange parameters corresponding to the constraints 2.27)

$$H\psi = \Lambda\psi, \quad \psi = (\psi_1, ..., \psi_N). \tag{2.28}$$

Equation 2.28 is identical within a unitary transformation to the Kohn-Sham equations, and the eigenvalues of the matrix Λ coincide with the occupied Kohn-Sham eigenvalues. This technique to minimize a function is called steepest descent algorithm.
Surprisingly, the fastest way to minimize the function $E_{tot}[\psi]$ is not achieved by moving in the direction of the negative gradient, in which the function decreases most rapidly. For the static computations in our simulations a more efficient scheme for dynamical minimization of the electrons was used, the conjugate gradient technique [182, 143, 152]. The main idea is instead of optimizing each move individually (as for steepest descent) to optimize each move with regard to all previous moves, i.e., to choose the moves conjugate to each other. In the following the concept is described in more detail:
Let x be a vector in a multidimensional space and $F(x)$ the objective function to be minimized. It is assumed that F can be approximated by a multidimensional quadratic form around some point x^1 taken as the origin of the coordinates, i.e.,

$$F(x) \approx c - g^1 \cdot x + \frac{1}{2} x \cdot G \cdot x, \tag{2.29}$$

where

$$c \equiv F(x^1), \quad g^1 \equiv -\nabla F(x)|_{x=x_1}. \tag{2.30}$$

The aim is to find a path $(x^1, x^2, ..., x^N)$ that needs as few steps as possible to minimize F, i.e., to find $\min_x F(x) = F(x^N)$. Obviously, the best choice for the first step is to move in the direction

$$d^1 = \frac{-\nabla F(x)|_{x=x_1}}{|-\nabla F(x)|_{x=x_1}|} = \frac{g^1}{|g^1|}. \tag{2.31}$$

Moving in the direction d^1 the minimum will occur at

$$x^2 = x^1 + b^1 \cdot d^1, \tag{2.32}$$

where b^1 satisfies

$$\frac{\delta F}{\delta b^1}(x^2) = -g^1 \cdot d^1 + (x^1 + b^1 \cdot d^1) \cdot G \cdot d^1 = 0. \tag{2.33}$$

In the steepest descent algorithm the second direction is chosen to be

$$d^2 = \frac{-\nabla F(x)|_{x=x_2}}{\left|-\nabla F(x)|_{x=x_2}\right|}. \tag{2.34}$$

Starting from x^2 in the direction d^2 yields

$$x^3 = x^2 + b^2 \cdot d^2, \tag{2.35}$$

where b^2 satisfies

$$\frac{\delta F}{\delta b^2}(x^3) = -g^1 \cdot d^2 + (x^1 + b^1 \cdot d^1 + b^2 \cdot d^2) \cdot G \cdot d^2 = 0. \tag{2.36}$$

However, 2.34 is not the best choice for d^2. The minimum of F in the two dimensional subspace defined by d^1 and d^2 requires b^2 to obey

$$\frac{\delta F}{\delta b^1}(x^3) = -g^1 \cdot d^1 + (x^1 + b^1 \cdot d^1 + b^2 \cdot d^2) \cdot G \cdot d^1 = 0 \tag{2.37}$$

and

$$\frac{\delta F}{\delta b^2}(x^3) = -g^1 \cdot d^2 + (x^1 + b^1 \cdot d^1 + b^2 \cdot d^2) \cdot G \cdot d^2 = 0. \tag{2.38}$$

The comparison with equations 2.33 and 2.36 leads to the requirement

$$d^1 \cdot G \cdot d^2 = d^2 \cdot G \cdot d^1 = 0, \tag{2.39}$$

i.e., to choose the directions d^1 and d^2 conjugate to each other.
This condition is generalized to

$$d^n \cdot G \cdot d^m = 0 \ \ for \ \ n \neq m \tag{2.40}$$

This requirement leads to the conjugate gradient algorithm [182, 152]

$$d^{(n)} = \begin{cases} g^{(0)} & , \ n = 0 \\ g^{(n)} + \gamma^{(n-1)} \cdot d^{(n-1)} & , \ n = 1, 2, ... \end{cases} \tag{2.41}$$

where

$$g^{(n)} = -\nabla F(x^n) \tag{2.42}$$

$$\gamma^{(n)} = \frac{\langle g^{(n+1)} | g^{(n+1)} \rangle}{\langle g^{(n)} | g^{(n)} \rangle}. \tag{2.43}$$

It can be shown that 2.40 holds [152]. The conjugate gradient algorithm converges considerably faster then the steepest descent scheme (see figure 2.2 and [182, 186, 143]). We applied the conjugate gradient scheme for almost all our static electronic structure computations. Only in a few cases where the scheme

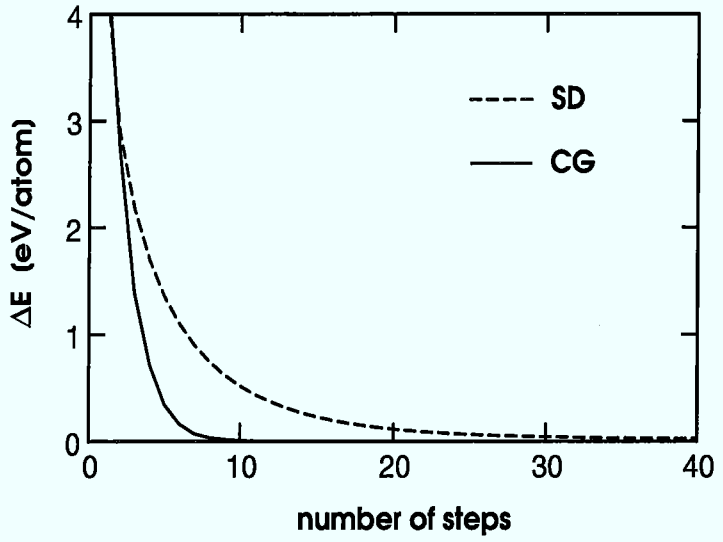

Figure 2.2: Comparison of the convergence of the steepest descent (dashed line) and the conjugate gradient (solid line) algorithm. The system investigated was a H_2 molecule. ΔE represents the energy difference between partly and completely converged total energies. The scale of the figure suggests an underestimation of the difference in performance, because the required convergence is much higher than can be resolved by the curves. Thus an energy resolution of 1 meV was achieved in 14 steps by conjugate gradient whereas the steepest descent algorithm needed about 390 steps. Even taking into account the higher computational cost (roughly a factor of 2) of conjugate gradient it vastly outperforms steepest descent. In practice, it is recommendable to have a simple, robust convergence method at hand, because in some situations the conjugate gradient runs into difficulties.

did not work properly we resorted to steepest descent.
A refinement of the conjugate gradient algorithm can be achieved by preconditioning [186, 143]. Comparable performance rates are reached by iterative diagonalization schemes as Davidson's scheme [44] or Lanczos' method [141] and iterative minimization by direct inversion in the iterative subspace (DIIS) developed by Hutter, Lüthi, and Parrinello [83].

It is important to note that the techniques described in this chapter work only if $E[\{\psi_i\}]$ has only one minimum. Experience has shown that this condition holds for the minimization of the electronic structure only. However, the energy surface of the coupled spaces of ionic and electronic coordinates exhibits local minima, and a global minimization has to be performed. The state of the art technique to deal with this formidable problem is described in the following section.

2.1.5 Simulated Annealing and the Car-Parrinello Method

In principle, the ground state geometry of a set of atoms can be determined by computing the total energy for all possible arrangements of atoms and selecting the geometry with the lowest energy. However, the point by point scanning of the energy surface is feasible only for systems with very few degrees of freedom. A more refined approach is to start with some guess for the structure and to follow the forces to the next local minimum (as discussed for electrons in the previous chapter). The number of local minima increases exponentially with the number of atoms N and in practice this straightforward way to compute the minimum-energy configuration becomes not feasible for already a few atoms. Probably, the determination of the ground state structure in condensed matter physics belongs to the NP-complete (nondeterministic polynomial time complete) class. No method for an exact solution with a computing effort bounded by a power of N has been found for any of these problems [91, 92].
In a seminal paper Kirkpatrick et al. [98] addressed this class of problems and pointed out a useful connection between statistical mechanics and the optimization of a given function depending on many parameters. They treated various problems, such as the travelling salesman problem or the optimization of the physical design of computers with the Metropolis algorithm [124]. Four ingredients are needed for their scheme:

1. A concise description of the configurations of the system

2. A random generator of "moves" or rearrangements of the elements in a configuration

3. A quantitative objective function E whose minimization is the goal of the procedure

4. A control parameter T that governs the annealing process

During the minimization process a series of configurations are generated. A new configuration ζ_{n+1} will be accepted if the objective function at this configuration $E(\zeta_{n+1})$ is smaller than its value at the previous configuration $E(\zeta_n)$. Otherwise, the move is accepted with a probability of $\exp\left(-[E(\zeta_{n+1}) - E(\zeta_n)]/k_B T\right)$. During the simulation T is slowly decreased from a high starting value to zero. Experience has shown that the procedure leads to either the global or an energetically low-lying local minimum. In the literature this procedure has been called "simulated annealing". Contrary to Kirkpatrick et al. who applied simulated annealing in the framework of Monte Carlo simulations, Car and Parrinello's scheme allows us to perform dynamical simulated annealing, i.e., simulated annealing in connection with molecular dynamics. The objective function in their scheme is $E_{tot}[\{\psi_i\}, \{\vec{R}_I\}]$, the total energy. A temperature T is introduced via the kinetic

energy of the ions

$$\frac{1}{2}\sum_{I=1}^{N} M_I \dot{\vec{R}}_I^2 = \frac{3}{2} N k_B T. \tag{2.44}$$

The dynamics is generated as described in section (2.2.2). Within this scheme local relaxation is feasible for a few hundred atoms (see, e.g., chapter 6) and simulated annealing has been successfully performed for clusters up to 10 atoms [91, 92]. In chapter 6 we use this method to search for structures of hydrogen at high pressures.

2.2 The Car-Parrinello Method and Molecular Dynamics

The use of computational devices for solving problems in Statistical Mechanics goes back to Enrico Fermi. In his book "From x-rays to Quarks" Segré relates (cited from [199]):" ... I know that Fermi had invented, but of course not named, the present Monte Carlo method when he was studying the moderation of neutrons in Rome. He did not publish anything on the subject, but he used the method to solve many problems with whatever calculating facilities he had, chiefly a small mechanical adding machine." The development of the Monte Carlo (MC) scheme was catalyzed by the war efforts, when von Neumann, Ulam, and Metropolis employed stochastic numerical methods on neutron diffusion problems in Los Alamos. A seminal paper was published in 1953 by Metropolis et al., which treated computations on a hard-sphere liquid via the Metropolis Monte Carlo method. The next major step was taken in 1957. B. J. Alder and T. E. Wainwright published the first results obtained by molecular dynamics, also on a hard-sphere liquid [4], and W. W. Wood and F. R. Parker introduced continuous potentials, treating a Lennard-Jones fluid with MC [200].
The following years brought about a rapid development of computer simulations in Statistical Mechanics [5, 66]. The key to the correct representation of a real physical system proved to be the adequate parametrization of the energy surface, i.e., the construction of a realistic interaction potential. In the beginning molecular dynamics simulations were mainly concerned with static and dynamic bulk properties of simple monoatomic fluids or solids, where particles interact with radial, short-range forces. The comparison with approximate theories was of major importance, i.e., molecular dynamics was frequently applied as a tool of statistical mechanics. When the art of constructing potentials developed more and more the simulation of more complex materials became feasible and MD extended its applicability into materials science.
The most sophisticated potentials used so far are constructed from quantum mechanical calculations (DFT) and were introduced by R. Car and M. Parrinello [29]. In the next section (2.2.1) some basic concepts of MD are presented. The

central role of the potential is outlined and it is motivated why a quantum mechanical potential extends the scope of MD. How we use a potential constructed from DFT in a MD scheme is described in the following three sections (2.2.2-2.2.5), and the last section (2.2.6) informs about some technical aspects.

2.2.1 Molecular Dynamics

Molecular Dynamics (and Monte Carlo) methods have been described in many monographs (see for example [21, 36, 5, 103]). Therefore, we will restrict ourselves to the basic ideas of molecular dynamics for a microcanonical ensemble (in section 2.2.4 canonical molecular dynamics via CP is explained).
For simplicity we consider an isolated system of N identical interacting particles with $3N$ degrees of freedom. The classical dynamics of this system is described by the Lagrangian

$$\mathcal{L} = T - V, \tag{2.45}$$

where T is the kinetic energy and V the potential energy. We assume T to have the form $T = \sum_{I=1}^{N} \dot{q}_I^2/2$ and V not to depend on the velocities $\{\dot{q}_i\}$. Furthermore, we introduce Cartesian coordinates $\{\vec{R}_I\}$. Then the equations of motion

$$\frac{d}{dt}\left(\frac{\partial \mathcal{L}}{\partial \dot{q}_i}\right) = \frac{\partial \mathcal{L}}{\partial q_i} \tag{2.46}$$

assume the form

$$M\ddot{\vec{R}}_I = -\nabla_{\vec{R}_I} V(\{\vec{R}_I\}), \quad I = 1, ..., N. \tag{2.47}$$

In this form the equations of motion are readily integrated by one of the numerical schemes described in [20, 5].
We assume the system to be ergodic. Performing simulations on mostly liquid or disordered systems one obtains the expectation values of a physical observable A_{obs} by way of Liouville's theorem

$$A_{\text{obs}} = \langle A \rangle_{time} = \lim_{t_{obs}\to\infty} \frac{1}{t_{obs}} \int_0^{t_{obs}} A(\Gamma(t))dt, \tag{2.48}$$

where $\Gamma(t)$ denotes the trajectory in the $6N$-dimensional phase space. That way we can compute not only static quantities like the primary thermodynamic variables (E, V, T, P, N), the heat-capacity c_v, the isothermic compressibility χ and the radial distribution function $g(r)$ as in Monte Carlo methods, but also transport properties, such as the self-diffusion constant D, the shear-viscosity η (and bulk-viscosity ζ), the thermal conductivity λ_T, and the dynamical structure-factor $S(k, \omega)$.

The key to an accurate description of the system is the set-up of the "right" potential, i.e., a potential that reproduces the physical properties of the system under investigation. The first simulations were performed on hard-sphere systems, i.e.,

$$V^{HS}(r) = \begin{cases} \infty & (r < \sigma) \\ 0 & (\sigma \leq r) \end{cases}, \tag{2.49}$$

where σ defines the radii of the spheres. A major improvement was achieved by the introduction of continuous potentials. The best-known is the Lennard-Jones potential

$$V^{LJ}(r) = 4\epsilon \left(\left(\frac{\sigma}{r}\right)^{12} - \left(\frac{\sigma}{r}\right)^{6} \right), \tag{2.50}$$

which provides a good description of many atomic system, like for example noble gases and polymers. More general, the first two or three terms of the expansion

$$V = \sum_i v_1(\vec{r}_i) + \sum_i \sum_{j>i} v_2(\vec{r}_i, \vec{r}_j) + \sum_i \sum_{j>i} \sum_{k>j>i} v_3(\vec{r}_i, \vec{r}_j, \vec{r}_k) + \ldots \tag{2.51}$$

already provide an adequate description for most atomic systems. For ionic systems, induction interaction must be taken into account: the ionic charge induces a dipole on a neighbouring ion. Some simple models have been developed to deal with the problem [5]. For binary systems the intramolecular distance is kept fixed and the molecule can be described as two hard spheres or two Lennard-Jonesians bound together [5]. However, these simple models rely on the assumption of pairwise additivity of the interaction between atoms, ions or molecules. Thus they fail to describe the breaking and forming of bonds of molecules as well as all other physical phenomena where many-body forces are crucial. For example, covalent bonding cannot be described by pairwise interactions, because it leads to highly directional forces between particles and an ensuing tendency towards bond-network formation, which, e.g., may be of tetrahedral symmetry (as in silicon). An adequate description of the system must explicitly take into account the electronic structure, which causes the directional forces (in silicon it is the p-orbitals in the outer shell that have non-spherical densities and lead to the directional bonds). For that reason the construction of a realistic potential requires quantum mechanical calculations.

2.2.2 Ab initio Molecular Dynamics

In principle, the discussion of how to construct the potential is superfluous, because the "true" potential is well known: Just solve the many-body Schrödinger equation. Let us assume that the Born-Oppenheimer approximation holds. Then the potential can be constructed by solving the instantaneous electronic problem, i.e., for some ionic configuration $\{R_I\}$ the potential $V(\{R_I\})$ is just the ground state expectation value of the Hamiltonian

$$V(\{R_I\}) = \langle \Psi_o | \mathcal{H} | \Psi_o \rangle, \tag{2.52}$$

where Ψ_o is the ground-state many-particle wave function. Car and Parrinello applied DFT to calculate $\langle\Psi_o|\mathcal{H}|\Psi_o\rangle$. The total energy $E_{\text{tot}}[\{\psi_i\},\{\vec{R}_I\}]$ is put together from the DFT expression for the energy of the electronic system, 2.24, and the potential energy of the ions,

$$E_{\text{tot}}[\{\psi\},\{\vec{R}_I\}] = E[\{\psi\},\{\vec{R}_I\}] + \frac{1}{2}\sum_{I\neq J}\frac{Z_I Z_J}{\vec{R}_I - \vec{R}_J}. \tag{2.53}$$

Then the potential is computed via

$$V(\{R_I\}) = \langle\Psi_o|\mathcal{H}|\Psi_o\rangle = \min_{\{\psi_i\}} E_{\text{tot}}[\{\psi_i\},\{\vec{R}_I\}], \tag{2.54}$$

where $\{\psi_i\}$ are the Kohn-Sham orbitals. In principle, you could set up a Lagrangian

$$\mathcal{L} = T - V = \frac{1}{2}\sum_{I=1}^{N} M_I \dot{\vec{R}}^2 - V[\{\vec{R}_I\}] \tag{2.55}$$

and perform MD by

1. minimize $E_{\text{tot}}[\{\psi_i\},\{\vec{R}_I\}]$ with regard to $\{\psi_i\} \longrightarrow V(\{R_I\})$
2. compute $\nabla_{\vec{R}} V(\{R_I\})$ (Hellman-Feynman forces)
3. move ions $\longrightarrow \{\vec{R}_I(t+\Delta t)\} \longrightarrow 1$

for each step of MD. Unfortunately, the computational effort for the first step, which consists of many iterations of one of the methods described in 2.1.4, is very high. To avoid this time consuming minimization Car and Parrinello used a trick:
They introduced a fictitious dynamics for electrons by inserting a kinetic energy term for the electrons,

$$T_e = 2\mu\sum_{i}^{occ}\int |\dot{\psi}_i(\vec{r})|^2 d\vec{r}, \tag{2.56}$$

into the Lagrangian 2.45. It is necessary to add constraints to ensure the orthonormality of the wave functions. With these changes the Car-Parrinello Lagrangian reads

$$\begin{aligned}\mathcal{L} &= 2\mu\sum_{i}^{occ}\int |\dot{\psi}_i|^2 d\vec{r} + \frac{1}{2}\sum_{I} M_I \dot{\vec{R}}^2 - E_{\text{tot}}[\{\psi_i\},\{\vec{R}_I\}] \\ &+ 2\sum_{ij}\Lambda_{ij}\left(\int d\vec{r}\,\psi_i^*(\vec{r})\psi_j(\vec{r}) - \delta_{ij}\right),\end{aligned} \tag{2.57}$$

where Λ_{ij} are the Lagrangian multipliers belonging to the orthonormality constraints. The corresponding equations of motion are

$$\mu\ddot{\psi}_i(\vec{r},t) = -\frac{1}{2}\frac{\delta E}{\delta\psi_i^*(\vec{r},t)} + \sum_j \Lambda_{ij}\psi_j(\vec{r},t) \tag{2.58}$$

and

$$M_I\ddot{\vec{R}}_I = -\frac{\delta E}{\delta\vec{R}_I(t)}. \tag{2.59}$$

The dynamics is performed in the following way:

1. compute $V(\{\vec{R}_I(t)\})$ for ionic coordinates $\{\vec{R}_I(t)\}$
2. compute forces on electrons and ions $\nabla_{\vec{R}_I}\mathcal{L}$, $\delta_{\psi_i^*}\mathcal{L}$
3. move electronic wave functions and ions simultaneously.

The costly minimization of the energy functional is replaced by one step of MD for the electronic wave functions.

2.2.3 The Separation of Electronic and Ionic Time Scales

For the following discussion it is assumed that in the beginning of the simulation the electrons are converged to their ground state. The crucial point in the treatment of the electrons is to introduce two different time scales by choosing $\mu \ll M_I$, i.e., by setting the electronic mass much smaller than the ionic one. Pastore, Samargassi, and Buda [142] showed that for small deviations from the ground state the dynamics of the orbitals is described by a superposition of harmonic modes with frequencies equal to

$$\omega_{ij} = \left[\frac{2(\epsilon_i^* - \epsilon_j)}{\mu}\right]^2, \tag{2.60}$$

where ϵ_i^* denotes an unoccupied and ϵ_j an occupied state. The smallest electronic frequency is

$$\omega_{\min} = \left[\frac{2E_g}{\mu}\right]^{\frac{1}{2}}, \tag{2.61}$$

where E_g is the Fermi energy gap. With a convenient choice of μ the condition $\omega_{min} \gg \Omega_{max}$ (where Ω_{max} is the maximum of the ionic frequencies) may be satisfied, i.e., a separation of time scales can be achieved.
The adiabatic theorem of classical mechanics states that for a time governed by the ratio $\omega_{min}/\Omega_{max}$ the trajectory of the ions in a slow-fast system is well approximated by the trajectory one obtains by averaging over the fast degrees

of freedom [131].[1] Since the electronic motion is determined by a second order equation of motion the electrons oscillate around their ground state and to a very good approximation the average wave functions coincide with the ground state wave functions, i.e., the average forces coincide with the Hellman-Feynman forces. In short:
trajectory of slow-fast system
$\approx$ trajectory averaged over fast degrees of freedom
$\approx$ trajectory with electrons in ground state
$\equiv$ physical trajectory on Born-Oppenheimer surface.
The separation of time scales keeps the system in a metastable state with a small kinetic energy of electrons. For small $\omega_{min}/\Omega_{max}$ equipartition of the system is reached only in a time much longer than the the usual simulation times ($\sim$ ps). The choice of the electronic mass leads to $T_e \ll T_i \equiv \frac{1}{2}\sum_I M_I \dot{\vec{R}}^2$ and, because of $T_e + T_i + V = constant$, $T_i + V$ is nearly constant, i.e., the dynamics can be used to sample the ionic microcanonical ensemble.
In practice, one has to compromise between the length of the simulation time step Δt and the size of T_e, because there is a maximum value of stability of $\Delta t^2/\mu$ in the Verlet algorithm (see equation 2.76), i.e., a smaller electronic mass (and smaller kinetic energy of electrons) leads to a shorter time step Δt.
It is important to note that the Newtonian dynamics of electron wave functions really *fictitious*. There is no physical meaning in the quantity μ and in the fast time scale. Only the time scale of ions has physical relevance; the small oscillations of the electrons around their (on the ionic time scale) instantaneous ground state is not a physical phenomenon.

2.2.4 The Treatment of Metallic Systems and the Nosé Thermostat

For metallic systems the Fermi energy gap E_g closes and in formula 2.61 it is no longer possible to achieve the separation of time scales by choosing μ small. To keep the electrons close to their ground state Blöchl and Parrinello [26] introduced the Nosé thermostat [135, 136, 77, 137, 138] into the CP scheme. The main idea is presented in the following:
For simplicity we confine ourself to a simple system governed by the equation of motion

$$M\ddot{\vec{R}} = -\nabla V. \tag{2.62}$$

[1] Although Schrödinger's equation has to be solved to set up the potential, the dynamics generated is classical for the electronic degrees of freedom, also. It is Newton's equation of motion (equation 2.58) that is integrated. The classical adiabatic theorem only holds for a certain class of systems to which the slow-fast systems under consideration belong, because the fast degrees of freedom are close to their (instantaneous) minimum, i.e. ground state. It is not our aim to go into the details of this complicated mathematical problem. A more satisfactory account can be found in [142].

The aim is to keep the system close to a fixed average temperature T_{av}. In Nosé's "extended system method" an additional degree of freedom $s(t)$ is introduced. For a canonical formulation it is necessary to introduce virtual variables (q_i,p_i,t) that are related to the real variables (q_i',p_i',t') by

$$\begin{aligned} q_i' &= q_i \\ p_i' &= \frac{p_i}{s} \\ t' &= \int^t \frac{dt}{s}. \end{aligned} \tag{2.63}$$

The virtual variable formulation allows us to retain the canonical treatment via the Hamilton formalism. Within the real variable formalism additional force terms (friction terms) appear that evade an elegant treatment [136]. Nosé postulated a Hamiltonian for the extended system of particles

$$H = \sum_i \frac{p_i^2}{2m_i s^2} + V(q) + \frac{p_s^2}{2Q} + g k_b T_{\mathrm{av}} \ln s, \tag{2.64}$$

where T_{av} is the externally set temperature and g will be explained below. From this Hamiltonian the equations of motion can be derived in the canonical way as it is described in [136]. Replacing the virtual variables by the real ones the equations of motion in their Lagrangian formulation become:

$$\begin{aligned} \frac{d}{dt'}\left(m_i s \frac{dq_i'}{dt'}\right) &= -s\frac{\partial V}{\partial q_i'} \\ \frac{d}{dt'}\left(\frac{Q}{s}\frac{ds}{dt'}\right) &= \sum_i m_i \left(\frac{dq_i'}{dt'}\right)^2 - g k_b T_{\mathrm{av}}. \end{aligned} \tag{2.65}$$

Using Cartesian coordinates $\{\vec{R}_I\}$ and introducing $x \equiv \ln s$, the equations of motion assume a form in which they are easily interpreted

$$M_I \ddot{\vec{R}}_I = -\nabla_{\vec{R}_I} V - M_I \dot{x} \dot{\vec{R}}_I \tag{2.66}$$

and

$$Q\ddot{x} = 2\left[\sum_i \frac{1}{2} M_I \dot{\vec{R}}_I^2 - \frac{1}{2} g k_b T_{\mathrm{av}}\right]. \tag{2.67}$$

From 2.66 it is clear that $\dot{x}$ plays the role of a friction coefficient. Equation 2.67 ensures that the kinetic energy of the ions oscillates around a set value $\frac{1}{2} g k_b T_{\mathrm{av}}$ consistent with a temperature T_{av} when g is set equal to the number of degrees of freedom of the system, i.e., $g = 3N$.[2] Inserting real variables into the Hamiltonian

[2]The total number of degrees of freedom is $3N + 1$, because x constitutes an additional degree of freedom. That is the reason why the method is called "extended system method".

2.64 with $x = \ln s$ and noting that $p_s = Qds/sdt' = Qd\ln s/dt' = Q\dot{x}$ one easily sees that the energy

$$E_{\text{tot}} = \sum_I \frac{1}{2} M_I \dot{\vec{R}}_I^2 + V(\{\vec{R}_I\}) + \frac{1}{2} Q\dot{x}^2 + g k_b T_{\text{av}} x \tag{2.68}$$

is conserved.

The first simulations of metallic systems via CP used the thermostat for the ions and quenched the electrons back to their ground state after a certain amount of steps. A more systematic approach was introduced by Blöchl and Parrinello [26] who added a thermostat for the electrons, too. The electrons are kept close to an energy $E_{\text{kin},0}$. The proper choice of $E_{\text{kin},0}$ is discussed in [26]. If its value is too large, the electronic wave functions will depart from the Born-Oppenheimer surface and if it is too small, the electrons will be hindered in following the atomic motion and the motion will be retarded.

The generalisation of the formalism to two heat baths is straightforward, the equations of motion become

$$\mu \ddot{\psi}_i(\vec{r}, t) = -\frac{1}{2} \frac{\delta E}{\delta \psi_i^*(\vec{r}, t)} + \sum_j \Lambda_{ij} \psi_j(\vec{r}, t) - \mu \dot{x}_e \dot{\psi}_i(\vec{r}, t) \tag{2.69}$$

and

$$M_I \ddot{\vec{R}}_I = -\frac{\delta E}{\delta \vec{R}_I(t)} - M_I \dot{x}_{\vec{R}} \dot{\vec{R}}_I. \tag{2.70}$$

The last term of each equation is the friction term which couples wave functions and atom dynamics to the Nosé thermostats for electrons and ions respectively. Together with the friction terms dynamical variables x_e and $x_{\vec{R}}$ were introduced which obey the equations of motion

$$Q_e \ddot{x}_e = 2 \left[\sum_i \mu \int \dot{\psi}^*(\vec{r}, t) \dot{\psi}(\vec{r}, t) d\vec{r} - E_{kin,0} \right] \tag{2.71}$$

and

$$Q_{\vec{R}} \ddot{x}_{\vec{R}} = 2 \left[\sum_i \frac{1}{2} M_I \dot{\vec{R}}_I^2 - \frac{3}{2} N k_b T \right], \tag{2.72}$$

where $E_{kin,0}$ is the average kinetic energy of the electronic wave functions and $\frac{3}{2} N k_b T$ is the average kinetic energy of the ionic degrees of freedom. The thermal fluctuations are governed by the masses Q_e and $Q_{\vec{R}}$. The conserved quantity corresponding to the equations of motion is

$$\begin{aligned} E_{\text{tot}} &= \sum_i \mu \int \dot{\psi}^*(\vec{r}, t) \dot{\psi}(\vec{r}, t) d\vec{r} + \sum_I \frac{1}{2} M_I \dot{\vec{R}}_I^2 + E_{\text{tot}}(\{\psi_i\}, \{\vec{R}_I\}) \\ &+ \frac{1}{2} Q_e \dot{x}_e^2 + 2 E_{kin,0} x_e + \frac{1}{2} Q_{\vec{R}} \dot{x}_{\vec{R}}^2 + f k_b T x_{\vec{R}}. \end{aligned} \tag{2.73}$$

It can be shown that both the fictitious dynamics of the wave functions and of the ionic degrees of freedom are canonical with different, pre-set temperatures [26].

2.2.5 Applicability and Limitations of the Car-Parrinello Method

As mentioned in section 2.2.1, CP dynamics will provide an improvement over classical MD for systems with highly directional, covalent bonding. Therefore, especially the liquid and amorphous phases of semiconductors as Si (see for example [181, 153, 180]), Ge ([104, 185]) and GaAs ([205]) or covalently bonded systems as C ([56]) were investigated with this method. All these simulations not only demonstrate the usefulness but also show the limitations of the method. In the applications cited above the system sizes were small (54-64 atoms) and the simulation times short ($\leq 10\ ps$). They show that the method is computationally very expensive, because

1. the computation of the forces on the electrons is expensive
2. the separation of the time scales leads to a small time step, typically $10^{-17}...10^{-16}$ s
3. the method scales as $O(N^3)$, N number of atoms, whereas classical MD scales as $O(N^1)$ or $O(N^2)$.

These drawbacks lead to some limitations. The system sizes are very small compared with classical MD. In the simulations presented in chapter 7 and 8 systems of 64-250 atoms have been treated. However, the systems with more than 100 atoms are only tractable, because we can use local pseudopotentials (see 3). The small system sizes lead to finite size effects which are most substantial in metallic systems where $\vec{k}$-point sampling would be desirable (see following section). The short simulation times (ps range) preclude the method for the study of a wide range of chemical and biological systems where longer relaxation times are essential.

2.2.6 Some Technicalities

Since the details of the implementation of the CP scheme are described in [29, 155] and the formalism for computing the total energy in [86, 85] we will restrict ourselves to the most important points, the use of periodic boundary conditions, the integration scheme, and the orthogonalization.
In our simulations the atoms are confined in a box. To avoid surface effects at the boundaries of the box periodic boundary conditions are used, i.e., the box is replicated throughout space. This replication of cells also is necessary for an

expansion of the Kohn-Sham orbitals $\{\psi_i\}$ and the electronic density in a discrete sum of plane waves. For a cubic box of length a the periodic boundary conditions restrict the wave vectors $\vec{g}$ to

$$\vec{g} = \frac{2\pi}{a} \sum_{i=1}^{3} n_i, \quad n_i \in \mathbb{N}. \tag{2.74}$$

For metallic systems where the electronic states are delocalized, one should allow for the wave function to extend over several replica of the box by introducing $\vec{k}$-points. In general, the index i counting the orbitals ψ_i is a multi-index $(m, \vec{k})$, where m numbers the solutions of Schrödinger's equation for fixed $\vec{k}_i$. The computation of the electronic density n and the total energy E_{tot} requires an integral over the Brillouin zone[3] and the expansion of the orbital with index $\vec{k}$ is

$$\psi_i(\vec{r}) = \mathrm{e}^{i\vec{k}_i \cdot \vec{r}} \sum_{\vec{g}} c_i(\vec{g}) \mathrm{e}^{i\vec{g}_i \cdot \vec{r}}. \tag{2.75}$$

Since the CP method is very time consuming and its applicability limited to small systems and short relaxation times (see section 2.2.5), most ab initio computations restrict $\vec{k}$-point sampling to the Γ-point only. This restriction imposes limitations, which are discussed in detail in chapter 7.
For the integration of the equations of motion the Verlet algorithm is used

$$\psi(\vec{r}, t + \Delta t) = -\psi_i(\vec{r}, t - \Delta t) + 2\psi_i(\vec{r}, t) + \frac{(\Delta t)^2}{\mu} \left(-\frac{1}{2} \frac{\delta E}{\delta \psi_i^*(\vec{r}, t)} \right) \tag{2.76}$$

$$\vec{R}_I(t + \Delta t) = -\vec{R}_I(t - \Delta t) + 2\vec{R}(t) - \frac{(\Delta t)^2}{M_I} \frac{\delta E}{\delta \vec{R}_I(t)}. \tag{2.77}$$

One obtains these equations by writing the second derivative in Newtons's equations as second order differential quotient and solving for the quantity at time $t + \Delta t$. It is convenient to use a low order formula such as the Verlet algorithm, because it saves computer memory which is important with respect to the large number of plane waves (typically several thousands) in the expansion of the wave functions and the electronic density.
The orthogonalization of the wave functions succeeds the integration 2.76. For the iterative minimization described in 2.1.4 usually the Gram-Schmidt algorithm is used in which a set of orthonormal wave functions ψ_i' is obtained by

$$\begin{aligned} \psi_i'' &= \psi_i - \sum_{j<i} \langle \psi_j' | \psi_i \rangle \, \psi_j' \\ \psi_i' &= \frac{\psi_i''}{|\psi_i''|}. \end{aligned} \tag{2.78}$$

[3] In principle, one has to include k-dependent weights in the individual terms of the fictitious kinetic energy. However, for a set of k-points with equal weights you can hide the weights in the electronic mass μ, and expression 2.57 is still correct.

The Gram-Schmidt scheme brings about a unitary transformation in the space of the occupied orbitals which leaves $E_{\rm tot}(\{\psi\})$ unchanged; yet is not compatible with the kinetic energy term T_e of the electronic degrees of freedom. To keep $T_e + T_i + V = constant$ another orthogonalization scheme must be used. Car and Parrinello applied the iterative scheme by Ryckaert, Ciccotti, and Berendsen [158], which is also described in [30, 57, 58]: Let $\tilde{\psi}_i(\vec{r}, t + \Delta t)$ be the orbitals computed by the Verlet algorithm 2.76. Comparison with 2.58 shows that the application of the orthonormality constraints leads to

$$\psi_i(\vec{r}, t + \Delta t) = \tilde{\psi}_i(\vec{r}, t + \Delta t) + \frac{\Delta t^2}{\mu} \sum_j \lambda_{i,j} \psi_j(\vec{r}, t). \tag{2.79}$$

The orthonormality conditions $\langle \psi_i(\vec{r}, t + \Delta t) | \psi_j(\vec{r}, t + \Delta t) \rangle = \delta_{i,j}$ lead to the following matrix equation for the Lagrange parameters $\lambda_{i,j}$

$$XX^+ + XB + B^+X^+ = 1 - A, \tag{2.80}$$

where $x_{i,j} = \delta t^2 / \mu \lambda_{i,j}$, $A_{i,j} = \left\langle \tilde{\psi}_i(\vec{r}, t + \Delta t) | \tilde{\psi}_j(\vec{r}, t + \Delta t) \right\rangle$, and $B_{i,j} = \left\langle \psi_i(\vec{r}, t) | \tilde{\psi}_j(\vec{r}, t + \Delta t) \right\rangle$. Then equation 2.80 is solved iteratively

$$\begin{aligned} X^{(n)} &= \frac{1}{2} \left[1 - A + X^{(n-1)} (1 - B) + (1 + B) X^{(n-1)} - X^{(n-1)^2} \right] \\ X^{(0)} &= \frac{1}{2} (1 - A). \end{aligned} \tag{2.81}$$

Figure 2.3: Flow Chart of an ab initio MD run

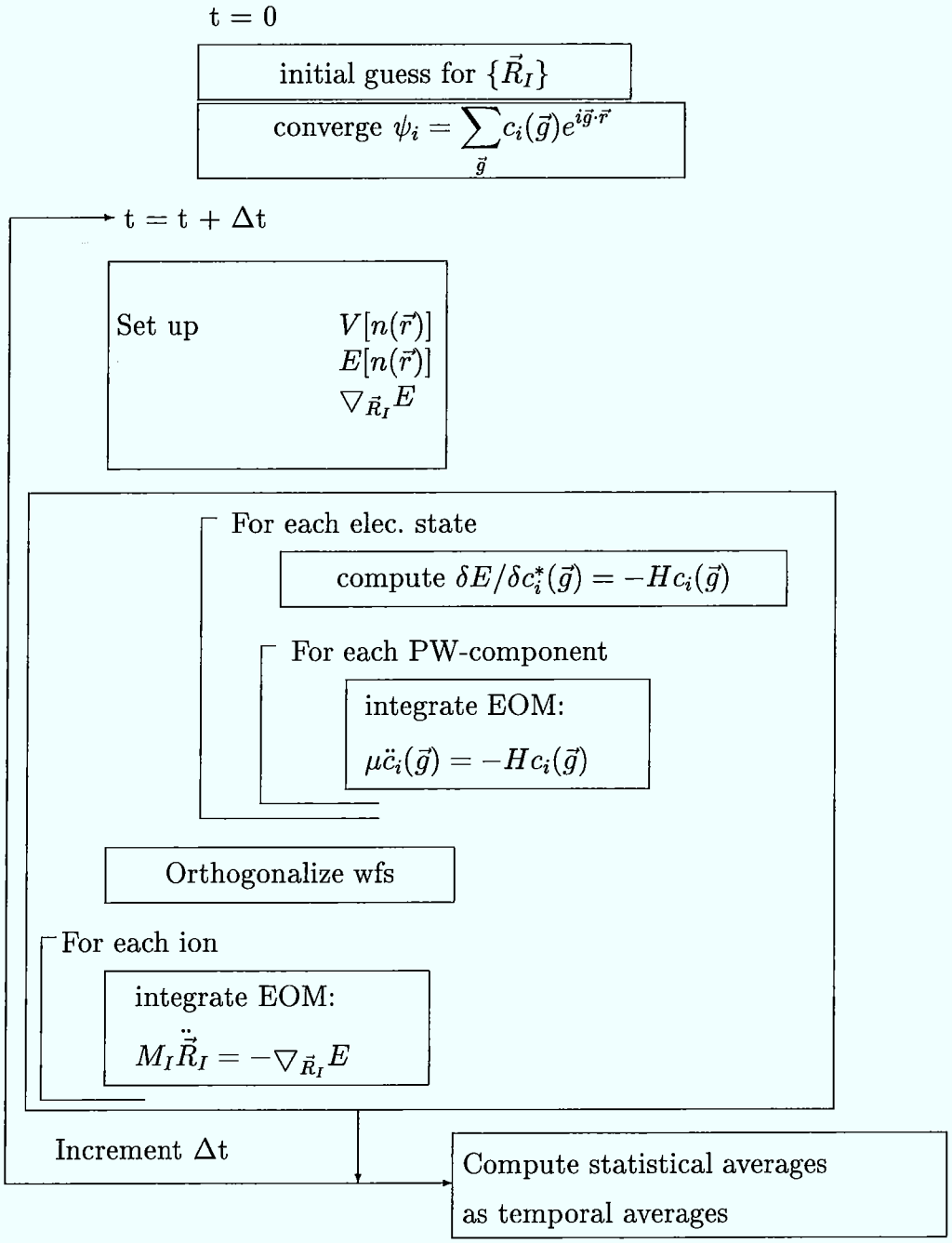

Chapter 3

Pseudopotentials for Hydrogen and Helium

As described in section 2.1.3, the major advantage of the pseudopotential method is to avoid the explicit treatment of the core electrons and to allow for an expansion into a manageable number of plane waves. However, the elements H and He only have valence electrons. In the following we justify the use of pseudopotentials for these elements and discuss the peculiarities involved. Our pseudopotentials for H and He are shown in figure 3.1. The cutoff r_c beyond which the pseudopotential and the true Coulomb potential coincide was 0.3 a.u. for H and 0.6 a.u. for He. The pseudopotentials shown were applied for a maximum density of $r_s = 1.0$. (For our simulations at $r_s = 0.5$ we generated a H pseudopotential with $r_c = 0.25$.) It is instructive to compare these values with the minimum distances between the individual atoms occurring in our simulations. The statistical measure for interatomic distances is the pair correlation function (see section 7.1). Since we are interested in the lower bound for the distance between atoms the relevant pair correlation functions are those for the highest temperature where the kinetic energy allows the atoms to come closer together than for lower temperatures. The H-H pair correlation function is zero for distances smaller than about 0.85 a.u., i.e., the probability to find two H atoms with a smaller distance vanishes (figure 7.2). The corresponding values for the H-He pair correlation function of the mixture and the He-He pair correlation function of the pure system are roughly 1.2 a.u. and 1.6 a.u. (figures 8.1 and 8.2). These values are significantly larger than the cutoff radius, i.e., r_c is chosen small enough with a vengeance for the atoms to feel the "true" Coulomb potential. The pseudopotential provides an adequate description, because configurations of the system where two atoms come close enough for the pseudopotential to differ from the Coulomb potential have virtually zero probability in phase space.

An obvious alternative to the use of pseudopotentials for H and He is the direct application of the Coulomb potential. It has been used in several computations, for example in [100]. Pseudopotentials have two advantages in combination with

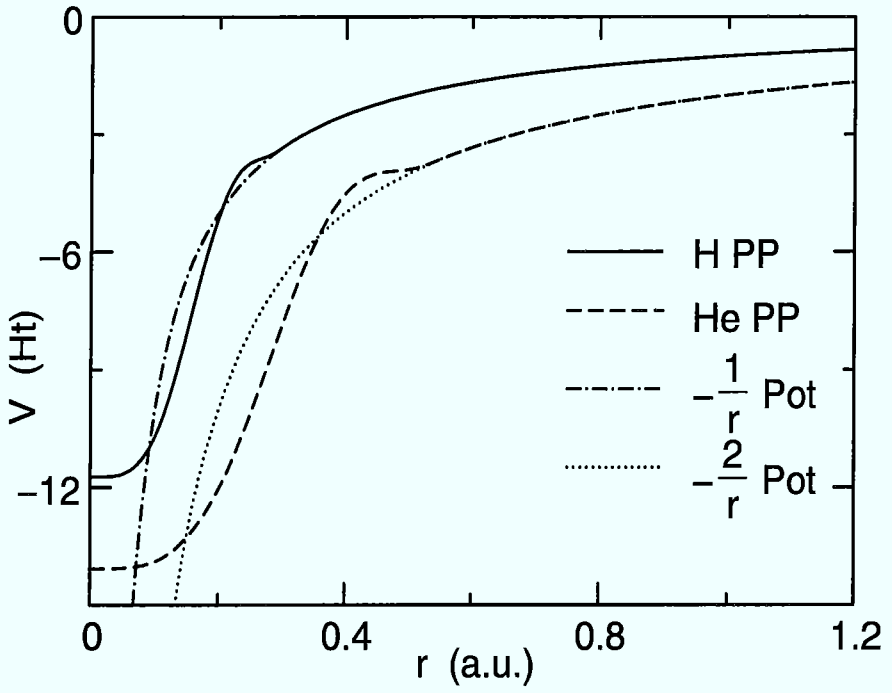

Figure 3.1: The pseudopotentials V of H (solid line) and He (dashed line) together with the "true" Coulomb potentials (dash-dotted and dotted line). The cutoff radii for the pseudopotentials were $r_c = 0.3$ a.u. for H and $r_c = 0.6$ a.u. for He.

plane wave codes: Because of the singularity at the origin it is impossible in a plane wave expansion to achieve complete convergence for the solutions of a Schrödinger equation with a $(1/r)$-potential. Thus the expansion has to be truncated. For the bare Coulomb potential the truncation consists of choosing an energy cutoff for the expansion in plane waves whereas in the pseudopotential approach a cutoff radius r_c is defined beyond which pseudopotential and Coulomb potential are identical (see section 2.1.3). The truncation in the pseudopotential method is better controlled than for a $1/r$-potential:

- A pseudopotential can be converged with a manageable number of plane waves. Usually, the expansion comprises all plane waves with a kinetic energy smaller than a chosen energy cutoff. For a pseudopotential the physical quantities will not change with a further increase of the number of plane waves if the cutoff is high enough. The energy cutoff where complete convergence is achieved represents an upper bound for the number of basis functions needed in the simulation. With a $1/r$-potential this strict criterion is missing.

Table 3.1: Binding energy E_b (eV), bond distance r_{eq} (a.u.) and vibration frequency ν_{eq} (cm^{-1}) for H_2. Two LDA pseudopotential calculations are compared with the experimental numbers. The plane wave cutoff energy for the electronic wave functions in this work was 50 Ry (Martins-Troullier pseudopotential), in [75] 60 Ry (Bachelet-Hamann-Schlüter pseudopotential). The experimental value was taken from [93].

H_2	TM	BHS	Expt.
E_b(eV)	4.83	4.82	4.78
r_{eq}(a.u.)	1.46	1.46	1.40
ν_{eq}(cm^{-1})	4100	3980	4395

- The pseudopotentials were constructed to be norm conserving, i.e., pseudo and "true" wave function give the same charge when integrated over the region where the pseudo wave function differs from the true one. However in a truncated Coulomb potential norm conservation is not explicitly built in and errors will be induced into the norm of the wave function due to the expansion into a finite number of plane waves.

Thus the use of a pseudopotential seems to be preferable over a $1/r$-potential. Because of the missing core the pseudopotentials of H and He are comparatively stiff and require a high cutoff energy. We tested the pseudopotentials by computing bond distances and bond energies of the H_2- and He_2-dimers and found 50 Ry to be sufficient (see tables 3.1 and 3.2). With an energy cutoff of 50 Ry we are able to reproduce (within reasonable accuracy) previous calculations performed in the framework of DFT/LDA. The comparison with the experimental data shows that the model (LDA) does not provide a good description for the He dimer whereas the results for the H dimer compare well with experiment. The reason for this discrepancy in the theoretical and experimental results for the He dimer is the inadequate treatment of the exchange correlation term. The two electrons of a He atom fill the 1s-orbital, i.e., He has a closed-shell structure. The He atoms interact merely via induced dipole-dipole (van-der-Waals) interaction which are intrinsically non-local and evade a local approximation for the exchange-correlation term. A more complete quantum chemical approach is provided by configuration interaction (CI) calculations which compare well with experiment but are prohibitively expensive [93]. It is a generic feature of the local density approximation that interactions between closed-shell systems are not well described. One special case is the H_2-H_2 interaction at ambient pressure. Thus

Table 3.2: Binding energy E_b (i.e., potential well depth) (eV) and bond distance r_{eq} (a.u.) for He_2. The LMTO result and the experimental value were taken from [90]. Any purely local approximation in DFT describes van der Waals-interaction and therefore the He dimer poorly. The interest in the present study lies with the *repulsive* branch of the potential, and a faithful description of the shallow binding region is performed for test purposes only.

He_2	TM	LMTO	Expt.
E_b(eV)	0.01	0.01	0.001
r_{eq}(a.u.)	4.45	4.55	5.86

H and He are difficult to treat within DFT/LDA. However, the situation changes substantially in the high-pressure regime. The applicability of the method is drastically better for high densities (see chapter 5).

Chapter 4

Molecular Dissociation in a One Dimensional System

In this short chapter a simple model is presented to provide a qualitative introduction to the more sophisticated (and quantitative) simulations later. Here we consider a linear, one-dimensional chain of H atoms and compute the ground state geometry. For low densities the ground state arrangement consists of aligned molecules with an intermolecular distance too large for the molecules to influence each other, i.e., a chain of free molecules. When the density increases the charge distributions of the individual molecules overlap. Two lengths, the inter- and the intramolecular distance, change as a function of density. The ground state configuration is completely characterized by these two lengths. Finally, for high densities the repulsive part of the H potential dominates and the H atoms will be equidistantly distributed, i.e., at some point a phase transition from a molecular to an atomic system occurs. It will be seen that this phase transition shows some qualitative features of the "real" H system. Of course other characteristics, especially the orientation of the molecules, are not represented.
The state of the system is defined by the density, which is measured in atoms/(a.u.). Within DFT/LDA we computed the bond length of the free molecule. The LDA result is 1.46 a.u. (see table 4.1), somewhat larger than the experimental result of 1.40 a.u. If the intramolecular distance remained rigid for increasing density the transition to an atomic chain would occur at a density of $1/1.46 \approx 0.68$ atoms/a.u. In the molecular solid at ambient pressure the intermolecular distance is 7.18 a.u. As mentioned in chapter 1.1, the charge distributions of the molecules in the solid hardly overlap and the molecules are essentially free. Therefore, 0.68 atoms/(a.u.) and $2/7.18 \approx 0.28$ atoms/(a.u.) provide two extremes between which the dissociation is likely to take place. We performed short static and dynamic computations with 5 molecules per unit cell (and Γ-point only) for densities of 0.4, 0.5, 0.56, 0.57, 0.59, 0.63, 0.71, and 0.83 atoms/(a.u.) and investigated the dissociation of the molecules.
A good starting point for the following discussion are the inter- and intramolecu-

lar distances as a function of density (see table 4.1). In the first column the values

Table 4.1: Calculated intramolecular (d_B) and intermolecular (d_I) distances for a variety of densities ρ.

ρ (atoms/(a.u.))	0.	0.4	0.5	0.56	0.57	0.59
d_B (a.u.)	1.46	1.47	1.49	1.55	1.60	1.70
d_I (a.u.)	∞	3.53	2.51	2.05	1.90	1.70

for the free molecule are shown. It is not surprising that intermolecular distances decrease with increasing density. The result for the intramolecular distances defies intuition. The molecules do not stay rigid, nor does the higher density (and pressure) reduce their bond length. The intramolecular distance increases, first slightly, but closer to the dissociation density the expansion of the molecules accelerates. At 0.59 atoms/(a.u.) (and for the higher densities that are not shown) inter- and intramolecular distances are equal, i.e., the system is atomic at a density substantially smaller than our first estimate of 0.68 atoms/(a.u.). Clearly, this trend is not readily explained and it is instructive to examine the changes in the electronic density.

In figure 4.1 the charge density of an individual hydrogen atom, of a free hydrogen molecule, and the molecule with the atomic charge densities subtracted are shown. Let us examine the change of the charge difference density under pressure. In figure 4.2 the charge densities for $\rho = 0.4$, 0.57, and 0.59 atoms/(a.u.) are plotted. The atomic densities were subtracted. For the smallest density, 0.4 atoms/(a.u.), the charge peaks corresponding to the individual molecules are close to the charge density of the free molecule. They are well separated, exhibit a small cusp and the (slightly depleted) charge density between the individual peaks is nearly constant. When ρ increases the cusp becomes more pronounced and the peaks widen (corresponding to the increased bond distance) and overlap. Between $\rho = 0.57$ and 0.59 atoms/(a.u.) the charge density changes drastically, the molecular peaks split in two and the system becomes atomic. For $\rho \geq 0.59$ the charge density oscillates with peaks at the positions of the atoms.

Obviously, close to the transition to an atomic system small changes in the density result in large changes in the electronic properties and ionic arrangement. To understand this effect it is helpful to investigate the potential surface close to the minimum energy configuration. For the quantitative description we introduce the displacement x from the fully symmetrical geometry, i.e., a linear chain of equally spaced atoms (see figure 4.3). When the intramolecular distance is increased

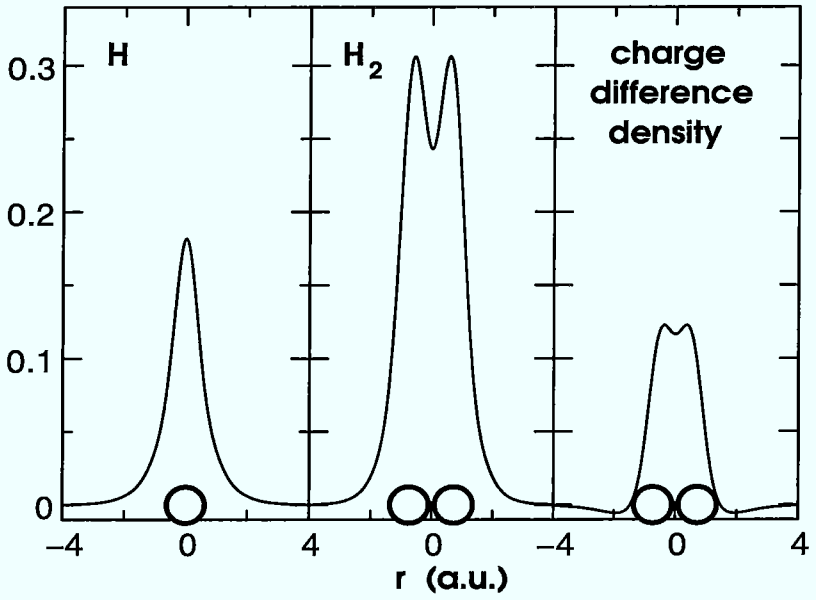

Figure 4.1: Electronic charge densities of the hydrogen atom, the hydrogen molecule and the molecule with the atomic charges subtracted. The atoms are represented as open circles.

the potential rises until all atoms are equally spaced (open circles in figure 4.3). At that point the constituent atoms in the molecules change partner to form new molecules. For this simple model the potential curves are symmetric with respect to equal spacing, i.e., $x = 0$, because the different minima merely correspond to an exchange of the bonding partners. The curves were fitted to the leading terms in a Taylor expansion $f(x) = \alpha + \beta \cdot x^2 + \gamma \cdot x^4$, where the origin is the reflection symmetry point of the potentials (i.e., $x = 0$ in figure 4.4). Close to dissociation the simple model exhibits two features that are also typical of the 3-dimensional simulations (figure 4.4):

1. The potential curves have a flat region close to $x = 0$. Only a small energy barrier has to be overcome to reach a new minimum. It is specific to this model that the geometries and the energies of the different minima are identical. As will be seen in chapter 6, in the regime of the dissociation of the molecules energy minima exist with comparable energies, but very different geometries. We believe the situation to be qualitatively similar to this model, i.e., very flat regions of the energy surface exist and only small energies are needed to change the geometries significantly.

2. In the regime of the dissociation of the molecules the potential is very anharmonic. The ratio of γ to β in the fit formula $f(x) = \alpha + \beta \cdot x^2 + \gamma \cdot x^4$ is about 10:1 for $\rho = 0.56$ atoms/(a.u.) and about 25:1 for $\rho = 0.57$

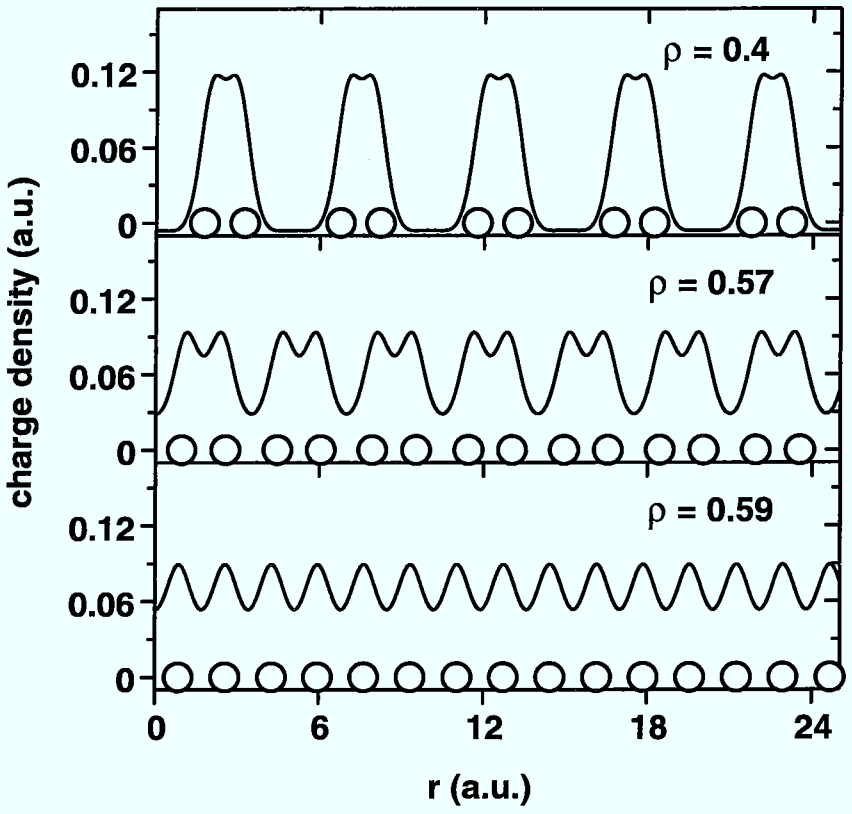

Figure 4.2: Electronic charge densities of a linear chain of hydrogen molecules at density $\rho = 0.4$, 0.57, and 0.59 atoms/(a.u.). The atoms are represented as open circles.

atoms/(a.u.) and 0.59 atoms/(a.u.), i.e., the quartic term will dominate over the quadratic one already at small x. This anharmonicity is due to many-body effects that are responsible for the fact that simple models, such as the pair potential approach, fail to provide a good description in this regime (see the discussion in chapter 5).

In figure 4.5 the potential is shown for $\rho = 0.63$, 0.71, and 0.83 atoms/(a.u.). With increasing density the potential grows stiffer and less anharmonic. In the high density limit the repulsive part of the potentials dominate.

The flattening of the potential is reflected by a weakening of the vibrational frequencies. In table 4.2 the vibrational frequencies for some densities are shown. Contrary to $\rho = 0.4$ atoms/(a.u.) where the frequency is only little lower than in the free molecule the weakening is substantial close to the dissociation. This result is easily understood with regard to the softer potential and the increased

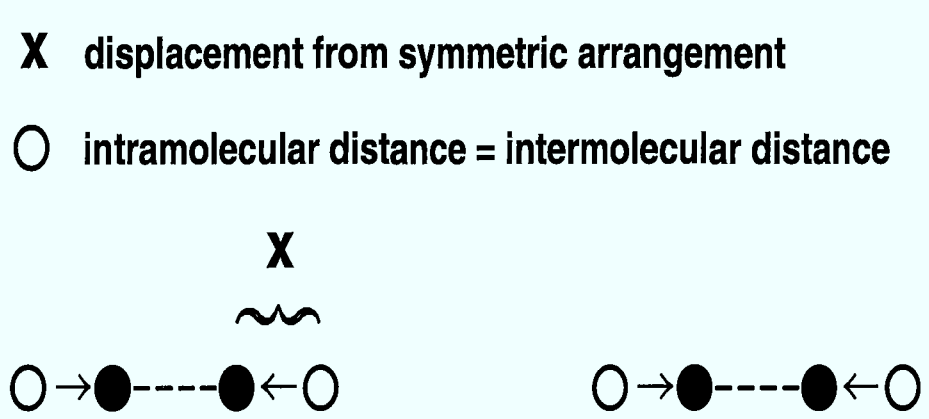

Figure 4.3: Definition of displacement x. The open circles denote the symmetric arrangement where intramolecular and intermolecular distances are equal. The length x is the displacement from the fully symmetric geometry.

bond length close to the molecular-atomic transition.

This trend of decreasing frequencies with increasing density is consistent with

Table 4.2: Vibrational frequencies λ (cm^{-1}) as a function of density ρ (atoms/a.u.).

ρ	0.	0.4	0.5	0.56	0.57
λ	4120	3980	3390	2260	1420

the experimental picture (see figure 1.5 in chapter 1.1).

Finally, it is interesting to note that the energy gap between the highest occupied and lowest unoccupied electronic state decreases from 10.1 eV at $\rho = 0.4$ to 4.3 eV at $\rho = 0.83$ atoms/(a.u.). The decrease of the gap indicates the density dependence of the electronic structure. We will address the pressure dependence of the electronic structure in chapter 7 and demonstrate there that H metallizes in the regime of the molecular-atomic transition.

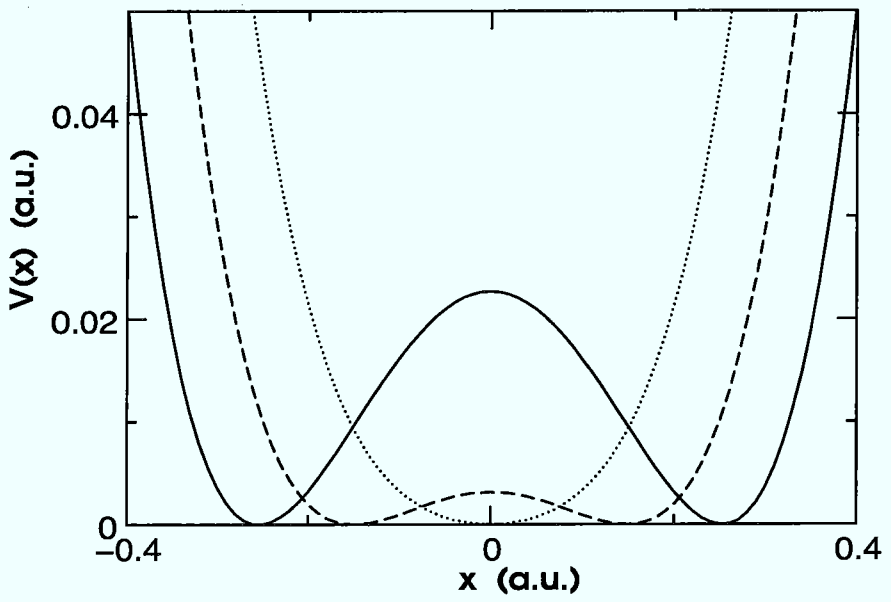

Figure 4.4: Potential curve $V(x)$ for $\rho = 0.56$ (solid line), 0.57 (dashed line), and 0.59 (dotted line) atoms/a.u. The abscissa shows the intramolecular distance for x smaller than zero. For x = 0 all the atoms are equally spaced. Negative and positive x values correspond to different pairing of the atoms. (Of course the situation is different for $\rho = 0.59$ where the molecules no longer exist. The abscissa simply denotes the deviation from the minimum.)

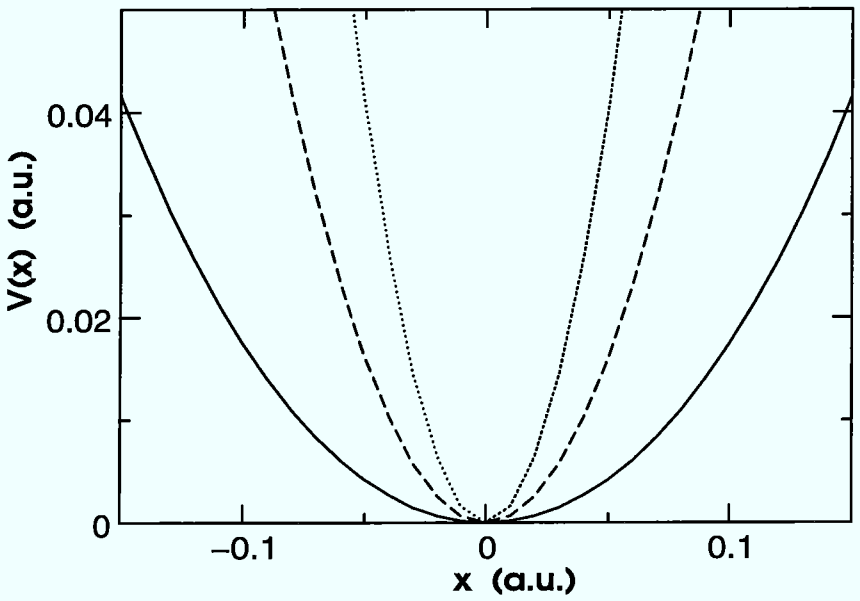

Figure 4.5: Potential curve $V(x)$ for $\rho = 0.63$ (solid line), 0.71 (dashed line), and 0.83 (dotted line) atoms/(a.u.). The abscissa shows the deviation from the minimum. The figure demonstrates the growing stiffness of the potential with increasing density.

Chapter 5

Equations of State at High Pressures

As argued in the previous chapter, DFT/LDA cannot provide a good description of the He-He and H_2-H_2 interactions for low pressures. In chapter 4 a qualitative picture of a pressurized H_2 system was presented. When the pressure increases the wave functions overlap and the nature of the bonding gradually changes from van-der-Waals type to covalent. A further increase in the pressure ionizes the atoms and the system becomes metallic. Finally, in the limit of infinite pressure the electronic and ionic systems decouple, i.e., the electron-ion interaction becomes negligible in comparison with the electron-electron and ion-ion interaction. Thus for very high pressures the electrons are virtually free and the LDA (which assumes the functional form of a homogeneous electron system) becomes exact. The same qualitative picture is true for He. Hence the errors stemming from the LDA, which are the cause for the inadequate treatment of van-der-Waals interactions eventually decrease to zero, and it is reasonable to expect DFT/LDA to provide a better description for H and He at high pressures. The aim of this chapter is twofold. On one hand we investigate quantitatively the accuracy of LDA for elevated pressures and justify the application of this approximation in the density range we studied ($r_s = 1.5 - 0.5$ for H and $r_s = 1.31 - 1.0$ for He and H-He). On the other hand we show that it is necessary to apply an ab initio potential. Simpler, empirical potentials will not provide a quantitative description at high pressures if they are fitted to experimental pressure data. Our gauges are the equations of state for H and He.

For low pressures H_2 and He two-body interaction potentials are often fitted to experimental and/or theoretical data. For a crystal lattice the internal energy is readily obtained from the potentials via

$$U = \frac{1}{2} \sum_{\vec{R}_i \neq \vec{R}_j} V(\vec{R}_i - \vec{R}_j), \tag{5.1}$$

where $\{\vec{R}_i\}$ are the lattice sites in the crystal and $V(\vec{R}_i - \vec{R}_j)$ is the interatomic (or intermolecular) pair potential. For our computations with empirical potentials we used hcp, fcc, and bcc lattices. The differences in the equations of state are very small, except for the very high pressure range where bcc is favored. A simple form for V is the Lennard-Jones potential (see 2.50). For H_2 a Lennard-Jones potential (and some other simple, empirical potentials) can be found in [171] (Lennard-Jones parameters: $\epsilon/k_b = 36.7\ K$ and $\sigma = 2.96$ Å) and for He in [73] (Lennard-Jones parameters: $\epsilon/k_b = 10.22\ K$ and $\sigma = 2.556$ Å). These potentials were fitted to experimental data at low pressures. The Lennard-Jones form for the potential is known to be far too inflexible in fitting both low- and high-pressure data [171, 71]. Nevertheless, we applied these Lennard-Jones potentials to compute the equations of state of H and He at high pressures. Our intention was to learn what a "naive" application of a simple, empirical potential amounts to. We find that at pressures of about 20 GPa where experimental data are still available the pressure computed with Lennard-Jones potentials is too high by a factor of 2-3 and for the Mbar pressures they give at least an order of magnitude higher pressures than more realistic potentials. The reason is easy to see. In the limit of very high pressures the electronic and the ionic degrees of freedom decouple. Then the total energy is the sum of the energies of the free electron gas and a ion lattice within a homogeneous background. The leading terms of the free electron gas in the high pressure limit are the kinetic ($1.105/r_s^2$ a.u.) and the exchange contribution (-$0.458/r_s$ a.u.). The energy of the ion lattice is $\alpha_M \cdot e^2/r_0 a.u.$, where r_0 is the next neighbor spacing and α_M is the Madelung constant. Therefore, the leading contributions of the total energy scale as $E \sim a \cdot 1/r_s + b \cdot 1/r_s^2$ in the high pressure limit. Obviously, the repulsive part of the Lennard-Jones potential $\sim 1/r^{12}$ is far too stiff for high pressures and doomed to overestimate the pressure enormously.

For higher pressures more realistic empirical potentials were designed (see [171] and especially [71], where a detailed discussion of empirical potentials for high pressure molecular H can be found). We chose the simplest of these potentials to compare with our ab initio results, the exponential-six (EXP-6) potential

$$V_{\text{EXP}-6}(r) = \frac{\epsilon}{\alpha - 6}\left\{6\exp\left[\alpha\left(1 - \frac{r}{R}\right)\right] - \alpha\left(\frac{R}{r}\right)^6\right\}. \tag{5.2}$$

For H we used the parameters $\epsilon/k_b = 36.4$ K, $R = 3.43$ Å and $\alpha = 11.1$ [157] and for He the parameters $\epsilon/k_b = 10.8$ K, $R = 2.9673$ Å and $\alpha = 13.1$ [202]. In these EXP-6 potentials the parameters ϵ and R were determined from experimental results at low pressures (see [157, 17] for H and [202] for He) whereas α was chosen to give good results at high pressures (for H α was derived from ab initio calculations of the repulsive H_2-H_2 interactions and for He α was fitted to experimental data up to 10 GPa).

As mentioned in section 2.1.2, gradient corrections provide in many cases an im-

provement over the LDA. In LDA the mutual influence of density fluctuations at different places are neglected. The gradient of the density contains some information about the density fluctuation of spatially close regions (gradient corrections are sometimes referred to as semilocal approximations). We expect them to provide a better description where the interactions of the chemical units have a van-der-Waals contribution. Therefore, we have computed the equation of state with gradient corrections in addition to the LDA calculations. For the exchange part we used the gradient corrections by Becke [18, 19] and for the correlation contribution an expression developed by Perdew [145].
For our calculations on H in the molecular phase we used an orthorhombic unit cell with two H_2 molecules on the positions of an hcp lattice sites and optimized orientation and bond lengths of the molecules. The c/a ratio was kept at the ideal value of $\sqrt{8/3}$. For the atomic phase a bcc lattice was assumed. The Brillouin zone was sampled with 10 Chadi-Cohen points [35]. Convergence tests performed by increasing the number of $\vec{k}$-points show that the error in the estimate of P is 10 % up to about 100 GPa for H and 1000 GPa for He. Close to the metallization pressure the accuracy of our computation decreases rapidly as more $\vec{k}$-points become necessary to sample the complex Fermi surface of a metal. Experimental data are available up to the GPa regime. The computed equations of state are compared with x-ray data of [71] in figure 5.1. The LDA curve is a bit too soft. The semilocal gradient corrections provide a better description. The EXP-6 potential agrees well being only slightly too stiff. As discussed in [71], attractive many-body forces (corresponding to a softening of the intramolecular potential) begin to play a role in this pressure range. For this reason two-body potentials are expected to overestimate the stiffness of the equation of state. Hemley et al. [71] added to another potential for high pressures, the Silvera-Goldman potential [172], an ad hoc attractive term to account for the many-body forces. This corrected potential reduced the overestimation by the EXP-6 potential. It is not our aim to discuss the different empirical forms for a H_2 potential. Indeed it is not surprising that one can improve the description by adding some fit parameter in a reasonable way (the Lennard-Jones potential has 2 fit parameters, the EXP-6 potential 3, the Silvera-Goldman potential 7, and the corrected form of [71] 9). Despite their correction terms all these potentials fail at higher pressures, because they cannot describe the dissociation of the molecules properly and are not suited for the atomic phase. At pressures beyond which experimental data are available the gradient correction curve is a benchmark for the quality of the LDA computations. Figure 5.2 extends the equation of state to higher pressures. Equations of state computed with LDA (solid line), gradient corrections (dashed line), EXP-6 potential (dotted line), and Lennard-Jones potential (dashed-dotted line) are presented. In the Mbar pressure range the deviations of the gradient correction and LDA curve is smaller than the finite-size error by the $\vec{k}$-point sampling. Therefore, we believe that the LDA allows a quantitative treatment of H

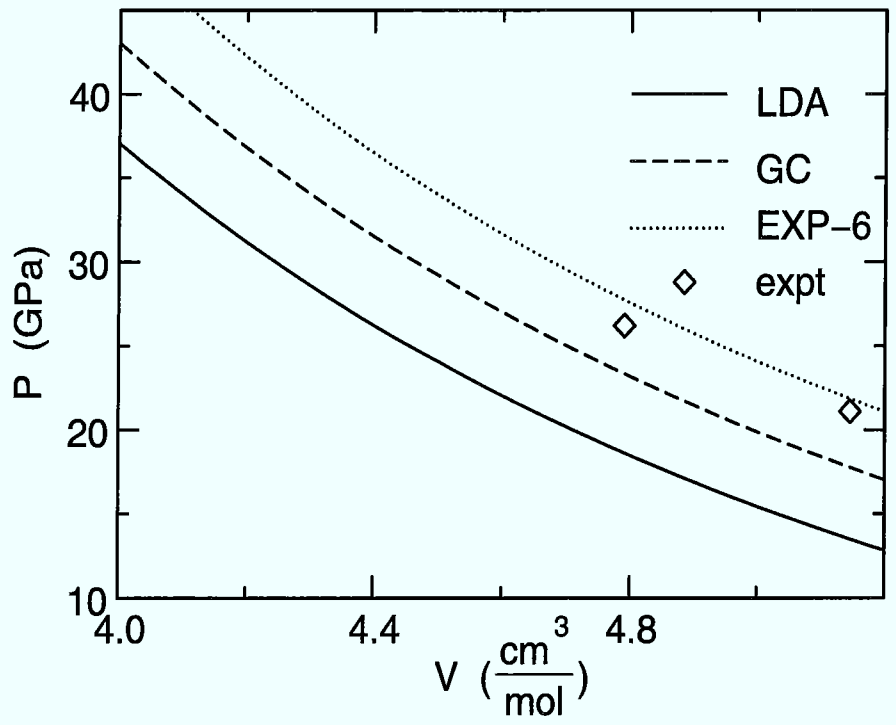

Figure 5.1: The equation of state of H_2 computed with LDA (solid line), the gradient corrections of [18, 19] (exchange) and [145] (correlation) (dashed line), and the empirical EXP-6 potential of [157] (dotted line) compared with the experimental results of [71] (diamonds).

in the high pressure regime. The EXP-6 is substantially stiffer than the ab initio curves (about 50 GPa or 20 % of the LDA curve at 2 cm^3/mol) in the molecular range. This softening is due to a change in chemical bonding of the molecules that is lacking in the EXP-6 curve. For higher pressures in the atomic regime the trend is reversed. The EXP-6 potential was fitted to reproduce the repulsion between H_2-molecules and does not describe the stronger repulsion of H-atoms properly. The Lennard-Jones form (dashed-dotted line) proves to be completely inadequate. The two experimental points at low pressure indicate where the pressure range accessible to reliable structure experiments, such as x-ray or neutron scattering ends.

We fitted the P-V data for H to a phenomenological equation of state, the Birch-Murnaghan equation [23, 24, 25]

$$P = 3K_o(V_o/V)^{5/3} f(1 + af + bf^2), \tag{5.3}$$

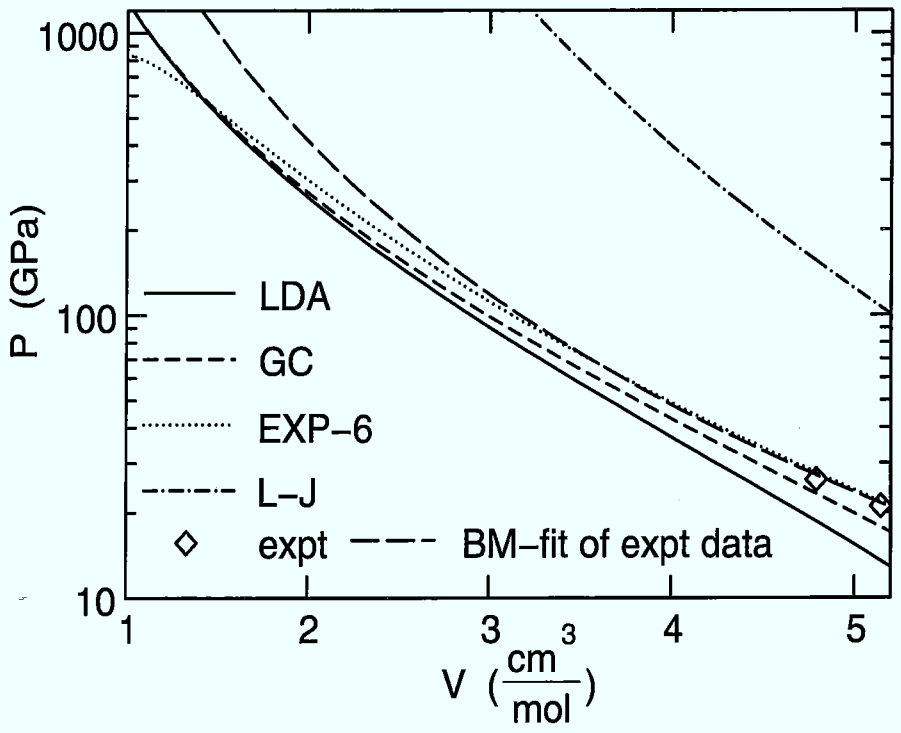

Figure 5.2: The equation of state of H in the high-pressure regime computed with LDA (solid line), gradient corrections (dashed line), empirical EXP-6 potential (dotted line), and the Lennard-Jones potential of [171] (dashed-dotted). Experimental data are represented by diamonds. Hemley et al. [71] fitted their experimental data to a Birch-Murnaghan equation of state (long dashes).

where f is the Eulerian strain, $f = \frac{1}{2}[(V_o/V)^{2/3} - 1]$, and

$$\begin{aligned} a &= \frac{3}{2}(K_o' - 4), \\ b &= \frac{3}{2}\left[K_o K_o'' + K_o'(K_o' - 7) + \frac{143}{9}\right]. \end{aligned} \tag{5.4}$$

The fit can be used to obtain the bulk modulus K_o' and its pressure derivatives K_o' and K_o''. If the equation of state is truncated at third order ($b = 0$), K_o'' is constrained by $K_o K_o'' = -(K_o')^2 + 7K_o' - 143/9$. Hemley et al. [71] investigated the quality of several phenomenological equations of state in fitting their experimental high pressure H data. We compare their fit to a third order Birch-Murnaghan equation of state in the pressure regime of 5.4-26.5 GPa with a fit to our LDA results from 10-100 GPa. (We restrict ourselves to a pressure range where H is unambiguously molecular. Phenomenological equations of state like the Birch-Murnaghan equation are not suited to account for the dissociation of

molecules.) The result is shown in table 5.1. With regard to the error induced

Table 5.1: Bulk modulus K_o and its derivatives K_o' and K_o'' obtained from theoretical LDA computations in comparison with a fit to experimental results of [71].

	V_o (cm^3/mol)	K_o (GPa)	K_o'	K_oK_o''	Pressure range (GPa)
LDA	23.00	0.182	5.35	-7.06	10-100
Expt.	23.00	0.362	4.71	-5.1	5.4-26.5

by LDA in the low pressure regime the fit parameter obtained by the fit to the experimental data agree reasonably well with our result. Since our fit is poor the agreement is fortuitous. The third order Birch-Murnaghan equation is too inflexible to provide an accurate fit across this wide pressure range (see also figure 5.2 where the Birch-Murnaghan equation of [71] is applied to pressures above the experimental values). Using the fourth order form of the Birch-Murnaghan equation we found unphysical results for the bulk modulus and its derivatives. This corroborates the conclusions we drew from the comparison of different equations of state (figures 5.1 and 5.2). Empirical fit expressions are not flexible enough to be applied to H across a wide pressure range. For the Birch-Murnaghan equation the limited applicability is comfirmed by Hemley et al. [71]. They combined their high pressure data with experimental low-pressure data and found the $P - V$ data to be not well represented by a third-order Birch-Murnaghan equation. The fourth-order parametrization led to unphysical results.

The static computations on H and He in this chapter lend credibility to our belief that the main error source of DFT/LDA computations at In our ab initio computations for He we considered the conventional unit cells with four atoms and hcp and fcc structures. The Brillouin zone was sampled with 10 Chadi-Cohen points [35]. In figure 5.3 computed equations of state are compared with the experimental data of [117]. The LDA curve (dashed) is too soft as for H_2 in the same pressure regime. The error due to the local approximation of the exchange-correlation part is mostly corrected by the gradient correction curve, which underestimates the pressure only slightly. The empirical EXP-6 calculation [202] provides a good equation of state at this pressure. For the determination of the fit parameters of the EXP-6 potential experimental data up to 10 GPa were used. Therefore, it is not surprising that at the somewhat higher pressures in figure 5.3 the description is still good. The last curve (dash-dot-dot) was computed by Young, McMahan, and Ross [202] with a DFT scheme, the linear-muffin-tin-

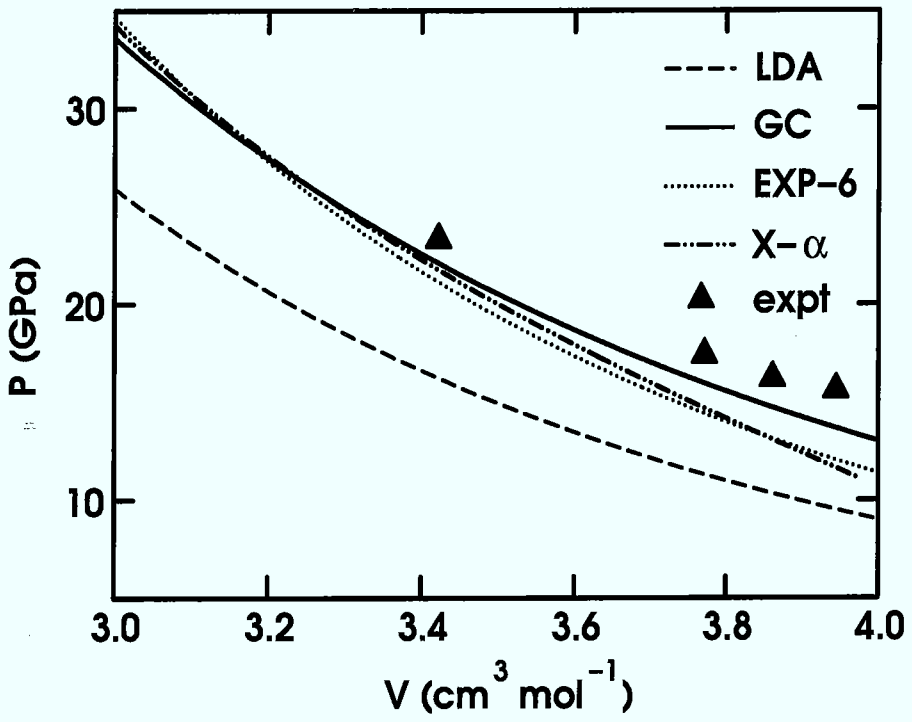

Figure 5.3: The equation of state of He in the high-pressure regime computed with LDA (solid line), gradient corrections (dashed line), the empirical EXP-6 potential of [202] (dotted line), and a DFT calculation [202] where the X-α approximation was used for the exchange contribution (dash-dot-dot). Experimental data are represented by triangles.

orbital (LMTO) method. The exchange contribution is represented by Slater's X-α term,

$$E_x^{X-\alpha} = -\frac{3}{2}\alpha C \int d\vec{r} n(\vec{r})^{4/3}, \tag{5.5}$$

where $n(\vec{r})$ is the one-particle density and $C = 3(3/4\pi)(1/3)$. For $\alpha = 2/3$ the exchange density at a point $\vec{r}$ is equal to that one of a homogeneous system of density $n_{\text{hom}} = n(\vec{r})$. Usually, α is chosen close to this value. Correlation is neglected. The X-α computations of Young, McMahan, and Ross were complementary to their EXP-6 calculations and published in the same paper [202]. The free parameter α was fitted to reproduce the EXP-6 equation of state at about 10 GPa (the EXP-6 potential for its part was fitted to experimental data at pressures up to 10 GPa). The chosen value for α was 0.6105. The correlation contribution scales only with $\ln r_s$ in the high pressure limit whereas the exchange part has a $1/r_s$ scaling. Thus the exchange contribution dominates in the exchange-correlation part and the LMTO calculations of Young, McMahan, and Ross provide a good

description in the high pressure limit, because their value for α (0.6105) is not far from 2/3. Figure 5.4 shows the equation of state of He for higher pressures. In the Mbar regime the LDA, gradient corrections, and LMTO curves are very

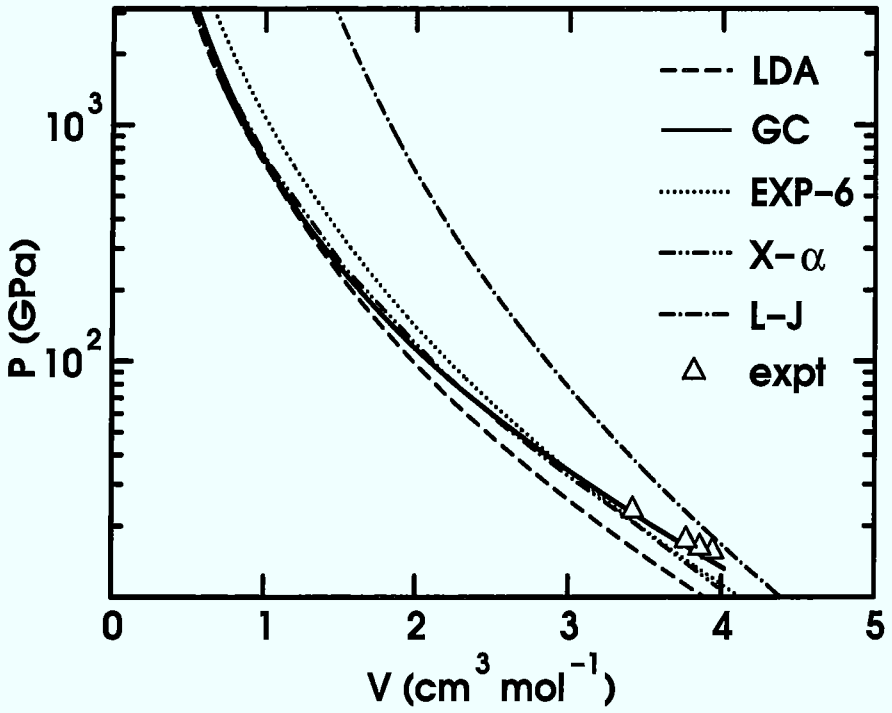

Figure 5.4: The equation of state of He in the very high pressure regime computed with LDA (solid line), gradient corrections (dashed line), empirical EXP-6 potential (dotted line), a DFT calculation with the X-α approximation for the exchange contribution (dash-dot-dot), and the Lennard-Jones potential of [73] (dashed-dotted line). Experimental data are represented by triangles.

close. The differences are smaller than the error induced by the $\vec{k}$-point sampling (10 %). In this pressure range a local description is adequate. From the good agreement with the X-α we deduce that the exchange part dominates the correlation contribution and we believe that all three ab initio computations provide an accurate description. However, the EXP-6 curve is too stiff for high pressures, because it does not account for the increase of attractive many-body forces at high pressures. It is an example that the predictive power of empirical potentials is very limited (concerning accuracy and reliability) for conditions different from those under which the fit data were obtained. Young, McMahan, and Ross [202] provide a correction term to their EXP-6 potential that allows them to reproduce

their LMTO data at high pressures. Their work nicely demonstrates the difference between ab initio and empirical potentials. A simple empirical potential can be determined only a posteriori, i.e., when experimental or ab initio data are available as a data base for fitting. Finally, an equation of state computed with the Lennard-Jones potential for He is presented. This potential was fitted to data at much lower pressures. It is not surprising that it fails completely to provide a reasonable agreement with the other results.
The static computations on H and He in this chapter lend credibility to our belief that the main error source of DFT/LDA computations at ambient pressure, the local approximation of the exchange-correlation contribution (LDA), induces only a small error at high pressures. Aside from the LDA there are three other sources for errors, namely (in the order of decreasing importance)

- the finite size of our system and the restricted $\vec{k}$-point sampling (only the Γ-point was used for the finite temperature calculations),
- the treatment of the ions as classical particles,
- and the adiabatic approximation, i.e., the assumption that the electrons are in their instantaneous ground state.

The first, in particular, but also the second source for errors mean by far more substantial limitations for the high-pressure regime than the LDA, as is discussed in chapter 7.

Chapter 6

Structures of Hydrogen at High Pressures and Low Temperatures

As discussed in section 1.1.4, the ground state structure of H in the pressure range from 42-1000 GPa is a much investigated, yet unsolved problem. It is of major importance to solve this problem in order to find the low temperature metallization pressure of H and the pressure of the molecular-atomic transition. Both strongly depend on the assumed ground state structure (see our introductory discussion in 1.1.4). In this section our results are presented for r_s = 1.5, 1.31, 1.2, 1.0 and 0.5 corresponding to pressures of P = 1.5, 4, 6, 24, and 110 Mbar. In all our computations we treated the ions as classical particles, i.e., their zero point motion was neglected. In addition the energy resolution of our computations is not high enough for a quantitative energetic ordering of very close structures (less than 0.01 eV/atom apart). Therefore, some of our results represent suggestions or trends rather than definitive answers.
In the discussion we stick not to the logical order but start with r_s = 1.31 and then proceed to r_s = 1.5, 1.2, 1.0 and 0.5, because our proposition for a ground state structure at r_s = 1.5 is derived from the result at r_s = 1.31. The result at the lower pressure will be better motivated if it succeeds the higher one.
Our starting point for calculations on pure H at r_s = 1.31 was a molecular hcp lattice with ideal c/a ratio. The orientation and the intramolecular distance was taken from the hcp-like structure found by Hohl et al. [75]. Local relaxation of the starting structure produced a new structure, which - as will be seen below - proved to be our best suggestion for the ground state structures of H at r_s = 1.31. The structure is built up of strings of atoms. We introduce a coordinate system to describe the structure. Let the x-axis be aligned parallel to the strings. A schematic sketch of the y-z plane is given in figure 6.1. The strings are represented as open and filled squares. They form a triangular lattice. The next neighbor distance between strings is drawn with solid lines. The average value for this distance is 2.673 a.u. As will be argued below, the strings can be viewed as composed of "molecules" with identical orientations. Thus the strings

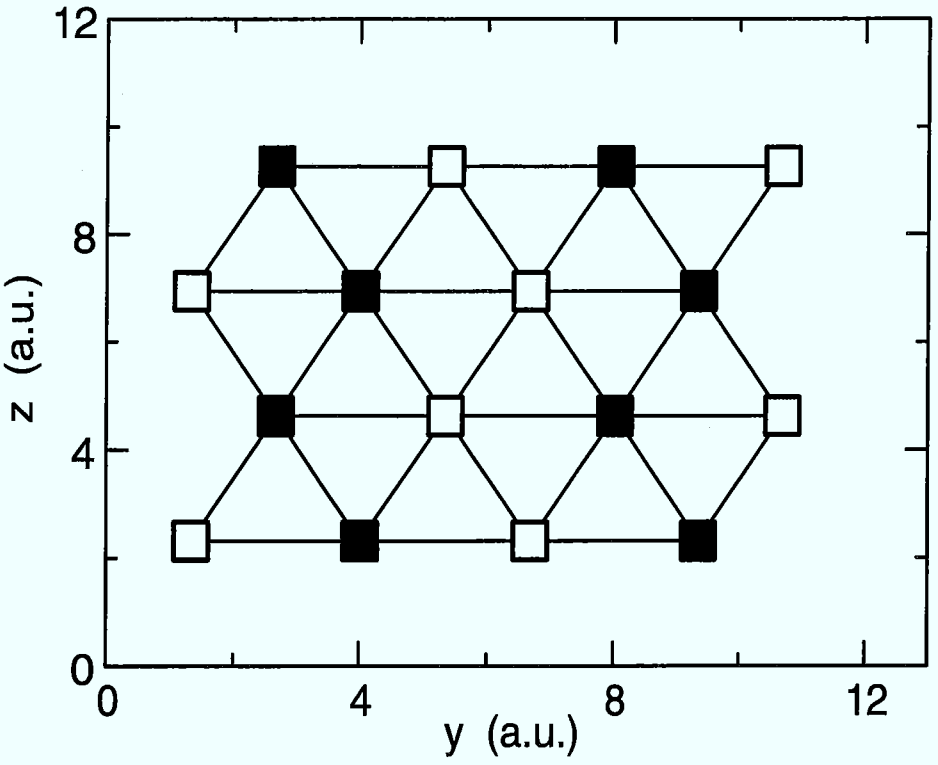

Figure 6.1: Schematic diagram of the string structure at r_s=1.31. The strings (filled and open squares) run perpendicular to the diagram. The strings represented by filled squares are displaced by 1.495 a.u. with respect to the other strings. The next neighbor distance between different strings (solid lines) is 2.673 a.u.

are symmetric with regard to a translation in the x-direction by the center of mass distance between two neighboring "molecules". The average of this distance was 2.99 a.u. The strings represented by solid squares are displaced by half this length (i.e., 1.495 a.u.) with respect to the other strings. In figure 6.2 a physical picture (i.e.,the circles correspond to real atomic coordinates in our simulation) of the x-y plane is given. The main characteristic of this structure is that the next neighbor distance (the average is 1.58 a.u.) is very close to the second next neighbor distance (average 1.60 a.u.). In figure 6.2 this has been emphasized by choosing the cutoff for drawing the bonds larger than the second next neighbor distance distance. In spite of the small difference of 0.02 a.u. next and second next neighbor distance can be unambiguously distinguished. Across the density range of $r_s = 1.31$ to 1.5 the molecules are gradually dissolving. Both the string structure and the other, sh-like structure we found at $r_s = 1.31$ (fig-

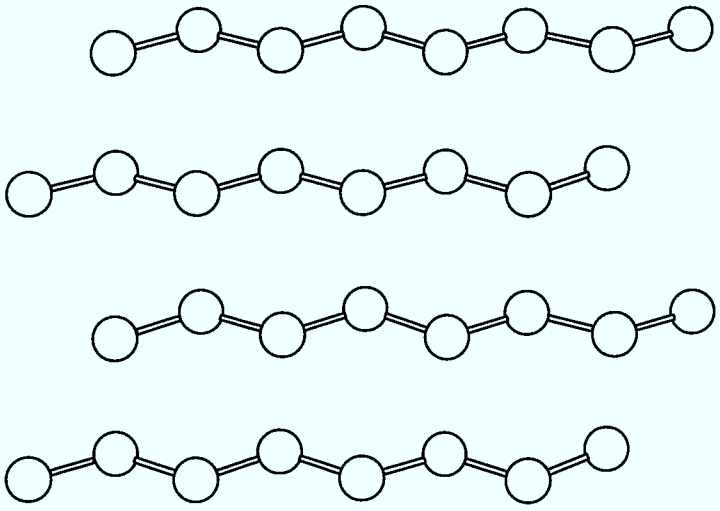

Figure 6.2: Physical picture of one x-y plane of the string structure at $r_s = 1.31$. First and second next neighbors are connected with bonds. The difference between first and second next neighbor distances are very small (0.02 a.u.). Thus the entities of which the structure is composed are classified as "strings".

ure 6.8) are characterized by two different lengths, the shorter corresponding to the dissolving molecules. In spite of the remnants of molecules these structures should be referred to as "atomic" rather than "molecular". As will be seen below, these structures are qualitatively different from "true" molecular structures (see the comparison of the string-structure and mhcp-o for $r_s = 1.5$). The first and second neighbor distances are very close so that at low temperatures the two distances are indistinguishable. (For example, in the pair correlation function of the string structure at $r_s = 1.5$ and 50 K first and second neighbor distances have completely merged.) For simplicity we will address next neighbor pairs of these structures as "molecules" where the apostrophes signalize that the structures should rather be classified as atomic. Figure 6.3 demonstrates the existence of "molecules" in the string structure at $r_s = 1.31$. The electronic density of five atoms belonging to one of these strings is shown in a plane that intersects their centers of masses. It can be seen that slightly stronger and weaker bonds alternate. The stronger bonds can be identified as "intramolecular" bonds. The strings and the composing "molecules" form an angle of 20.1^o and the angle of

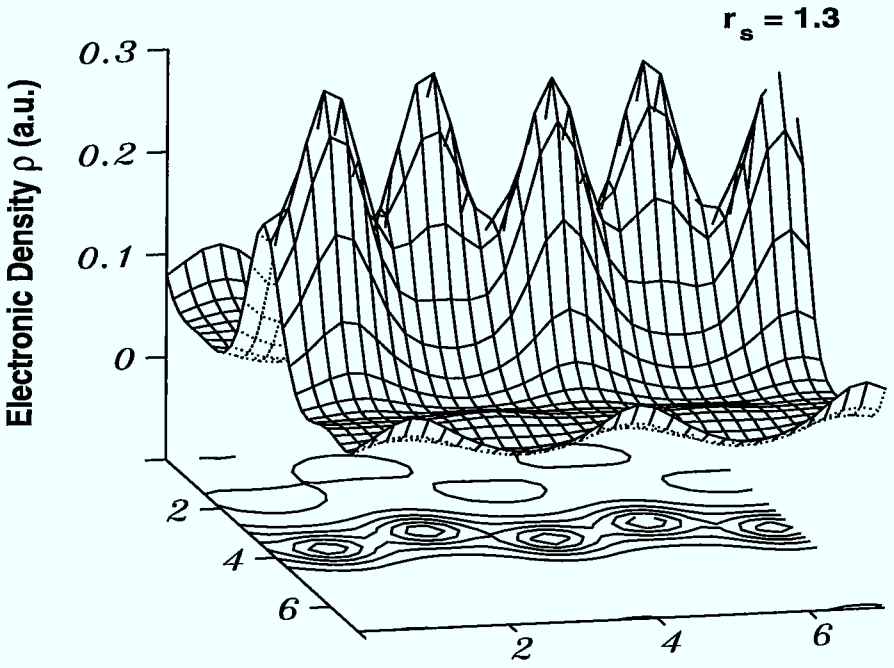

Figure 6.3: Electronic density ρ of five atoms belonging to one string in a plane intersecting the string. It can be seen that (slightly) stronger and weaker bonds alternate.

the "molecules" with the z-axis is 78.2^o (average values; the standard deviations are 1.2^o and 0.9^o, respectively).
In figure 6.4 the entire cell with 128 atoms is shown. As mentioned above, this structure was a product of a local relaxation and its stability has to be verified before it may be regarded as a reasonable candidate for the ground state structure. Therefore, we performed an extended MD simulation ($\sim$ 2 ps) at finite temperatures (up to 1000 K) and quenched down to 0 K. The quench was performed in small temperature steps to give the atoms time to find their energetically favored positions ("simulated annealing"). The resulting configuration at 0 K is shown is figure 6.5. The structure has a lot of defects but some tendencies are obvious. It consists of 5 layers. In figure 6.6 the middle layer is shown in which the atoms are symmetrically arranged. From figure 6.6 it is easy to see that the structure within the layer is characterized by two, slightly different lengths. We idealized the positions of the "molecular" centers and optimized the "molecular" orientation and the "intramolecular" distance. As seen in figure 6.5, the structure is built up of individual planes. The distance between two neighboring planes is about 2.3 a.u. The planes consist of equilateral parallelograms where the lateral

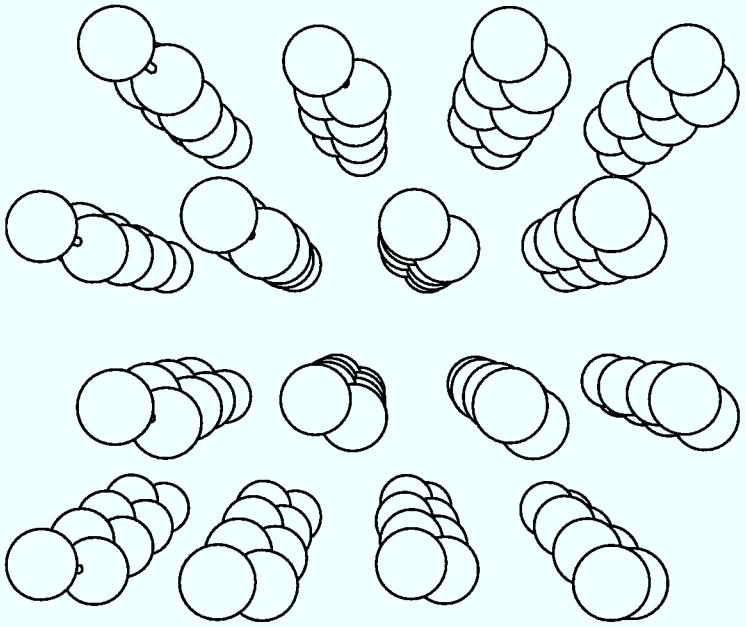

Figure 6.4: Physical picture of the string structure at r_s =1.31. The triangular arrangement of the individual strings can be seen. The structure also served us as a starting structure for a simulated annealing investigation.

axes form an angle of 52^o (figure 6.7).

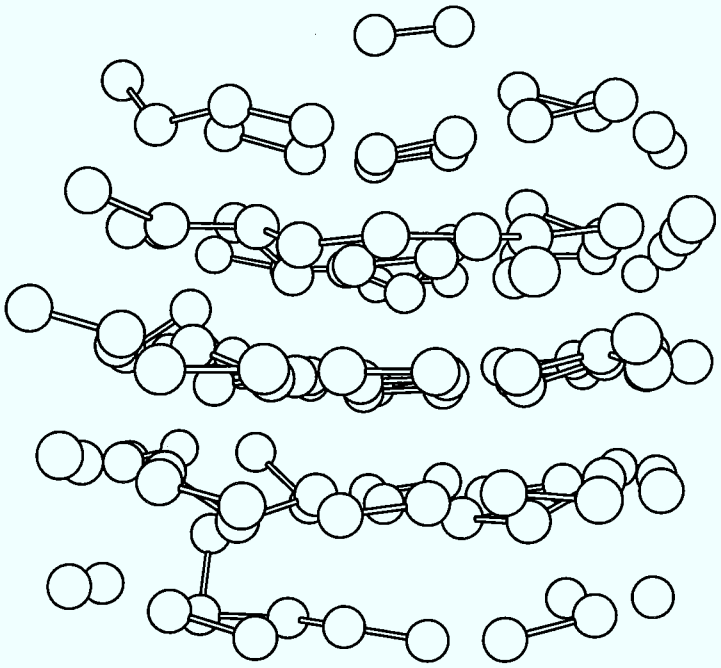

Figure 6.5: Quenched structure after simulated annealing at r_s =1.31. Although a lot of defects are present the composition of layers can be clearly identified.

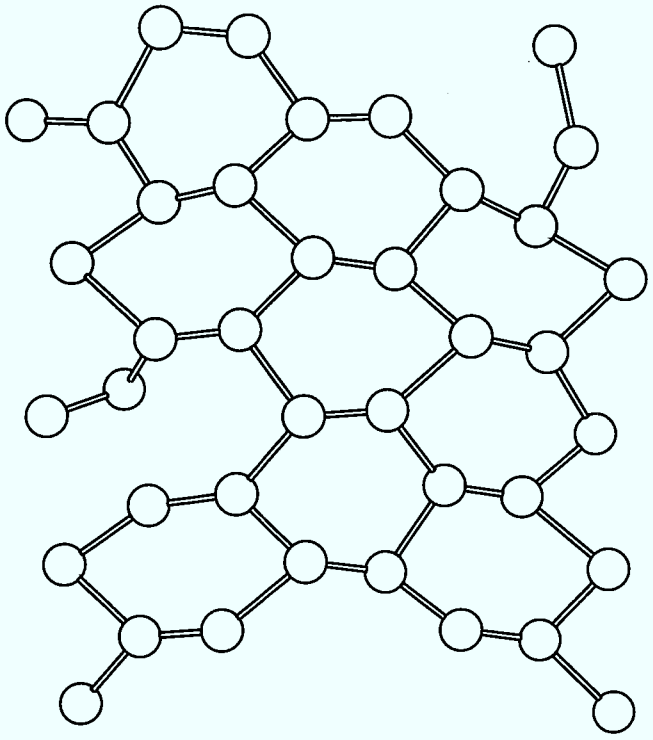

Figure 6.6: The middle layer of the quenched structure at $r_s = 1.31$. Next and second next neighbor distances are drawn. The distances have comparable length; the structure is atomic.

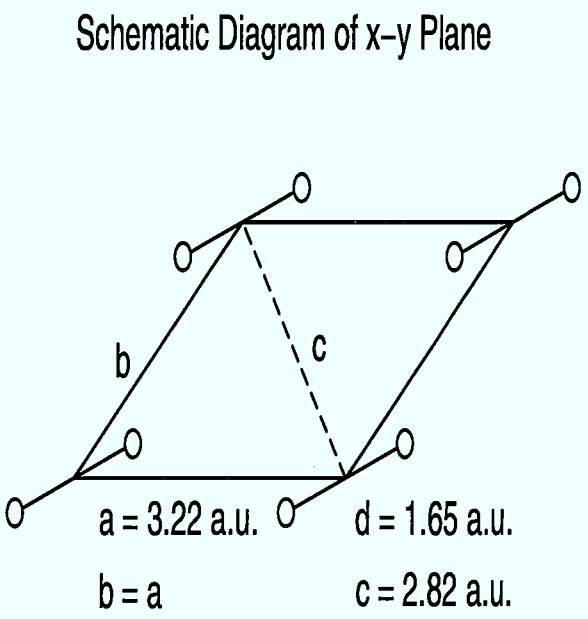

Figure 6.7: Schematic diagram of the idealized structure in the planes at $r_s = 1.31$. It consists of equilateral parallelograms with lateral length of 3.22 a.u. The sharp angle of the parallelogram is about 52^o. Atoms represented by open circles and "molecules" connected by solid lines. The "molecules" form an angle of 18^o with the plane and are symmetrically aligned with respect to the lateral axis.

The next neighbor distance of the "molecular" centers is 3.22 a.u. The "intramolecular" distance is 1.65 a.u. and the second next neighbor distance of the H atoms is 2.0 a.u. The molecules form an angle of about 18^o with the plane and 31.5^o with the line that connects two neighboring "molecular" centers. A physical picture of the structure is given in figure 6.8. This picture is rotated by 90^o

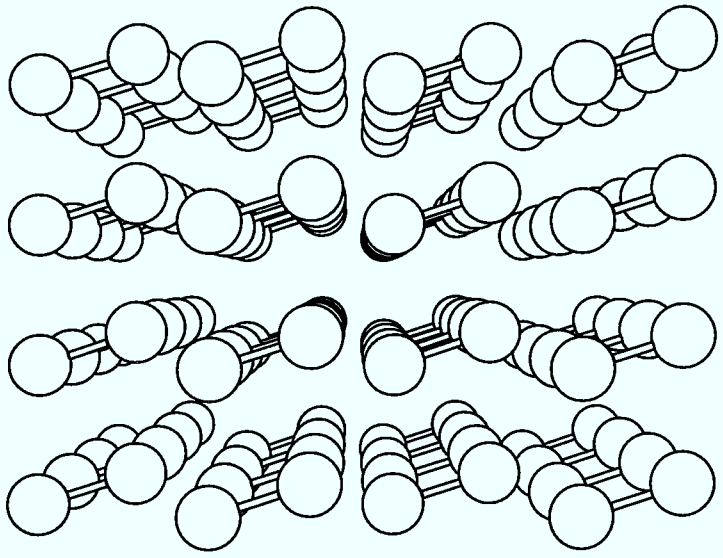

Figure 6.8: The second (idealized) structure at r_s =1.31. The picture is rotated by 90^o with respect to the schematic representation in figure 6.7.

with respect to the schematic diagram in the previous figure, i.e., the planes are seen sideways. It is instructive to compare the structure with two other similar structures:

- The positions of the "molecules" lie on a distorted simple hexagonal lattice with a c/a ratio of 0.71. In the ideal simple hexagonal lattice the (sharp) angle of the parallelogram of figure 6.7 is 60^o instead of 52^o.

- The structure is very close to the structure of D. Hohl et al. [75]. The two main differences are that the parallelogram in [75] has two different lateral lengths instead of one (a $\neq$ b in figure 6.7) and that their structure consists of alternating planes, the molecules of the next plane lying in the

centers of the parallelograms. In our structure we shifted every other plane to reproduce the layering in [75] and found the energy of the structure to be practically unchanged (the energy difference is about 0.001 eV/atom). Thus qualitatively the structures are related, whereas the details depend too strongly on the form of the simulation cell and the sample size for a reasonable quantitative comparison.

The string-structure presented first is by about 0.002 eV/atom more stable than the structure obtained by simulated annealing. This energy difference is smaller than the energy resolution of our method (about 0.05-0.1 eV/atom). Obviously, structures with very different geometries lie energetically very close together in the molecular-atomic transition regime. The energy surface is comparatively flat. For a reliable quantitative treatment many $\vec{k}$-points and zero point motion have to be included.
Nevertheless, especially the string-structure is intriguing. On one hand the molecules have virtually given up their identity. Thus the structure corresponds to the final stage of a continuous transition to an atomic structure. The situation is similar to that one in the simple picture presented in section 4, because the angle between the "molecules" and the string axis is not large. On the other hand strings were predicted by Brovman, Kagan, and Kholas [27] for metallic H at ambient pressure. The most stable structure in their calculations is a "triangular family" of strings that corresponds precisely to what is shown in figure 6.1. In a consecutive paper, Brovman, Kagan, and Kholas [28] addressed the structure of metallic H at higher pressures. They predicted the filamentary structures formed by strings to become unstable at about 0.25 Mbar, substantially below the pressure at r_s =1.31 (4 Mbar). Their computation was based on crude approximations and it is well possible that the string structure we found is the true ground state structure in the range of 1.5 - 4 Mbar (concerning 1.5 Mbar see below). The trend to anisotropic structures is confirmed by the structure found by Tse and Klug [191], which, however, is only a local minimum at these pressures [146].

For $r_s = 1.5$ (1.5 Mbar) we expanded and locally relaxed the string structure found at $r_s = 1.31$. The relaxation proved the structure to be (at least locally) stable. Again intra- and intermolecular distances are close (1.69 a.u. and 1.82 a.u.) and the charge distributions of the atoms within one string strongly overlap (figure 6.9). The angle of the "molecules" within the string has decreased to

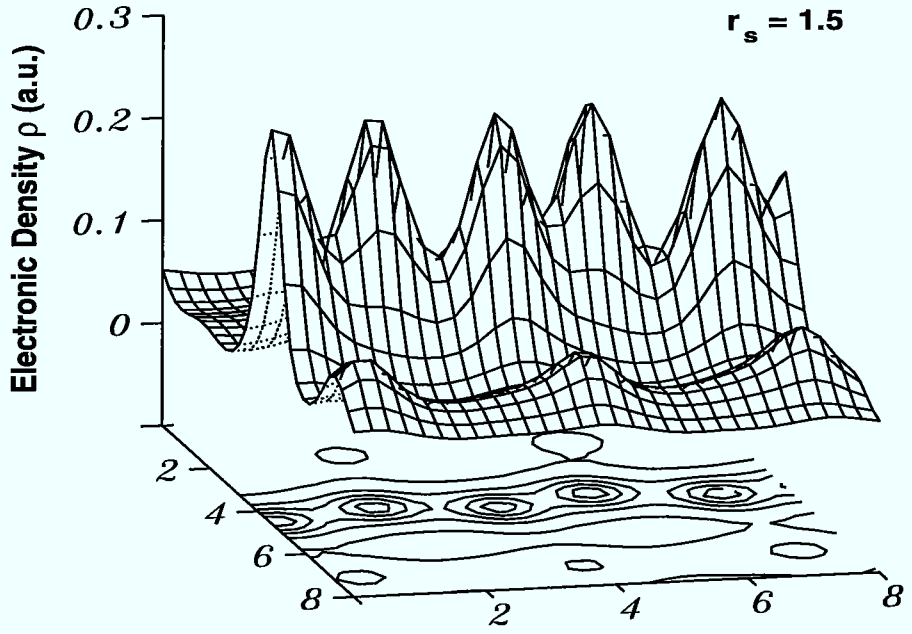

Figure 6.9: Electronic density of five atoms belonging to one string in a plane intersecting the string at r_s =1.5. The structure is atomic, but (slightly) stronger and weaker bonds alternate. The charge density is considerably enhanced between the atoms.

about 12°. We compared the string structure with two other structures, mhcp-c and mhcp-o (see figures 1.8 and 1.9). For the comparison we use the same cell (ideal c/a ratio, 64 molecules). We optimized the intramolecular distance, which was found to be 1.36 a.u. for mhcp-c and 1.41 a.u. for mhcp-o. The corresponding second next neighbor distances are 2.40 a.u. and 2.54 a.u. The total energies are shown in table 6.1. To reduce the finite size effects we also computed the energy differences at the Baldereschi-point [11], which provides a better $\vec{k}$-space integration than the Γ-point. The energetical order of the three structures is not changed by the different sampling. In agreement with the studies of [130] and

Table 6.1: Total energies E_{tot} (eV/atom) of three different structures, mhcp-c, mhcp-o, and string structure, at r_s =1.5. The calculation was performed with 128 atoms at the Γ-point and at the Baldereschi-point.

E_{tot}	mhcp-c	mhcp-o	strings
Γ-point	-1.74	-1.83	-1.94
B-point	-1.72	-1.79	-1.85

[94], we found the mhcp-o structure to be favored over the mhcp-c structure at $r_s = 1.5$. Our computed energy difference at the Γ-point is the same Natoli, Martin, and Ceperley [130] found in their LDA computations at $r_s = 1.45$ with a similar system (96 atoms, Γ-point, c/a =1.58 instead of the ideal ratio). In our computations mhcp-c lies not only energetically higher than mhcp-o but is not even a local minimum (but a saddle point of the energy surface). The mhcp-c structure relaxes without barrier to the mhcp-o structure. However, our best candidate for the absolute minimum is not the mhcp-o structure but the string structure which is favored by 0.06 eV/atom (0.11 eV/atom with Γ-point) over the mhcp-o structure.

In the spirit of chapter 4 the differences especially in the first and second neighbor distances between the different structures can be explained in a simple model. Imagine the interaction with the first and second neighbors represented by two different springs with spring constants k_1 and k_2. At ambient pressure the intramolecular bond is much stronger, i.e., $k_1 \gg k_2$. When the system is pressurized both springs are compressed, i.e., first and second next neighbor decrease. However, the relative size of the spring constants is a highly nonlinear function of the interatomic distances (in principle of all distances, but especially of the first and second neighbor distance). When the charge distributions overlap sufficiently charge transfer takes place, i.e., the electrons delocalize and partially are shared by neighboring molecules. In the picture of the spring constants this behavior is expressed by a rapid decrease of k_1 with respect to k_2 (and a deceleration of the growth of k_2 with increasing pressure, which is expressed by attractive many-body forces in the language of the empirical potentials discussed in section 5). Finally, (at the molecular-atomic transition) both spring constants will are equal. Thus (assuming a suitable functional dependence of k_1 and k_2 on pressure) it is plausible that the intramolecular distance increases until a "critical charge overlap" of the neighboring molecules is reached where the distance begins to diminish. Above the critical pressure the attractive many-body forces dominate the (at high

density) repulsive two-body forces between the molecules. The scenario is clearly different from a physical situation where the molecules are too far apart for the critical overlap to occur. Usually, the structure is dominated by the repulsion of the molecules, i.e., the tendency to be as far as possible separated from the other molecules. Yet, above the "critical density" the molecules tend to bind together in strings when they come close enough together. Under normal circumstances this critical distance is practically never reached (except for very high temperatures where the entropy destroys the aggregation of molecules immediately). At high pressures it is not only seen in our candidate for the ground state structure but also in the formation of strings at higher temperatures (see chapter 7). In both the mhcp-c and mhcp-o structure the molecular repulsion plays the major role. The molecular densities barely overlap. This feature is underlined by figure 6.10 where the charge density of three neighboring molecules in the mhcp-o structure are shown (compare with figure 6.9). The difference in the density in

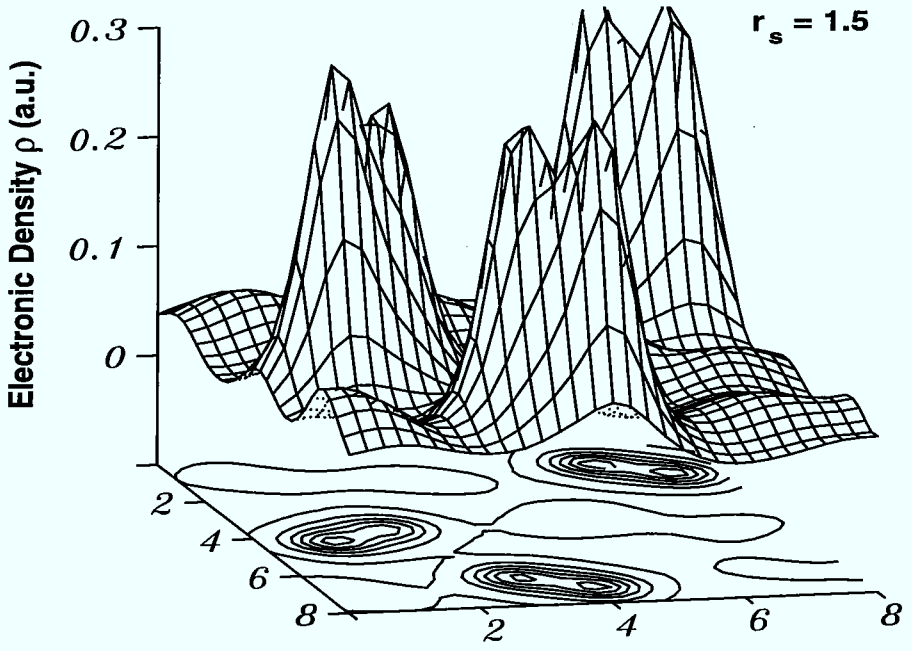

Figure 6.10: Electronic density ρ of three neighboring molecules in the mhcp-o structure ar $r_s = 1.5$. The plane shown is defined by the molecular centers. The molecules are well defined units that barely overlap.

between neighboring molecules in the string structure and the mhcp-o structure is

striking. In the language of the simple spring picture the spring constants k_1 and k_2 are barely affected by charge transfer (but by the compression of the system which leads to a reduced intramolecular distance) and the molecules repel each other. Now it is easy to understand why the mhcp-o structure is favored over the mhcp-c structure. In both structures the repulsion between the atoms dominate, however, in the mhcp-c structure the molecules are closer together. The second next neighbor distance is smaller (2.40 a.u. versus 2.54 a.u.). Therefore, the repulsion in the mhcp-c structure is stronger, the molecules are compressed to 1.36 a.u., and the system relaxes to a higher second neighbor distance of 2.54 a.u. and higher first neighbor distance of 1.41 a.u., realized in the mhcp-o lattice. In both structures the molecules are compressed with respect to the free molecule (1.46 a.u. within LDA). If the molecules came close enough together to reach the critical overlap the molecules would attract each other and bind together. This is realized in the string structure where enough charge transfer has taken place for the intramolecular distance to increase considerably (1.69 a.u.) with respect to the free molecule and the second next neighbor distance to shrink to 1.82 a.u. Thus the hcp structures are simply separated by an energetical barrier from the more favorable strings. This weakening of the intramolecular bond may be the reason for the decrease of the experimental Raman vibron frequency as a function of pressure (see figure 1.5).
To check the influence of the zero point motion of protons on the string structure S. Biermann, D. Hohl, and D. Marx [22] have started ab initio DFT path integral molecular dynamics calculations on this structure. These computations indicate that the strings are stable for $r_s = 1.5$ and 1.31 even if the protons are treated quantum mechanically.

Upon compression to $r_s = 1.2$ (7 Mbar calculated pressure) we observe a phase transition to yet another qualitatively different structure. To the best of our knowledge, no systematic search for stable structures in hydrogen at this density has been reported thus far. Natoli et al. [129] reported the results of LDA calculations on a few prominent atomic structures, and they find the bcc, sc, β-Sn and diamond structures all degenerate within 0.05 eV/atom. Such small energy differences are beyond the resolution of our 128-atom, Γ-point only calculations (estimated to be 0.1–0.2 eV/atom), but it is possible that other, qualitatively different candidate structures were "missed" in all previous studies. Therefore, we have performed an unbiased simulated annealing search. Starting from a compressed structure with 64 H_2 molecules on fcc lattice sites in a simple cubic unit cell we heat the sample to 3000 K and cool to 200 K in about 1 ps. At the end of this procedure we obtain a 4-fold coordinated structure resembling the structure of β-Sn (see Fig. 6.11 and the description in [45]). This distorted structure still contains a significant number of coordination defects (only 50 % of all atoms are indeed 4-fold coordinated) because of the fast quenching procedure. Energetically, it is 0.18 eV/atom more stable than any other structure we have explicitly

Table 6.2: Relative total energies E_{tot} (eV/atom) of four different atomic structures, bcc, diamond, β-Sn (with ideal c/a ratio of 0.9129) and the structure from a simulated annealing (SA) run, at r_s =1.2. The calculations were performed with 128 (108 for β-Sn) atoms at the Γ-point. CN is the coordination number. d is the next-neighbor distance in a.u. (an average in case of the disordered SA structure).

	E_{tot}	CN	d
diamond	0.00	4	1.67
β-Sn	-0.04	4	1.75
SA	-0.22	4	1.70
bcc	0.00	8	2.12

tested (see Table 6.2), but distortions from more symmetric structures are often a consequence of Jahn-Teller-like effects. In our calculations, too, incompletely occupied free-electron bands (see chapter 7) occur at the Fermi energy and will distort structures with degenerate space-group representations such as bcc and diamond (both with triply degenerate representations).

Still, it is interesting that hydrogen at r_s=1.2 unequivocally prefers higher coordinated structures (4- and 8-fold, see Table 6.2) than at r_s=1.31 and 1.5 (2-fold coordination). Only subsequent, more detailed calculations with many $\vec{k}$-points and a better treatment of exchange and correlation will be able to decide what the "true" structure of hydrogen at and around r_s=1.2 is. Our results indicate that isotropic structures with intermediate coordination numbers such as diamond and β-Sn are good candidates. We have not encountered new, complex and uncommon, structures in our dynamical geometry searches at r_s=1.2 as we have at r_s=1.31 and 1.5.

At r_s = 1.0 (24 GPa) the ground structure is commonly believed to be bcc [16, 14, 128]. We performed computations on two structures, bcc and fcc. We tried to compensate the poor $\vec{k}$-space sampling represented by the restriction to the Γ-point by large unit cells with 256 atoms in the fcc and 250 atoms in the bcc cell. In our computations we found the bcc structure to be more stable by 0.04 eV/atom.

For r_s = 0.5 we confimed the local and global stability of the bcc structure, the commonly believed ground state structure at this density.

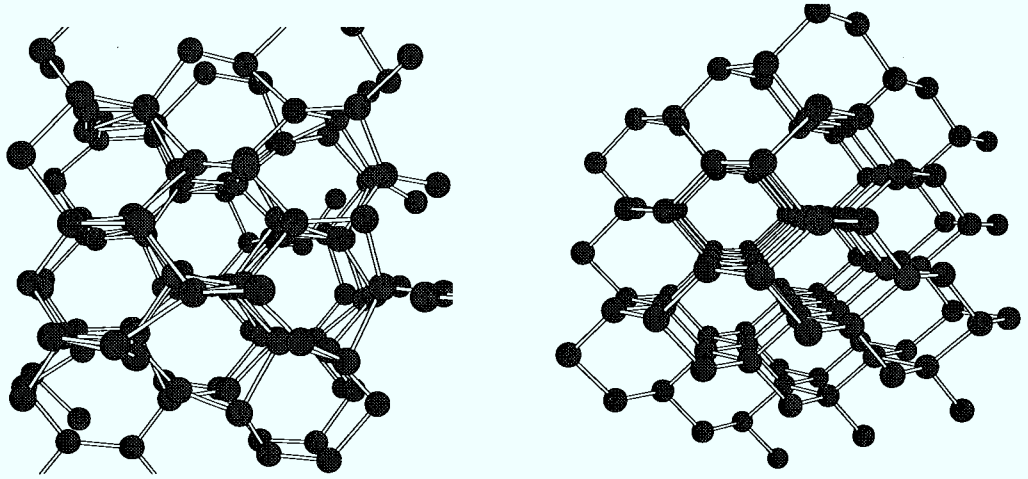

Figure 6.11: Comparison of the structure obtained by simulated annealing (*left*) and the β-Sn structure (*right*) at $r_s = 1.2$ (see text).

Chapter 7

Hydrogen at Elevated Temperatures

In the previous chapter the ground state properties of H as a function of pressure were described. For a complete picture of the phase diagram of H it is necessary to include the third variable of the phase diagram, the temperature T. As discussed in the introductory section 1.1.5, less theoretical investigations deal with finite temperatures in the pressure range of the phase transition(s) to an atomic, conducting system than at 0 K, mainly because an adequate treatment is more difficult. The inadequacy of the pair potential approach was demonstrated in chapter 5. For H far in the metallic regime the system can be treated as ions embedded into a negative background. The polarization of the electrons by the ions can be approximated by a screening function that screens the bare Coulomb potential. However, this description is no longer valid when the polarization of the electrons (i.e., the electron-ion interaction) ceases to be a small perturbation of the homogeneous system. This is the case for H in the regime of the molecular-atomic transition. Figure 7.1 demonstrates this point. The pair correlation function (for the definition see below) of ab initio simulations for H at a density of $r_s = 1.31$ (4 Mbar) and a temperature of 1500 K is compared with a pair potential simulation [38]. The pair potential describes the interaction of screened protons, where screening is based on the Thomas-Fermi screening function. This kind of potential is known as Moliere potential and was successfully applied to H at substantially higher pressure and temperatures [40]. The ionic pair potential gives the $g(r)$ of an atomic system (compare with the pair correlation functions at $r_s = 0.5$, figure 7.5). In the ab initio model the system is far from being a simple atomic liquid. In this intermediate pressure regime the molecular-atomic transition takes place, and the system consists not only of atoms and molecules but also of more complex entities, strings of three or more atoms. To explore the complex behavior of the system in this pressure range we performed dynamical simulations at $r_s = 1.5$, 1.31, 1.2, 1.0, and 0.5. In the following the simulations for the first four densities are used to provide some insight

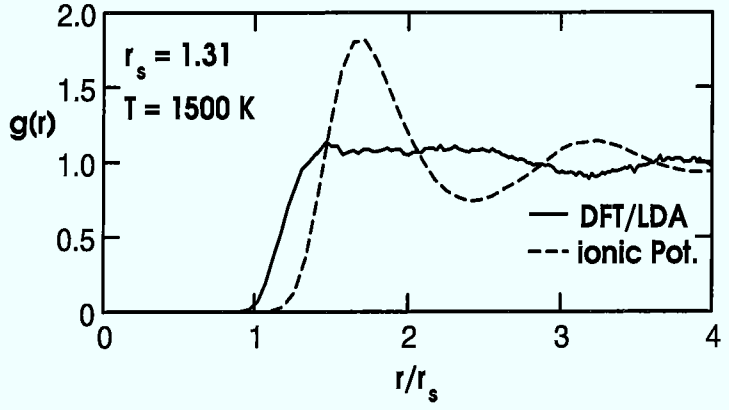

Figure 7.1: Pair correlation functions $g(r)$ of H at $r_s = 1.31$ and $T = 1500$ K obtained with DFT/LDA (solid line) and an ionic pair potential (Moliere potential) based on the Thomas-Fermi screening function (dashed line). The DFT/LDA curve is shapeless whereas the ionic potential produces a common atomic $g(r)$. The figure shows that a simple treatment fails when the system is composed of several species (i.e., atoms, molecules, and strings).

into the physical processes in the transition regime. At $r_s = 1.0$ the transition to an atomic, conducting system is complete. The density $r_s = 0.5$ is far in the metallic regime and addresses a different question from the other simulations. In the high pressure limit ($r_s \longrightarrow 0$) the electrons are barely polarized and they can be regarded as free, or, at lower pressures, the polarization can be treated perturbatively. The description worsens when r_s is increased. The simulations at $r_s = 0.5$ examine the role of the polarization, i.e., the strength of the perturbation by the electron-ion interaction. To pose this problem in a more quantitative form it is helpful to introduce three parameters from plasma physics [84]. The first is the Coulomb coupling constant of a classical ion system

$$\Gamma \equiv \frac{(Ze)^2}{ak_bT}, \tag{7.1}$$

where a is the Wigner-Seitz radius of the ion system ($a = (3/4\pi n_i)^{1/3}$) and measures the average volume occupied by one ion. For H $a = r_s \cdot r_b$ and $Z = 1$. Therefore, $\Gamma = (r_s k_b T)^{-1}$ with k_bT in a.u. The value of this parameter measures the ratio of the Coulomb energy of a pair of ions separated by a and the mean kinetic (thermal) energy k_bT. In our computations Γ is just another way to label

our results in order to make the comparison with the results of plasma physics more transparent. It is also suitable to introduce a similar parameter for the electrons, the Fermi degeneracy parameter

$$\theta \equiv \frac{k_b T}{E_F}, \tag{7.2}$$

where E_F is the Fermi energy of a homogeneous electron gas. It is useful to write E_F in terms of a temperature [8]

$$\frac{E_F}{k_b} = \frac{58.2}{r_s^2} \cdot 10^4 K. \tag{7.3}$$

For $\theta \ll 1$ the electrons have to be treated as a (Fermi) quantum gas whereas for $\theta \gg 1$ they can be treated classically. The highest temperature in our simulations for $r_s = 0.5$ was 10000 K, i.e., $\theta = 0.004 \ll 1$. If there was no electron-ion interaction we could describe H as two different systems, a classical ion system, interacting by Coulomb forces, usually called one-component plasma (OCP), and a degenerate electron gas, that is conventionally referred to as jellium model or free electron gas. The importance of the polarization of the electrons by the ions can be estimated in a simple model for screening, the Thomas-Fermi model [8]. In this model the bare Coulomb interaction is replaced by a screened interionic potential $V(r) = (Ze)^2 \exp(-r/\lambda_{\mathrm{TF}})/r$. The Thomas-Fermi screening length, which can be expressed as (in a.u.)

$$\lambda_{\mathrm{TF}} = \left(\frac{\pi}{12Z}\right)^{\frac{1}{3}} \cdot \left(\frac{1}{r_s}\right)^{\frac{1}{2}} = 0.64 \left(\frac{1}{r_s}\right)^{\frac{1}{2}}, \tag{7.4}$$

where the last equation is only true for H (Z =1), plays a central role in this model. If the screening length is much smaller than the average spacing a of the ions, they will practically interact via the bare Coulomb potentials, and the polarization of the electrons is negligible. For densities as small as $r_s = 0.5$ the Fermi screening length ($\lambda_{\mathrm{TF}} = 0.45$) is of the same order as the ionic spacing ($a = r_s = 0.5$) and the polarization is expected to be important. This is quantitatively shown for the ion dynamics in the following section and for the electronic structure in the second part of this chapter.

The system size of our simulations was 96 atoms for $r_s = 1.5$, 128 atoms for r_s = 1.31, 1.2, and 1.0, and 250 atoms for r_s=0.5. The systems were equilibrated at each temperature for at least 1000 steps of molecular dynamics. The length of the molecular dynamics runs was mostly about 0.5 ps, in some cases longer. In comparing these simulation times with ab initio simulations of other systems it is important to keep in mind that H (and He) have small masses that lead to smaller time scales in the evolution of the system than for heavier elements, e.g., $\nu_{\mathrm{H-H}} \approx 4000\ \mathrm{cm}^{-1}$.

This chapter is divided into two parts. First the structural properties of the H system are discussed and the second part is devoted to electronic properties.

7.1 Ionic Properties

One of the most common tools in molecular dynamics in describing the structural properties of liquid systems is the *pair-correlation function* $g(r)$. It measures the probability to find two atoms at a distance r. Let $\langle n_{ij}(r, r+\Delta r)\rangle$ represent the average number of pairs of atoms of species i and j with a distance larger or equal than r and smaller than $r+\Delta r$. Then the pair-correlation function is computed via

$$g(r) = \frac{V}{N_i(N_j N - \delta_{ij})4\pi r^2 \Delta r} \langle n_{ij}(r, r+\Delta r)\rangle\,, \tag{7.5}$$

where V is the sample volume, N_i the total number of atoms of species i, N_j the total number of atoms of species j, and δ_{ij} Kronecker's delta function. In the form of equation 7.5 the pair-correlation function of a homogeneous system is normalized to $g_{\mathrm{hom}}(r) = 1$. For systems with no long range order (like liquids, gases, and amorphous solids) $g(r)$ will tend to one for large distances, i.e. it is "normalized to one". Since this chapter deals only with pure H we have $i = j$. In chapter 8 where H-He mixtures are treated, the pair-correlation function of unequal species is examined, too (i = H, j = He). In figure 7.2 the pair correlation functions of H at r_s = 1.5, 1.31, 1.2, and 1.0 for two temperatures (800 K and 3000 K) are shown. Only the sample at r_s = 1.5 and T = 800 K displays unequivocally molecular nature: A narrow intramolecular peak at 1.47 a.u. and a broad intermolecular signal around 3.3 a.u. show that the vast majority of atoms (95 %) exists in the form of H_2 molecules, i.e., are onefold coordinated. Occasionally molecules collide and stay in contact for several vibrational periods (3 fs), so that on average 5 % of the atoms are threefold coordinated. We count all atoms within the coordination sphere of radius 1.9 a.u. (first minimum in $g(r)$) of an atom to calculate its "coordination number". This is only a meaningful convention if there is a clearly defined minimum in $g(r)$ separating first and higher neighbors. At 3000 K inter- and intramolecular distances "overlap" completely, and H_2 molecules have such a short average lifetime (8 fs) that the sample cannot be described as molecular in nature any more. The featureless shape of $g(r)$ has been observed by many other workers in the hydrogen plasma near this density and temperature [204, 105, 106] and is caused by the coexistence of molecules, atoms, and strings of atoms in the same sample. Using - somewhat arbitrarily - again a coordination radius of 1.9 a.u., only 60 % of all atoms are on average onefold coordinated, and 20 % each are either isolated atoms or threefold coordinated. This can be compared with the free energy model calculations of Nellis et al. who list a dissociation fraction of only 15% of all molecules at the same density and ~3800 K[134].

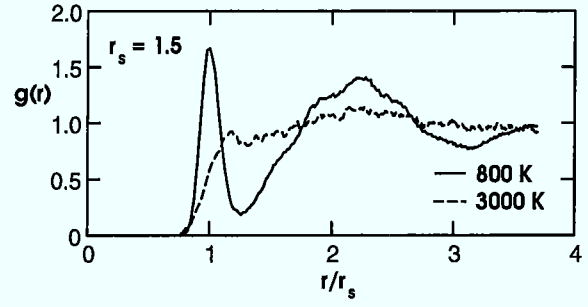

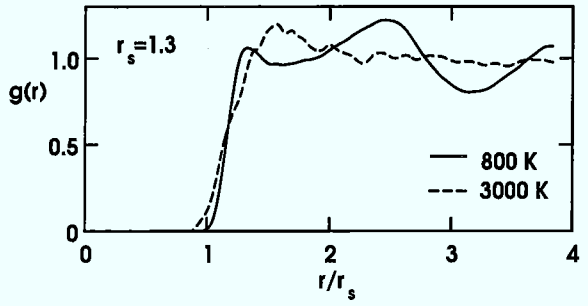

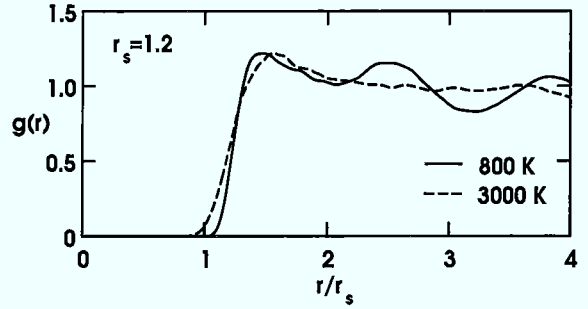

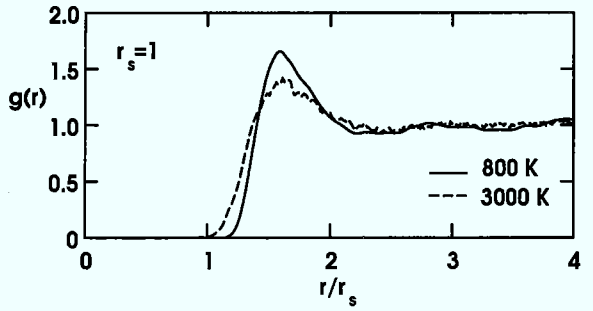

Figure 7.2: Pair correlation functions $g(r)$ at $r_s = 1.5$, 1.31, 1.2, and 1.0 a.u. At $r_s = 1.5$ and 800 K the system is clearly molecular exhibiting a narrow intramolecular peak at 1.47 a.u. At 3000 K the molecules are largely dissociated.
For $r_s = 1.31$ and 800 K there is a small molecular shoulder left. The system is more complex than a simple mixture of atoms and molecules. Strings of 3 or more atoms form that smear out the valley between the intra- and intermolecular peak seen for $r_s = 1.5$. At the higher temperature the pair correlation is even more shapeless.
At $r_s = 1.2$ the situation is similar as for $r_s = 1.31$. The tendency to string and cluster formation has even increased.
Finally, at $r_s = 1.0$ the transition to a an atomic system is complete. The pair correlation function shows the typical broad atomic peak which decreases with increasing temperature but has no clear minimum. Over the density range from $r_s = 1.5$ to 1.0 a.u. the first peak has not only considerably broadened (expressed in an increase of the coordination number from 2 to ≈ 13) but also shifted from $r/r_s \approx 1.0$ to $r/r_s \approx 1.6$.

The pair correlation functions at $r_s = 1.31$ and 1.2 show the same shapeless form as for $r_s = 1.5$ and 3000 K indicating varying coordination numbers. This is underlined by figure 7.3 that shows a snapshot of H at $r_s = 1.31$ and 1500 K. We

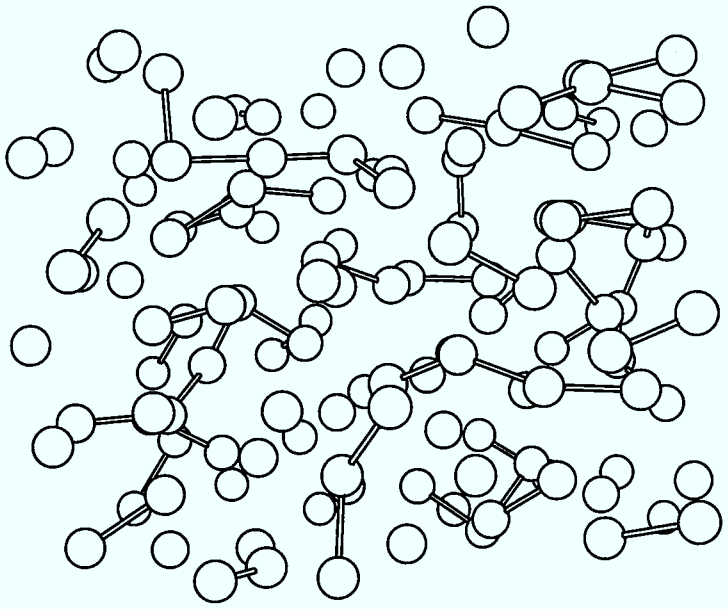

Figure 7.3: A snapshot of the system at $r_s = 1.31$ and $T = 1500$ K. The atoms line up to form strings. This geometry is typical of the samples at $r_s = 1.5$ and $T = 3000$ K, $r_s = 1.31$ and $r_s = 1.2$. Bonds were drawn between atoms less than 1.78 a.u. apart, the maximum bond stretch in a free molecule at comparable internal thermal energy.

investigate a string of three atoms more closely in figure 7.4, where the charge density in the plane formed by these atoms is presented. Two of the atoms are more strongly bound and the third is attached to the pair. The picture is similar to that one of the string ground structure in figure 6.3. The charge density is strongly enhanced along the filament. This tendency of H to form twofold coordinated strings in the regime where the molecules dissociate was also reported by [75, 105, 3]. At $r_s = 1.0$ the pair correlation function exhibits a peak more typical of atomic liquids. The change is most notable in the first peak. The slender molecular peak with a coordination number close to 1 has shifted from $r/r_s = 1$ to about $r/r_s = 1.6$ and broadened substantially (from less than 0.4 to

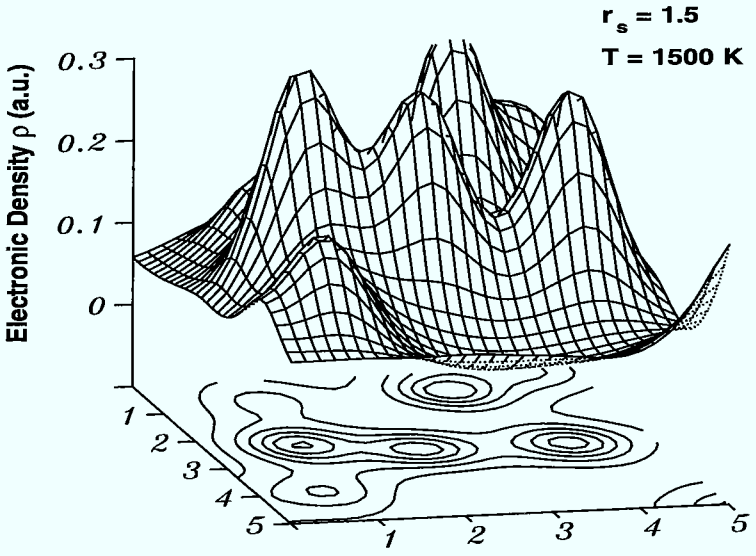

Figure 7.4: The charge density ρ of three atoms forming a string at $r_s = 1.31$ and $T = 1500$ K is presented. The charge is enhanced along the string.

more than 1.0). The coordination number has increased to more than 12.
For $r_s = 0.5$ the pair correlation function at 8000 K is compared with the OCP result in figure 7.5 ($\Gamma = 80$, [113]). The comparison shows that there are still considerable differences in the dynamics of the system. The lower peaks and partly smeared out valleys in the DFT/LDA pair correlation function correspond to a softer interaction potential, i.e., the strong Coulomb interactions are screened. In the framework of the Thomas-Fermi approximation this corresponds to a moderation (screening) of the potential by an exponential $\exp(-r/\lambda_{\mathrm{TF}})$.
Another important characteristic of the system where the effect of screening should be conspicuous is diffusion. We computed *diffusion coefficients* for several temperatures with the Einstein relation (see e.g. [5])

$$D = \frac{1}{6t} \left\langle |\vec{r}(t) - \vec{r}(0)|^2 \right\rangle , \tag{7.6}$$

where $\langle |\vec{r}(T) - \vec{r}(0)| \rangle$ is the average mean square displacement of an atom after the simulation time t. The computed diffusion coefficients are presented in figure 7.6. As expected, diffusion decreases with density. The more tightly packed the system is, the more restrained are the ions from moving. It is instructive to compare with the diffusion coefficients obtained from the OCP model. Hansen, McDonald, and Pollock [67] performed molecular dynamics simulations of the OCP and provided a simple fit formula for their results

$$D = 2.95 \cdot \omega_p \cdot a^2 \Gamma^{-1.34}, \tag{7.7}$$

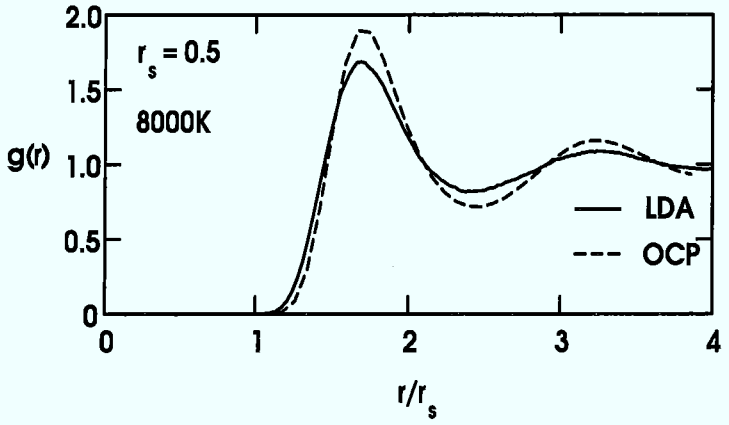

Figure 7.5: DFT/LDA pair correlation function $g(r)$ compared with the OCP result at $r_s = 0.5$ and $T = 8000$ K ($\Gamma = 80$). The conspicuous softening in the ab initio curve demonstrates the importance of screening effects at this density.

where Γ and the Wigner-Seitz radius a were defined above and the plasma frequency ω_p can be expressed via the ion mass M, $\omega_p^2 = (4\pi Ze)^2 a^3/3M$. This fit formula was used for figure 7.7. Subsequent computations showed that this simple fit formula tends to overestimate diffusion in the OCP model [84]. For $r_s = 1.5$ to 1.0 the diffusion coefficients computed via DFT/LDA are at least a factor of 3 larger than the OCP results and even at $r_s = 0.5$ where the OCP is a better approximation the difference is still a factor of 2 (figures 7.6 and 7.7). Intuitively the trend to lower diffusion at higher densities can be explained by the stronger (repulsive Coulomb) forces that prevent the ions from changing their places. Using this picture the OCP model underestimates the diffusion, because the stiff, bare Coulomb potential leads to stronger forces than the screened ab initio potential. Of course this intuitive picture is only valid at $r_s = 1.0$ and 0.5, where H is an atomic system and the dynamics is dominated by the repulsive part and not at the lower densities where the chemical composition is different. Naively, one would expect this trend of the OCP to prevent diffusion also to be visible in the *melting temperature*. A stiffer (unscreened) potential should stabilize the lattice, i.e., the barriers for the ions to change their places are overestimated. The OCP is well-known to melt at $\Gamma_m = 178$ [84], i.e., for $r_s = 1.5$, 1.31, 1.0, and 0.5 at temperatures of 1180, 1360, 1770, and 3550 K. We tried to obtain the melting temperatures for $r_s = 1.5$, 1.31, and 1.0. For several temperatures we performed molecular dynamics runs and computed the average internal

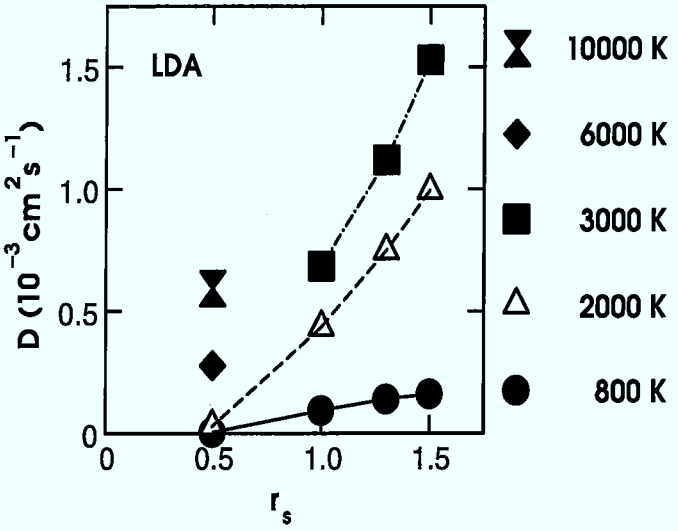

Figure 7.6: Diffusion coefficients D at $r_s = 1.5$, 1.3, 1.0, and 0.5. D decreases with increasing density.

energies. The internal energy differences were fitted to a specific heat of the form

$$c_v = \alpha + \{\beta \cdot \Theta(T_0 - T) + \gamma \cdot \Theta(T - T_0)\} \cdot \exp\left[-\left(\frac{T - T_0}{\delta}\right)^2\right], \qquad (7.8)$$

where α, β, γ, T_0, and δ are parameters to be determined by the fit. The exponential is to account for finite size effects and β and γ allow for a change in the slope of the internal energies across the melting transition. In principle there should be a sharp discontinuity in c_v for a first order phase transition. It is well-known that in (comparatively) small systems as ours the region of the transition is broadened [164]. We ensured that our procedure is reversible by computing selected internal energy averages two times where we approached the temperature both from higher and lower temperatures. In figures 7.8, 7.9, and 7.10 the fits are shown together with the statistical error bars. For $r_s = 1.5$ we obtained a melting temperature of 1125 K. It is certainly fortuitous that it is so close to the OCP value (1180 K), because at this comparatively low density and temperature we expect the OCP to provide a very poor description of the system. A more reasonable comparison is with melting temperatures computed within the pair potential approach. Ross, Graboske, and Nellis [156] used a Silvera-Goldmann type pair potential to compute the demixing temperatures. At 150 GPa they find an about 200 K higher melting temperature. The agreement is reasonable, especially because we expect the pair potential to be too stiff and therefore to overestimate the melting temperature (see the discussion of empirical

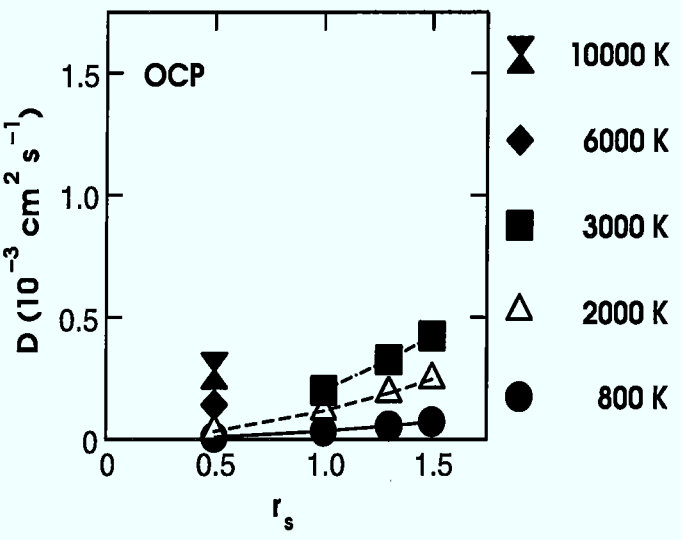

Figure 7.7: Diffusion coefficients D at $r_s = 1.5$, 1.31, 1.0, and 0.5 computed with equation 7.7. The OCP gives much lower diffusion coefficients than the ab initio simulations. This effect is due to the softening of the ab initio potential by screening.

pair potentials in chapter 5). At the higher pressures this procedure proved to be very difficult for H. The discontinuity of the specific heat is known to decrease with increasing metallic character of the system and is too small at $r_s = 1.0$ for a reliable fit (see figure 7.10). The result for $r_s = 1.31$ has a large error bar due to the small discontinuity, too. These curves should be compared with figures 8.6 and 8.7 for He in chapter 8 where the fits are much better, because He - an insulator in this pressure range - has a much larger discontinuity in c_v. Our calculated melting temperatures were 1150 K at $r_s = 1.31$ and 1840 K at $r_s = 1.0$. Our results suggest that the OCP does well in approximating the melting temperatures in the metallic regime at still comparatively low densities. Much lower melting temperatures were found in other ab initio computations. Kohanoff and Hansen [100] used Lindemann's criterion to estimate melting temperatures of 350 K at $r_s = 1.0$ and 2200 K at $r_s = 0.5$. Theilhaber [189] used a similar criterion and found $T = 900$ K to be an upper bound for the melting temperature at $r_s = 1.0$. Our approach suffers from the uncertainties in the fit whereas the simple rules applied by [100] and [189] are uncertain to work in such a complex system like H in the transition regime. One possible reason for the lower melting temperatures in the other ab initio calculations can be proposed. In both computations the system size was small (54 atoms). They started with a bcc lattice in a cubic cell. It is possible that at finite temperatures a phase transition to a fcc (of hcp) lattice

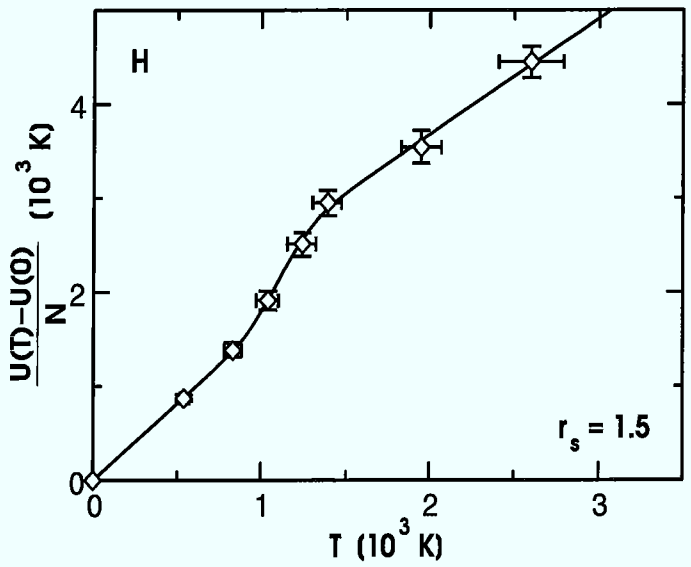

Figure 7.8: Fit of the internal energies $U(T)$ U versus T at $r_s = 1.5$. The fit formula was chosen to give a (finite-size) broadened discontinuity in the specific heat. Statistical error bars were added. The fit gives a melting temperature of 1125 K.

takes place. For the OCP model simulations have been performed that suggest a crystallization to a fcc lattice to occur at $\Gamma = 196$ [84](the melting temperatures given above correspond to the melting of the bcc lattice at $\Gamma = 178$). It has been concluded that the bcc lattice is more stable than the fcc lattice in the OCP. The situation may change when the bare Coulomb interaction is screened. It is well possible that at higher temperatures the bcc-crystalline phase may become unstable, because entropy favors the more close-packed fcc lattice. This hypothesis is lent some credibility by the small energy difference between both structures at $r_s = 1.0$ (0.04 eV/atom, see chapter 6). A cubic cell with 54 atoms is not well compatible with an fcc lattice (32, 108, or 256 atoms on a fcc lattice would fit into a cubic cell). For our larger system (128 atoms) the constraints imposed by the cell shape and size can be expected to be smaller.

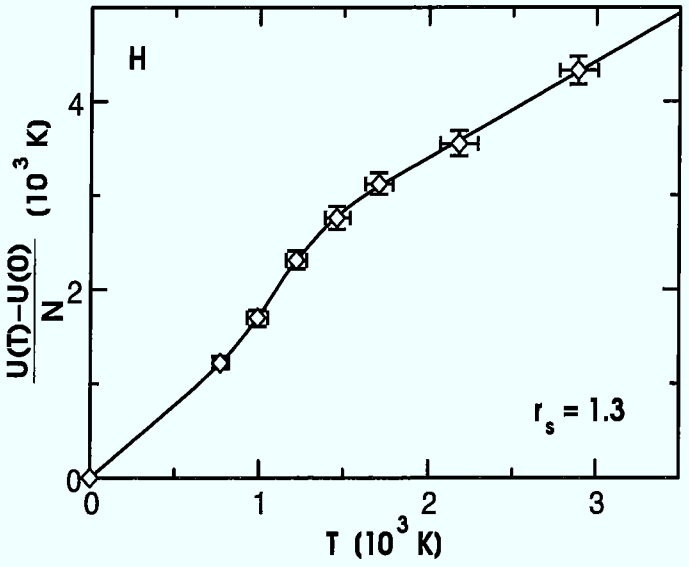

Figure 7.9: Fit of the internal energies U versus T at $r_s = 1.31$. Statistical error bars were added. The fit gives a melting temperature of 1150 K.

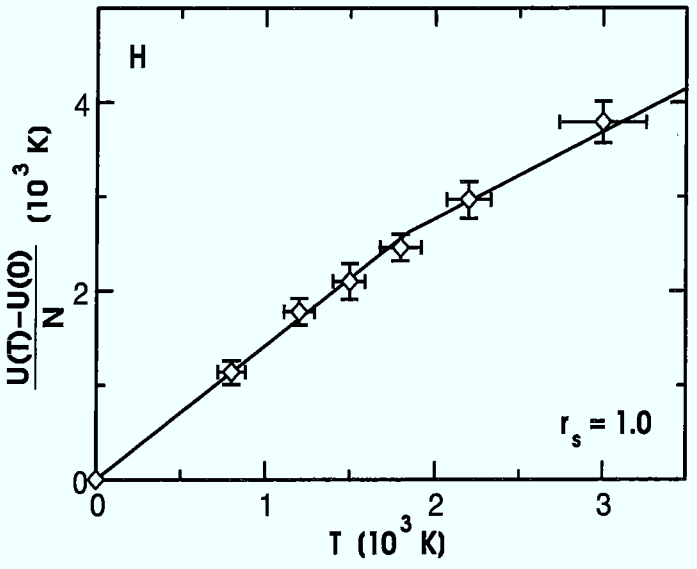

Figure 7.10: Fit of the internal energies U versus T at $r_s = 1.0$. The fit gives a melting temperature of 1840 K. The error bars are too large for the fit to be reliable. The temperature is probably an overestimation.

7.2 Electronic Properties

Before discussing the "true" electronic properties, we investigate the coupling of the electrons and ions. A quantitative measure is provided by the spherical average of the *electron-ion pair correlation function* $g_{ei}(r)$ (see appendix B). In the previous section the ion-ion pair correlation functions were presented (figure 7.2). At $r_s = 1.5$ they indicated a fundamental change in the structure of the system, from molecular (800 K) to a more complex state, where atoms, molecules, and strings occur (3000 K). We wondered whether this trend is discernible from the electron-ion correlation. In figure 7.11 the $g_{ei}(r)$ for H at $r_s = 1.5$, $T = 800$ K and 3000 K are shown together with the $g_{ei}(r)$ of the possible ground state structures at $r_s = 1.5$, mhcp-o and string structure. These were compared in chapter 6. The four curves are very similar. The correlation between electrons

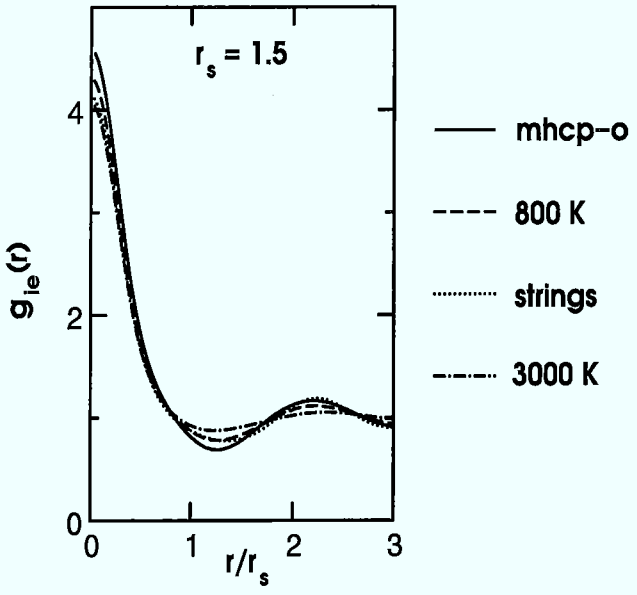

Figure 7.11: Spherical part of the electron-ion pair correlation functions $g_{ei}(r)$ of the mhcp-o lattice (solid line), the H sample at $r_s = 1.5$ and $T = 800$ K (dashed line), the string structure (dotted line), and the H sample at $r_s = 1.5$ and 3000 K (dashed-dotted). The curves of the mhcp-o lattice and the sample at 800 K show the strongest correlation, whereas for the string structure and the sample at 3000 K the first peak is slightly higher.

and ions decreases slightly with T and in the mhcp-o lattice electrons and ions are a bit more correlated than in the string structure. Thus the $g_{ei}(r)$ of 800 K might be paired with that of the mhcp-o structure and the $g_{ei}(r)$ at 3000 K is closer to

the $g_{ei}(r)$ of the string structure. However, the curves are too similar to establish a reliable connection. As can be seen in figure 7.14, too, the sphericalized average of the electron-ion pair correlation function changes only little with temperature and serves us mainly as a measure to investigate the density dependence of the electron-ion correlation rather than the temperature dependence. A better tool to investigate the temperature induced changes at $r_s = 1.5$ is the average over the first momenta in the expansion of the correlation function into spherical harmonics (the $\bar{g}_1^m(r)$ are defined in appendix B)

$$g_{ei}^1(r) \equiv \sum_{m=-1}^{1} |\bar{g}_1^m(r)|^2 , \tag{7.9}$$

which includes information about the anisotropy in the electron-ion distribution around the ions. In the following $g_{ei}^1(r)$ will be referred to as the p-component of the electron-ion pair correlation function. The forming of bonds is accompanied by an accumulation of charge between the bonding atoms, a change in the bonding behavior should lead to a different angular dependence of the charge around the atoms. In figure 7.13 $g_{ei}^1(r)$ is shown for 800 K, 3000 K, the mhcp-o structure and the string-structure. What we guessed from the spherical averaged contribution is confirmed by the $g_{ei}^1(r)$. The averaged first momentum is drastically different for the two structures from chapter 6. The mhcp-o structure was characterized by a density distribution that peaked at the sites of the molecules and decreased to almost zero between the molecules (figure 6.10). There is a very strong directional dependence of the charge density for distances smaller than the intramolecular stretching. This leads to sharp, pronounced peak in $g_{ei}^1(r)$, which decline fast when r exceeds the bonding distance. The distribution of the electronic charge in the string structure is substantially different (figure 6.9). The charge is enhanced along the "ridges" formed by the strings. The next neighbor spacing of the atoms is considerably larger than in the molecules of the mhcp-o structure (1.69 to 1.41 a.u.). Consequently, the accumulation of charge between next neighbor atoms is considerably smaller for the string structure. It follows that on a sphere with a radius r smaller than the next neighbor distance the variation of the charge density as a function of the angular degrees of freedom is much stronger in the mhcp-o lattice. The first peak of the $g_{ei}^1(r)$ in the string structure is much lower and - because of the larger next neighbor distance - broader. The average of the first momentum is a kind of signature of the bonding characteristics of the studied systems. Thus figure 7.12 indeed corroborates the trend seen in the ion-ion pair correlation functions: The $g_{ei}^1(r)$ wanders from a form similar to the "molecular" $g_{ei}^1(r)$ of the mhcp-o structure to a $g_{ei}^1(r)$, that indicates an anisotropy of the charge distribution and resembles the $g_{ei}^1(r)$ of the twofold coordinated string-structure. Thus the temperature dependence of the structural properties at $r_s = 1.5$ is conspicuously non-linear. At zero temperature the internal energy favors strings with overlapping charge distributions and

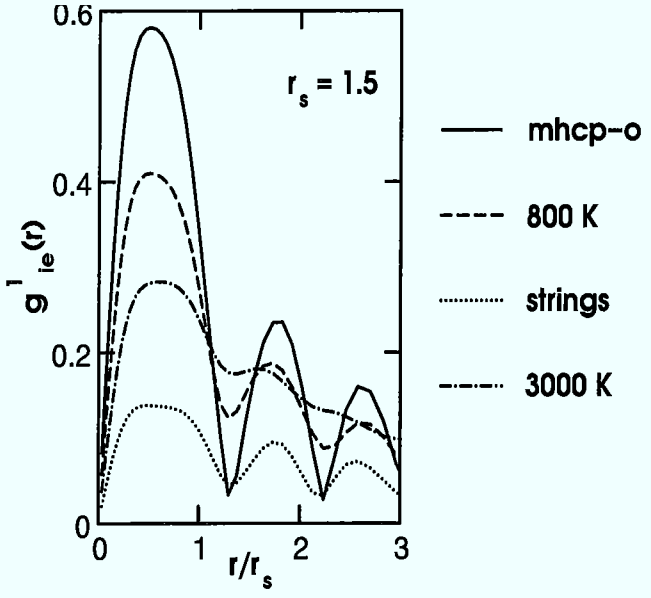

Figure 7.12: The averaged first momentum of the electron-ion pair correlation functions $g^1_{ei}(r)$ of the mhcp-o lattice (solid line), the H sample at $r_s = 1.5$ and $T = 800$ K (dashed line), the string structure (dotted line), and the H sample at $r_s = 1.5$ and 3000 K (dashed-dotted). The first momentum serves as a quantitative tool to measure the anisotropy of the electron-ion correlation. Obviously, there is a temperature induced change in the H sample. The curve for 800 K resembles the $g^1_{ei}(r)$ of the mhcp-o structure, whereas at 3000 K the $g^1_{ei}(r)$ of the H sample is close to the string structure. This trend indicates a change in the bonding characteristics.

comparable first and second next neighbor distances, i.e., a coordination number of two. At small temperatures the strings are broken up. The entropy stabilizes well-defined molecules. At higher T the electron-ion correlation has decreased, the molecular bonds are weakened and partial dissociation takes place. On the other hand conglomerates of more than two atoms (strings) form that share their electrons (charge transfer). The characteristics of the system at 3000 K are much closer to those of the ground state structure (string structure) than those at 800 K.

In figure 7.13 the $g^1_{ei}(r)$ at 800 K (1000 K for $r_s = 0.5$) for all r_s are shown. As expected, the correlation decreases with increasing density, corresponding to a reduction of the screening (also seen in the spherical average, figure 7.14). Again the $g^1_{ei}(r)$ of the string structure is presented. It resembles closely the $g^1_{ei}(r)$ of the system at $r_s = 1.31$, corroborating the conclusions of the previous section: The sample at $r_s = 1.31$ is characterized by string formation (see figures 7.3 and 7.4).

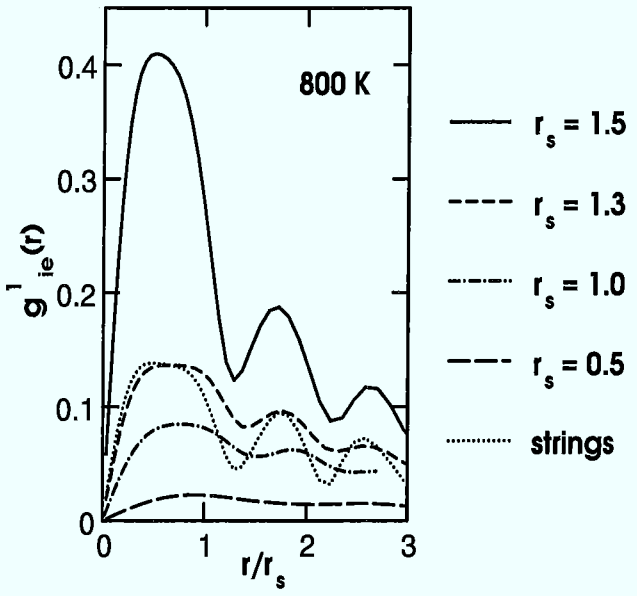

Figure 7.13: The p-component of the electron-ion pair correlation function $g^1_{ei}(r)$ at 800 K for $r_s = 1.5$ (solid line), $r_s = 1.31$ (dashed line), $r_s = 1.0$ (dashed-dotted), $r_s = 0.5$ (long dashes), and the string structure (dotted). The $g^1_{ei}(r)$ decreases considerably with increasing density. The $g^1_{ei}(r)$ for $r_s = 1.31$ is very close to that one of the string structure, indicating similar structural properties.

It instructive to examine $g_{ei}(r)$ as a function of density, also (figure 7.14). Obviously the coupling between electrons and ions weakens with increasing density. (The $g_{ei}(r)$ is normalized to one for a homogeneous system.) An interesting feature is the reversal of the temperature trend of $g_{ei}(r)$. At $r_s = 1.5$ it decreases with T. This decrease is easily understood with the help of figure 7.11. The structural changes induced by the higher temperature lead to a rearrangement of the electron levels. As figure 7.15 shows in more detail, the temperature dependence at $r_s = 0.5$ is different. The $g_{ei}(r)$ increases with higher temperatures, i.e, the correlation rises. This phenomenon can be related to the temperature dependence of the electronic density of states (see figure 7.25 and the discussion at the end of this section). A possible explanation is a tendency of the electronic states to localize at high T due to increased geometrical disorder.
In many respects figures 7.16 to 7.19 that present the *electronic density* in a randomly chosen section in a plane at $r_s = 1.5$ to $r_s = 0.5$ and $T = 800$ K (1000 K for $r_s = 0.5$) confirm the tendencies seen in the $g_{ei}(r)$ and $g^1_{ei}(r)$. Figure 7.16 demonstrates that at $r_s = 1.5$ the charge is strongly concentrated at the units (here still molecules) of which the system is composed. At $r_s = 1.31$ (figure 7.17) the character of the H sample has changed. The tight-bound molecules have broken up. From time to time H atoms aggregate to form short-lived entities

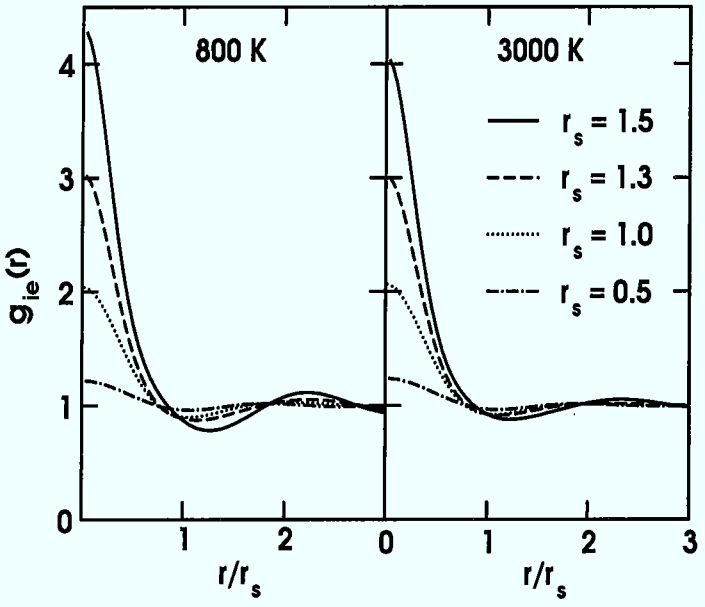

Figure 7.14: The density dependence of the sphericalized electron-ion pair correlation function $g_{ei}(r)$ at two temperatures, 800 K and 3000 K. The correlation function substantially decreases with pressure, indicating the decrease of the strength of the electron-ion interaction.

like pairs or strings. While the density has increased the average next neighbor distance has decreased considerably. Figures 7.18 ($r_s = 1.0$) and 7.19 ($r_s = 0.5$) show the trend to increasing uniformity of the charge distribution with increasing density. This corresponds to a decreasing relative importance of the electron-ion interaction or a weaker screening, respectively. At $r_s = 0.5$ the inhomogeneities caused by the atoms are much smaller than the (in comparison with the previous densities strongly) enhanced average density. The electronic part of the system approaches the jellium. The figures showing the electronic charge distribution may be compared with the (instructive) density plots of Clérouin, Pollock, and Zérah [37], who show the polarization of the electronic system at $r_s = 1.0$, 0.5, 0.1, and 0.01. Their plots suggest that while at $r_s = 0.5$ the ions still mean a major perturbation to the electron gas, the perturbation is small at $r_s = 0.1$ and has practically disappeared at $r_s = 0.01$. Thus the jellium model will provide a reasonable description at densities higher than $r_s = 0.1$. The absence of oscillations of the charge density around the ions in their figures is due to the simplified treatment of the screening (Thomas-Fermi method).

The trend of the electrons to a homogeneous distribution for increasing charge density is accompanied by a delocalization of the Kohn-Sham orbitals, which in the limit of infinite density will tend to plane waves, the eigenfunctions of the homogeneous (free) electron gas. We introduced a measure of delocalization, the

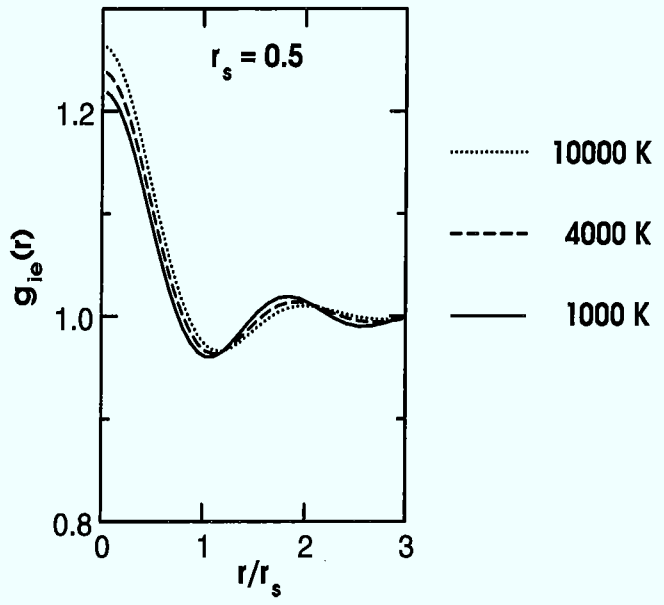

Figure 7.15: The temperature dependence of the sphericalized electron-ion pair correlation function $g_{ei}(r)$ at $r_s = 0.5$. Three temperatures, 1000 K (solid line), 4000 K (dashed line) and 10000 K (dotted line) are shown. The correlation function decreases with temperature, possibly due to localization of the electron levels.

inverse participation ratio, which for a Kohn-Sham orbital decomposed in plane waves ($\psi_{\mathrm{KS}}(\vec{r}) = \sum_i c_i \exp(-\vec{g}\vec{r})$) is obtained by summing up the squared moduli of the expansion coefficients ($\sum_i |c_i|^4$). Since the number of coefficients c_i that contribute with an essential weight will decrease with increasing delocalization (for $r_s \longrightarrow 0$ only one remains) the inverse participation ratio will be the larger, the more delocalized the system is (and equal to one in the high density limit). In figure 7.20 the inverse participation ratios at 800 K (1000 K for $r_s = 0.5$) for $r_s =$ 1.31, 1.0, and 0.5 are presented. The inverse participation ratio increases roughly by a factor of 5 between $r_s = 1.5$ and $r_s = 1.0$ and a factor of 20 from $r_s = 1.0$ to $r_s = 0.5$. The trend of the orbitals to delocalization is obvious. The decrease of the delocalization of the Kohn-Sham orbitals with the size of the eigenvalue in figure 7.20 is an artifact of the expansion into one-particle orbitals.
Although the wave functions in DFT are constructed to give the electronic density that minimizes the total energy and not to provide good approximations to the "true" many-body wave functions numerous previous computations (see the list of review articles on DFT given at the beginning of chapter 2.1) have shown that the Kohn-Sham eigenvalues and eigenstates are good indicators of many physical properties of the system under investigation. For example, they allow a quantitative description of the band structure of solids. A quantitatively bad, but

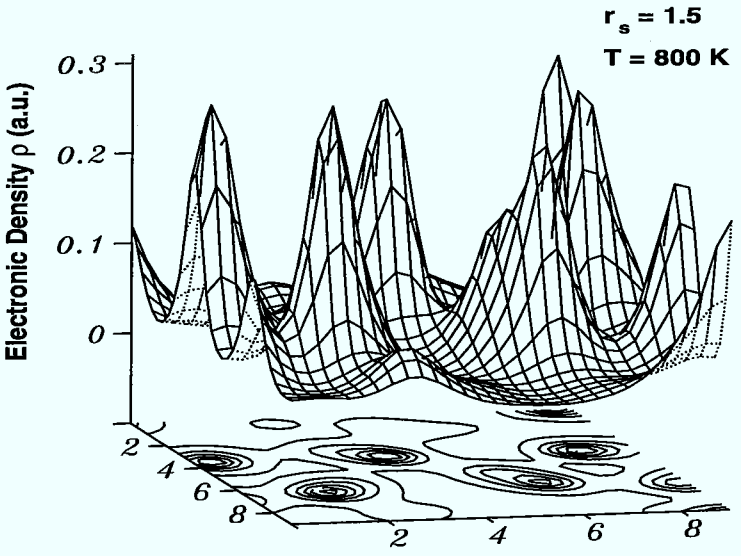

Figure 7.16: The density ρ in a randomly chosen plane of a sample configuration at $r_s = 1.5$ and $T = 800$ K. The molecules are clearly discernible as sharp, pronounced peaks. The charge density falls off to almost zero between the molecules.

qualitatively mostly correct indicator is the band gap in insulators and semiconductors of which LDA systematically underestimates the size by about a factor of 2. Therefore, in the following the *electronic densities of state* (EDOS) of H for r_s = 1.5, 1.31, 1.0, and 0.5 are presented. Figure 7.21 shows the EDOS for the lowest density. The Fermi energy (which we simply define to lie in the middle between highest occupied and lowest unoccupied state) is represented by a vertical solid line and the faint, dotted lines indicate the eigenvalues of an equivalent (i.e., with identical periodic boundary conditions) free electron gas. The presented EDOS are averages over a few samples at the investigated temperatures. At $T = 800$ K there is a clear gap in the eigenvalue spectrum that indicates the system to be insulating. This agrees well with the notion of well separated, hardly overlapping molecules, which was mediated by the earlier discussion (see e.g. figure 7.19). At the higher temperature we found a change in the structure expressed by overlapping charge distributions and the occurrence of different coordination numbers in the bonding of the atoms. Figure 7.19 suggests that these structural changes are accompanied by the closing of the band gap, i.e., the metallization of the system. This trend is also seen in the computed conductivities at $r_s = 1.5$ (chapter 10). So far the EDOS fit well into the earlier considerations. However, at the higher density $r_s = 1.31$ the Fermi gap at 800 K is somewhat surprising (figure 7.22). As we argued before, the physical properties of the system at $r_s = 1.31$ and 800 K should be close to those at $r_s = 1.5$ and $T = 3000$ K. The pressure at $r_s =$

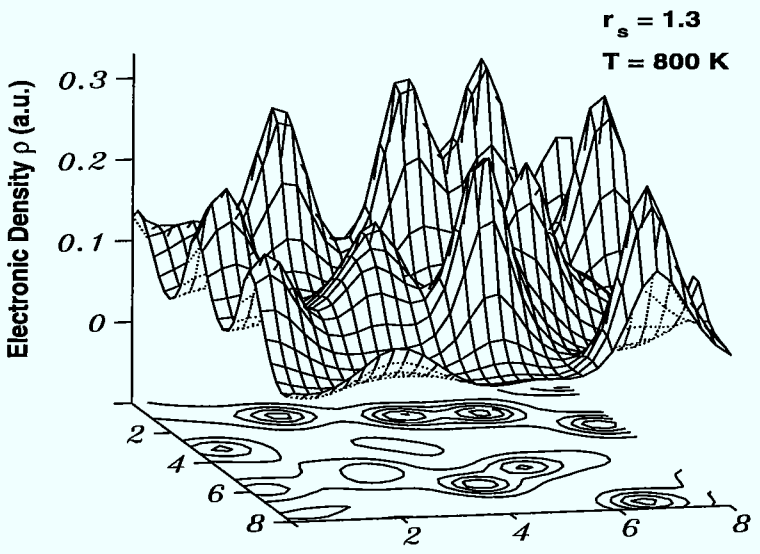

Figure 7.17: The electronic density ρ in a randomly chosen plane of a sample geometry at $r_s = 1.31$ and $T = 800$ K. The atomic charge distributions tend to overlap and to form strings of two, three, and more atoms. With respect to the charge density for $r_s = 1.5$ the peaks have shrunken, whereas the average charge density (and the charge density between the strings) has increased.

1.31 is about 3.5 Mbar and practically all of the more recent zero temperature computations of the metallization pressure obtain pressures equal or smaller than 3 Mbar (see section 1.1.4). It is necessary to comment on our treatment of the electronic structure before the subsequent EDOS can be explained properly. For our simulations we used boxes with a diameter of typically 12 a.u. of diameter together with periodic boundary conditions. For the electronic structure this results in a good description as long as the electronic wave functions extend over a spatial range considerably less than the box diameter. This seems to be the case for $r_s = 1.5$ and 800 K where the electrons are still strongly localized around the molecules (figure 7.16). However, in the metallization regime the electronic properties change swiftly. The wave functions of a metal are characterized by delocalization which proceeds with increasing metallic character (in our study equivalent with increasing density). As soon as the orbitals extend over a spatial range exceeding the cell dimensions, they are forced into a spurious symmetry, the symmetry of the cell. In the language of band-structure calculations we are performing simulations on only one $\vec{k}$-point, the Γ-point, however, with a large unit cell. In the metallic regime a much better approximation is to perform the simulation with a (as large as possible) set of $\vec{k}$-points. This would provide a more realistic representation of the electronic structure. Following Bloch's the-

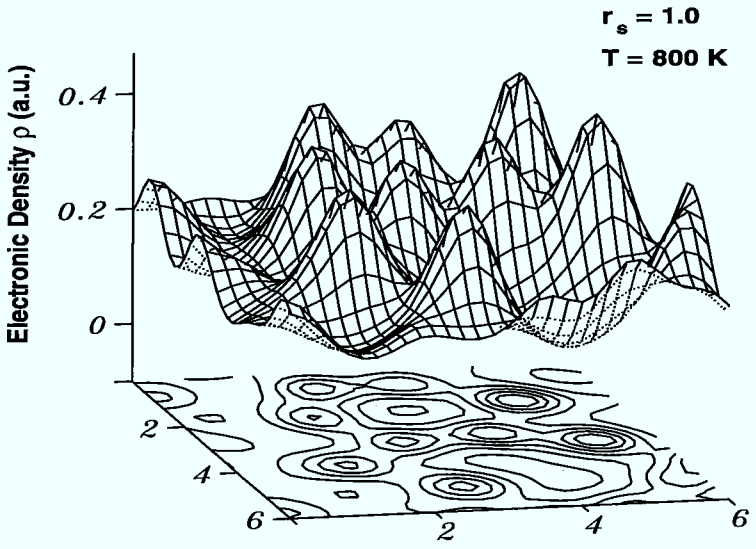

Figure 7.18: The density ρ in a randomly chosen plane of a sample geometry at $r_s = 1.0$ and $T = 800$ K. The system is atomic at this density. Nevertheless, the atoms show still the trend to conglomerate (also expressed in the absence of second next neighbor correlation in the ion-ion pair correlation function (figure 7.2)). The average density is higher than for the smaller densities, yet the inhomogeneity has diminished.

orem a wave function with wave vector $\vec{k}$ has the form $\psi_{\vec{k}}(\vec{r}) = \exp(i\vec{k}\vec{r})u_{\vec{k}}(\vec{r})$, where $u_{\vec{k}}(\vec{r})$ has the symmetry of the unit cell. The restriction of $u_{\vec{k}}(\vec{r})$ to the same symmetry as the unit cell is not severe, because for metallic systems $u_{\vec{k}}$ is only weakly dependent on $\vec{r}$ and approaches 1 for complete delocalization of the orbitals (jellium). Therefore, in the high pressure limit the description is exact apart from the finite number of $\vec{k}$-points. However, the inclusion of $\vec{k}$-points in the CP scheme is prohibitively expensive. For technical reasons (complex wave functions instead of real ones) the computation time increases by about a factor of 2 for $\vec{k}$-points different from the Γ-point. Thus a simulation with 10 $\vec{k}$-points is computationally 20 times more expensive than the "conventional" computations. To our knowledge no one has performed CP simulations with inclusion of $\vec{k}$-points in a realistic computation.

Most of the gaps in the EDOS at $r_s = 1.31$ and $T = 800$ K are due to finite-size effects (i.e., the restriction to the Γ-point). To test the influence of finite-size effects on the gap at the Fermi edge, we recomputed the EDOS including another $\vec{k}$-point (1/4,1/4,1/4). The result is shown in figure 7.23. The finite-size gaps close. The closing of the gap between the highest occupied and the lowest unoccupied states indicates that the system is metallic and that the gap at the

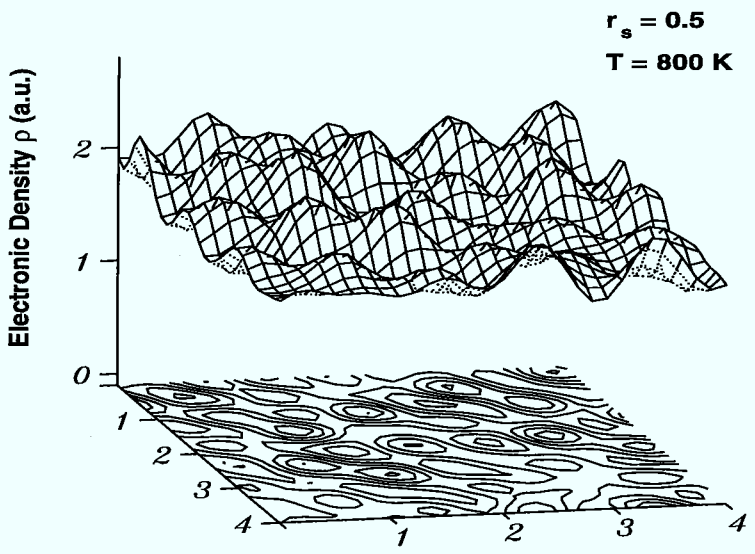

Figure 7.19: The density ρ in a randomly chosen plane of a sample geometry at r_s = 0.5 and T = 1000 K. The average density is much higher than for all other r_s. The peaks caused by the ions have decreased considerably, indicating a relative weakening of the electron-ion interaction compared with the lower densities.

Fermi edge is a finite-size artifact. Figures 7.24 and 7.25 show the EDOS at r_s = 1.0 and r_s = 0.5. They demonstrate how the peaks in the EDOS approach the values of the homogeneous electron gas. It is interesting that the peaks in figure 7.25 broaden with increasing T. Possibly this behavior indicates localization of orbitals at higher temperatures due to increasing disorder. This would explain the temperature trend in the electron-ion pair correlation function at r_s = 0.5 (figure 7.15). In figure 7.26 the average inverse participation ratio over a few configurations at r_s = 0.5 for T = 1000 K and T = 10000 K is presented. The orbitals close to the Fermi energy show the tendency to localize at the higher temperature. The effect is more clearly seen in figure 7.27 where we plotted the charge density of the 96th occupied orbital of two configurations at 1000 K and 10000 K.

It should be emphasized that the EDOS at higher pressures, e.g. figure 7.25, are unsatisfactory. The EDOS of the highest density, in particular, should mirror the form of the free-electron EDOS which is a continuous curve that increases proportional to the square root of the energy. However, this shape is completely lost in the finite-size splitting. This poor EDOS points to one of the most severe limitations of the method when applied to high pressure H:

- The electronic structure is only inadequately represented in a Γ-point simulation. Especially for systems with metallic character the inclusion of $\vec{k}$-

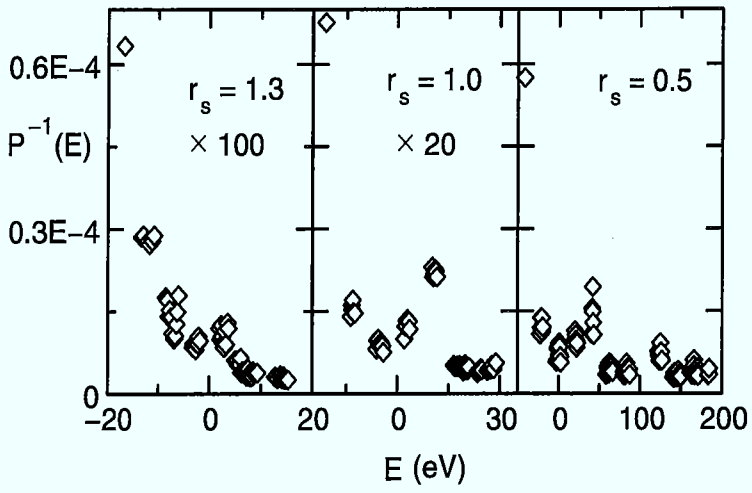

Figure 7.20: The inverse participation ratios P^{-1} of the Kohn-Sham orbitals for $r_s = 1.31$ and $r_s = 1.0$ at 800 K and for $r_s = 0.5$ at 1000 K plotted versus the value of the corresponding Kohn-Sham eigenvalue. The orbitals are considerably delocalized with increasing density. The inverse participation ratios at $r_s = 0.5$ are still much smaller than the inverse participation ratio of a free electron gas, which is equal to one.

points is mandatory when the increase of computer power allows to afford them.

- The classical treatment of the ions is not well justified. A classical treatment is in order as long as the Wigner radius is much larger than the de Broglie wavelength, i.e., $a \gg \hbar(Mk_BT)^{-1/2}$. For $r_s = 0.5$ and $T = 1000$ K, our worst case at finite temperatures, the ratio is $a/\hbar(Mk_BT)^{-1/2} \approx 1.2$. Quantum effects can be expected to be not negligible. As mentioned before, a quantum path integral CP scheme exists [121]. However, its applicability is limited by the computational expenses.

Nevertheless, even at $r_s = 0.5$ and low T, where the two shortcomings are most severe, the CP approach represents a major improvement over the "conventional" MD methods as OCP or screened OCP. It was demonstrated in this chapter that the interplay of electrons and ions is crucial for an understanding of this system. Only in the very high P (or T) limit two separate species exist, electron and ions. Unless for densities substantially higher than those treated here the notion of two systems that are perturbed by the (weak) reciprocal interaction is not correct. In general we have a system of two species, electrons and ions, that cannot be treated

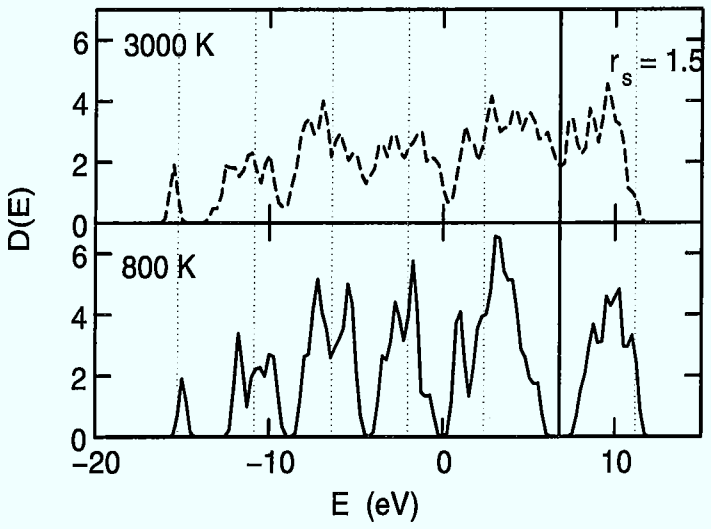

Figure 7.21: Electronic density of states $D(E)$ for $r_s = 1.5$ at $T = 800$ K and $T = 3000$ K. The Fermi energy is represented by a solid line. The faint, dotted lines indicate the values of an equivalent (same periodic boundary conditions) free electron gas. The gap at the Fermi energy at 800 K closes at 3000 K. At the higher temperature the system is a metal.

separately. The distinction of ionic and electronic properties made in this chapter is misleading in so far as electronic and ionic properties strongly influence each other. The properties of one species cannot be understood without the inclusion of the properties of the other species, such as the dynamics of the ions without screening or the electronic properties without studying the influence of the ionic temperature or the geometrical arrangement of the ions.

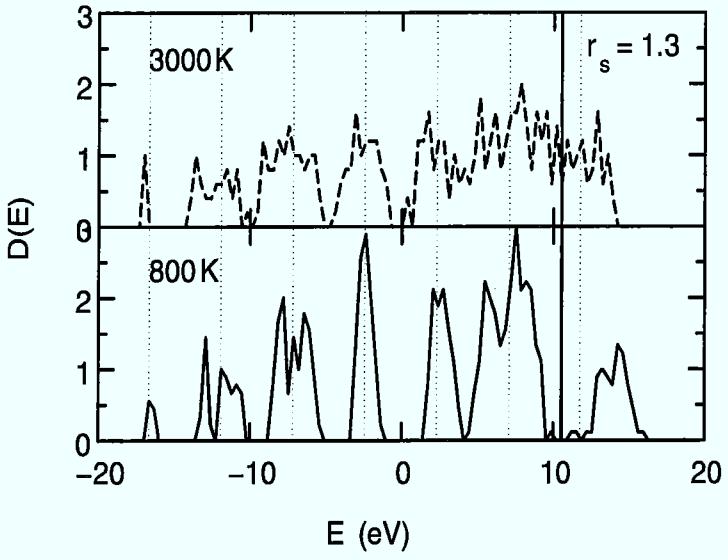

Figure 7.22: Electronic density of states $D(E)$ for $r_s = 1.31$ at $T = 800$ K and $T = 3000$ K. The Fermi energy is represented by a vertical line (solid). The faint, dotted lines indicate the values of an equivalent (same periodic boundary conditions) free electron gas. The gap at the Fermi energy at 800 K closes at 3000 K. The EDOS at 800 K displays a substantial finite-size discretization.

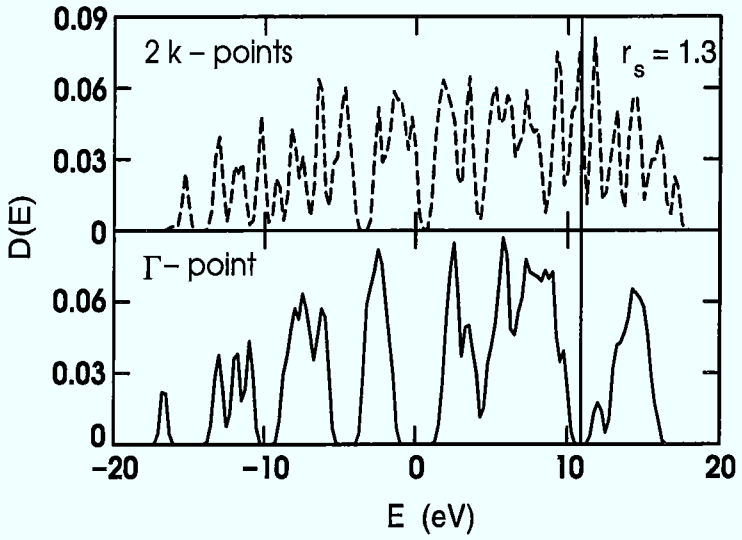

Figure 7.23: Electronic density of states $D(E)$ for $r_s = 1.31$ at $T = 800$ K computed at the Γ-point only (lower curve) and with inclusion of another $\vec{k}$-point (upper curve). The Fermi energy is represented by a vertical line (solid). The better $\vec{k}$-point sampling leads to a EDOS in which the finite size gaps are closed, including the gap at the Fermi edge. The gap at the Fermi energy of the Γ-point simulation is an artifact of the incomplete treatment of the electronic structure.

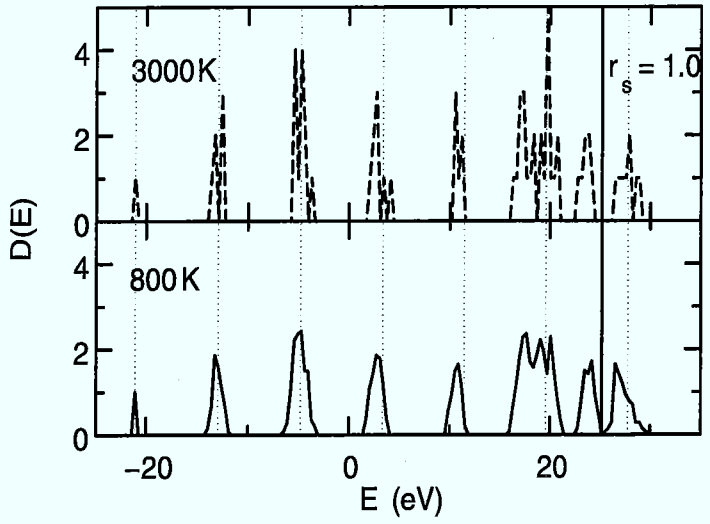

Figure 7.24: Electronic density of states $D(E)$ for $r_s = 1.0$ at $T = 800$ K and $T = 3000$ K. The Fermi energy is represented by a vertical line (solid). The faint, dotted lines indicate the values of an equivalent (same periodic boundary conditions) free electron gas. The density of states displays a considerable finite-size splitting into individual peaks. These peaks are centered at the positions of the equivalent free electron system.

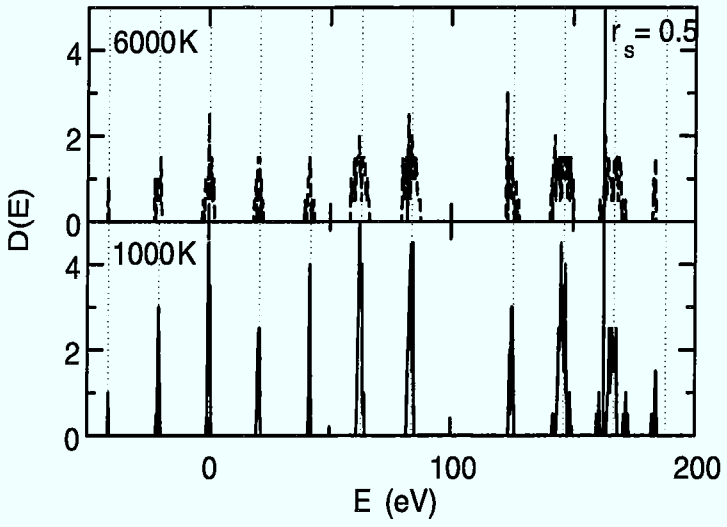

Figure 7.25: Electronic density of states $D(E)$ for $r_s = 0.5$ at $T = 800$ K and $T = 3000$ K. The Fermi energy is represented by a vertical line (solid). The faint, dotted lines indicate the values of an equivalent (same periodic boundary conditions) free electron gas. The EDOS exhibits sharp, narrow peaks at the positions of the equivalent free electron gas. Obviously, the eigenstates are considerably free-electron like. The broadening of the peaks at the higher temperature may indicate a trend of the orbitals to localize at higher temperature.

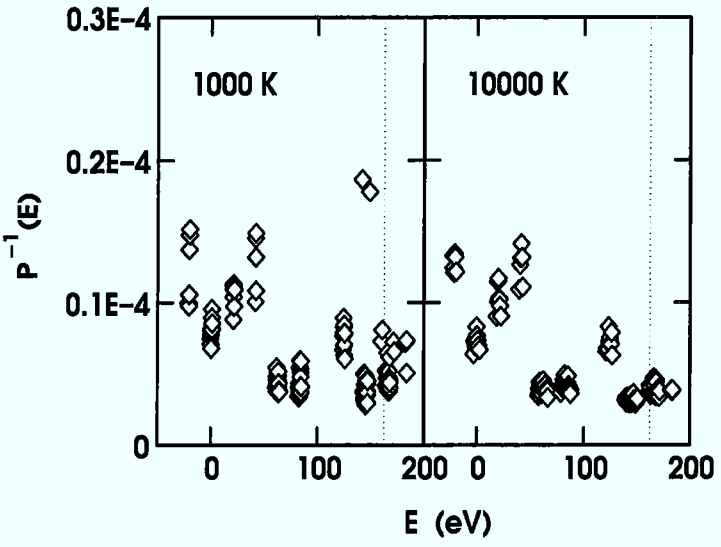

Figure 7.26: Inverse participation ratio P^{-1} of the Kohn-Sham orbitals at $r_s = 0.5$ for $T = 1000$ K and $T = 10000$ K. The inverse participation ratio of the first eigenvalue is not shown. The orbitals close to the Fermi energy exhibit a tendency to localize.

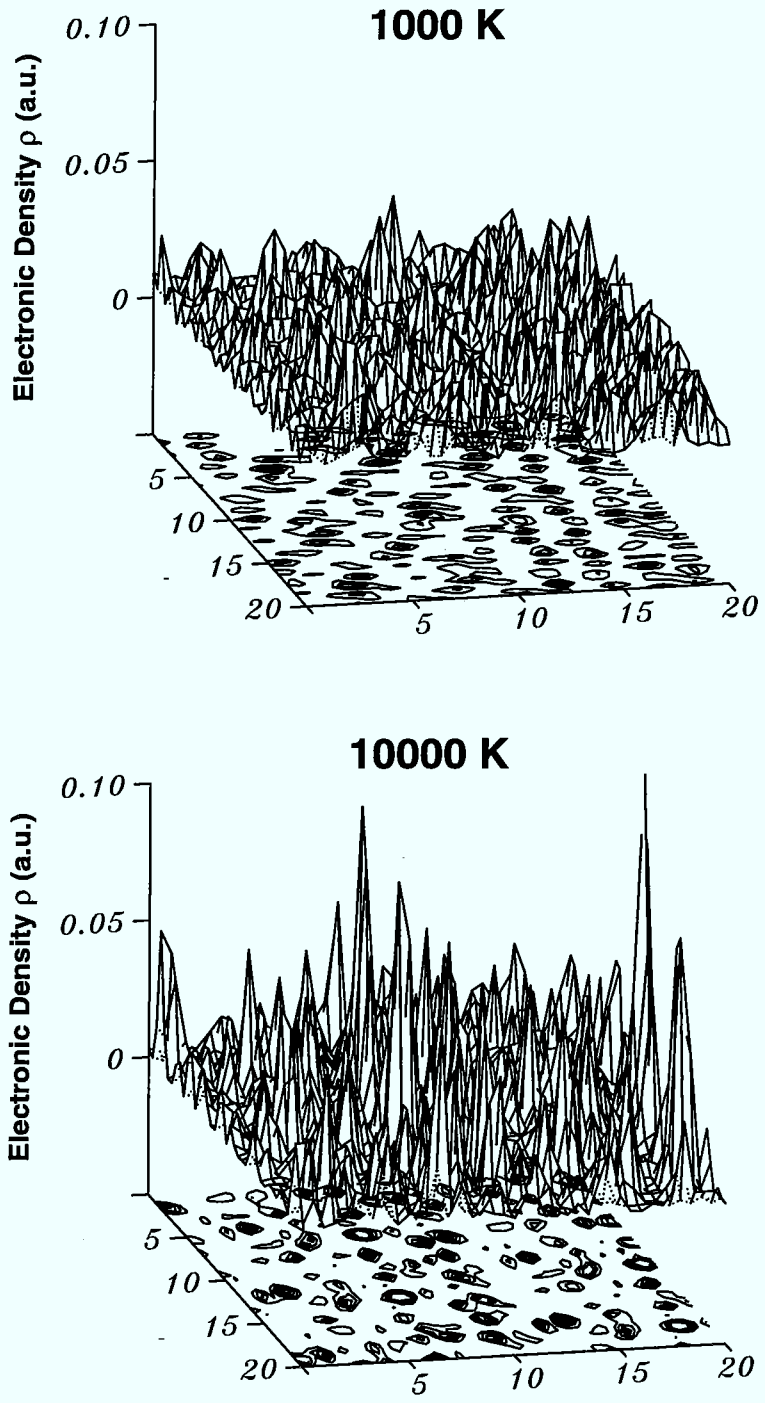

Figure 7.27: The density of one orbital ρ (the 96th occupied) for two configurations at 1000 K and 10000 K for $r_s = 0.5$. The orbital is more localized at the higher temperature.

Chapter 8

Helium and Hydrogen-Helium Mixtures at Elevated Temperatures

In chapter 5 we discussed the equations of state of H and He in the high pressure regime. Figure 5.3 showed that in the Mbar pressure regime many-body effects lead to large deviations from equations of state computed with pair potentials. The importance of many-body effects in high pressure He are well-known from previous investigations, too. For example, Loubeyre [111] investigated the three-body exchange interactions in pressurized He, and Younger [203] explored the effect of many-atom screening on diffusion in dense He (1.5 ... 8 g/cm^3) at high temperature (5 eV). Similar to H (see the discussion in the previous chapter), the many-body forces result in a softening of the effective potential. For He this softening in the intraatomar potential was experimentally observed in the two-stage gas-gun experiments of Nellis et al. [132]. The theoretical study of high-pressure He requires to include the effect of electronic screening in an adequate way. Thus the investigation of He under high pressures, especially in the pressure regime close to metallization (112 GPa, the highest metallization pressure of any element [202]), would be a rewarding objective for an ab initio investigation. However, this is not our aim. To us He mainly serves as a reference system in the study of a H-He mixture. We intend to understand the impact of He alloying on pure H. Especially with regard to the composition of astrophysical objects, such as the giant planets Jupiter and Saturn, it is interesting to perturb the H system by a smaller amount of He (7-10 atomic per cent). We treated a mixture of about 90 % H and 10 % He. The study was performed for significantly lower temperatures than those prevailing in Jupiter and Saturn at comparable densities ($\sim$ 10000 K). In the temperature range we treated in our studies the mixture is metastable, demixing in H-rich and He-rich phases. Nevertheless, for many properties our investigations contribute to the understanding of the state of matter deep within the giant planets (e.g., the ion-electron pair correlation

function is quite insensitive to temperature changes of a few thousand K). The stability bounds of the mixture will be addressed in the next chapter.
For He and H-He we performed simulations for two densities, $r_s = 1.31$ and $r_s = 1.0$. In our simulations we kept the number of electrons constant, i.e., our system sizes were 64 and 116 (104 H and 12 He) atoms for He and H-He, respectively. Analogous to the previous chapter this chapter is divided into two parts about the ionic and electronic properties. Because of its simplicity pure He is discussed first, followed by the mixture.

8.1 Ionic Properties

In figure 8.1 the *pair correlation functions* $g(r)$ for He at $r_s = 1.31$ and $r_s = 1.0$ and temperatures of $T = 800$ K and 3000 K are presented. The first peaks of

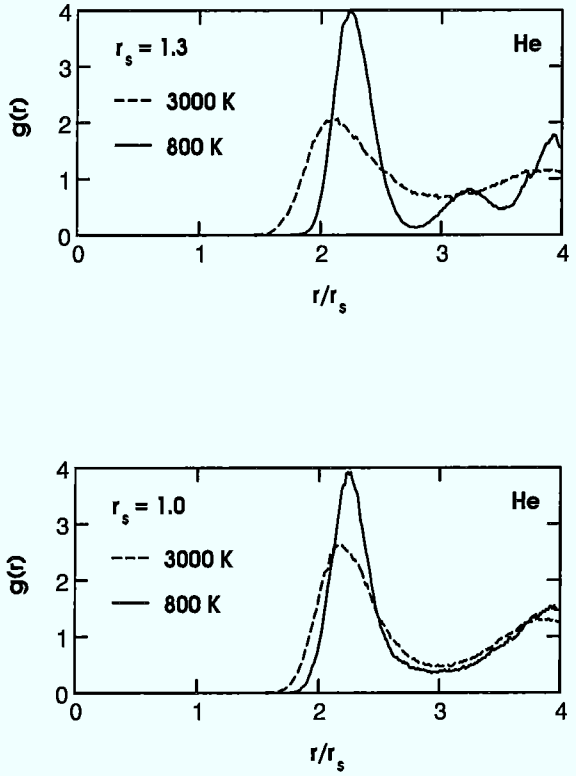

Figure 8.1: Pair correlation functions $g(r)$ of He for $r_s = 1.31$ and $r_s = 1.0$ and temperatures of 800 and 3000 K. At 800 K He crystallizes for both densities in a close packed lattice (fcc or hcp). At 3000 K the higher first peak at $r_s = 1.0$ indicates that the system is close to melting at this density, whereas at $r_s = 1.31$ the system is far in the liquid phase.

the g(r) at 800 K are nearly identical for the two densities. The integral over

the pair correlation function at $r_s = 1.31$ and 800 K is about 12 at its first minimum and 18 at its second minimum, corresponding to 12 next and 6 second next neighbors. As will be seen soon, He at 800 K is a solid for both densities. Thus the underlying structure is a close packed lattice, i.e., hcp or fcc (consistent with the phase diagram 1.16). The reason why the second peak is missing at $r_s = 1.0$ and 800 K is insufficient equilibration. At 3000 K and $r_s = 1.31$ the first peak is significantly broader and lower than at $r_s = 1.0$. Helium is barely melted at $r_s = 1.0$ and 3000 K whereas the melting temperature at $r_s = 1.31$ is nearly a factor of two lower ($T_m \approx 1630$ K for $r_s = 1.31$ and $T_m \approx 3120$ K for $r_s = 1.0$, see below).

In figure 8.2 the H-H, H-He, and He-He pair correlation functions of the mixture are shown for $r_s = 1.31$ and $r_s = 1.0$, and two temperatures for each density, $T =$ 800 K and 3000 K. In all four figures the first peak of the H-He pair correlation function does not lie in the middle between the first peaks of the pure elements, but instead close to the He-He peak. Thus H-He is not an ideal mixture, where the position of the first peak can be obtained by interpolating between the peaks of the constituents. The H-H pair correlation functions are close to those of the pure systems (figure 7.2). Apart from two peculiarities the He-He pair correlation functions closely resemble those of pure He, too. We believe the strange shape of the first peak in the He-He pair correlation function at $r_s = 1.31$ and 3000 K to be due to bad statistics. The MD run that produced the corresponding data was comparatively short for technical reasons. (For consistency all runs at $r_s =$ 1.31 were performed without Nosé thermostat.) At 3000 K the system is metallic enough for the electrons to take up too much energy only after few thousands of steps.) In addition the number of He atoms in the sample is small (12), giving rise to poor statistics. The shift of the first peak at 800 K from about 2.2 (pure He) to 2.0 (mixture) is not an artifact. It is easy to understand. Pure He forms a fcc or hcp lattice. For H we found bcc to be most stable at $r_s = 1.0$. Since the mixture is predominantly H it can be imagined (in the solid phase) as a H lattice with point defects consisting of the replacement of two H atoms by one He atom. The resulting lattice is distorted. The lattice constants in the alloyed system will reflect the fact that the lattice constant of pure H is significantly smaller than that of pure He.[1] Obviously, the same argument applies for $r_s = 1.31$, also, apart from the fact that at this density the H lattice is more complicated than bcc.

[1] With the help of the conventional unit cells the difference in the lattice constants of the pure systems are easily computed. As the number of atoms is constant, it holds that $a_{n.n.}(fcc, He) = \sqrt{2}/2 a_{lat}(fcc, He) = \sqrt{2}/2\sqrt[3]{4} \cdot a_{lat}(bcc, H) = \sqrt{2}/2\sqrt[3]{4} \cdot 2/\sqrt{3} a_{n.n.}(bcc, H) \approx 1.3 \cdot a_{n.n.}(bcc, H)$.

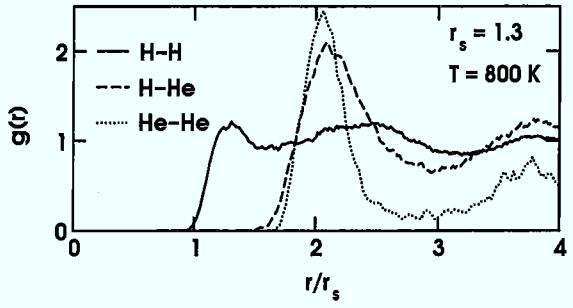

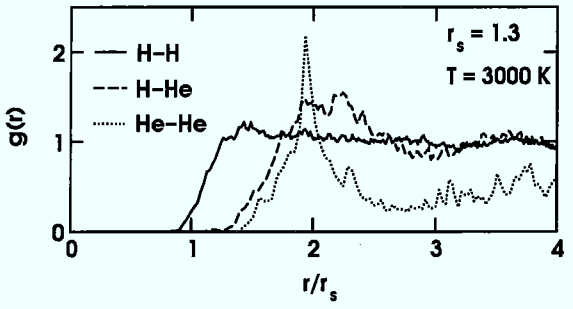

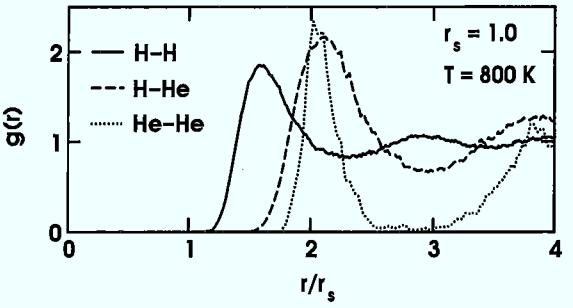

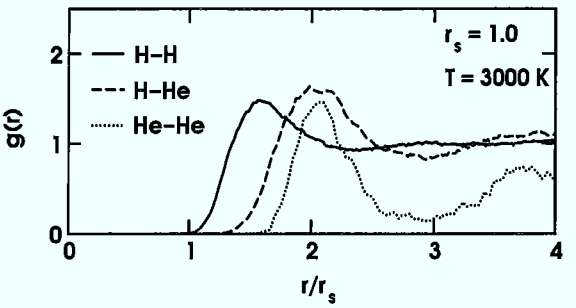

Figure 8.2: H-H, H-He, and He-He pair correlation functions $g(r)$ of the mixture at $r_s = 1.31$ and 1.0 and two temperatures, 800 K and 3000 K. The He-He pair correlation function was scaled by a factor 1/2 to fit into the figure. The H-H pair correlation functions closely resemble those of the pure H system.
The same is true for He except for the first peak at 800 K to have wandered inwards in the mixture. (The curious shape of the He-He peak at $r_s = 1.31$ and 3000 K is an artifact of the limited statistics.)
The first peak of the H-He pair correlation function indicates that H-He is not an ideal mixture, because it lies nearly at the same position as the He-He peak instead of being in the middle of the peaks of the constituents.

In figures 8.3 and 8.4 we compare the *self-diffusion coefficients* of H and He in the mixture and in the pure phases. The overall decrease of the diffusion

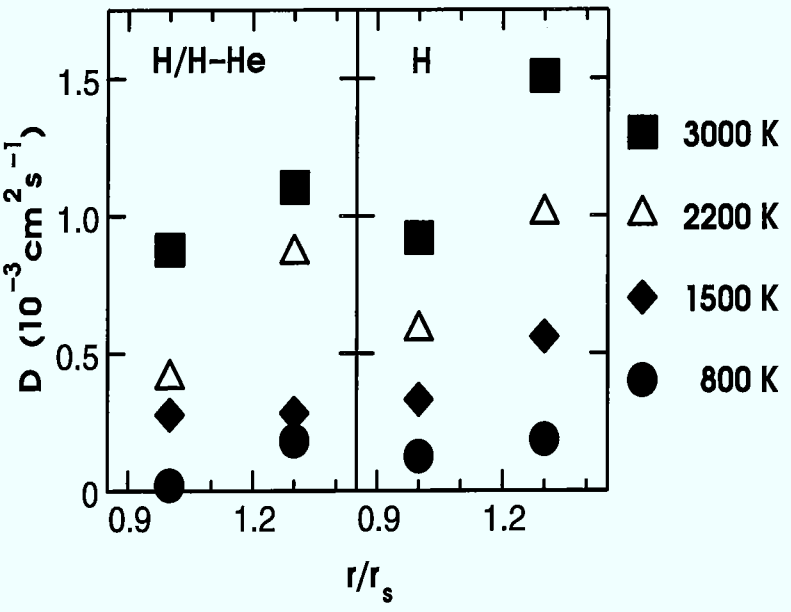

Figure 8.3: Self-diffusion coefficients D of H in the pure system and in the mixture with 10% He for $r_s = 1.31$ and 1.0 and temperatures of 800, 1500, 2200, and 3000 K. The self-diffusion coefficients in the mixture are slightly smaller than in the pure system. The decrease with increasing density is due to excluded volume effects and reduced screening.

coefficient with density is a well-known effect, partly due to the reduced screening, i.e., stronger effective forces at higher density. Partly, it represents structural effects in the medium, i.e., volume exclusion by nearest neighbors (the only effect in models that do not include screening such as OCP). The trend from the pure phases to the mixture is different for H and He. As will be seen below, H is solid or close to the melting temperature at 800 K and 1500 K for $r_s = 1.31$ and at all temperatures smaller or equal 3000 K at $r_s = 1.0$. (The diffusion coefficient for 4000 K was only added to underline the increase of diffusion in the fluid phase.) Obviously, for the solid phase the diffusion coefficient has to come out very small. The present values are overestimations due to the finite lengths of our trajectories. For $r_s = 1.31$ it is more rewarding to compare the diffusion coefficients at 2200 K and 3000 K than those in the solid phase. Interestingly, the self-diffusion coefficients for He increase in the mixture. For a consistent

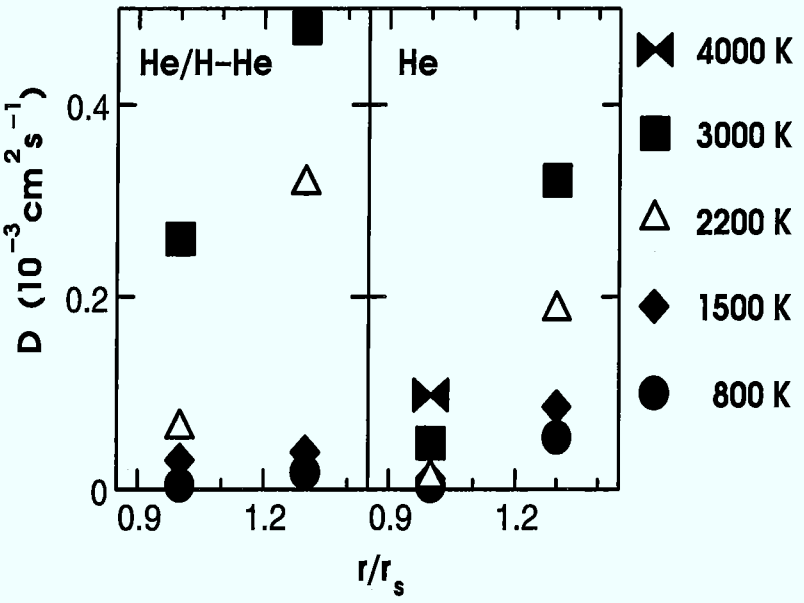

Figure 8.4: The self-diffusion coefficients D of He in the pure system and in the mixture with 10% He for $r_s = 1.31$ and 1.0 and temperatures of 800, 1500, 2200, and 3000 K. For $r_s = 1.0$ and pure He we have added the diffusion coefficient at $T = 4000$ K to illustrate the increase in the fluid phase (the melting temperature is about 3120 K). The diffusion coefficients of the fluid phase are larger in the mixture than in pure He. The strong increase of the diffusion coefficient at $r_s = 1.0$ and 3000 K is owing to the fact that the mixture is in the fluid phase whereas the pure system is close to melting.

picture of diffusion it would be necessary to compute the interdiffusion, too. We attempted to do so but found that the trajectory length required for sufficient convergence it is too long for an ab initio simulation. The drastic increase in the diffusion coefficient at $r_s = 1.0$ and 3000 K is easy to understand. It reflects the fact that the mixture is liquid at this temperature whereas He is close to the melting temperature (see figure 8.7). For H the diffusion coefficient decreases moderately with respect to the pure phase. Possibly the reason is a strengthening of the H bonds between pairs of H atoms close to the He atoms.
In figure 8.5 we plotted the *H-H distance in isolated pairs of H atoms* (i.e., within the distance of the two atoms they are onefold coordinated) versus the distance to the closest He atom. There is a strong tendency for pairs separated by a small distance to be close to a He atom. In particular the smallest distances will occur next to a He atom. The He atoms seem to strengthen the H bonds of the H atoms surrounding them. It is interesting to compare the smallest H-H distance at 800

K in figure 8.5 with the free H molecule. To reach a comparable distance in the free molecule it would require an excitation energy of more than 10000 K. The small H-H distances occurring reflect the weakening of the intramolecular bonds with pressure, which was mentioned in the introductory chapter. The grouping of the H atoms around He atoms is illustrated by figure 8.11 (next section), which shows the density distribution around a He atom.

We also tried to compute the *melting temperature* of these systems with the method proposed in the previous chapter, i.e., by a fit of the internal energies to a finite-size broadened specific heat expression. The results for He are shown in figures 8.6 and 8.7. He is a good insulator at the densities treated (see the EDOS in the next section). Both sets of data points exhibit a clear discontinuity and allow a reliable fit leading to melting temperatures of 1630 K ($r_s = 1.31$) and 3120 K ($r_s = 1.0$). Unfortunately, the discontinuities in the corresponding curves for the mixture are too small to allow a reasonable fit within the statistical error bars. An example is given in figure 9.6 of chapter 9.2 where the fit is needed for thermodynamic integration and serves to underline one source for uncertainties.

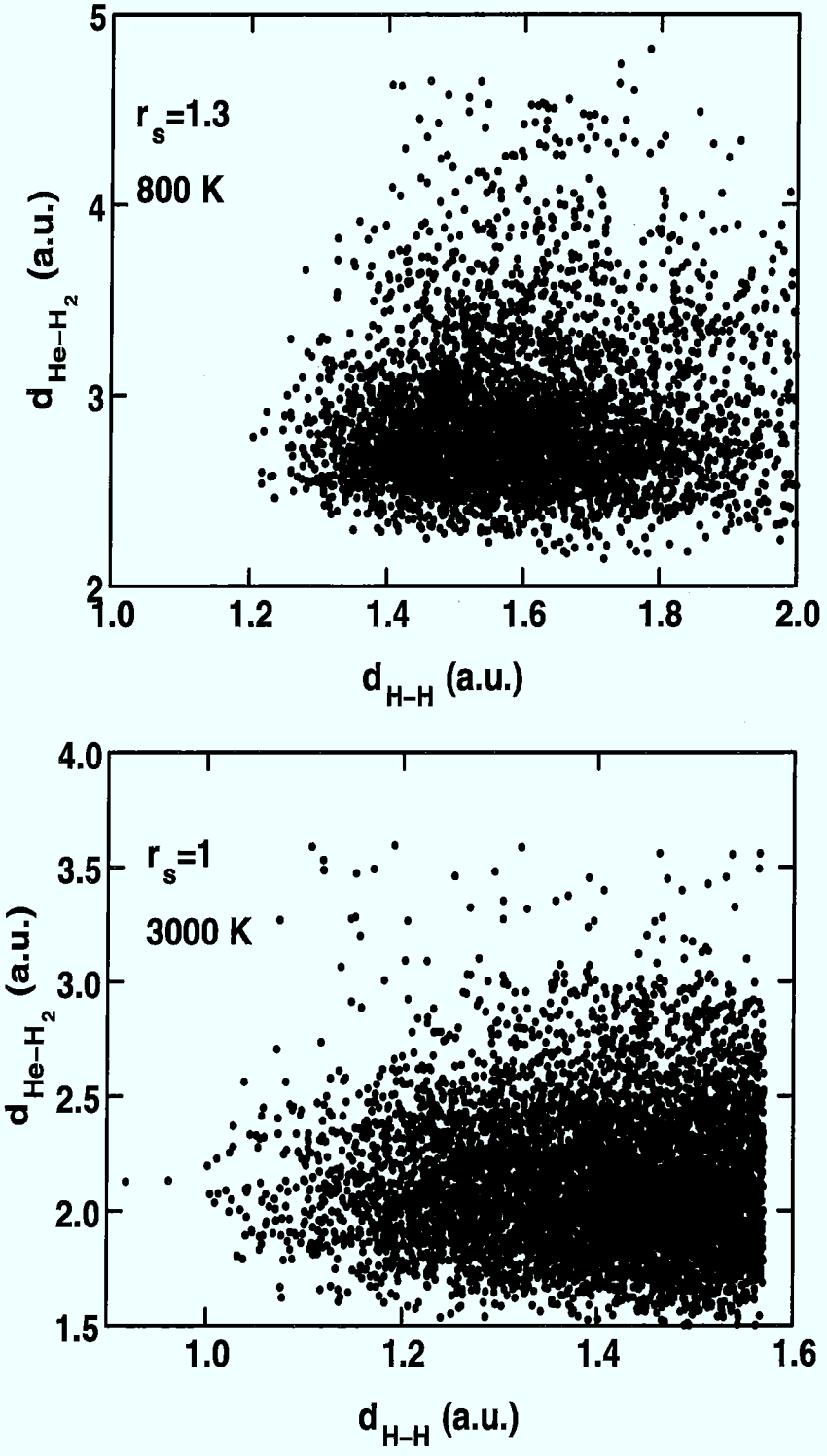

Figure 8.5: The distances of isolated pairs of atoms (i.e., the atoms are onefold coordinated within $d_{\mathrm{H-H}}$) plotted versus the distance of the pair to the closest He atom for $r_s = 1.31$ and 800 K and $r_s = 1.0$ and 3000 K. The distribution of the pair distances resembles a wedge: The smallest distances of the pairs are likely to occur close to the He atoms, i.e., the He atoms strengthen the bonds between neighboring H atoms.

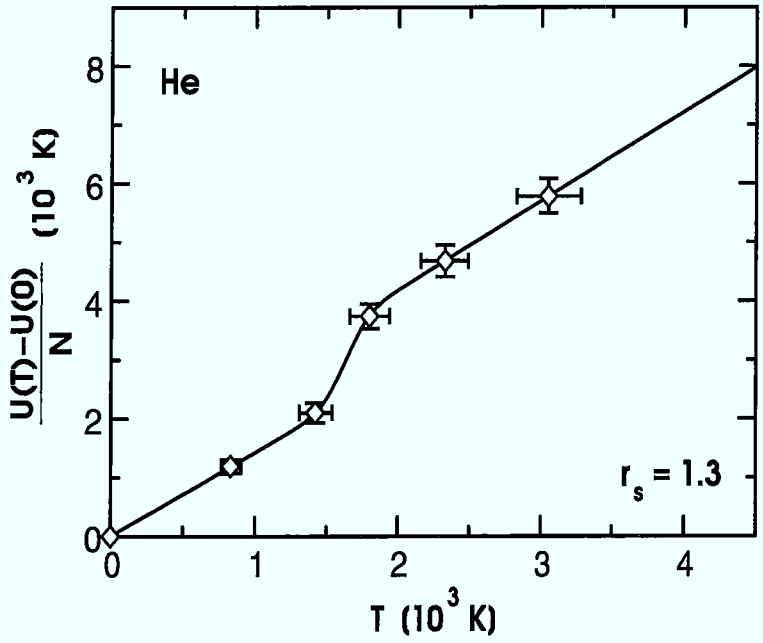

Figure 8.6: Fit of the internal energies $U(T)$ of He at $r_s = 1.31$. The fit formula was chosen to give a (finite-size) broadened discontinuity in the specific heat. Statistical error bars were added. The fit gives a melting temperature of 1630 K.

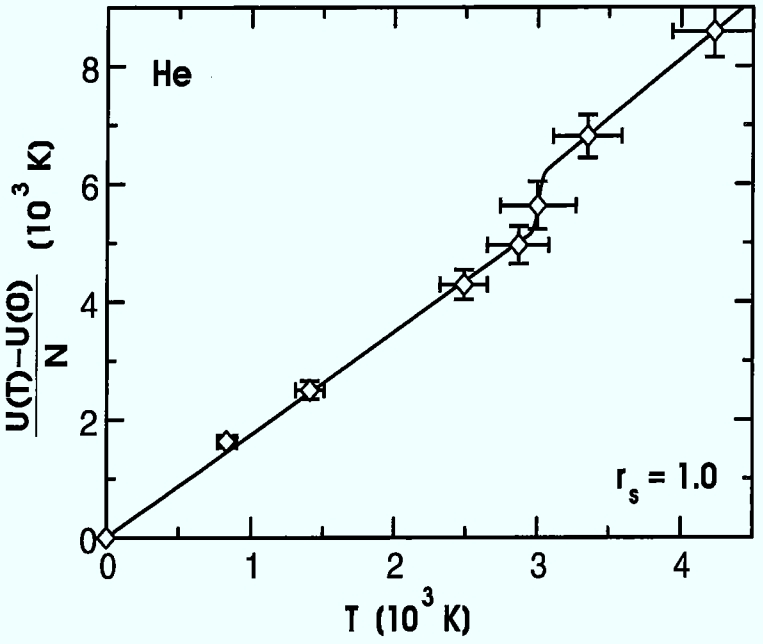

Figure 8.7: Fit of the internal energies $U(T)$ of He at $r_s = 1.0$. Statistical error bars were added. The fit gives a melting temperature of 3120 K.

8.2 Electronic Properties

The *ion-electron pair correlation function* $g_{ie}(r)$ probes the strength of the interaction between the ionic and electronic degrees of freedom. For He it is shown in figure 8.8. The correlation is much stronger than for H, indicating that the

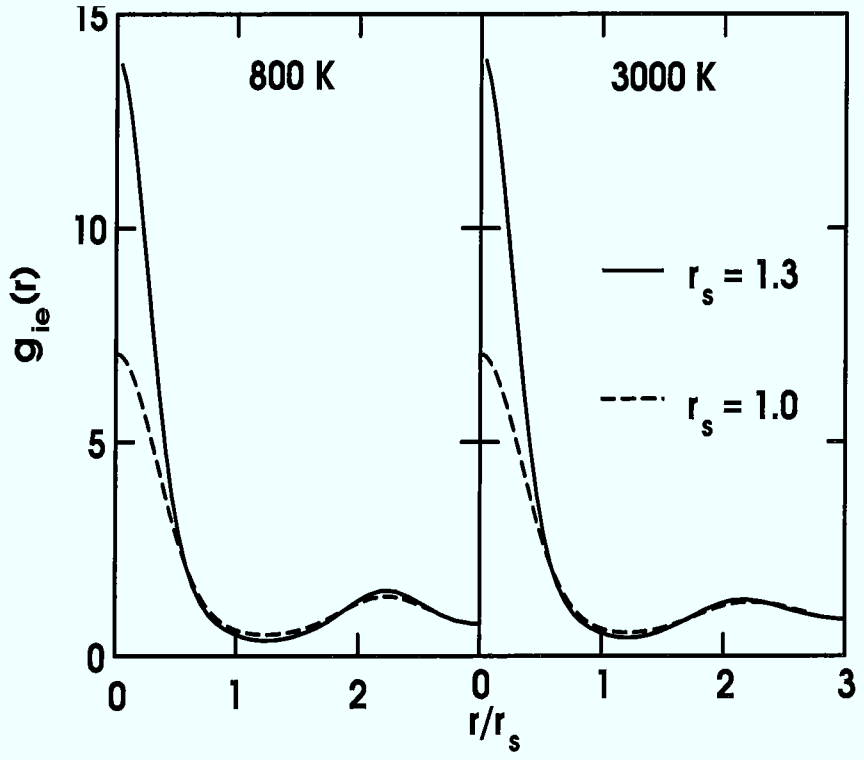

Figure 8.8: s-component of the ion-electron pair correlation function $g_{ie}(r)$ for He at $r_s = 1.31$ and $r_s = 1.0$ and 800 K and 3000 K. The correlation is much stronger than for H, indicating that the electrons of the He atoms are more tightly bound. Similar to H the temperature dependence of the pair correlation function is very small.

two electrons belonging to each He atom are tightly bound to their cores. The anisotropic p-component has about the magnitude of the p-component of H and is - in comparison with the much larger s-component - negligible. The corresponding ion-electron pair correlation functions of H and He in the mixture are virtually identical with those of the pure systems and are therefore omitted.
In figures 8.9 to 8.12 the *electronic charge densities* of H and H-He across a plane in a section of the systems are shown. For He the situation changes little from $r_s = 1.31$ to $r_s = 1.0$. Pronounced charge density peaks that represent the individual

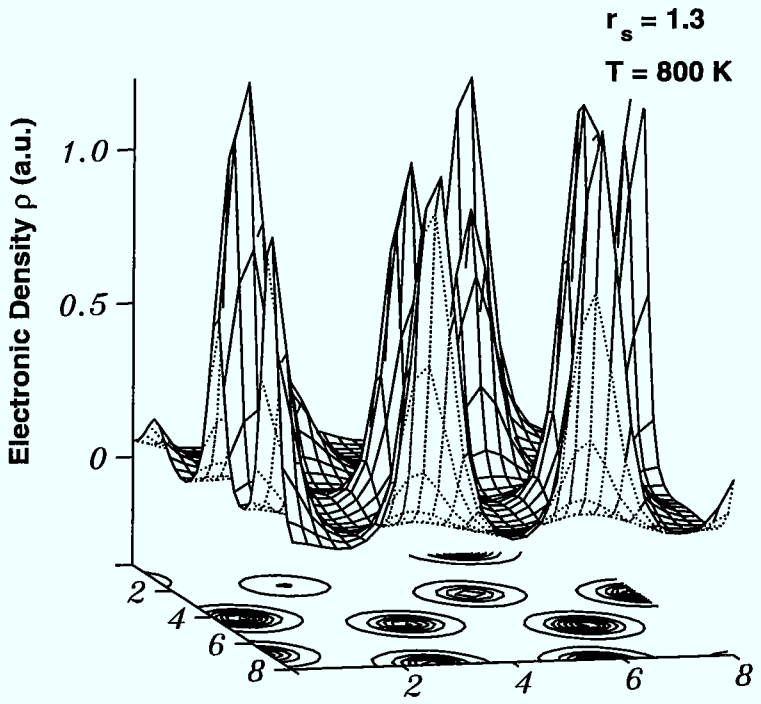

Figure 8.9: The charge density ρ in a plane for He at $r_s = 1.31$. The system is characterized by pronounced, clearly separated charge peaks at the positions of the atoms.

He atoms dominate. The overlap of the peaks is small. The base charge level, i.e., the (comparatively small) charge density in the valleys, is slightly higher at $r_s = 1.0$ with respect to $r_s = 1.31$, reflecting the higher average charge density. Figure 8.11 presents the charge density of the mixture close to a He atom. The He atom digs a charge hole around itself pushing away the H atoms. The tendency of the H atoms surrounding the He to come close to each other and form bonds is most evident for $r_s = 1.0$ where nearly a ring of H atoms around the He has formed. To conclude the presentation of the electronic properties the *electronic densities of state* (EDOS) are shown (figures 8.13 to 8.16). All EDOS are at $\vec{k} = \Gamma$ only. The purpose of figures 8.13 and 8.14, which present the EDOS of He is mainly to demonstrate that He is still a good insulator at these densities. There is a large gap at $r_s = 1.31$ separating the occupied and unoccupied states. At $r_s = 1.0$ the gap has shrunken, yet is still sizeable. The EDOS of the mixture (figures 8.15 and 8.16) should be compared with those of pure H (figures 7.22 and 7.24). The most important difference is that the peaks due to finite size splitting are broadened or even smeared out. This change indicates that there are lower, more tightly bound electron states due to the He atoms. As discussed in the previous chapter, in the

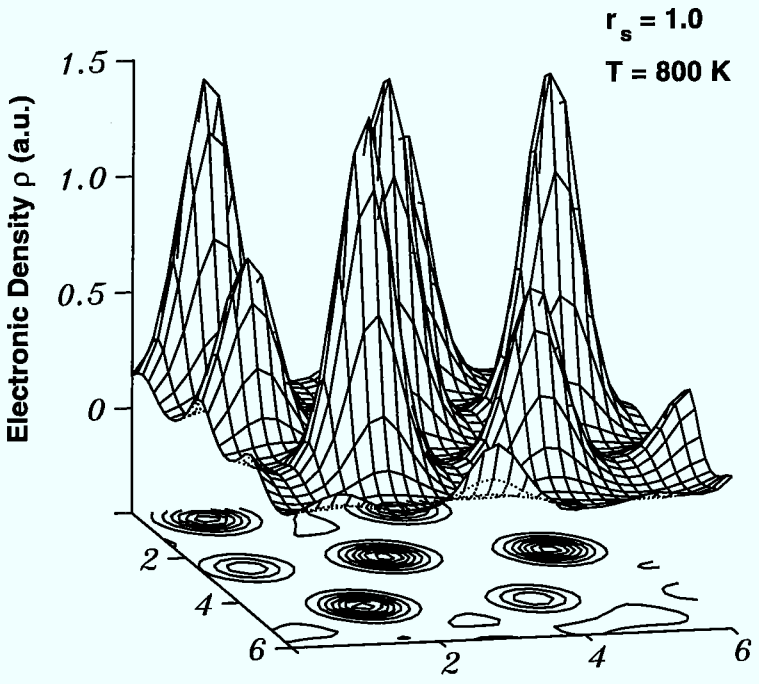

Figure 8.10: The charge densities ρ in a plane for He at $r_s = 1.0$. The situation changes only little from $r_s = 1.31$ to $r_s = 1.0$. The He atoms are characterized by pronounced charge peaks that fall off to nearly zero in the valleys between the atoms.

limit of infinite pressure the EDOS will coincide with the faint dotted lines, the eigenvalues of a homogeneous electron gas with periodic boundary conditions. At $r_s = 1.0$ and 3000 K the EDOS of H (figure 7.24) consists of slender peaks at the free electron levels. The conspicuous broadening in the EDOS of the mixture implies that the He insertion reduces the free-electron character considerably, i.e., leads to more tightly bound (and more localized) electron states.

As seen in the EDOS, the mixture is substantially different from the pure systems, H and He. He is the simplest case. Over the density range from $r_s = 1.31$ to $r_s = 1.0$ no major changes take place. The system is characterized by repulsive, hardly overlapping charge peaks, representing the He atoms. He is still a good insulator in this density range. The pressure ionization of the atoms and the metallization of He will occur only at higher pressures.

The behavior of the other pure system, H, is drastically different. Attractive forces and charge transfer prevail in H at $r_s = 1.31$ and 1.0 (see chapter 7). Therefore, it is not surprising that He alloying has a major effect on the H system. The properties of the mixture cannot simply be obtained by interpolating

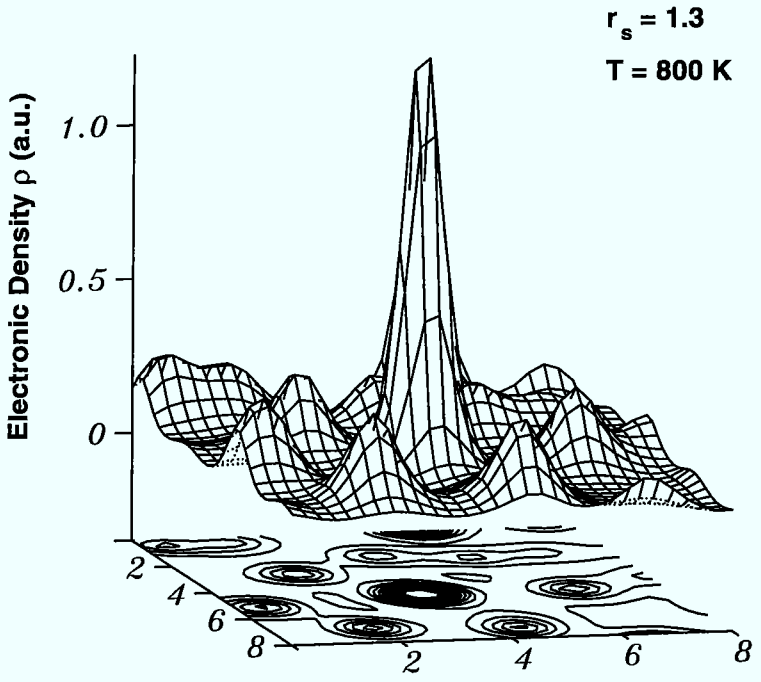

Figure 8.11: The charge densities ρ in a plane for a H-He mixture with a He contribution of $x = 0.1$. The density is $r_s = 1.3$. A He atom together with the surrounding H atoms are shown. he He digs a sizeable charge hole around it. The H atoms respond to the perturbation of the He atom by forming tight bonds.

between the pure systems. The pair-correlation functions show that H-He is not an ideal mixture. The density plots (figure 8.11 and 8.12) prove the He atoms to repel the surrounding H atoms. The H atoms close to He atoms tend to form tighter bonds. The EDOS of the mixture demonstrate the existence of more tightly bound states in comparison with H. The coexistence of low-lying He states and nearly free-electron like H states in astrophysical mixtures is the very reason why the system is difficult to treat. In the introductory chapter we argued that a perturbative treatment of screening is inadequate. As demonstrated in the preceding chapter, weak screening is even a bad approximation for pure H in a wide pressure range. Thus the He alloyed system completely eludes the scope of simple models. Therefore, many properties of the mixture under astrophysical conditions are precarious and require a better, more quantitative treatment. One of them is addressed in the following chapter, the demixing range of pressurized H-He mixtures.

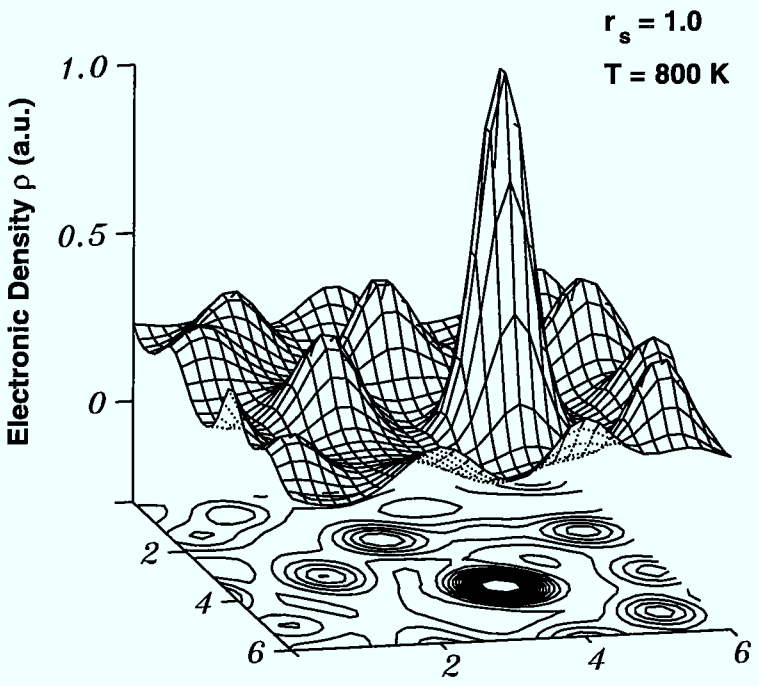

Figure 8.12: The charge densities ρ in a plane for a H-He mixture with a H-He contribution of $x = 0.1$. The density is $r_s = 1.0$. The H atoms have linked together to a ring around the He atom.

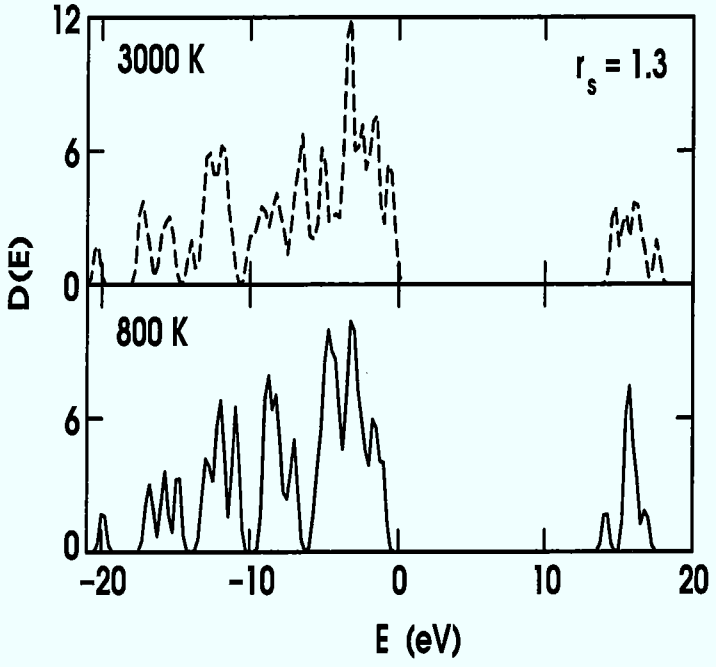

Figure 8.13: The electronic density of states $D(E)$ of He at $r_s = 1.31$ and temperatures of 800 K and 3000 K. There is a large gap between occupied and unoccupied states, indicating that He is a good insulator at this density and temperatures.

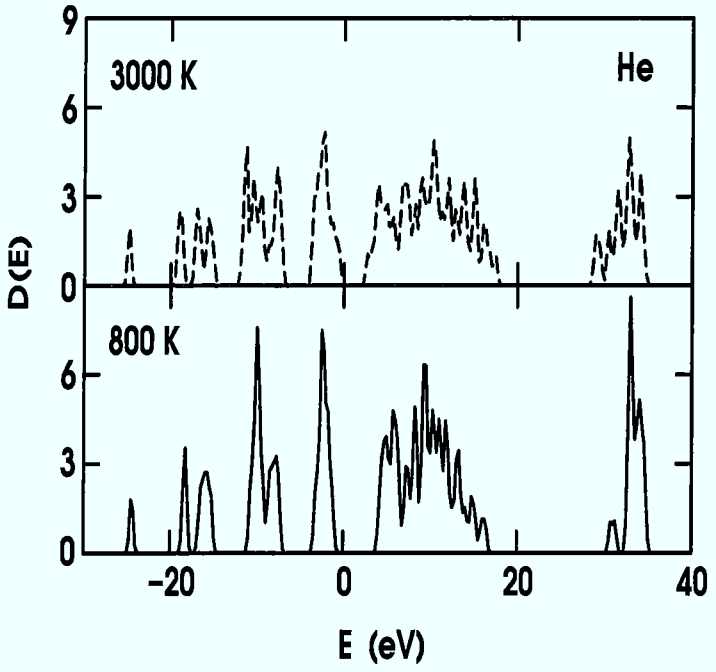

Figure 8.14: The electronic density of states $D(E)$ of He at $r_s = 1.0$ and temperatures of 800 K and 3000 K. The gap has shrunk in comparison with $r_s = 1.31$ but is still sizeable. He is an insulator for $r_s = 1.0$ and temperatures smaller or equal to 3000 K.

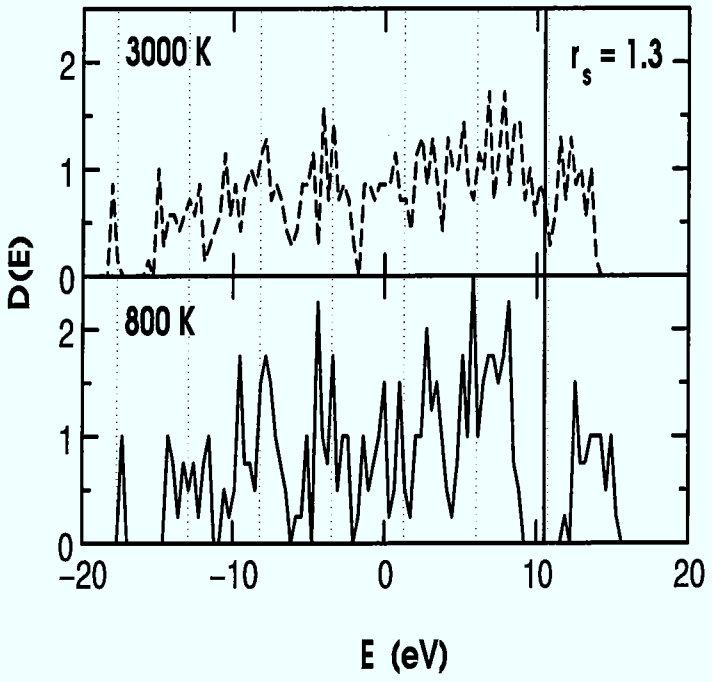

Figure 8.15: The electronic density of states $D(E)$ of the H-He mixture at $r_s = 1.31$ and temperatures of 800 K and 3000 K. The gap at 800 K is probably a finite-size effect as it is for H at the same density and temperature.

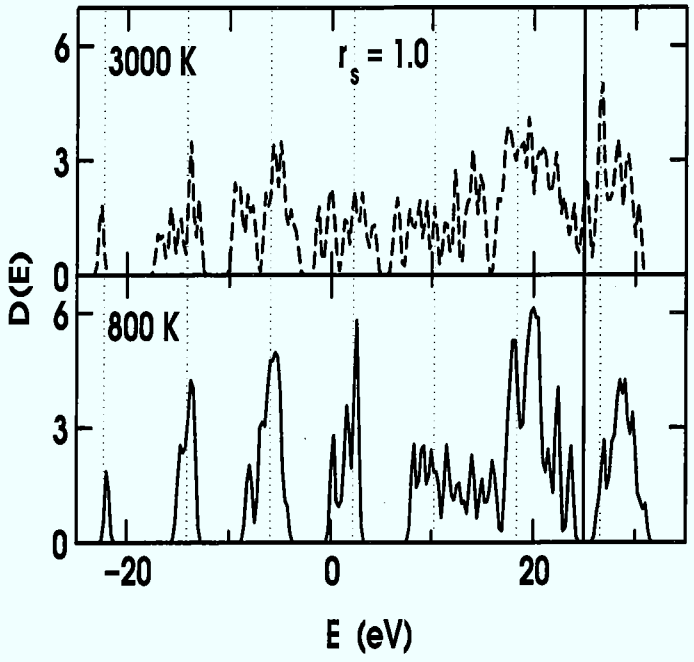

Figure 8.16: The electronic density of states $D(E)$ of the H-He mixture at $r_s = 1.0$ and temperatures of 800 K and 3000 K. It is interesting to compare with the EDOS of pure H (figure 7.24) at the same density. The EDOS of the mixture is significantly broadened with respect to the pure system owing to more tightly bound He levels.

Chapter 9

Demixing in the Giant Planets

The quantity that determines the mixing properties under isothermal, isobaric conditions in planetary interiors is the excess Gibbs free energy of mixing, defined by

$$\Delta G(x) = G(x) - xG(He) - (1-x)G(H), \tag{9.1}$$

where $G(H)$, $G(He)$, and $G(x)$ are the Gibbs free energies of pure H, He, and the mixture, respectively, computed for the same thermodynamical state. This quantity can be analysed in terms of internal energy $\Delta U(x)$, volume $P\Delta V(x)$, and entropy $T\Delta S(x)$ contributions, defined by relations analogous to equation 9.1 above. In the first part of this chapter we are mainly be concerned with $\Delta U(x)$. Since the additive volume law,

$$V(x) \approx xV(x=1) + (1-x)V(x=0) \tag{9.2}$$

is found by [99] and [82] to be satisfied within few per cent, one could jump to the assumption that this contribution was small. An estimate of this second term is given in the first section, too. It will be seen to be smaller than the internal energy contribution, but not negligible, because the pressure is very high. In the first part of this chapter only the ideal part of the entropy term $T\Delta S(x)$ is considered. We go beyond this approximation in the second section.

9.1 The Role of the Internal Energy

In this section we consider only the ideal part of the $T\Delta S(x)$ contribution, the configurational entropy

$$T\Delta S_{\text{con}}(x) = k_b T(x\log(x) + (1-x)\log(1-x)). \tag{9.3}$$

At first we also assume that the additive volume law holds exactly, i.e., $P\Delta V = 0$. Then the total energy term $\Delta U(x)$ determines the demixing temperature completely. We can obtain a first intuitive view by comparing the internal energy

of the mixed system with those of the two corresponding pure systems. At low pressures the constituents of the mixture, H_2, and He, interact via van-der-Waals forces. The induced dipole-dipole interaction is well-known to be weak. Therefore, the internal energy differences between the mixture and the pure systems should be small and the critical temperature for demixing cannot be high. Indeed, experiments prove the demixing temperature to be small at low pressure (below 50 K for P $\leq$ 1 kbar [167]). With increasing pressure H (and to a lower degree He) change in the way they interact. Finally, in the metallic regime the electronic wave functions of H are fairly delocalized and the charge density is enhanced along the bonds formed by H. However, as seen in figures 8.11 and 8.12, the He atoms are still characterized by pronounced charge peaks that push away the surrounding H atoms. Intuitively, one can imagine the effect of the He alloying to be the breaking of H next neighbor bonds. For example, let us assume H crystallizes in a bcc lattice. Then the replacement of one H atom by a He atom would break 8 H next neighbor bonds. This simple picture leads to two suggestions:

- The energy cost for breaking a covalent or metallic bond obviously is higher than the energy differences involved deep in the molecular regime where the H_2 molecules and He atoms behave similarly (i.e., the interactions have a van-der-Waals contribution). The individual charge peaks representing the molecules and atoms are less affected by their environment, because the overlap is small. Therefore, in the atomic regime of H we expect the demixing temperature to be higher.

- If the energy loss can be associated with the breaking of H-H bonds it will be reasonable to assume that the energy loss is the larger the more bonds are broken by the substituted He. For $r_s = 1.31$ our ground state structure for H was the string structure with a coordination number of 2. For $r_s = 1.2$ we found 4-fold coordinated structures to be preferred, and finally at $r_s = 1.0$ bcc was stable with a coordination number of 8. Thus we would expect the demixing temperature to rise according to the increased number of H-H bonds the He alloying is going to break.

The most accurate investigation of the electronic structure of H-He alloys so far was performed by Klepeis et al. [99], who considered ordered alloys crystallizing in a bcc and fcc lattice. In their band structure calculations on the lattices they demonstrated impressively how the He alloying changes the character of the energy bands in the metallic regime. In addition to the nearly free electron-like bands stemming from the H levels more tightly bound He bands appear. Thus their band structure computations corroborate the trend we found in our analysis of the EDOS in the previous chapter. They also applied their computations to estimate the demixing temperature, by combining the internal energy differences of the alloyed and pure lattices $\Delta U(x)$ with an estimate for the $P\Delta V(x)$ term

(small in their computations) and the ideal contribution for the entropy (equation 9.3). The result is a demixing temperature of $T_{\text{mix}} = 15000 \pm 2000$ K for a He contribution of $x = 0.07$ and a critical temperature of $T_c = 40000 \pm 12000$ K at a critical concentration of $x_c = 0.43$. They found the demixing temperature to be virtually constant between 5 and 10 Mbar. At higher pressures the demixing temperature decreases slowly. As discussed in the introductory chapter, their result represents the highest demixing temperature computed so far (roughly 5000 K higher than the OCP results). Two major approximations (and sources of uncertainty) are [99]

- the neglect of the influence of finite temperatures on ΔH. Klepeis et al. argue this restriction is less severe. The main contribution to ΔH comes from the electronic energy. Since the Fermi temperature is roughly a factor of 40 higher than the astrophysical temperatures of interest ($k_b T \approx 1$ eV compared with 40 eV) it is reasonable to assume the temperature dependence of ΔH to be weak for the temperatures of interest.

- The inclusion of only the ideal entropy of mixing neglects other contributions such as the vibrational or rotational entropy. This problem will be addressed in the next chapter.

We found another approximation of [99] to be more severe than both reported above: Geometrical effects play a crucial role. In terms of the simple picture of broken H-H bonds one limitation is the restriction to bcc and fcc lattices. As demonstrated in chapter 6, the coordination number increases from 1 to 8, the bcc lattice being only stable at pressures higher than about $\sim$ 10 Mbar [16, 14, 128]. Thus we expect the demixing temperature to rise in the pressure range of 5 to 10 Mbar instead of being constant. Another shortcoming is much more crucial. The He insertion will distort the H lattice. As can be seen from the pair correlation functions (figure 8.2), the average H-He distance is significantly larger than the average H-H distance. The He atoms push away the surrounding H atoms, and the H atoms tend to form tight bonds around the He atoms (figures 8.3 and 8.11). The change of the geometrical arrangement (and of the electronic structure) can be viewed to counteract the perturbation caused by the He insertion. This phenomenon will be referred to as "ionic relaxation effects". It is obvious that the ionic relaxation effects increase the stability of the mixture, i.e., the results of Klepeis et al. represent an upper bound. The effect of relaxation is demonstrated in figure 9.1. The pure H system at $r_s = 1.0$ is alloyed with roughly 10 % and relaxed. The He insertion completely destroys the lattice order and leads to the formation of pairs and strings of H atoms.
In the following our computations for $r_s = 1.31$, 1.2, and 1.0 are described. We started with the ground state structures of H discussed in chapter 6. For $r_s = 1.0$ the simulation was performed with 250 atoms. At the lower densities the unit cell contained 128 atoms. We randomly selected next neighbor pairs of H

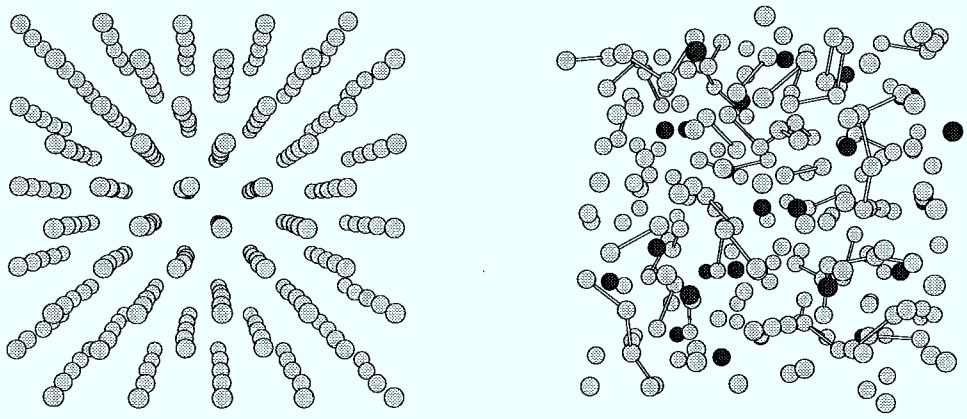

Figure 9.1: The effect of relaxation at $r_s = 1.0$. The pure H system (H_{250}) is alloyed with about 10% He (H_{202}-He_{24}). Bonds are drawn for distances up to 85 % of the next neighbor distance in the bcc lattice. The relaxation leads to disorder and the aggregation of H atoms to pairs and strings.

and substituted them with He atoms. Random pairs were chosen to simulate the geometries of the mixture with the highest configurational entropy, presumably the most relevant ones under planetary interior conditions. We continued with locally relaxing the H-He geometry.[1]We computed the excess internal energy for a He contribution of $x = 0.1$, 0.23, 0.39, and 0.6. We found that an accurate interpolation of the simulated results can be given by the purely density dependent form $\Delta U(x) = 1.63x(1-x)/r_s^3$ eV/atom, valid for all the densities $r_s = 1.31$, 1.2, and 1.0. In figure 9.2 the results for $\Delta U(x)$ are shown. The solid lines are the interpolations of internal energy differences at $r_s = 1.31$ (solid circles), 1.2 (open circles), and 1.0 (squares). The dashed line corresponds to an interpolation of the unrelaxed internal energy differences at $r_s = 1.0$. The effect of relaxation is dramatic. We performed static computations on the pure systems and one mixed

[1]To improve the speed of relaxation we applied a small technical trick. Although it is only a small change and trivial to implement it is worth saying a few words about it, because it proved to be very helpful. We performed MD runs and quenched the system for $(d/dt)\,E(t) = \sum_{\vec{R}_I} \vec{F}_{\vec{R}_I} \cdot \vec{V}_I = 0$. In the multidimensional space of the $\{\vec{R}_I(t)\}$ the quench corresponds to a minimization in the direction where the $\{\vec{R}_I(t)\}$ vary most, i.e., the direction of the gradient. The forces computed after the quench at time $t + \Delta t$ are orthogonal to the previous direction of minimization and again represent the direction of the most rapid change in the subspace orthogonal to the previous gradient. After the quench the evolution to the next point where $(d/dt)\,E(t) = 0$ starts slowly, because the velocities are zero after the quench and it takes some time until the system picks up speed again. Therefore, we scaled the velocities at the first step after quenching $(t + \Delta t)$ to a temperature $T(t + \Delta t) = \alpha T(t)$, where $T(t)$ is the temperature after the quench. Obviously, α has to be smaller than 1 for the method to converge. In practice $\alpha = 2/3$ allowed us to perform local relaxation in 100-300 MD steps.

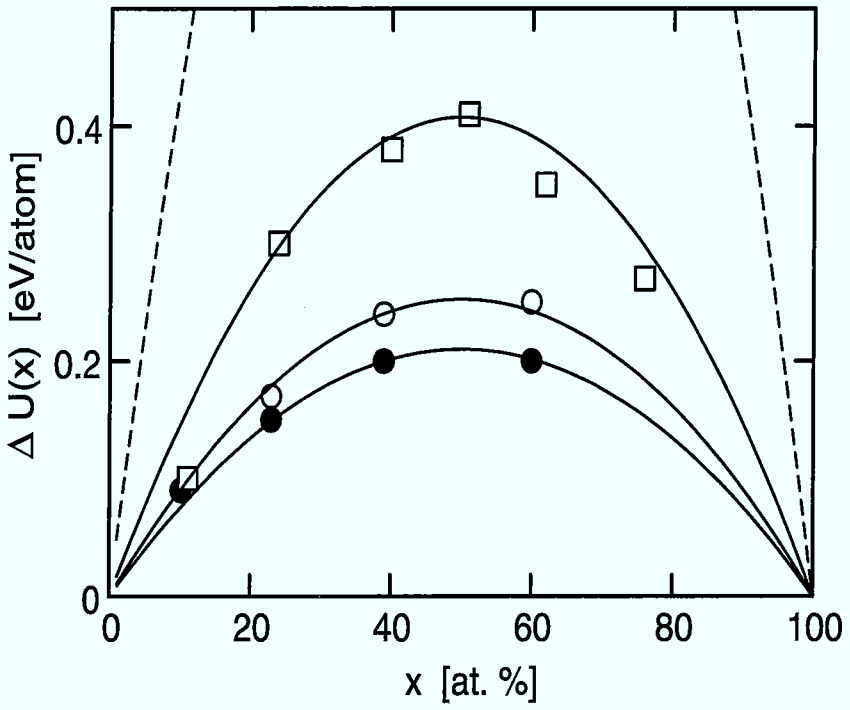

Figure 9.2: The excess internal energy differences $\Delta U(x)$ at $r_s = 1.31$ (solid circles), $r_s = 1.2$ (open circles), and $r_s = 1.0$ (squares) as a function of the He contribution x. The data were interpolated by the simple interpolation formula $\Delta U(x) = 1.63x(1-x)/r_s^3$ eV/atom (solid lines). The dashed line is the interpolation for the unrelaxed internal energy differences at $r_s = 1.0$. Obviously relaxation plays a major role for a quantitative calculation of demixing.

configuration ($x = 0.39$) to estimate the $P\Delta V(x)$ term. It contributes about 25 % to the total $\Delta H(x)$. Then we added the ideal entropy part (equation 9.3) and constructed the demixing curves via a double tangent construction. The construction is illustrated schematically in figure 9.3 for $r_s = 1.31$. The solid curves represent the Gibbs excess energy (in eV/atom) as a function of concentration and temperature. For a given temperature $T < T_c$, there is a concentration regime in which the Gibbs energy isotherm is concave downward, so that a straight line (dashed) may be drawn tangent to the curve at two points. The solubility limits $x_1(T)$ and $x_2(T)$ are the abscissae of the two points of tangency. When T is increased x_1 and x_2 move closer together, until at $T = T_c$ they coincide in x_c. For $T > T_c$, the isotherms are concave downward at all x, the tangent construction is impossible, and the mixture is stable against separation at any concentration. The inversion of $x_1(T)$ and $x_2(T)$ renders the demixing curves. In figure 9.4 the resulting demixing curves are presented for pressures of 4, 10, and 24 Mbar

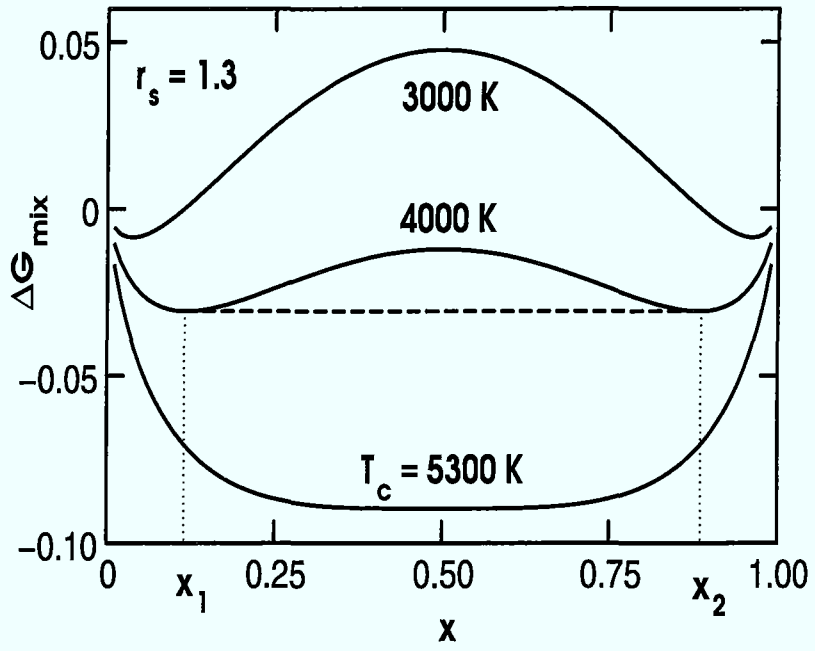

Figure 9.3: Excess Gibbs free energy differences ΔG_{mix} as a function of temperature and concentration at $r_s = 1.31$. The dashed line is drawn tangent to the isotherm at two concentrations that represent the solubility limits (x_1 and x_2) of the H-He mixture at the corresponding temperature. The curve for 4000 K corresponds to an astrophysical He contribution of $x = 0.1$ and the bottom curve to the critical composition of $x_c = 0.5$. $T(x_1)$, $T(x_2)$, and $T(x_c)$ are three points used to construct the bottom curve in figure 9.4.

(solid lines). The dashed curves are the DFT/LDA computations of Klepeis et al. [99] and the dotted curve is an OCP result (from [99]), both at about 10 Mbar. Clearly, the ionic relaxation plays a dominant role, the static computations of Klepeis et al. overestimate the demixing temperature significantly. The OCP result is surprisingly close to our DFT/LDA curve at 10 Mbar.
To decide if phase separation is an ongoing process in Saturn or even in both giant planets the demixing temperatures have to compared with models of the interior of Jupiter and Saturn. In the introductory chapter a crude approximation to the adiabats describing the giant planets has been presented. We used it to estimate a critical temperature of 9000 K for Saturn and 10500 K for Jupiter at about 3 Mbar. For an astrophysical mixture of about 10 % He the demixing temperatures are roughly 4000 K for 3.5 Mbar, 6000 K for 10 Mbar, and 8500 K for 24 Mbar (figure 9.4). Judging from Stevenson's data our demixing temperatures

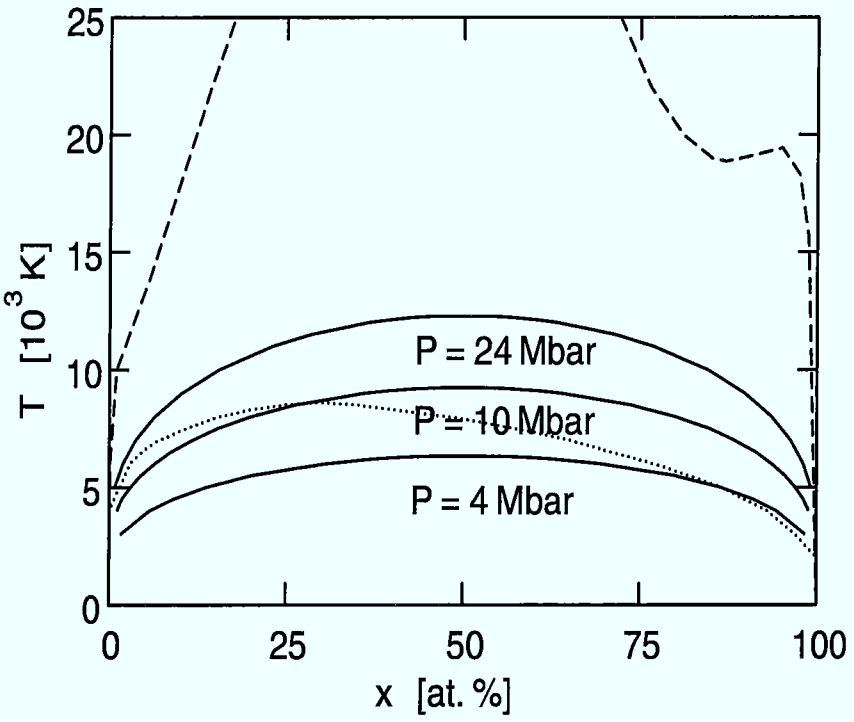

Figure 9.4: Demixing temperature T (in K) as a function of the He concentration x. The solid lines represent the present DFT/LDA calculations at 3.5, 10, and 24 Mbar. The dashed line is the result form the static DFT/LDA calculations of Klepeis et al. [99] and the dotted line is computed via OCP [99]. Both were computed for a pressure of 10 Mbar.

are too low by a factor of 2 for phase separation to be relevant in Jupiter and Saturn. However, the early models for the interiors of the giant planets tend to overestimate the internal temperatures significantly, because they fail to account for the energy that goes into the dissociation of the H molecules and thus lowers the internal temperatures. Saumon and Chabrier [162] developed a model for the Helmholtz free energy of fluid H at high density where they tried to include properly the effect of both pressure and temperature dissociation and ionization of H. They used this Helmholtz free energy to model the interior of the giant planets [33, 163]. The adiabats presented in [33] provide interior temperatures of about 6300 K and 7900 K at 3.5 Mbar and 10000 K and 12600 K at 10 Mbar for Saturn and Jupiter, considerably lower than Stevenson's model but still too high for demixing to occur in both planets. However, Nellis, Ross, and Holmes [134] demonstrated in recent shock compression experiments that Saumon and Chabrier's model still overestimates considerably the measured shock temperatures. Furthermore, their model fails to represent qualitative features of the

process of pressure dissociation. In contradiction to the model of [162], [134] find the pressure dissociation of the H molecules to be a continuous process starting at about 20 GPa. Holmes, Ross, and Nellis [76] developed a new model for H that agrees with the measured shock temperatures. They predict the energy going into the dissociation of the molecules to be higher than hitherto assumed and the temperature in the molecular envelope to be substantially lower [134]. They computed an adiabat for pure H starting at 165 K and 1 bar (surface parameters of Jupiter) and found it to deviate from the pure H adiabats of Saumon and Chabrier [33] in the density range where the dissociation process begins. At 180 GPa, the highest pressure they regarded, the predicted temperature is about 25 % lower. A decrease of the internal temperatures by 25 % at 3.5 Mbar (4700 K instead of 6300 K for Saturn and 5900 K instead of 7900 K for Jupiter) would move the internal temperatures close to our results. So far their new model has not been applied to develop complete models for the interiors of the giant planets and the final solution of the problem awaits further, more refined investigations. An improvement on the computation of demixing is attempted in the next chapter where non-ideal contributions of the entropy are included.

9.2 Free Energy Calculation

We apply a technique derived from classical MD to compute the Helmholtz free energy, the overlapping distribution method or "umbrella sampling". As the method is described well in [53, 54], we deal with the theoretical part only briefly. The starting point for computing free energy differences in an isothermal ensemble is the partition function of the system

$$Q(N,V,T) = \frac{q^N(T)}{N!} \int_0^L \ldots \int_0^L d\vec{q}^N \exp(-\beta U(\vec{q}^N)), \tag{9.4}$$

which is conveniently written with scaled coordinates $\vec{s}$:

$$Q(N,V,T) = \frac{(q(T)V)^N}{N!} \int_0^1 \ldots \int_0^1 d\vec{s}^N \exp(-\beta U(\vec{s}^N)). \tag{9.5}$$

The expression for the Helmholtz free energy is

$$\begin{aligned} F(N,V,T) &= -k_b T \ln Q \\ &= -k_b T \ln\left(\frac{(q(T)V)^N}{N!}\right) - k_b T \ln\left(\int d\vec{s}^N \exp\left[-\beta U(\vec{s}^N)\right]\right) \\ &= F_{\mathrm{id}}(N,V,T) + F_{\mathrm{ex}}(N,V,T). \end{aligned} \tag{9.6}$$

In the last line the free energy was written as a sum of the ideal gas expression plus an excess part. The free-energy difference between two systems 1 and 0 is given by

$$F_1 - F_0 = \Delta F_{10} = -k_b T \ln(Q_1/Q_0). \tag{9.7}$$

With the help of equation 9.6 the excess term of ΔF_{10} can be expressed as the logarithm of the expectation value of $\exp[-\beta\Delta U]$:

$$\begin{aligned}\Delta F_{10} &= \Delta F_{10,\mathrm{id}} - k_b T \ln\left(\frac{\int \exp[-\beta(U_0+\Delta U)]d\vec{q}^N}{\int \exp[-\beta U_0]d\vec{q}^N}\right) \\ &= \Delta F_{10,\mathrm{id}} + k_b T \left\langle \exp[-\beta\Delta U]\right\rangle_0 \end{aligned} \tag{9.8}$$

or

$$\Delta F_{10,\mathrm{ex}} = -k_b T \ln \left\langle \exp[-\beta\Delta U]\right\rangle_0 . \tag{9.9}$$

Equation 9.9 allows to compute free energy differences of two systems 1 and 0 without performing explicit simulations on both of these systems. The central quantities are the internal energy differences ΔU for several configurations of the reference system 0. For the other system 1 only the internal energy at the configurations of the reference system has to be computed. For our practical application of the scheme presented below three points are important:

- For the method to work it is important that internal energy differences ΔU are reasonably small (i.e. not much larger than $k_b T$). Otherwise, the statistical error in $\left\langle \exp[-\beta\Delta U]\right\rangle_0$ would be too large for a reliable computation. Therefore, the system investigated should not be very different. This criterion is satisfied in our computations where the pure H system is perturbed by a small amount of He (10 %).

- For mixtures the difference in the ideal part of the free energy, defined in equation 9.6, is (in general) not equal zero. This part leads to the ideal (configurational) part of the entropy (equation 9.3) which has to be added to the excess term. In the following presentation and discussion of our quantities the ideal part is left out. It plays the same role as in the previous section and can be added trivially.

- As will be seen below, we keep the number of electrons fixed instead of the number of particles. This procedure is reasonable, because the main internal energy differences stem from the change in the electronic structure (and because it simplifies the relaxation of the electronic structure after the substitutions). The change of the number of particles does not affect the validity of formula 9.9. In 9.8 the derivation assumes identical dimensions of the configuration space. Formally, this is achieved by the transformation

$$\begin{aligned} U_{\mathrm{mix}}(x_1,...,x_{N_{\mathrm{H}}+N_{\mathrm{He}}}) &= \int dx_{N_{\mathrm{H}}+N_{\mathrm{He}}+1}... \int dx_{N_{\mathrm{H}}+2N_{\mathrm{He}}} U_{\mathrm{mix}}(x_1,...,x_{N_{\mathrm{H}}+N_{\mathrm{He}}}) \\ &\cdot\ \delta\left(x_{N_{\mathrm{H}}+1}, x_{N_{\mathrm{H}}+N_{\mathrm{He}}+1}\right)...\delta\left(x_{N_{\mathrm{H}}+N_{\mathrm{He}}}, x_{N_{\mathrm{H}}+2N_{\mathrm{He}}}\right) \\ &\equiv \int dx_1... \int dx_{N_{\mathrm{H}}+2N_{\mathrm{He}}} U'(x_1,...,x_{N_{\mathrm{H}}+2N_{\mathrm{He}}}), \end{aligned} \tag{9.10}$$

where N_H is the number of H atoms and N_{He} is the number of He atoms in the mixture. The only difference to substitutions where the number of particles is conserved is that we cannot refer the internal energy differences to the number of particles. Instead we consider the energy per electronic state. Thus our results for the free energy differences F_{mix} - F_H are obtained in units of energy per electronic state. For the computation of the excess free energy of mixing we change the picture. We construct F_H by thermodynamical integration (see below). Then we add F_H (in energy per electronic state) to F_{mix} - F_H to obtain F_{mix}. For F_{mix} the unit is converted to energy per particle and in constructing ΔF_{mix} all quantities are referred to energy per particle.

We performed umbrella sampling for $r_s = 1.31$ at temperatures of 800 K and 3000 K and for $r_s = 1.0$ at 800 K. After a certain number of steps of molecular dynamics for the H system (we reduced the number from 200 to 100 for the lower temperatures and to 50 for the simulation at 3000 K) we chose randomly 12 next neighbor pairs of H and replaced them by He atoms. Then we converged the electronic structure and computed the internal energy difference U_{mix} - U_H. The internal energy differences were used in formula 9.9 to obtain the excess part of the free energy difference of the mixture and pure H. The number of samples was 130 for $r_s = 1.31$ and $T = 800$ K, 320 for $r_s = 1.31$ and $T = 3000$ K, and 140 for $r_s = 1.0$ and 800 K. The statistical average was more difficult to converge for $T = 3000$ K than for $T = 800$ K because of the larger Boltzmann factor k_bT in equation 9.9. The evolution of the value for the free energy differences ΔF_{ex} together with the statistical error as a function of the number of samples is shown in figure 9.5. It demonstrates that the method is reasonably converged for the final number of samples. Below we discuss that the statistical error is not the main source for uncertainty. In table 9.1 the result is shown. For convenience we present F_{mix} instead of $F_{mix} - F_H$ provided by formula 9.9. The excess free energy of mixing is

$$\Delta F_{mix} = F_{mix} - xF_{He} - (1-x)F_H, \tag{9.11}$$

where F_{mix} is the free energy of the mixture, F_{He} the free energy of the pure He system, F_H the free energy of the pure H system, and x the percentage of He in the mixture. To compute ΔF_{mix} it is necessary to know the free energies of the pure systems F_H and F_{He}. The internal energies $U_H(T)$ and $U_{He}(T)$ are obtained from the simulations of the pure systems at 800 K and 3000 K (we took the averages over the trajectories). The entropies are constructed by thermodynamical integration. From the fit to the internal energies (figures 7.9, 7.10, 8.6, and 8.7) the specific heat $C_v^H(T)$ and $C_v^{He}(T)$ are obtained as functions of temperature. Then the entropy can be computed via

$$S(T) - S(T_0) = \int_{T_0}^{T} \frac{C_v(T')}{T'} dT'. \tag{9.12}$$

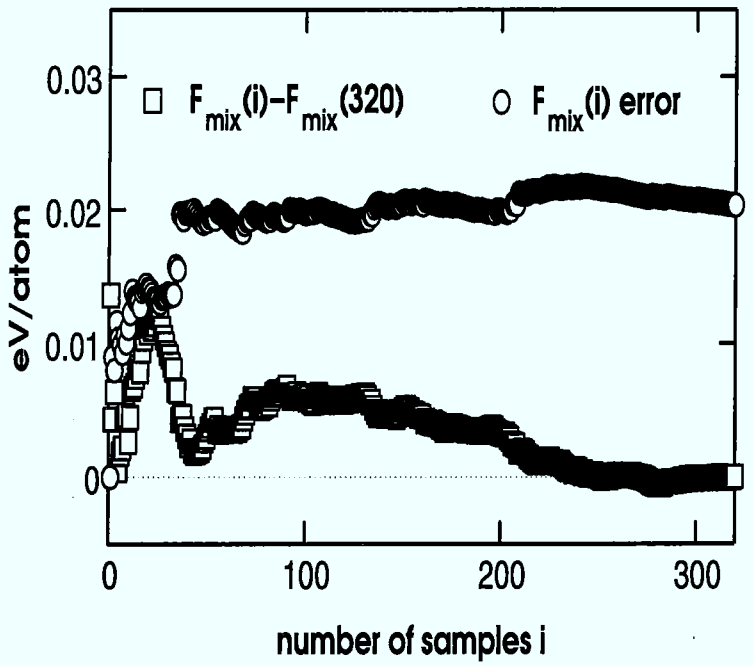

Figure 9.5: The evolution of the result for F_{mix} for $r_s = 1.31$ and 3000 K as a function of the number of samples normalized to the final result obtained with 320 samples (squares). The corresponding statistical error is represented by circles.

The results are summed up in table 9.1. Combining these data with the umbrella sampling results for F_{mix} we obtain the excess free energies of mixing ΔF_{mix} (table 9.2). Since ΔF_{mix} does include neither the ideal contribution nor a PV term, the results for ΔF_{mix} have to be compared with the zero temperature internal energy difference ΔU of the previous section. Using the simple interpolation formula $\Delta U(x) = 1.63x(1-x)/r_s^3$ eV/atom we find (for $x = 12/116 \approx 0.1$) $\Delta U(x) = 0.07$ eV/atom for $r_s = 1.31$ and 0.15 eV/atom for $r_s = 1.0$. Thus the umbrella sampling leads to two conclusions:

- The free energy differences computed via umbrella sampling are higher than the zero temperature estimates of the previous chapter.
- For higher temperatures the larger excess free energy is partly compensated by an increase of the non-ideal excess entropy.

From 800 K to 3000 K ΔF_{mix} is lowered by 0.05 eV/atom from 0.17 eV/atom to 0.12 eV/atom. If we assume the decrease to be the same between 3000 K and 5000 K, at about 5000 K ΔF_{mix} will be close to the value of $\Delta U(x)$, 0.07

Table 9.1: The free energies F_{H} and F_{He} of pure H and He at $r_s = 1.31$ and 800 K and 3000 K, and at $r_s = 1.0$ and 800 K constructed by thermodynamical integration. All quantities are in eV/atom.

	U_{H}	U_{He}	$S_{\mathrm{H}}\,T$	$S_{\mathrm{He}}\,T$	F_{H}	F_{He}
$r_s = 1.31$, 800 K	-13.79	-73.29	0.10	0.09	-13.89	-73.38
$r_s = 1.31$, 3000 K	-13.52	-72.91	0.92	1.02	-14.44	-73.92
$r_s = 1.0$, 800 K	-9.51	-67.87	0.10	0.12	-9.60	-67.99

Table 9.2: The free energy of the mixture F_{mix} and the excess free energy ΔF_{mix}. In addition the excess internal energy ΔU_{mix} obtained from zero-temperature substitutions (previous section) and the statistical error from umbrella sampling Δ are shown. The unit of all quantities is eV/atom.

	F_{mix}	ΔF_{mix}	ΔU_{mix}	Δ
$r_s = 1.31$, 800 K	-19.87	0.17	0.07	0.02
$r_s = 1.31$, 3000 K	-20.48	0.12		0.02
$r_s = 1.0$, 800 K	-15.38	0.26	0.15	0.02

eV/atom. As seen in the previous section for $r_s = 1.31$, the ideal part balances the $\Delta U(x)$ (or ΔF_{mix}) at 4000 K. Thus the umbrella sampling suggests the demixing temperature to be a little bit higher.
In order to check the results obtained by umbrella sampling we used the same thermodynamical integration as for the pure systems to construct the internal energy differences, i.e., we fitted the average internal energies to a finite size broadened specific heat (formula 9.12). For $r_s = 1.31$ the fit is shown in figure 9.6. Unfortunately, the fit to the mixture is poor in this respect that qualitatively different fits are possible within the statistical error bars. (For $r_s = 1.0$ the fit for the mixture is much worse than for $r_s = 1.31$. Therefore, we abstained from thermodynamical integration of the H-He results at the higher density.) In figure 9.7 the results for the free energy differences obtained via thermodynamical integration (solid line) are compared with the results from umbrella sampling (diamonds). The dashed line are results from a slightly different fit (the melting

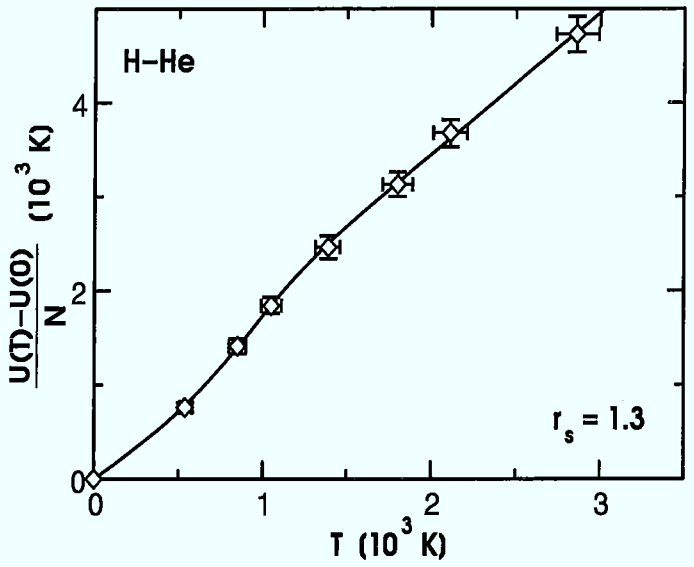

Figure 9.6: Fit of the internal energies $U(T)$ of a H-He mixture at $r_s = 1.31$ and $x_{\mathrm{He}} = 0.1$. The fit formula was chosen to give a (finite-size) broadened discontinuity in the specific heat. Statistical error bars were added. The fit gives a melting temperature of 850 K.

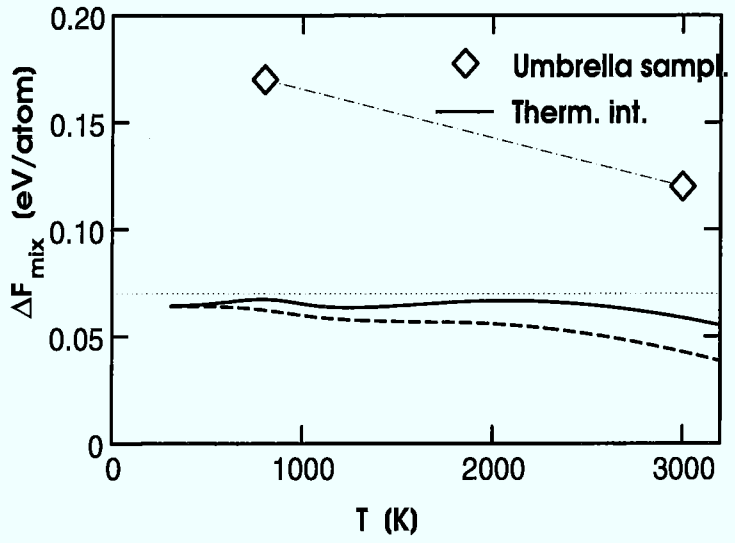

Figure 9.7: The excess free energies of mixing ΔF_{mix} computed via thermodynamical integration (solid line) compared with the results obtained from umbrella sampling (diamonds). The dashed line was produced from a slightly different fit to the internal energies of the H-He mixture. The zero temperature result is represented by a faint dotted line.

temperatures given by the fits differ only by 15 K). It can be seen from figure 9.7 that

- umbrella sampling gives considerably higher excess free energy differences than thermodynamical integration and
- the dependence of the results on the fit to the internal energies is strong.

On the one hand the uncertainties in the procedure of fitting the internal energies are large, on the other the computed quantities (excess free energy differences) are small. In addition to the poor fit for the mixture the errors in the other integrations (especially for H) are considerable, too. Since the free energies computed via thermodynamical integration were also used to extract the excess free energy for the umbrella sampling the systematical errors from the integration pervade all our finite temperature results. Therefore, we believe the zero temperature estimations of the last section (which are represented by the faint dotted line in figure 9.7) to be our best estimate of the demixing temperature.

Chapter 10

Electronic Conductivities of Hydrogen under High Pressures

In several respects the computations of electronic conductivities complements the investigation of the electronic structure of H in chapter 7. The changes of the electronic properties induced by the variation of pressure and temperature is reflected in the value of the conductivities. For example, the increase of the conductivities with pressure corresponds to the reduction of the electron-ion coupling (see the argumentation below). The conductivities can be used to determine the conditions under which high pressure H metallizes. For the physics of the giant planets this transport coefficient plays an important role. The electronic conductivities are needed as an input to models of the external magnetic fields of Jupiter and Saturn, caused by convective dynamo motion of conducting fluid H at pressures up to few 100 GPa and temperatures up to several 1000 K (see, e.g., [97]).
For the computation of the conductivities we used the trajectories that we generated by ab initio MD runs for different pressures ($r_s = 1.5$, 1.31, 1.0, and 0.5) and different temperatures (800 K - 10000 K). From these trajectories we extracted instantaneous configurations for our conductivity calculations. For these configurations we computed the electronic structure and applied the formula of Kubo and Greenwood for a discrete eigenvalue spectrum

$$\sigma(\omega) = \frac{2\pi}{\Omega}\frac{1}{\Delta\omega}\sum_i\sum_f \frac{|\langle E_i|\partial_x|E_f\rangle|^2}{E_f - E_i}, \tag{10.1}$$

where Ω is the sample volume. The physical idea behind the formula is to relate the conductivity to the probability that an electron is excited by the external field from its initial state E_i to a former unoccupied ("final") state E_f. (see appendix A). The sum goes over all pairs of (initially) occupied and unoccupied states $\{E_i, E_f\}$ with $|E_f - E_i| < \Delta\omega$. This formula can be easily derived from equation (3.87) in [68] by inserting the Fermi distribution at $T = 0$ and averaging over

a frequency interval $\Delta\omega$ to smear out the delta function. A different derivation and more details are given in appendix A.
In our computations the electrons are in their ground state, leading to occupation numbers of $f = 2$ for occupied and $f = 0$ for unoccupied states. This assumption is justified with regard to the much higher Fermi temperature increasing from $\sim 2.5 \cdot 10^5$ K at $r_s = 1.5$ to $\sim 2.3 \cdot 10^6$ K at $r_s = 0.5$. Our unit cell contained 96 atoms for the simulations for $r_s = 1.5$, 128 atoms for $r_s = 1.31$, and $r_s = 1.0$ and 250 atoms for $r_s = 0.5$. $\vec{k}$-space sampling was restricted to the Γ-point, leading to 48, 64 and 125 occupied states, respectively. We added 12 unoccupied states for $r_s = 1.5 - 1.0$ and 25 for $r_s = 0.5$. In the Kubo-Greenwood formula we included pairs of occupied and unoccupied eigenvalues with $|E_f - E_i| < \Delta\omega$. For a chosen frequency interval $\Delta\omega$ the formula provides an approximation for the ac conductivity at the frequency $\omega = \Delta\omega/2$. In practice the method is restricted to a finite range of frequencies. As soon as only very few energy pairs are included the averaging over the interval $\Delta\omega$ becomes unreliable. On the other hand the formula ceases to be a good approximation when $\Delta\omega$ exceeds the energy differences between the highest occupied and highest unoccupied orbital in our calculation. In the frequency range where our approach is reliable we find the conductivity either to decline (especially for $r_s = 1.5$) or to rise nearly monotonically as a function of ω. To calculate DC conductivity we extrapolate the results for finite ω to zero frequency. For most cases we used a second degree polynomial, for some cases a first degree polynomial proved to be more reliable. In figure 10.1 an example for a fit for $r_s = 1.5$ and $T = 2000$ K is given. In some cases the frequency range across which we extrapolate the conductivities is not small ($\leq$ 1eV). The corresponding error is discussed at the end of this section. In table 10.1 the computed conductivities for H are presented. At $r_s = 1.5$ the

Table 10.1: DC conductivities σ in $10^5/(\Omega\text{cm})$. At $r_s = 1.5$ the temperature was 2000 K instead of 2200 K. The experimental result at $r_s = 1.5$ and 3000 K was taken from [195]

.

T (K)	r_s=1.5	r_s=1.31	r_s=1.0	r_s=0.5
1500	0.0005	0	0	
2200	0.022	0.032	0.22	
3000	0.030 (expt. 0.02)	0.22	0.56	
6000				18
8000				14
10000				10

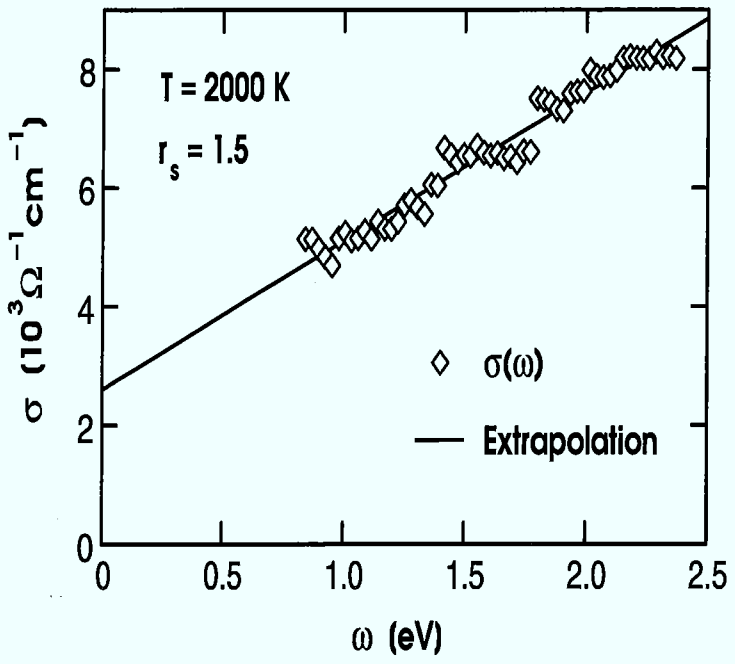

Figure 10.1: An example ($r_s = 1.5$ and T = 2000 K) for the extrapolation of the conductivity to $\omega = 0$.

conductivity increases by two orders of magnitude between 1500 K and 2000 K. In chapter 7 we discussed the structural changes of the system at $r_s = 1.5$ as a function of temperature. In figure 7.2 the pair correlation function was shown for 800 K and 3000 K. At low temperature the system is still molecular whereas at 3000 K a major part of the molecules have dissociated. The structural change can also be seen in the ion-electron pair-correlation functions g^1_{ie} (figure 7.12). It is accompanied by the closing of the band gap in the electronic structure (figure 7.21). The band gap closure signalizes metallization of the system, which is quantitatively confirmed by the strong increase in the conductivity. Weir, Mitchell, and Nellis [195] investigated the metallization of fluid H in the pressure range from 93-180 GPa and 2200-4400 K by shock compression experiments. They reported a sharp resistivity decrease from about 1 Ω-cm at $P = 93$ GPa to $5{\cdot}10^{-4}$Ω-cm at 140 GPa. Between 140 and 180 GPa the resistivity remained constant at about $5{\cdot}\ 10^{-4}$ Ω-cm. They concluded that fluid hydrogen metallizes at about 140 GPa and 3000 K through a continuous transition from a semiconducting to metallic fluid. Our results agree with the experiments of [195]. Metallization occurs below 3000 K. We predict the metallization temperature at $r_s = 1.5$ (155 GPa) to lie between 1500 K and 3000 K. The resistivity of $5{\cdot}\ 10^{-4}$ Ω-cm corresponds to a

conductivity of $0.02 \cdot 10^5 \Omega^{-1}\text{cm}^{-1}$ compared with our theoretical values of $0.022 \cdot 10^5 \Omega^{-1}\text{cm}^{-1}$ at 2000 K and $0.030 \cdot 10^5 \Omega^{-1}\text{cm}^{-1}$ at 3000 K. Weir, Mitchell, and Nellis claim the error bars on their experiments to be mostly about 25%, some are up to 50%. Our error bars are larger (see below).
At $r_s = 1.31$ the results of table 10.1 indicate metallization to occur in the same temperature range as for $r_s = 1.5$. Unfortunately that is an artifact of the poor EDOS. As discussed in chapter 7, finite-size effects lead to a gap in the EDOS at low temperatures (see figures 7.22 and 7.23). This spurious gap enters in the denominator of formula 10.1 and causes the conductivity to go to zero. To check the error induced by the poor EDOS we recomputed the conductivities at the Baldereschi-point $\vec{k} = (1/4,1/4,1/4)$ [11] that provides a better $\vec{k}$-space representation than the Γ-point (table 10.2). At low temperatures finite-size effects are

Table 10.2: Conductivities σ in $10^5/(\Omega\text{cm})$ computed with poor (Γ-point) and improved (Baldereschi-point) $\vec{k}$-space sampling at $r_s = 1.31$ and 1500 K and 3000 K.

T	B-point	Γ-point
1500	0.30	0
3000	0.33	0.22

responsible for the zero conductivity, i.e., the system is metallic for 1500 K and $r_s = 1.31$. The conductivities at 1500 K and 3000 K are virtually equal, and the conductivity values can be expected to decrease at higher temperatures as an effect of increased scattering. The comparison shows that the Γ-point value at 3000 K is a good estimate.
At $T = 3000$ K the metallic character of the H sample increases from $r_s = 1.5$ to $r_s = 1.31$ by roughly one order of magnitude (from 0.030 to $0.22 \cdot 10^5(\Omega\text{cm})^{-1}$, table 10.1). The rise of the conductivity between $r_s = 1.31$ and $r_s = 1.0$ (0.22 to $0.56 \cdot 10^5(\Omega\text{cm})^{-1}$ is considerably less although the pressure change in the system is much larger ($P \approx 150$ GPa at $r_s = 1.5$, 350 GPa at $r_s = 1.31$, and 2400 GPa at $r_s = 1.0$). The system transforms substantially in the pressure range of a few Mbar. This trend correlates with the substantial decrease in the ion-electron interaction over this pressure range (see the ion-electron pair-correlation function in figure 7.14 of chapter 7).
Finally, at $r_s = 0.5$ the conductivity exhibits the correct temperature trend of a metal: its value decreases with temperature. At the highest temperature

(10000 K) the value of the conductivity is not far from that of copper at room temperature ($6.4{\cdot}10^5(\Omega\mathrm{cm})^{-1}$). It is instructive to compare with other models. Stevenson and Salpeter [178] provided a simple formula for computing the conductivities in an astrophysical environment

$$\sigma \approx \frac{5 \cdot 10^{20} \rho^{4/3}}{T(1+3x)} esu, \tag{10.2}$$

where ρ is the density in g/cm^3, T the temperature in K, and x the He number fraction. For pure H ($x = 0$) we compare the results at $r_s = 1.5$, 1.31, 1.0, and 3000 K and $r_s = 0.5$ and 6000 K in figure 10.2. The approximation from

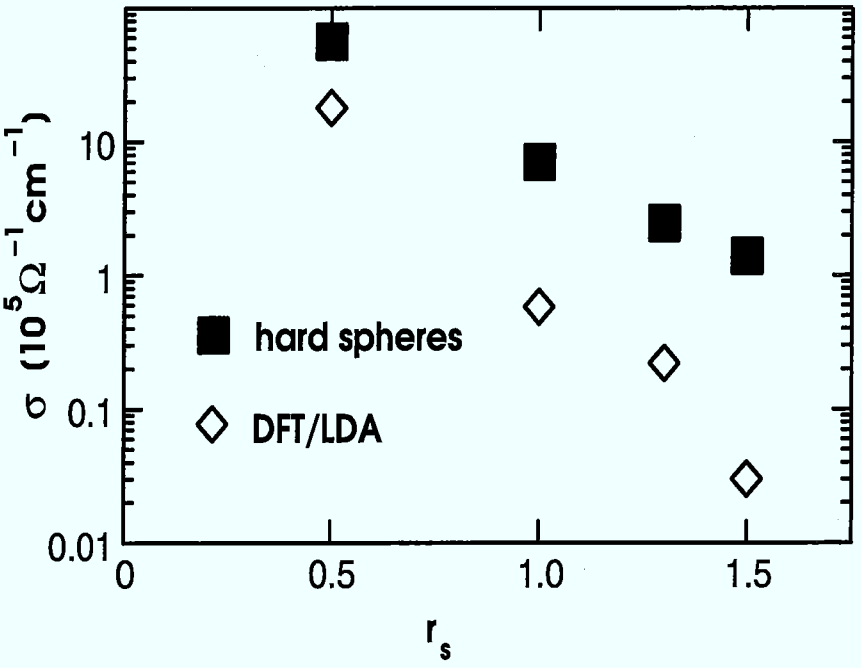

Figure 10.2: Comparison of our results at at $r_s = 1.5$, 1.31, 1.0 and 3000 K and $r_s = 0.5$ and 6000 K with conductivities computed with a hard sphere model [176].

Stevenson and Salpeter considerably overestimates the conductivities. For example, they propose for the conditions at the Jovian core ($P \approx 45$ Mbar, $T \approx 20000$ K) the conductivity to be close to those of room-temperature alkali metals at normal conditions whereas in our computations comparable values are only realized at much higher pressures ($r_s = 0.5$ corresponding to about 110 Mbar). Formula 10.2 was originally derived (in a more general form) by Stevenson and

Ashcroft [176] within a hard-sphere model for conduction in fully ionized liquid metals. The discrepancy with our results reflect the considerable screening in the system. We may expect the results to differ even more for H-He mixtures, because the He insertion leads to more tightly bound states (see the discussion in the previous chapter). The effect of He alloying on the conductivity in Stevenson and Ahscroft's model is easily seen from equation 10.2. For an astrophysical He contribution the conductivity is reduced by about 25 %. We computed the conductivity of the mixture for $r_s = 1.0$ and 3000 K. The result is shown in table 10.3. The He alloying is seen to reduce the conductivity by almost a factor of

Table 10.3: The conductivities σ of pure H and a H-He mixture of astrophysical composition at $r_s = 1.0$ and 3000 K (σ in $10^5/(\Omega\text{cm})$).

	H	$H_{0.9}He_{0.1}$
σ	0.56	0.23

3. This large effect reflects the substantial changes in the electronic structure caused by He insertion (see, e.g., figures 7.18 and 7.24 of H-He in comparison with figures 8.11 and 8.16).

Because of the better description of the electronic structure we believe our results to be more reliable than those from simpler models as Stevenson and Salpeter's formula or the results of OCP, at least for the temperature and density range investigated. After pointing out the discrepancies and giving some qualitative arguments concerning the accuracy of our approach a more detailed discussion of the approximations in our computations is in mandatory. There are five main sources of error, the usage of DFT/LDA, the relaxation-time approximation, finite size effects, statistical errors, and methodical inaccuracies.

The applicability of DFT with the local density approximation for the exchange-correlation part was discussed in chapter 7. What concerns the computation and inclusion of unoccupied states the same arguments apply as in chapter 7 where we used the band gap in the EDOS as an indicator for metalization. Band gaps are known to come out too small by roughly a factor of two, and one may expect the the conductivity to be overestimated. (The denominator in equation 10.1 becomes smaller). The induced error is of the same order as the other errors. Partly, we profit from error cancellation as the finite-size effects are likely to underestimate the conductivity.

The effect of the relaxation-time approximation, i.e., the assumption that collisions do not alter the form of the distribution function is a very common approximation for conductivity computations. Its effect is difficult to estimate but likely to be smaller than most of the other errors.
A severe limitation is the finite size of our system. The Bloch character of the electrons in the metallic regime is not well described by including the Γ-point only. As seen above, the error decreases with temperature. The reason is easy to understand. The finite temperatures tend to smear out the artificial gaps. In addition our computations with improved $\vec{k}$-space sampling showed that the gap at the Γ-point is an overestimation. However, the errors introduced into the values at $T \geq 3000$ K are not large (table 10.2). Apart from the computations at $r_s = 1.31$ we performed also computations with the Baldereschi-point at $r_s = 0.5$ and found the conductivities to lie in the range of the Γ-point results. Therefore, we believe the induced error at higher temperatures to be not larger than 25 - 50%.
We incur statistical errors, too. For $r_s = 1.5 - 1.0$ we calculated σ for at least two ionic configurations and took the average. The values of the conductivities varied typically by a factor of 2-3. $r_s = 0.5$ proved to be the most delicate problem. The electrons are nearly degenerate leading to very small energy denominators in formula 10.1 and stronger variations in the conductivity from sample to sample. For each conductivity more than ten configurations were sampled. The statistical error are presented in table 10.4.
There is the error from extrapolating the conductivities to ω =0. We tried dif-

Table 10.4: Conductivities σ in $10^5/(\Omega\text{cm})$ at $r_s = 0.5$ and their statistical errors.

T/K	σ
6000	18 ± 14
8000	14 ± 1
10000	10 ± 3

ferent interpolation strategies. If the form of the curve close to ω =0 is not very different from higher ω, the induced error will not be larger than 25% – 50 %. In addition there is a certain arbitrariness in choosing $\Delta\omega$ in formula 10.1. By varying $\Delta\omega$ the values for σ do not change substantially. An upper bound for this error is 20 %.

Finally, there is the approximation of zero temperature for electrons. For one sample we compared the result with those of L. Collins, J. Kress, and I. Kwon [39], who used finite temperature in the occupation of the electronc states, which enabled them to take the limit $\omega \to 0$ more accurately. Their result was larger by 25 %. The difference disappeared when they used $T = 0$ in the Fermi distribution function. The approximation of zero temperature for the electrons is most crucial in the semiconducting phase. Since we do not excite electrons into the conducting levels we obtain zero conductivity for finite ionic temperatures, too. In addition there is a technical reason why it is impossible in our scheme to compute the conductivity of semiconductors. The ac $\to$ dc extrapolation will not work if the ac conductivities are not of the same order as the dc conductivities. Taking all sources of errors into account we believe our results to be accurate within a factor of 2-3.

Chapter 11

Conclusions

"Simple" hydrogen is a complex system. It is only the extreme cases, very strong and very weak coupling of electrons and protons, where a faithful description of hydrogen can be achieved by simple models. Between the two extremes the situation is more complicated and the physics more complex due to the subtle interplay of electrons and protons. For an accurate description of the system the inclusion of the electronic structure is mandatory. We have used the Car-Parrinello method, a combination of molecular dynamics and density functional theory. The expensive computation of the electronic structure is rewarded by two major advantages:

- The Car-Parrinello method allows us to treat the system for a wide range of pressures and temperatures, and physical processes that cannot be described adequately with empirical potentials, such as the forming and breaking of bonds.

- In addition to the quantities provided by "conventional" molecular dynamics, the Car-Parrinello method allows us to investigate the electronic properties and the coupling of electronic and ionic degrees of freedom.

In our study of hydrogen we have aimed at regions of the phase space where simple, empirical methods fail. The treatment of molecular hydrogen with empirical pair potentials deteriorates with increasing pressure, and the induced errors are substantial above $\sim$ 1 Mbar, where the molecules begin to dissociate (chapter 5). At very high pressures, where hydrogen is atomic, pair potentials are constructed from the bare Coulomb potential and including the polarization of the electrons by perturbative methods. These potentials fail for lower pressures in the region of strong screening. We have demonstrated that, at pressures as high as $\sim$ 100 Mbar, the screening effects are underestimated and that these methods fail to give a quantitative description below $\sim$ 25 Mbar (chapter 7). Hydrogen-helium mixtures, in particular, cannot be described by perturbative treatment of screening effects because of the tightly bound helium states (chapter 8).

One focus of our studies has been the part of the **phase diagram of hydrogen** that is inaccessible to simple models, and we performed simulations for pressures of P = 1-110 Mbar and temperatures of T = 0-3000 K. Across this pressure range the hydrogen molecules give up their identities.

- The system changes drastically in **structural properties**, and complex intermediate stages appear in the transformation from a molecular system to an atomic one. These stages are characterized by the coexistence of hydrogen in different forms, atom, molecules, and short-lived conglomerates of atoms that align in filaments or strings (chapter 7). The structural changes are accompanied by

- A **transformation of the bonding characteristics**. At a pressure of several Mbar when the molecules lose their identities, directional bonds prevail in the system, typical of covalent systems. A very good example where the directional bonding plays a role is the string structure described in chapter 6 and discussed below. At the high edge of the transition regime hydrogen crystallizes in a close packed lattice, bcc, typical of a metal. In the electronic properties the structural changes are reflected in the delocalization of the electronic orbitals and the closing of the band gap in the electronic density of states (chapter 7). The changes in the electronic properties influence the transport properties.

- **Hydrogen becomes a conductor** in this pressure range. At normal conditions hydrogen is a good insulator. The increase in pressure reduces the band gap in the solid, and a sharp rise in the electronic conductivities signalizes metallization in the Mbar range (chapter 10).

Hydrogen is therefore transformed from a **covalent molecular insulator** to a **metallic atomic conductor** by increasing pressure.
A second focus of our studies comprised **astrophysical mixtures**. The envelope of the giant planets, Jupiter and Saturn, can be modelled by a hydrogen-helium mixture with about 10 % He. The pressures in these planets range from 1 bar to 45 Mbar, i.e.,the physics in the molecular-atomic transition of hydrogen applies to these planets. We have analyzed the effect of helium alloying on the structural and electronic properties (chapter 8). With regard to the astrophysical importance we have computed the free energies of high-pressure hydrogen-helium mixtures and used them to determine the miscibility gap (see chapter 9 and below).
We have studied physical phenomena and compute structural and electronic properties, such as the ionic pair correlation function, s- and p-component of the electron-ion pair correlation function, self diffusion coefficients, the delocalization of the orbitals with pressure, melting temperatures, electronic densities of state, demixing temperatures of H-He mixtures, and electronic conductivities. Here we seek quantitative understanding. Our goal here is quantitative understanding, and our method avoids some sources of errors typical of simpler models

and provides more reliable data, that are needed, e.g., in astrophysics to understand the interiors of planets. Let us finally summarize the two main results:

1. The metallization of hydrogen has been called the "holy grail of high-pressure physics" [9]. The theoretical investigation of the metallization depends strongly on the knowledge of the true ground state structure for high pressures (chapter 1). We have investigated possible structures and found new candidates for the ground state structures at $P = 1.5$ Mbar and $P = 3.5$ Mbar (chapter 6). The structure where the hydrogen molecules align in strings is particularly intriguing. The difference between inter- and intramolecular distance is small and decreases with pressure, and the structure is energetically favored over the molecular structures of previous studies ([94] and [130]). In addition there is a qualitative difference. The structures of [94] and [130] are characterized by clearly defined, tightly bound molecules. The alignment in strings in our structure is accompanied by the gradual dissociation of the molecules, which is consistent with the decrease in the Raman and IR vibron frequencies found in diamond-anvil cell experiments (chapters 1 and 6).

2. Jupiter and Saturn radiate about twice the energy they absorb from the sun. The energy of the excess heat radiation arises in part from internal cooling of the planets. For Saturn the cooling rate would be too high as sole energy source, and phase separation of hydrogen and helium has been proposed as an additional energy source. We have determine the internal energy differences between hydrogen-helium mixtures and the pure systems. The inclusion of structural relaxation and electronic screening is crucial, and computations that neglect either lead to overestimations of the demixing temperature. We have combined the computed internal energy differences with estimates of the volume ($P\Delta V(x)$) and entropy ($T\Delta S(x)$) terms to determine the demixing temperatures, and our results suggest no demixing in either Jupiter or Saturn. However, the demixing temperatures lie close to the internal temperatures of Saturn and a definite answer to this problem awaits improved models for the interior of the giant planets.

Appendix A

Derivation of the Kubo-Greenwood Formula

The Kubo-Greenwood formula is derived in several textbooks (e.g. [126],[68]). However, it is non-trivial (and usually not discussed) that the formula is compatible with periodic boundary conditions. Therefore, we derive equation 10.1 in extending the argument in [126] to periodic boundary conditions. The calculation is carried out for a degenerate electron gas at zero temperature, states being occupied up to the Fermi energy E_F. We consider the effect of the perturbation by the potential

$$U(x,t) = e \cdot F \cdot \frac{1}{k}\sin(kx)\cos(\omega t), \tag{A.1}$$

where k is the smallest reciprocal vector consistent with periodic boundary conditions and F is the strength of the applied electric field. Time-dependent perturbation theory gives for the transfer probability per unit time from the initial state $|E_i, \vec{q}_i\rangle$ to the final state $|E_f, \vec{q}_f\rangle$ (only stimulated emission)

$$w_{i\to f} = \frac{1}{4}e^2F^2\frac{2\pi}{\hbar}\left|\left\langle E_i+\hbar\omega, \vec{q}_f \left|\frac{1}{k}\sin(kx)\right| E_i, \vec{q}_i\right\rangle\right|^2 \delta(E_f, E_i+\hbar\omega). \tag{A.2}$$

The matrix element $\left\langle E_i+\hbar\omega, \vec{q}_f \left|\frac{1}{k}\sin(kx)\right| E_i, \vec{q}_i\right\rangle$ can be recast in the following way:

$$\begin{aligned}
&\left\langle E_i+\hbar\omega, \vec{q}_f \left|\frac{1}{k}\sin(kx)\right| E_i, \vec{q}_i\right\rangle = \\
&\quad = \frac{1}{k}\left\langle E_i+\hbar\omega, \vec{q}_f \left|\frac{1}{2}\left(\exp(ikx)-\exp(-ikx)\right)\right| E_i, \vec{q}_i\right\rangle \\
&\quad = \frac{1}{2k}\left(\left\langle u_{E_i+\hbar\omega,\vec{q}_f}\left|u_{E_i,\vec{q}-\vec{k}}\right\rangle - \left\langle u_{E_i+\hbar\omega,\vec{q}_f}\left|u_{E_i,\vec{q}_f+\vec{k}}\right\rangle\right.\right) \\
&\quad = -\left\langle u_{E_i+\hbar\omega,\vec{q}_f}\left|\frac{\partial}{\partial k_x}\,u_{E_i,\vec{q}_f}\right\rangle + O(k_x^2)\right.
\end{aligned}$$

$$= -\frac{1}{m\omega} \langle E_i, \vec{q}_f \left| \mathbf{p_x} \right| E_i + \hbar\omega, \vec{q}_f \rangle + O(k_x^2). \tag{A.3}$$

For the last transformation $\vec{k}$-$\vec{p}$ perturbation theory was applied. Furthermore, the decomposition of a Bloch function in plane wave and periodic part,

$$\left| E, \vec{k} \right\rangle = \exp\left(i\vec{k}\vec{r}\right) \left| u_{E,\vec{k}} \right\rangle \tag{A.4}$$

and the relation

$$\left\langle E, \vec{q} \left| \exp\left(i\vec{k}\vec{r}\right) \right| E', \vec{q}' \right\rangle = \delta\left(\vec{q}', \vec{q} - \vec{k}\right) \left\langle u_{E,\vec{q}} \left| u_{E',\vec{q}-\vec{k}} \right\rangle \right. \tag{A.5}$$

(which is easy to prove) were used.
Because here the proof differs from [126] where periodic boundary conditions are not taken into account we discuss the last transformation where transformation $\vec{k}$-$\vec{p}$ perturbation theory was used in more detail:
The starting point is Schrödinger's equation

$$\mathbf{H}\psi_{n\vec{k}}(\vec{r}) = \mathrm{E}_{n\vec{k}}\psi_{n\vec{k}}(\vec{r}). \tag{A.6}$$

Let $\mathrm{E}_{n\vec{k}}$ be non degenerate in the neighborhood of $\vec{k} = \vec{k_o}$. The periodic part of the Bloch function $\psi_{n\vec{k}}(\vec{r})$, $u_{n\vec{k}}(\vec{r})$ is expanded with regard to the complete function system $\left\{u_{n'\vec{k_o}}, n' = 1, 2, 3, ...\right\}$:

$$u_{n\vec{k}}(\vec{r}) = \sum_{n'} c_{n'n} u_{n'\vec{k_o}}(\vec{r}). \tag{A.7}$$

The variational principle of quantum mechanics leads to the eigenvalue problem

$$\sum_{n''} \left\langle n'\vec{k_o} \left| \mathbf{H}_{\vec{\mathbf{k}}-\vec{\mathbf{k_o}}} \right| n''\vec{k_o} \right\rangle c_{n''n} = \mathrm{E}_{n\vec{k}} c_{n'n} \text{ for all } n', \tag{A.8}$$

where

$$\begin{aligned} \mathbf{H}_{\vec{\mathbf{k}}-\vec{\mathbf{k_o}}} &\equiv \exp\left(-i\left(\vec{k} - \vec{k_o}\right)\vec{r}\right) \mathbf{H} \exp\left(i\left(\vec{k} - \vec{k_o}\right)\vec{r}\right) \\ &= \mathbf{H} + \hbar(\vec{k} - \vec{k_o})\frac{\vec{\mathbf{p}}}{m} + \frac{\hbar^2}{2m}(\vec{k} - \vec{k_o})^2. \end{aligned} \tag{A.9}$$

Let $\vec{q} \equiv \vec{k} - \vec{k_o}$. We expand $c_{n'n}$ and $\mathrm{E}_{n\vec{k}}$ in powers of $\vec{q}$

$$\begin{aligned} c_{n'n} &= \sum_{\mu=0}^{\infty} c_{n'n}^{(\mu)} \\ \mathrm{E}_{n\vec{k}} &= \sum_{\mu=0}^{\infty} \mathrm{E}_{n\vec{k}}^{(\mu)}. \end{aligned} \tag{A.10}$$

Then we insert this ansatz into A.8 and choose the free phase by requiring c_{nn} to be real. For our purpose it is sufficient to consider the first order of $\vec{q}$. We obtain for $n' = n$ $c^{(1)}_{nn} = 0$ and for $n' \neq n$:

$$c^{(1)}_{n'n} = \frac{\hbar}{m} \frac{\vec{q} \left\langle n'\vec{k}_o \left| \vec{\mathbf{p}} \right| n\vec{k}_o \right\rangle}{\mathrm{E}_{n\vec{k}_o} - \mathrm{E}_{n'\vec{k}_o}}. \tag{A.11}$$

Inserting the expansion A.10 into A.7 we find that

$$\left\langle u_{n'\vec{k}} \left| \frac{\partial}{\partial k_x} \right| u_{n\vec{k}} \right\rangle = \frac{\partial}{\partial k_x} c^{(1)}_{n'n} = \frac{\hbar}{m} \frac{\left\langle n'\vec{k}_o \left| \vec{\mathbf{p}} \right| n\vec{k}_o \right\rangle}{\mathrm{E}_{n\vec{k}_o} - \mathrm{E}_{n'\vec{k}_o}} \text{ for } n' \neq n, \tag{A.12}$$

i.e, the used identity.
We define the conductivity $\sigma(\omega)$ by Joule's law which gives the energy loss rate in terms of the conductivity $\sigma(\omega)$ and the electric field $\vec{E}$:

$$\frac{dE}{dtd\Omega} = \sigma(\omega)\vec{E}^2 = \frac{1}{4}\sigma(\omega)F^2, \tag{A.13}$$

where an average over space and time has been taken and for the last relation A.1 was applied. In microscopic terms the energy loss per unit space and time can be expressed as sum over the energy differences of the contributing energy levels times the probability for emission, i.e.,

$$\frac{dE}{dtd\Omega} = \frac{1}{\Omega} 2\hbar\omega \sum_{E > E_F - \hbar\omega} w_{E \to E+\hbar\omega}, \tag{A.14}$$

where Ω is the sample volume, $w_{E\to E+\hbar\omega}$ the probability for stimulated emission from state E to state $E + \hbar\omega$. The sum goes over all occupied states (with energies equal or larger than $E_F - \hbar\omega$ where E_F is the Fermi energy, because the other states cannot contribute anyhow). The factor two takes account of the spin orientations. With A.2 and A.3 we obtain for $\sigma(\omega)$

$$\sigma(\omega) = \frac{4\pi e^2}{\Omega m^2 \omega} \sum_{E > E_F - \hbar\omega} \left| \langle E \left| \mathbf{p_x} \right| E_f \rangle \right|^2 \delta(E_f - E + \hbar\omega). \tag{A.15}$$

In this equation the wave vector $\vec{q}$ has been left out, because nearly all our calculations have been performed for the Γ-point only. The generalisation to more than one $\vec{q}$-vectors is trivial

$$\sigma(\omega) = \sum_{\vec{q}} \sigma(\omega, \vec{q}) \cdot W_{\vec{q}}, \tag{A.16}$$

where $\sigma(\omega, \vec{q})$ is defined by A.15 but for the states in the matrix element being taken at $\vec{q}$ instead at the Γ-point. $W_{\vec{q}}$ is the weight of $\vec{q}$.

For practical applications a technical trick must be used. Since our eigenvalue spectrum is discrete $\sigma(\omega)$ is zero except at a finite number of frequencies. This unphysical feature springs from the finite size discretization of the eigenvalue spectrum. To get rid of it we average of a small, but finite frequency range, i.e.,

$$\sigma(\omega) \approx \frac{1}{\Delta\omega} \int_{\omega-\frac{1}{2}\Delta\omega}^{\omega+\frac{1}{2}\Delta\omega} \sigma(\omega) d\omega. \tag{A.17}$$

The conductivity becomes

$$\sigma(\omega) = \frac{1}{\Delta\omega} \frac{4\pi e^2}{\Omega m^2} \sum_{\left\{E_f \left| |E_f - \hbar\omega| \leq \frac{1}{2}\hbar\Delta\omega \right.\right\}} \sum_{E_i > E_F - (E_f - E_i)} \frac{\left| \langle E_i \left| \mathbf{p_x} \right| E_f \rangle \right|^2}{E_f - E_i}. \tag{A.18}$$

The double sum goes over all energy pairs (E_i, E_f) of unoccupied and occupied energy levels which correspond to frequencies in the frequency interval $\Delta\omega$, i.e., $|E_f - E_i - \hbar\omega| \leq \frac{1}{2}\hbar\Delta\omega$. In practice the energy interval must be chosen large enough that at least a few energy pairs (E_i, E_f) to contribute to the result.

Appendix B

Electron-Ion Pair Correlation Function

The inclusion of the electronic structure in dynamical simulations allows us to compute some additional physical quantities to compute in comparison with "conventional" molecular dynamics. One of them is the electron-ion pair correlation function, which provides a quantitative measure of the ion-electron correlations. It is usually not found in textbooks, for example [5], because the introduction of the electronic structure is only a recent development (Car-Parrinello 1985 [29]). Therefore, we provide a derivation of the spherical average of the first three momenta. Usually, only the first is computed, because the others are small. However, the p-component can provide valuable information about the bonding characteristics (see section 7.
The electron-ion pair correlation function is defined as

$$g_{eI}(\vec{r}) \equiv \frac{\Omega}{N_e N_I} \frac{1}{(2\pi)^3} \int d^3\vec{k} \left\langle \rho_e(\vec{k}) \rho_I(-\vec{k}) \right\rangle \exp(-i\vec{k}\vec{r}). \tag{B.1}$$

The bracket $\langle ... \rangle$ denotes the sample average. The aim of the following transformations is to make an angular momentum decomposition of g_{eI}. It is convenient to work with real spherical harmonics Y_l^m, which are obtained from the well-known complex ones $\mathcal{Y}_l^m$ by

$$\mathrm{Y}_l^m \equiv \begin{cases} \mathcal{Y}_l^m & : \quad m = 0 \\ \sqrt{\frac{1}{2}} \left(-\mathcal{Y}_l^m + \mathcal{Y}_l^{-m} \right) & : \quad m > 0 \\ \sqrt{\frac{1}{2}} i \left(-\mathcal{Y}_l^{-m} + \mathcal{Y}_l^m \right) & : \quad m < 0 \end{cases} \tag{B.2}$$

The pair correlation function is written in terms of its momenta

$$g_{eI}(\vec{r}) \equiv \sum_{lm} \tilde{g}_l^m(r) \mathrm{Y}_l^m(\vec{r}^o) \equiv \sum_{lm} g_l^m(\vec{r}). \tag{B.3}$$

The $\tilde{g}_l^m(r)$ are readily obtained by the decomposition of the exponential function into real spherical harmonics:

$$\exp(-i\vec{k}\vec{r}) = 4\pi \sum_l \sum_{m=-l}^{l} (-i)^l j_l(kr) \mathrm{Y}_l^m(\vec{k}^o) \mathrm{Y}_l^m(\vec{r}^o), \tag{B.4}$$

where the $j_l(kr)$ are the spherical Bessel functions. The quantity usually computed are the spherical averages of the momenta given by

$$\bar{g}_l^m(r) \equiv \sqrt{\frac{\langle g_l^m(\vec{r}) \,|\, g_l^m(\vec{r}) \rangle}{\langle 1 \,|\, 1 \rangle}} = \frac{1}{\sqrt{4\pi}} \left| \tilde{g}_l^m(r) \right|, \tag{B.5}$$

where the matrix elements are taken over the unit sphere. For the implementation it is convenient to express the $\bar{g}_l^m$ in Cartesian coordinates. In the following the momenta for the first three angular momenta are given

$$\bar{g}_o^o = \frac{\Omega}{N_e N_I} j_o(kr) Re \left\langle \sum_{\vec{k}} \rho_e(\vec{k}) S(-\vec{k}) \right\rangle \tag{B.6}$$

$$\bar{g}_1^m = \frac{\Omega}{N_e N_I} j_1(kr) Im \left\langle \sum_{\vec{k}} \rho_e(\vec{k}) S(-\vec{k}) \right\rangle \cdot \begin{cases} \sqrt{3}\frac{x}{r} & : \quad m = 1 \\ \vdots & \\ \sqrt{3}\frac{y}{r} & : \quad m = 0 \\ \vdots & \\ \sqrt{3}\frac{z}{r} & : \quad m = -1 \end{cases} \tag{B.7}$$

$$\bar{g}_2^m = \frac{\Omega}{N_e N_I} j_2(kr) Re \left\langle \sum_{\vec{k}} \rho_e(\vec{k}) S(-\vec{k}) \right\rangle \cdot \begin{cases} \sqrt{5}\sqrt{3}\frac{x}{r}\frac{y}{r} & : \quad m = 2 \\ \vdots & \\ \sqrt{5}\sqrt{3}\frac{x}{r}\frac{z}{r} & : \quad m = 1 \\ \vdots & \\ \sqrt{5}\left(\frac{z^2}{r^2} - \frac{x^2+y^2}{2r^2}\right) & : \quad m = 0 \\ \vdots & \\ \sqrt{5}\sqrt{3}\frac{y}{r}\frac{z}{r} & : \quad m = -1 \\ \vdots & \\ \sqrt{5}\frac{\sqrt{3}}{2}\left(\frac{x^2}{r^2} - \frac{y^2}{r^2}\right) & : \quad m = -2 \end{cases} \tag{B.8}$$

where $S(\vec{k}) \equiv \sum_{\vec{k}} \exp(-i\vec{k}\vec{r})$ is the structure factor and Re and Im denote the real and imaginary part. The ionic density is expressed via the structure factor

using

$$\rho_I(\vec{r}) = \sum_I \delta(\vec{r} - \vec{R}_I) = \sum_I \frac{1}{\Omega} \sum_{\vec{k}} \exp\left(i\vec{k}\left(\vec{r} - \vec{R}_I\right)\right). \tag{B.9}$$

It follows

$$\rho_I(\vec{k}) = S(\vec{k}). \tag{B.10}$$

Bibliography

[1] A. Alavi. private communication.

[2] A. Alavi, J. Kohanoff, M. Parrinello, and D. Frenkel. *Phys. Rev. Lett.*, 73:2599, 1994.

[3] A. Alavi, M. Parrinello, and D. Frenkel. *Science*, 269:1252, 1995.

[4] B. J. Alder and T. E. Wainwright. *J. Chem. Phys.*, 27:1208, 1957.

[5] M. P. Allen and D. J. Tildesley. *Computer Simulations of Liquids.* Clarendon, Oxford, 1987.

[6] N. W. Ashcroft. *Phys. Rev. Lett.*, 21:1748, 1968.

[7] N. W. Ashcroft. The dense hydrogen plasma: Translational, orientational, and electronic structure. In S. Ichimaru and S. Ogata, editors, *Proc. Oji. Int. Seminar on Elementary Processes in Dense Plasmas*, page 251, Reading, MA, 1995. Addison-Wesley.

[8] N. W. Ashcroft and N. D. Mermin. *Solid State Physics.* Saunders College, Philadelphia, 1976.

[9] Neil Ashcroft. *Physics World*, 8(7):43, 1995.

[10] G. B. Bachelet, D. R. Hamann, and M. Schlüter. *Phys. Rev. B*, 26:4199, 1982.

[11] A. Baldereschi. *Phys. Rev. B*, 7:5212, 1973.

[12] Pietro Ballone. *Physics World*, 6(11):25, 1993.

[13] T. W. Barbee III and Marvin L. Cohen. *Phys. Rev. B*, 43:5269, 1991.

[14] T. W. Barbee III and Marvin L. Cohen. *Phys. Rev. B*, 44:11563, 1991.

[15] T. W. Barbee III, A. Garcia, and M. L. Cohen. *Nature*, 340:369, 1989.

[16] T. W. Barbee III, A. Garcia, M. L. Cohen, and J. L. Martins. *Phys. Rev. Lett.*, 62:1150, 1989.

[17] W. Bauer, B. Lantzsch, J. P. Tönnies, and K. Walaschewski. *Chem. Phys.*, 17:19, 1976.

[18] A. D. Becke. *J. Chem. Phys.*, 84:4524, 1986.

[19] A. D. Becke. *J. Chem. Phys.*, 85:7184, 1986.

[20] H. J. C. Berendsen and W. F. van Gunsteren. Practical algorithms for dynamic simulations. In G. Ciccotti and W. G. Hoover, editors, *Molecular Dynamics Simulation in Statistical Mechanical Systems.* North Holland, 1986.

[21] B. J. Berne. *Statistical Mechanics.* Plenum Press, New York and London, 1977.

[22] S. Biermann, D. Hohl, and D. Marx. unpublished result.

[23] F. Birch. *Phys. Rev.*, 71:809, 1947.

[24] F. Birch. *J. Geophys. Res.*, 57:227, 1952.

[25] F. Birch. *J. Geophys. Res.*, 83:1257, 1978.

[26] P. E. Blöchl and M. Parrinello. *Phys. Rev. B*, 45:9413, 1992.

[27] E. G. Brovman, Yu. Kagan, and A. Kholas. *Sov. Phys. JETP*, 34:1300, 1972.

[28] E. G. Brovman, Yu. Kagan, and A. Kholas. *Sov. Phys. JETP*, 35:783, 1972.

[29] R. Car and M. Parrinello. *Phys. Rev. Lett.*, 55(22):2471, 1985.

[30] R. Car and M. Parrinello. The unified approach for molecular dynamics and density functional theory. In A. Polian, P. Loubeyre, and N. Boccara, editors, *Simple Molecular Systems and Very High Density*, page 455, New York, 1988. Plenum Press.

[31] D. M. Ceperley and B. J. Alder. *Phys. Rev. B*, 36:2092, 1987.

[32] G. Chabrier. private communication.

[33] G. Chabrier, D. Saumon, W. B. Hubbard, and J. I. Lunine. *Astrophys. J.*, 391:817, 1992.

[34] H. Chacham and S. G. Louie. *Phys. Rev. Lett.*, 66:64, 1991.

[35] D. J. Chadi and M. L. Cohen. *Phys. Rev. B*, 8:5747, 1973.

[36] G. Ciccotti and W. G. Hoover. *Molecular Dynamics Simulation in Statistical Mechanical Systems.* North Holland, 1986.

[37] J. Clérouin, E. L. Pollock, and G. Zérah. *Phys. Rev. A*, 46:5130, 1992.

[38] L. Collins. The pair correlation function was kindly provided by L. Collins.

[39] L. Collins, J. Kress, and I. Kwon. private communication.

[40] L. Collins, I. Kwon, J. D. Kress, N. Troullier, and D. Lynch. *Phys. Rev. B*, 50:9118, 1994.

[41] L. A. Collins, J. D. Kress, D. L. Lynch, and N. Troullier. *J. Quantum Spectrosc. Radiat. Transfer*, 51:65, 1994.

[42] L. Cui, N. H. Chen, and I. F. Silvera. *Phys. Rev. Lett.*, 74:4011, 1995.

[43] W. D. Daniels. Helium phase diagram. In A. Polian, P. Loubeyre, and N. Boccara, editors, *Simple Molecular Systems and Very High Density*, page 13, New York, 1988. Plenum Press.

[44] E. R. Davidson. *J. Comput. Phys.*, 17:87, 1975.

[45] J. Donohue. *The Structures of the Elements.* Wiley, New York, 1974.

[46] R. M. Dreizler and E. K. U. Gross. *Density Functional Theory: An Approach to the Quantum Many Body Problem.* Springer-Verlag, Berlin Heidelberg, 1990.

[47] T. S. Duffy, W. L. Vos, C. Zha, R. J. Hemley, and H. Mao. *Science*, 263:1590, 1994.

[48] J. H. Eggert, K. A. Goettel, and I. F. Silvera. *Europhys. Lett.*, 11:775, 1990.

[49] J. J. Mac Farlane. *Astrophys. J.*, 289:339, 1984.

[50] J. J. Mac Farlane and W. B.Hubbard. *Astrophys. J.*, 272:301, 1983.

[51] P. Focher, G. L. Chiarotti, M. Bernasconi, E. Tosatti, and M. Parrinello. *Europhys. Lett.*, 26:345, 1994.

[52] R. H. Fowler. *Mon. Not. R. Astron. Soc.*, 87:114, 1926.

[53] D. Frenkel. Free-energy computations and first-order phase transitions. In G. Ciccotti and W. G. Hoover, editors, *Molecular Dynamics Simulation in Statistical Mechanical Systems.* North Holland, 1986.

[54] D. Frenkel. Lecture notes on: Free-energy calculations. In M. Meyer and V. Pontikis, editors, *Computer Simulation in Materials Science*, page 257, New York, 1991. Plenum Press.

[55] C. Friedli and N. W. Ashcroft. *Phys. Rev. B*, 16:662, 1977.

[56] G. Galli, R. M. Martin, R. Car, and M. Parrinello. *Phys. Rev. B*, 42:7470, 1990.

[57] G. Galli and M. Parrinello. Ab-initio molecular dynamics: Principles and practical implementations. In M. Meyer and V. Pontikis, editors, *Computer Simulation in Materials Science*, page 283, New York, 1991. Plenum Press.

[58] G. Galli and A. Pasquarello. *Computer Simulations in Chemical Physics*, pages 261–313. Kluwer, Netherlands, 1993.

[59] A. Garcia, T. W. Barbee III, M. L. Cohen, and I. F. Silvera. *Europhys. Lett.*, 13:355, 1990.

[60] M. J. Gillan. Calculating the properties of materials from scratch. In M. Meyer and V. Pontikis, editors, *Computer Simulation in Materials Science*, page 257, New York, 1991. Plenum Press.

[61] V. Ginzburg. *Key Problems in Physics and Astrophysics.* Mir, Moscow, 1978.

[62] E. K. U. Gross and R. M. Dreizler. *Density Functional Theory.* Plenum Press, New York, 1995.

[63] B. I. Halperin and T. M. Rice. The excitonic state at the semiconductor-semimetal transition. In F. Seitz D. Turnbull and H. Ehrenreich, editors, *Solid State Physics*, volume 21, New York, 1968. Academic Press Inc.

[64] D. R. Hamann, M. Schlüter, and C. Chiang. *Phys. Rev. Lett.*, 43:1494, 1979.

[65] M. Hanfland, R. J. Hemley, and K. H. Mao. *Phys. Rev. Lett.*, 70:3760, 1993.

[66] J. P. Hansen. An introduction to molecular dynamics, with applicationsto the glass transition. In M. Meyer and V. Pontikis, editors, *Computer Simulation in Materials Science*, page 3, New York, 1991. Plenum Press.

[67] J.-P. Hansen, I. R. McDonald, and E. L.Pollock. *Phys. Rev. E*, 11:1025, 1975.

[68] W. A. Harrison. *Solid State Theory.* McGraw-Hill, New York, 1970.

[69] R. J. Hemley and H. Mao. *Phys. Rev. Lett.*, 61:857, 1988.

[70] R. J. Hemley and H. Mao. Progress on hydrogen at ultrahigh pressures. In S. Ichimaru and S. Ogata, editors, *Proc. Oji. Int. Seminar on Elementary Processes in Dense Plasmas*, page 271, Reading, MA, 1995. Addison-Wesley.

[71] R. J. Hemley, H. Mao, L. W. Finger, A. P. Jephcoat, R. M. Hazen, and C. S. Zha. *Phys. Rev.B*, 42:6458, 1990.

[72] F. Hensel, P. P. Edwards, and W. J. Nellis. submitted to *Nature.*

[73] J. O. Hirschfelder, C. F. Curtiss, and R. B. Bird. *Molecular Theory of Gases and Liquids.* John Wiley and Sons, New York, 1954.

[74] P. Hohenberg and W. Kohn. *Phys. Rev.*, 136:B864, 1964.

[75] D. Hohl, V. Natoli, D. M. Ceperley, and R. M. Martin. *Phys. Rev. Lett.*, 71:541, 1993.

[76] N. C. Holmes, M. Ross, and W. J. Nellis. *Phys. Rev. B*, 52:15835, 1995.

[77] W. G. Hoover. *Phys. Rev. A*, 31:1695, 1985.

[78] J. Hu, H. K. Mao, J. F. Shu, and R. J. Hemley. High-pressure energy dispersive x-ray diffraction technique with synchrotron radiation. In S. C. Schmidt J. W. Shaner G. A. Samara and M. Ross, editors, *High-Pressure Science and Technology*, page 441, New York, 1993. American Institute of Physics.

[79] W. B. Hubbard. *Phys. Earth Planet. Interiors*, 176:525, 1972.

[80] W. B. Hubbard. Models of jovian planets. In A. Polian, P. Loubeyre, and N. Boccara, editors, *Simple Molecular Systems and Very High Density*, page 203, New York, 1988. Plenum Press.

[81] W. B. Hubbard and H. E. de Witt. *Astrophys. J.*, 290:388, 1976.

[82] W. B. Hubbard and H. E. de Witt. *Astrophys. J.*, 290:388, 1985.

[83] Jürg Hutter, Hans Peter Lüthi, and Michele Parrinello. *Comput. Math. Sci.*, 2:244, 1994.

[84] S. Ichimaru, H. Iyetomi, and S. Tanaka. *Phys. Rep.*, 2&3:92, 1987.

[85] J. Ihm. Total energy calculations in solid state physics. *Rep. Prog. Phys.*, 51:105, 1988.

[86] J. Ihm, A. Zunger, and M. L. Cohen. *J. Phys. C*, 12:4409, 1979.

[87] K. Inoue, H. Kanzaki, and S. Suga. *Solid State Commun.*, 30:627, 1979.

[88] D. Jerome, T. M. Rice, and W. Kohn. *Phys. Rev.*, 158:462, 1967.

[89] T. V. Johnson. *Scientific American*, 273(6):28, 1995.

[90] R. O. Jones. *J. Chem. Phys.*, 71:1300, 1979.

[91] R. O. Jones. Density functionals, molecular dynamics, and more. In D. Neilson and M. P. Das, editors, *Computational Approaches to Novel Condensed Matter Systems*, page 37, New York, 1995. Plenum Press.

[92] R. O. Jones. Molecules and molecular dynamics. In E. K. U. Gross and R. M. Dreizler, editors, *Density Functional Theory*, page 273, New York, 1995. Plenum Press.

[93] R. O. Jones and O. Gunnarsson. The density functional formalism, its applications and prospects. *Reviews of Modern Physics*, 61(3):689, 1989.

[94] E. Kaxiras and J. Broughton. *Europhys. Lett.*, 17:151, 1992.

[95] E. Kaxiras, J. Broughton, and R. J. Hemley. *Phys. Rev. Lett.*, 67:1138, 1991.

[96] E. Kaxiras and Z. Guo. *Phys. Rev. B*, 49:11822, 1994.

[97] R. L. Kirk and D. J. Stevenson. *Astrophys. J.*, 316:836, 1987.

[98] S. Kirkpatrick, C. D. Gelatt, and M. P. Vecchi. *Science*, 220:671, 1983.

[99] J. K. Klepeis, K. J. Schafer, T. W. Barbee III, and M. Ross. *Science*, 254:986, 1991.

[100] J. Kohanoff and J. P. Hansen. *Phys. Rev. Lett.*, 74:626, 1995.

[101] W. Kohn. Overview of density functional theory. In F. Bassani, F. Fumi, and M. T. Tosi, editors, *Highlights of Condensed Matter Theory*, page 1, Amsterdam, 1985. North-Holland.

[102] W. Kohn and L. J. Sham. *Phys. Rev.*, 140:A1133, 1965.

[103] K. Kremer. Molekulardynamikmethoden. In *Computersimulation in der Physik*, Juelich, 1989. KFA Juelich GmbH.

[104] G. Kresse and J. Hafner. *Phys. Rev. B*, 49:14251, 1994.

[105] I. Kwon, L. A. Collins, J. D. Kress, N. Troullier, and D. L. Lynch. *Phys. Rev. E*, 49:R4771, 1994.

[106] I. Kwon, J. D. Kress, and L. A. Collins. *Phys. Rev. B*, 50:9118, 1994.

[107] R. LeSar. *Phys. Rev. Lett.*, 61:2121, 1988.

[108] D. H. Levy, E. M. Shoemaker, and C. S. Shoemaker. *Scientific American*, 273:68, 1995.

[109] M. Levy. *Proc. Natl. Acad. Sci. (USA)*, 76:6062, 1979.

[110] H. E. Lorenzana, I. F. Silvera, and K. A. Goettel. *Phys. Rev. Lett.*, 63:2080, 1988.

[111] P. Loubeyre. *Phys. Rev. Lett.*, 58:1857, 1987.

[112] P. Loubeyre, R. LeToullec, J. P. Pinceaux, H. Mao, J. Hu, and R. J. Hemley. *Phys. Rev. Lett.*, 71:2272, 1993.

[113] W. L.Slattery, G. D. Doolen, and H. E. DeWitt. *Phys. Rev. A*, 21:2087, 1980.

[114] K. J. Runge M. P. Surh C. Mailhiot and E. L. Pollock. *Phys. Rev. Lett.*, 69:3527, 1992.

[115] H. Mao and R. Hemley. *American Scientist*, 80:234, 1992.

[116] H. Mao and R. Hemley. *Rev. Mod. Phys.*, 66:671, 1994.

[117] H. Mao, R. J. Hemley, Y. Wu, A. P. Jephcoat, L. W. Finger, C. S. Zha, and W. A. Basset. *Phys. Rev. Lett.*, 60:2649, 1988.

[118] H. Mao, A. P. Jephcoat, R. J. Hemley, L. W. Finger, C. S. Zha, R. M. Hazen, and D. E. Cox. *Science*, 239:1131, 1988.

[119] H. K. Mao and R. J. Hemley. *Science*, 244:1462, 1989.

[120] M. S. Marley and W. B. Hubbard. *Icarus*, 73:536, 1987.

[121] D. Marx and M. Parrinello. *Z. Phys. B*, 95:143, 1995.

[122] A. K. McMahan, B. L. Hord, and M. Ross. *Phys. Rev. B*, 15:726, 1977.

[123] A. Messiah. *Quantenmechanik*, volume 2. Walter de Gruyter, Berlin, New York, 1985.

[124] N. Metropolis, A. W. Rosenbluth, M. N. Rosenbluth, A. H. Teller, and E. Teller. *J. Chem. Phys.*, 21:1087, 1953.

[125] B. I. Min, H. J. F. Jansen, and A. J. Freeman. *Phys. Rev. B*, 33:6383, 1986.

[126] N. F. Mott and E. A. Davis. *Electronic Processes in non-crystalline Materials.* Clarendon Press, Oxford, 1979. second edition.

[127] H. Nagara and T. Nakamura. *Phys. Rev. Lett.*, 68:2468, 1992.

[128] V. Natoli. *Quantum Monte Carlo Study of the High Pressure Phases of Solid Hydrogen.* PhD thesis, University of Illinois at Urbana-Champaign, 1994.

[129] V. Natoli, R. M. Martin, and D. M. Ceperley. *Phys. Rev. Lett.*, 70:1952, 1993.

[130] V. Natoli, R. M. Martin, and D. M. Ceperley. *Phys. Rev. Lett.*, 74:1601, 1995.

[131] A. I. Neishtadt. *Sov. Phys. Dokl.*, 21:80, 1976.

[132] W. J. Nellis, N. C. Holmes, A. C. Mitchell, R. J. Trainor, G. K. Governo, M. Ross, and D. A. Young. *Phys. Rev. Lett.*, 53:1248, 1984.

[133] W. J. Nellis, A. C. Mitchell, P. C. McCandless, D. J. Erskine, and S. T. Weir. *Phys. Rev. Lett.*, 68:2937, 1992.

[134] W. J. Nellis, M. Ross, and N. C. Holmes. *Science*, 269:1249, 1995.

[135] S. Nosé. *Mol. Phys.*, 52:255, 1984.

[136] S. Nosé. *J. Chem. Phys.*, 81:511, 1984.

[137] S. Nosé. *Mol. Phys.*, 57:187, 1986.

[138] S. Nosé. *Prog. Theor. Phys. Suppl.*, 103:1, 1991.

[139] T Oguchi and T. Sasaki. *Progress of Theoretical Physics Supplement*, (103):93, 1991.

[140] J. Oliva and N. W. Ashcroft. *Phys. Rev. B*, 23:6399, 1981.

[141] B. N. Parlett. *The symmetric Eigenvalue Problem.* Prentice-Hall, Englewood Cliffs, New York, 1980.

[142] G. Pastore, E. Samargassi, and F. Buda. *Phys. Rev. A*, 44:6334, 1991.

[143] M. C. Payne, M. P. Teter, D. C. Allen, T. A. Arias, and J. D. Joannopoulos. Iterative minimization techniques for ab-initio total-energy calculations: Molecular dynamics and conjugate gradient. *Reviews of Modern Physics*, 64(4):1045, 1992.

[144] J. I. Penman, J. Clérouin, and G. Zérah. *Phys. Rev. E*, 51:R 5224, 1995.

[145] J. P. Perdew. *Phys. Rev. B*, 33:8822, 1986.

[146] O. Pfaffenzeller, D. Hohl, and P. Ballone. unpublished result.

[147] J. P.Hansen, G. M. Torrie, and P. Vieillefosse. *Phys. Rev. A*, 16:2153, 1977.

[148] J. C. Phillips and L. Kleinman. *Phys. Rev.*, 116:287, 1959.

[149] Physics World. vol. 8, no. 7, July 1995.

[150] W. Pickett. *Comput. Phys. Rep.*, 9:115, 1989.

[151] E. L. Pollock and B. J. Alder. *Phys. Rev. A*, 15:1263, 1977.

[152] W. H. Press, B. P. Flannery, S. A. Teukolsky, and W. T. Vetterlin. *Numerical Recipes: The Art of Scientific Computing.* Cambridge University Press, Cambridge, 1992.

[153] Q. Qian, M. Weinert, G. F. Fernando, and J. W. Davenport. *Phys. Rev. Lett.*, 64:1146, 1990.

[154] D. E. Ramaker, L. Kumar, and F. E. Harris. *Phys. Rev. Lett.*, 34:812, 1975.

[155] D. K. Remler and P. A. Madden. *Molecular Physics*, 70(6):921, 1990.

[156] M. Ross, H. C. Graboske, and W. J. Nellis. *Phil. Trans. R. Soc. Lond.*, A 303:303, 1981.

[157] M. Ross, F. H. Ree, and D. A. Young. *J. Chem. Phys.*, 79:1487, 1983.

[158] J. P. Ryckaert, G. Ciccotti, and H. J. C. Berendsen. *J. Comput. Phys.*, 23:327, 1977.

[159] E. E. Salpeter. *Astrophys. J.*, 181:L83, 1973.

[160] D. Saumon and G. Chabrier. *Phys. Rev. Lett.*, 62:2397, 1989.

[161] D. Saumon and G. Chabrier. *Phys. Rev. Lett.*, 62:2397, 1989.

[162] D. Saumon and G. Chabrier. *Phys. Rev. A*, 44:5122, 1991.

[163] D. Saumon, W. B. Hubbard, G. Chabrier, and H. M. van Horn. *Astrophys. J.*, 391:827, 1992.

[164] J. Schnakenberg. *Algorithmen in der Quantentheorie und Statistischen Physik.* Verlag Zimmermann-Neufang, Ulmen, 1995.

[165] J. A. Schouten. Experimental studies of mixtures at very high pressures. In A. Polian, editor, *Simple Molecular Systems at Very High Density*, page 33, New York, 1988. Plenum Press.

[166] J. A. Schouten. *J. Phys.: Condens. Matter*, 7:469, 1995.

[167] J. A. Schouten, L. C. van den Bergh, and N. J. Trappeniers. *Chem. Phys. Lett.*, 114:401, 1985.

[168] I. Silvera. The phase diagram and excitations in solid hydrogen: Prospects for metallization. In A. Polian, editor, *Simple Molecular Systems at Very High Density*, page 33, New York, 1988. Plenum Press.

[169] I. Silvera. *Arkhimedes*, 2:108, 1992.

[170] I. Silvera, J. Eggert, K. Goettel, and H. Lorenzana. Towards metallic hydrogen at high pressures. In R. Pucci and G. Piccitto, editors, *Molecular Systems under High Pressure*, page 181, Amsterdam, 1991. Elsevier Science Publishers B.V. (North Holland).

[171] I. F. Silvera. *Rev. Mod. Phys.*, 52:393, 1980.

[172] I. F. Silvera and V. V. Goldman. *J. Chem. Phys.*, 69:4209, 1978.

[173] R. Smoluchowski. *Nature*, 215:691, 1967.

[174] G. P. Srivastava and D. Weaire. The theory of the cohesive energies of solids. *Advances in Physics*, 36(4):463, 1987.

[175] D. J. Stevenson. *Phys. Rev. B*, 12:3999, 1975.

[176] D. J. Stevenson and N. W. Ashcroft. *Phys. Rev. A*, 9:782, 1974.

[177] D. J. Stevenson and E. E. Salpeter. *Astrophys. J. Suppl. Ser.*, 35:239, 1977.

[178] D. J. Stevenson and E. E. Salpeter. *Astrophys. J. Suppl. Ser.*, 35:221, 1977.

[179] J. D. Stevenson. *Journal de Physique*, 41:C2–53, 1980. Colloque C2, supplément au n 3.

[180] I. Štich and R. Car. *Phys. Rev. B*, 44:4262, 1991.

[181] I. Štich, R. Car, and M. Parrinello. *Phys. Rev. Lett.*, 63:2240, 1989.

[182] I. Štich, R. Car, M. Parrinello, and S. Baroni. *Phys. Rev. B*, 39:4997, 1989.

[183] D. M. Straus and N. W. Ashcroft. *Phys. Rev. Lett.*, 38:415, 1977.

[184] M. P. Suhr, T. W. Barbee III, and C. M. Mailhiot. *Phys. Rev. Lett.*, 67:1138, 1991.

[185] N. Takeuchi and I. L. Garzón. *Phys. Rev. B*, 50:8342, 1994.

[186] M. P. Teter, M. C. Payne, and D. C. Allan. *Phys. Rev. B*, 40:12255, 1989.

[187] The Economist. vol. 336, no. 7926, p. 68, 5.8.1995.

[188] J. Theilhaber. *Phys. Fluids*, B 4:2044, 1992.

[189] J. Theilhaber. *International Journal of Quantum Chemistry, Quantum Chemistry Symposia*, 28:611, 1994.

[190] N. Troullier and J. L. Martins. *Phys. Rev. B*, 43:1993, 1991.

[191] J. S. Tse and D. D. Klug. *Science*, 378:595, 1995.

[192] L. C. van den Bergh and J. A. Schouten. *J. Chem. Phys.*, 89:2336, 1988.

[193] van Kranendonk. *Solid Hydrogen.* Plenum Press, New York, 1985.

[194] S. H. Vosko, L. Wilk, and M. Nusair. *Can. J. Phys.*, 58:1200, 1980.

[195] S. T. Weir, A. C. Mitchell, and W. J. Nellis. *Phys. Rev. Lett.*, in press.

[196] E. Wigner and H. B. Huntington. *J. Chem. Phys.*, 3:764, 1935.

[197] D. M. Wodd and N. W. Ashcroft. *Phys. Rev. B*, 25:2532, 1982.

[198] S. Chakravarty J. H. Rose D. Wood and N. W. Ashcroft. *Phys. Rev. B*, 24:1624, 1981.

[199] W. W. Wood. Early history of computer simulations in statistical mechanics. In G. Ciccotti and W. G. Hoover, editors, *Molecular Dynamics Simulation in Statistical Mechanical Systems.* North Holland, 1986.

[200] W. W. Wood and F. R. Parker. *J. Chem. Phys.*, 27:720, 1957.

[201] D. A. Young. *Phase Diagrams of the Elements.* University of California Press, Berkeley, 1991.

[202] D. A. Young, A. K. McMahan, and M. Ross. *Phys. Rev. B*, 24:5119, 1981.

[203] S. M. Younger. *Phys. Rev. A*, 45:8657, 1992.

[204] G. Zérah, J. Clérouin, and E. L. Pollock. *Phys. Rev. Lett.*, 69:446, 1992.

[205] Q.-M. Zhang, G. Chiarotti, and A. Selloni. *Phys. Rev. B*, 42:5071, 1990.

Danksagung

Besonders herzlich danke ich Herrn Dr. Detlef Hohl für die interessante Themenstellung und hervorragende Zusammenarbeit, für das freundschaftliche Arbeitsklima und viele wertvolle Anregungen, Hilfestellungen und Ratschläge.

Sehr dankbar bin ich Herrn Dr. Pietro Ballone für eine großartige Zeit der Zusammenarbeit, für seine große Hilfsbereitschaft und stete Ansprechbarkeit.

Ich danke Herrn Prof. Dr. Dederichs sehr herzlich für die Betreuung meiner Arbeit. Seine Freundlichkeit, sein Humor und seine Hilfsbereitschaft machten den Umgang mit ihm zu einem Vergnügen.

Frau Silke Biermann, Frau Dr. Angela Borrmann und Herrn Dipl.-Phys. Stefan Hunsicker danke ich für zahlreiche interessante Diskussionen über Physik und andere Dinge des Lebens.

Für ein angenehmes Arbeitsklima und viele fachliche Gespräche danke ich Herrn Dr. Michael Eisele, Herrn Dr. Andreas Körner und Herrn Dr. Christian Schroer.

Sehr dankbar bin ich Herrn Dr. Jones für seine Hilfe bei vielen kleinen und großen Problemen, die nicht nur Computer betrafen.

Herrn Prof. Dr. Eilenberger danke ich vor allem für viele weltanschauliche und philosophische Anregungen. Aber auch an dem angenehmen Arbeitsklima in der Theorie I hat er den größten Anteil.

Herrn Dr. Andreas Bringer und Herrn Prof. Dr. Sturm danke ich für ihre Hilfsbereitschaft und Umgänglichkeit.

Schließlich bedanke ich mich bei allen anderen Mitgliedern unserer Gruppe. Sie haben einen großen Anteil daran, daß die drei Jahre in der KFA für mich eine schöne, interessante Zeit waren.

FORSCHUNGSZENTRUM JÜLICH GmbH

KFA

Jül-3281
September 1996
ISSN 0944-2952